WEARABLE ANTENNAS:
DESIGN, CONNECTIVITY AND
EVALUATION MEASUREMENT
TECHNIQUES

By

Aris Tsolis

A Doctoral Thesis Submitted in Partial Fulfilment of the Requirements for the Award of the Degree of Doctor of Philosophy (PhD) of Loughborough University under a Joint PhD Programme with the National Centre for Scientific Research "Demokritos", Greece.

May 2016

Loughborough University

DEMOKRITOS
NATIONAL CENTER FOR SCIENTIFIC RESEARCH

στη μνήμη της αγαπημένης μου Θείας, Ντίνα Ζώη-Τίλα

στους γονείς μου, Γιώτα και Γιώργο

στην αγαπημένη μου, Αγγελική

&

στον δάσκαλο, Τραϊανό Β. Γιούλτση

Abstract

Wearable antennas and electronics technology rapidly grows the last decades and leads to a future where smart textiles will be integrated into our garments. However the wearable technology research includes unsolved or of different approach challenges. This thesis deals with challenges regarding wearable antenna characterization and measurements, textile antennas feeding and textile transmission lines interconnecting. Regarding the wearable antenna characterization and measurements, a novel design of a liquid torso phantom and a new methodology for evaluating wearable antenna performance by using the cylindrical near field measurement technique are proposed. As for the textile antennas and transmission lines feeding and interconnecting, two novel methods are proposed.

This thesis presents the design, realization and evaluation of a low cost and lightweight hollow oval cross-section (HOCS) torso phantom appropriate for wearable antenna performance assessment in the frequency range of 2-6GHz. The phantom consists of an empty inner space (hollow) surrounded by a shell with double plastic walls between which there is a tissue simulating liquid. The phantom's plastic shell is made of a low loss cast acrylic and the liquid is a commercially available one. The HOCS phantom is compared with a corresponding full liquid torso phantom and a numerical heterogeneous anthropomorphic voxel phantom via simulations. Measurements with the realized HOCS phantom are compared with human subjects and a realistic homogeneous anthropomorphic solid phantom. The proposed HOCS phantom is evaluated as a good candidate for wearable antenna performance assessment including reflection coefficient, near field (E-field), on-body communication link budget and far field measurements.

Additionally a new methodology, which uses the cylindrical near field (CNF) measurement technique, to evaluate wearable antennas performance parameters, is presented. For this methodology the proposed HOCS phantom and three patch antennas operating at 2; 2.5 and 5GHz, appropriate for Off-body communication link, are used. The main advantage of this methodology is that less measurement space is required compared to a conventional far field test site and the use of a heavy duty roll axis, so as to rotate the phantom for 3D pattern coverage is excluded compared to a conventional spherical near field test site. An evaluation technique which is targeted for the CNF test site appropriate for wearable antenna measurements mounted

on HOCS torso phantom is proposed and described. The goal of the evaluation technique is to find the optimum CNF measurement volume which would result into transformed far field parameters which will be closest to the simulation far field results. The evaluation technique is assessed by comparing the far field performance parameters (gain, directivity and efficiency), derived from the CNF measurements, with simulations and with direct far field measurements carried out inside a characterized full wave chamber. Validation of the evaluation technique is carried out by applying the derived optimum CNF volumes on the HOCS phantom, for the three antennas, and then measuring and comparing the results with simulations. Finally, the new methodology is described by measuring the patch antennas performance on HOCS phantom by using the CNF technique. The patch antennas are mounted in different locations on the HOCS phantom. The new methodology can be summarized as follows: *The near field (E-field) for each antenna in each location is recorded; from the E-field results, assumptions for the maximum direction of radiation are derived and verified from the transformed far field radiation patterns.The far field parameters (gain, directivity) are produced from the near field results, verifying the assumptions made from the near field results about the directivity.*

Regarding the textile transmission lines (TL), two new methods for interconnecting textile TL are presented in terms of design and fabrication: (a) "*slotted overlap*" (SO) and (b) "*complementary overlap*" (CO). The proposed TL interconnection models follow the basic structure of a stripline. A straight stripline, without interconnections, is used as a reference and it is compared with the proposed interconnection methods. The investigated methods exclude the use of rigid coaxial connectors for the interconnection. The most efficient method, CO, is fabricated with purely textile materials (all-textile) so as to meet the "*wearable criteria*". For this method the use of Velcro is investigated to provide practical and flexible interconnection characteristics. Additionally, the two interconnecting methods (SO and CO) described above are also investigated for feeding textile patch antennas with striplines. This result into corresponding structures which include a feeding stripline and a textile patch antenna (operating at 2.5GHz). The proposed antennas are probe and microstrip fed ones corresponding to the SO and CO interconnecting methods respectively. For the evaluation of the CO interconnecting/feeding method, an antenna prototype is designed and fabricated as an all-textile, practical and flexible structure. From measurements and simulations the CO antenna feeding method is proved as an efficient one. Finally, the CO concept implementation is enhanced by the demonstration of a real life wearable scenario.

Acknowledgments

List of Publications

J1. <u>A. Tsolis</u>, A.A. Alexandridis, W.G. Whittow, J.C. Vardaxoglou, "All-textile and flexible interconnecting and feeding of striplines and wearable patch antennas", IET, Microwaves, Antennas & Propagation (in preparation)

J2. <u>A. Tsolis</u>, A. Paraskevopoulos, W.G. Whittow, A.A. Alexandridis, J.C. Vardaxoglou, " Design, Realization and Evaluation of a Liquid Hollow Torso Phantom Appropriate for Wearable Antenna Assesment", IET, Microwaves, Antennas & Propagation (Submitted March 2016)

J3. A. Paraskevopoulos, <u>A. Tsolis</u>, A.A. Alexandridis, J.C. Vardaxoglou, "Cylindrical Near-Field Assessment of Wearable Antennas for Body-Centric Communications", IET, Microwaves, Antennas & Propagation, (Submitted August 2016)

J4. <u>A. Tsolis</u>, A.A. Alexandridis, W.G. Whittow, J.C. Vardaxoglou, "Connecting wearable textile transmission lines: all-textile fabrication solutions and design techniques", IET Electronics Letters, Vol. 51, No. 15, pp. 1136-1138, 23rd July, 2015

   o Featured article: "*Flexible use*"

J5. <u>A. Tsolis</u>, W.G. Whittow, A.A. Alexandridis, J.C. Vardaxoglou, "Embroidery and related manufacturing techniques for wearable antennas: challenges and opportunities", Electronics, Vol. 3, No. 2, pp. 314-338, May 2014, *Review*

C1. <u>A. Tsolis</u>, W.G. Whittow, A. Chauraya, A.A. Alexandridis, J.C. Vardaxoglou, "A calibration of a cylindrical near field test site appropriate for wearable antenna measurements on a liquid torso phantom at 2GHz", Proc. of the 11th Loughborough Antennas & Propagation Conference (LAPC 2015), Loughborough, UK, 2-3 November 2015

C2. <u>A. Tsolis</u>, A.A. Alexandridis, W.G. Whittow, J.C. Vardaxoglou, "Investigation of textile striplines connectivity for feeding and connecting wearable antennas", Proc. of the 9th European Conference on Antennas & Propagation (EuCAP 2015), Lisbon, Portugal, 12-17 April 2015

C3. <u>A. Tsolis</u>, W.G. Whittow, A. Chauraya, A.A. Alexandridis, J.C. Vardaxoglou, "Evaluation of a realized hollow torso phantom for wearable antenna measurements", Proc. of the 10th

Loughborough Antennas & Propagation Conference (LAPC 2014), Loughborough, UK, 10-11 November 2014

C4. <u>A. Tsolis</u>, W.G. Whittow, A.A. Alexandridis, J.C. Vardaxoglou, "Evaluation of a Human Body Phantom for Wearable Antenna Measurements at the 5.8GHz Band", Proc. of the Loughborough Antennas & Propagation Conference, (LAPC 2013), Loughborough, UK, 11-12 November 2013

Acronyms

AUT	Antenna under test
BW	Bandwidth
CDP	Conducting plate
CO	Complementary overlap
CPW	Coplanar waveguide
CNF	Cylindrical near field
dB	Decibels
dBi	Decibels compared to an isotropic radiator
EBG	Electromagnetic bandgap
EM	Electromagnetic
EGSP	Evaluated geometrical setup parameters
FDTD	Finite difference time domain
FF	Far field
FFT	Fast Fourier transform
FM	Frequency modulation
GND	Ground plane
GPS	Global positioning system
GSM	Global system for mobile
GSM1900	Global system for mobile at 1900MHz
HOCS	Hollow oval cross-section
IEEE	Institute of electrical and electronics engineers
ISM	Industrial, scientific and medical

LNA	Low noise amplifier
LOS	Line of sight
MFPA-CO	Microstrip fed patch antenna – complementary overlap
NFtoFF	Near field to far field transform
PFPA-SO	Probe fed patch antenna – slotted overlap
PIFA	Planar inverted F antenna
RAMS	Rapid antenna measurement system
RF	Radio frequency
RFID	Radio frequency identification
SIW	Substrate integrated waveguide
SMA	SubMiniature version A
SO	Slotted Overlap
ST	Straight
TC	Test cases
TE	Transverse electric
TM	Transverse magnetic
TEM	Transverse electromagnetic
TL(s)	Transmission line(s)
UHF	Ultra high frequency
UWB	Ultra wideband
VHF	Very high frequency
VNA	Vector network analyser

Wi-Fi   Wireless fidelity

WLAN   Wireless local area network

List of Symbols

ρ	Resistivity ($\Omega \cdot$m)
σ	Conductivity (S/m)
σe	Electric conductivity of absorber (S/m)
σm	Magnetic conductivity of absorber (S/m)
δ	Skin depth (μm)
ε_0	Permittivity of free space (8.85×10^{-12} F/m)
ε_r	Relative permittivity
$\varepsilon r2$	Dielectric constant of absorber
$\varepsilon r1$	Dielectric constant of HOCS phantom shell
μ_0	Permeability of free space ($4\pi \times 10^{-7}$ H/m)
μ_r	Relative permeability
μr	Relative permeability of absorber
λ	Wavelength (m)
c	Free-space velocity of light (3×10^8 m/s)
F or f	Frequency (Hz)
f_0	Resonant frequency (Hz)
$\tan\delta$	Loss tangent
D	Largest dimension of the radiator of an antenna (m)
Z_0	Characteristic impedance (Ω)
Z_{in}	Input impedance (Ω)
ZF	Absorber impedance (Ω)
ZF0	Free space impedance (377 Ω)

E_{total}	Electric field intensity (V/m)
Q	Quality factor
A	Electric field attenuation (dB)
abs	absorption rate of RF absorber (dB/mm)
T	Hollow oval cross-section phantom liquid thickness (mm)
$e_{rad,}$ e	Radiation efficiency of an antenna (%)
A_V	Near field amplitude component on Y-axis – Vertical component (dB)
A_H	Near field amplitude component on Theta-axis – Horizontal component (dB)
T_X	Transmitting antenna
R_X	Receiving antenna
ΔY	Sampling on the linear Y-axis of the cylindrical near field setup (mm)
$\Delta \theta$	Sampling on the Azimuth of the cylindrical near field setup (°)
r	the radius of the minimum cylinder that is centred on the axis of rotation (Azimuth) and encloses the AUT in a CNF measurement site (m)
D	Measured directivity of the AUT (dBi)
Prm	Maximum power measured at the AUT during the scan
{Prm}	The all over directions average power measured at the AUT during the scan
G	Measured Gain of the AUT (dBi)
$(P_r\text{-}P_t)$	Far field peak ratio of the received power at the AUT aperture to the input power at the probe antenna calculated by MiDAS
G_P	Measured Gain of the probe antenna
M	Mismatch losses factor of the probe antenna and the AUT
Γ_s	Source return loss

Γ_a	AUT return loss
Γ_p	Probe antenna return loss
Γ_x	Receiver return loss
L	Cylindrical near field linear scan length (mm)
d	Cylindrical near field separation distance between T_X and R_X (AUT) (cm)
θ_{FF}	Far field valid angle (º)
α	Height of the AUT (m)
$\Delta 1$	Near field amplitude difference, of the co-polarized component of the AUT with the Tx, between the maximum (peak) value with the value on the positive linear scan edge (dB)
$\Delta 2$	Near field amplitude difference, of the co-polarized component of the AUT with the Tx, between the maximum (peak) value with the value on the negative linear scan edge (dB)
S_{ij}	Scattering parameters (Reflection coefficient when i=j and Transmission coefficient when i≠j)
W_{GD}	Ground plane width of a stripline (mm)
W	Feeding width of a stripline (mm)
b	Dielectric substrate height of a stripline (mm)
f_c	TE mode cut-off frequency (GHz)
λ_d	Wavelength in a dielectric medium (m)
D_i	Physical discontinuity in the i-axis where i could be x,y and z (mm)

Contents

1. Introduction

2. Hollow oval cross-section (HOCS) liquid torso phantom: design, realization and evaluation

3. Cylindrical near field measurement technique for wearable antennas mounted on HOCS torso phantom

4. Textile transmission lines interconnection methods

5. Feeding methods for wearable textile patch antennas

6. Conclusions and future work

Appendix A – Dipole and monopole antennas

Appendix B – Patch antennas

CHAPTER 1

INTRODUCTION

1.1 Overview of wearable antennas

Antennas technology exists in lots of modern applications which facilitate and improve the quality of humans' day life. Such applications include: mobile phones, satellite communications, Wi-Fi, GPS, Bluetooth, Zig-bee, television, telemedicine radio, RFID cards [1],[2]. An important category which belongs in the antennas technology is the wearable antennas one. Wearable antennas are supposed to be worn (placed on or are part of the garment) and to operate on a live tissue (e.g. human body) environment. Wearable antennas technology has rapidly grown over the last couple of decades. It could be said and assumed that this technology is the future of smart garments and furthermore the future of our daily life. A wearable antenna or electronic is meant by definition to be part of the garments worn by humans or animals. Smart garments will emerge in various applications including: sports, emergency workers, military, medical and space applications or even in casual clothes or fashion [3], [4]. So far, a large number of wearable antennas has been already proposed for many different applications including miniaturized or low profile rigid and flexible textile antennas [4] emerging radiation characteristics appropriate for On/Off-body communication link requirements [3].

1.1.1 Rigid wearable antennas

A shorted spiral-like patch antenna operating at 430 MHz suitable for military RF Communications was presented in [5] (Fig. 1-1 a). This antenna was etched on rigid FR4 dielectric. The use of an electromagnetic bandgap (EBG) structure makes this antenna suitable for wearable applications by reducing the power radiated towards the wearer. The overall size of this antenna is 11.4 cm × 7.6 cm, which is small compared to the wavelength at the resonant frequency. In [6] a dipole and a spiral antenna (Fig. 1-1 b) for military wearable applications (100–500 MHz) were proposed. These antennas are unobtrusive and low profile.

In [7] three antennas: (a) $\lambda_g/4$ antenna with ground shield; (b) a dipole V antenna and (c) a square dipole antenna were made out of copper with a glass—epoxy substrate (ε_r = 4.8) and proposed for operation at 868 MHz, for medical tele-monitoring applications. These antennas would be more suitable for a patient to wear if they were textile which will make them more flexible and comfortable. In [8] Salonen presented a dual band (900 MHz & 2.4 GHz) Planar Inverted-F Antenna (PIFA) antenna for wearable applications suitable for the Global System for Mobile Communications (GSM) and for short range Bluetooth bands. The antenna was designed as a PIFA so as to radiate away from the human body. A dual mode antenna for on/off-body communications (10 MHz/2.45 GHz) was proposed in [9] (Fig. 1-1c). This antenna consists of an L-shaped slit loaded for the 2.45 GHz band (off-body link) connected with an electrode which is mounted on the body and is suitable for the 10 MHz (on-body) link. In [10] a four arm spiral slot patch antenna for radio telemetry capsules was proposed for operation at 915 MHz. In terms of miniaturization a reduced ground plane shorted patch antenna for on-body communications at 2.45 GHz was proposed by Scanlon *et al*. [11] with a miniaturized ($\sim\lambda/5$) ground plane. A monopole antenna mounted vertically on the body radiates the same way (energy is directed tangential to the surface of the human body) as this shorted patch [11]. However, this shorted patch proved to be more suitable for the on-body link because it is compact. In [12] a miniaturized diversity antenna dedicated to wireless body area network was proposed. The antenna was printed on FR4. The combination of a PIFA and a top-loaded monopole yielded distinct patterns. The strong isolation observed between the broadside and the end-fire radiation of the antenna is a significant feature which limits the correlation between the received signals. Other miniaturized wearable antenna designs appropriate for UHF and RFID operation are described in [13],[14],[15].

1.1.2 Textile wearable antennas

Smart clothes evolution will eventually result in the establishment of textile antennas in widespread use. This may mean that clothes and wearable textile antennas or electronics will be designed to be integrated in one garment. A textile antenna (2.45GHz – ISM band) suitable for fire fighters jackets was presented in [16] (Fig. 1-1e). The substrate shell of jacket was made of aramid fabric which is fireproof. In [17],[18] a flexible dual resonance frequency (S-band) PIFA was proposed for commercial smart clothing. An inexpensive textile patch antenna for off-body wireless sensor communications for monitoring patients at the 915 MHz Industrial, Scientific and Medical (ISM) radio frequency band is presented in [19]. Zelt was

used for the conducting parts and felt for the substrate of this antenna. The cost per square meter of Zelt and Felt is equal to $20 [19]. With one square meter of these two materials about 5–6 such antennas can be fabricated. This has demonstrated a possible low cost advantage of the wearable textile antennas. A dual band E-shaped patch textile antenna made from felt and copper tape is presented by Salonen in [20]. This antenna operates at 1850 MHz (BW = 100 MHz) and 2450 MHz (BW = 110 MHz). The wearer with this antenna can access GSM1900 and Wi-Fi communication links. Additionally a dual-band wearable textile antenna for the same communication links was proposed in [21]. A novel circularly polarized textile antenna for personal satellite communications (GPS / L-band) is proposed in [22]. Two textile antennas using Nora Dell for conducting sections and Nomex for the substrate were designed in [23]. The two antennas were proposed to be integrated in an extravehicular suit (astronaut suit) for space network applications. The eight e-textile patch antenna array is shown in Fig. 1-1f. A complementary-8 shape e-textile antenna element can be used as part of a body worn communication and navigation antenna system that supports many different bands, including those used by both 802.11 and 802.16 bands. A system of six complementary-8 shape e-textile antennas shifted by 90 degrees can be used for polarization diversity and omnidirectional coverage most of the observable sphere surrounding the astronaut. This is an important requirement for the astronaut communication and navigation. In [24] a fabric equiangular spiral antenna (2-4GHz) using Nora Dell for the conductive sections was fabricated and presented. The earliest wearable active textile receiving antenna in the 2.45 GHz ISM band was proposed in [25],[26]. An LNA was fabricated on a hybrid textile fabric and positioned directly underneath a wearable patch antenna. In [27] a dual band (2.45 & 5.7GHz) coplanar waveguide feed patch antenna was designed. Zelt is used for the conductive parts of the antenna and felt for the substrate. The use of an electromagnetic bandgap (EBG) substrate under the patch antenna improves the gain and reduces the back radiation by at least 13dB making the antenna suitable for wearable applications and more tolerant to the effects of the lossy human body in terms of antenna efficiency. Another triangular textile patch antenna over an EBG structure was presented in [28]. Two novel, for UWB operation, textile antenna designs were proposed in [29]. The conducting parts of the antennas were made with Shieldit and the substrate is a thick felt. These antennas are fed by a coplanar waveguide. Because of the lack of a ground plane between the antenna and the human body the placement of the antennas on the body degraded the S11 at most locations. The dielectric coupling between the antennas and the body introduced a down shift of the resonant frequencies. The coupling with the lossy body is expected to degrade the efficiency and the gain of these antennas. Therefore,

the use of an EBG structure as previously referred will improve the performance of the coplanar waveguide feed textile antennas. A broadband waveguide slot antenna (5GHz) was proposed where denim (which is a very common material found in every day garments) was used as the substrate filling the waveguide. The proposed waveguide slot antenna was cheap to manufacture [30]. A novel wearable substrate integrated waveguide (SIW) antenna (2.45GHz) fabricated entirely from textile materials was presented in [31]. The SIW-on-textile integration results in an antenna exhibiting high robustness against bending, low influence of the human body and high front-to-back ratio. In addition this antenna is light weight, flexible and low cost, thus making this antenna well suited for on-body use.

Various embroidered textile antennas have been proposed for different applications. A low frequency (COSPAS/SARSAT satellite beacon—406 MHz) embroidered spiral antenna was proposed in [32] (Fig. 1-1g). An embroidered wearable multi-resonant folded dipole antenna for FM reception was fabricated in [33]. Also an UWB embroidered antenna design where stainless steel thread was used for the conductive thread is presented in [34] (Fig. 1-3 d). GSM and Wi-Fi embroidered textile antennas were fabricated onto regular fabrics using an automated embroidery procedure with high density stitching [35]. The proposed antennas offer user-comfort and flexibility.

As it can be concluded from the above, various designs of wearable antennas for lots of applications have been successfully proposed. These designs take into account the "wearable" criteria such as: miniaturization, flexibility, textile, lossy human body operating environment. From the engineering point of view there are many open issues related with the wearable antennas design implementation and characterization. Issues such as: the facilitation and the cost of the wearable antenna performance measurement and assessment, the physical space of the measurement test site required and the flexible, textile and "wearable practical" feeding and interconnecting of wearable textile antennas and transmission lines. In the framework of this thesis we have focused on two major research challenges: (a) wearable antenna measurements (Section 1.2) and (b) wearable textile antennas and transmission lines feeding and interconnecting (Section 1.3). Additionally, the novel contributions of this thesis which propose a solution to each unsolved challenge are described in the fourth section of this chapter (Section 1.4). Finally, the fifth section of this chapter (Section 1.5) outlines all the chapters of this thesis, in order to prepare the reader for the contents of this thesis.
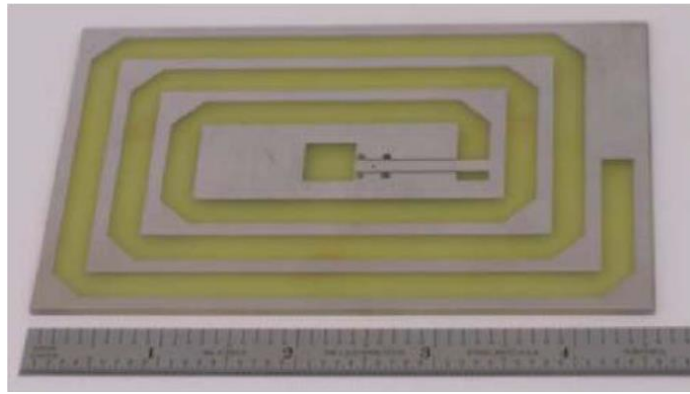
a)

b)
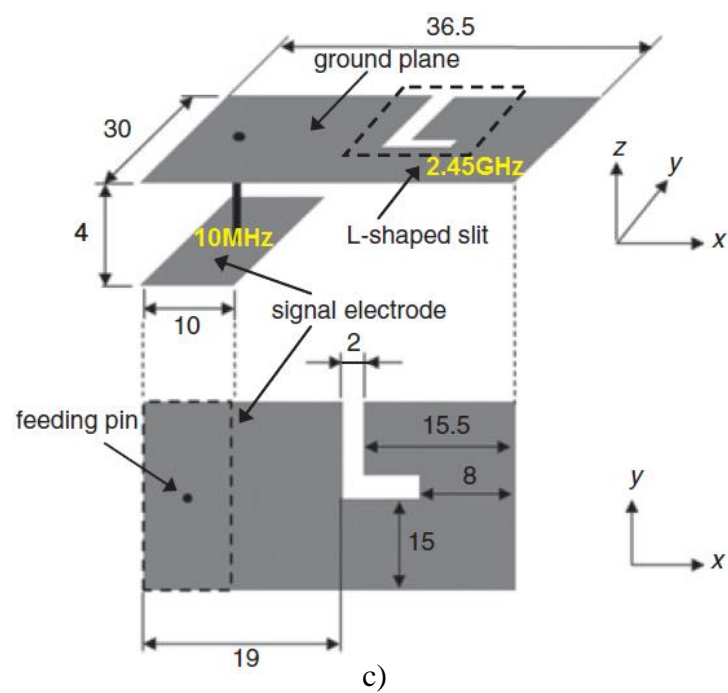
c)

d)
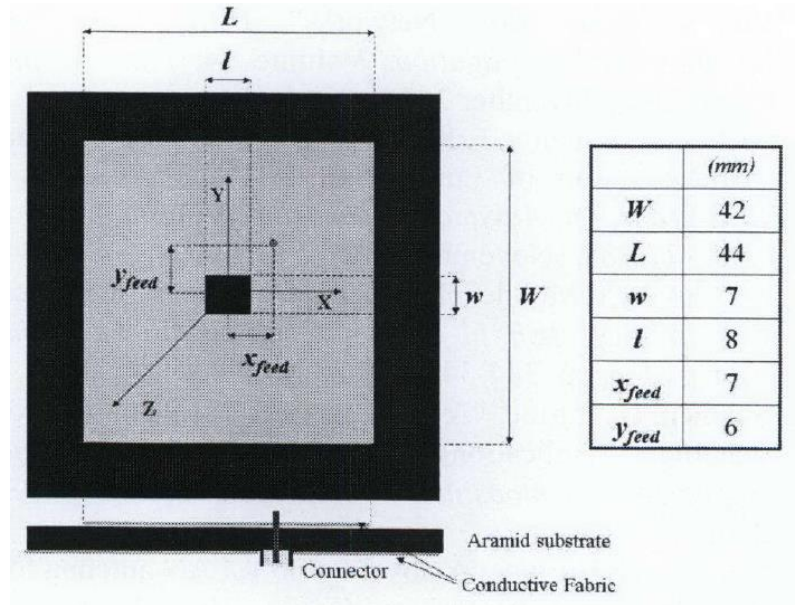
e)
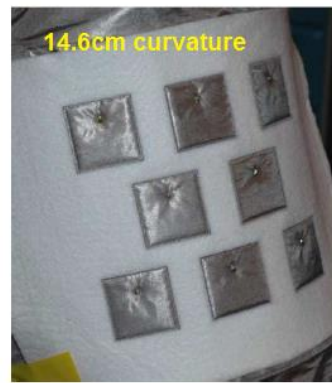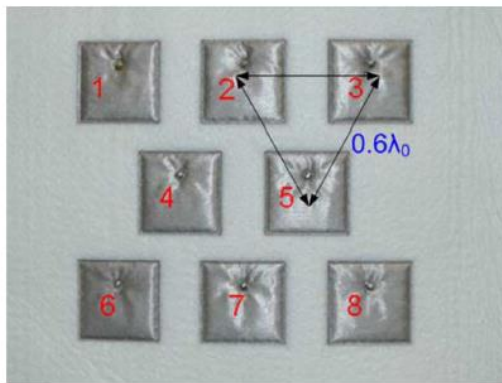
f)
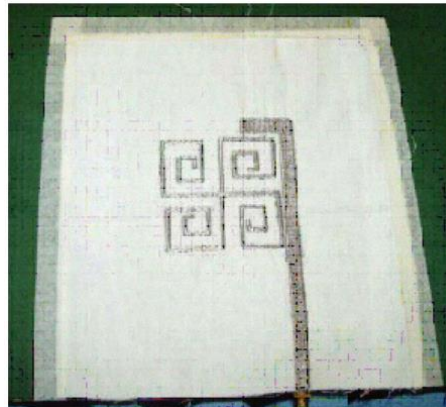
g)

Fig. 1- 1 a) Shorted spiral like patch antenna operating at 430MHz suitable for military radio frequency communications [5], b) Spiral antenna with human torso fitting curvature for military applications (100-500MHz) [6], c) Structure of dual-mode (10MHz/2.45GHZ) for On/Off body operation respectively: 3D view and top view (units in mm) [9], d) wearable fully embroidered textile UWB antenna [34], e) 2.45GHz textile ring patch antenna for protective fire fighter clothing [16], f) eight element e-textile patch array antenna straight and bent outward for body-worn flexibility assessment operating at 802.11 access point appropriate for an extravehicular (EVA) astronaut suit [23] and g) embroidered spiral antenna for COSPAS/SARSAT satellite beacon at 406MHz [32]

1.2   Research challenges of wearable antenna measurements

Once the wearable antenna is manufactured then the step of characterizing it is the next in line. Characterize how the wearable antenna operates in Free Space and when mounted on a human body. This section addresses some of the challenges of measuring wearable antennas. Initially it is useful to measure the antenna performance (gain, impedance matching (S11), directivity, efficiency, *etc.*) in free space [2],[36],[37]. Then, if the wearable antenna is a textile one it will generally operate under the movement of human body, some specific deformations on the antenna such as bending (on cylinder or on a human arm) [13],[38],[39],[40],[41] and crumpling [42],[43] must be considered. The antenna should be measured under different environmental conditions such as high humidity to represent perspiration or exposure to water [44],[45]. Additionally, the wearable textile antennas are supposed to be a part of the garment. So testing the durability of the antenna in terms of performance after washing is required [46]. Also the repeatability in terms of performance of a specific textile antenna should be examined [47]. Measurements on a real human body [48],[49] or with a human phantom [50],[51] should take place. The antenna on-body or on-phantom should be measured in terms of S11, near-field and far-field parameters [52],[53],[54],[55],[56],[57]. The antenna-body interactions need to be fully characterized. Measurements can take place in an anechoic chamber or in a real environment (outdoors [58] and indoors). Measurements are an important and the final step to characterize an antenna system. For most antennas practical applications simulation results are not enough and measurements are necessary.

However, there are still open research issues related with the phantoms used for wearable antenna performance assessment. They are usually heavy, especially when they represent the torso or the full body [59]. This adds the difficulty of manipulating and setting up such phantoms in a test site (e.g. anechoic chamber – Fig. 1-2). Additionally, phantoms are expensive [59]. So, the need for low cost and lightweight phantoms is derived by this challenge. Another challenge is linked with the wearable antenna performance measurement methodology, when it is mounted On-phantom. More specifically, in a far field test site the complete wearable antenna radiation pattern coverage is an issue in terms of space and money. For far field conditions at least 10λ or $10D$ or $2D^2/\lambda$ space is required [60]. Also, an issue linked with the phantom weight, is that a heavy duty roll (in [55] the roll axis can handle weight of AUTs up to 250kg and the phantom weights 40 kg) positioner axis is required, so as to rotate the phantom in the roll axis, in combination with rotation in the azimuth axis, for 3D

full pattern coverage. So, an efficient measurement methodology which will solve the above mentioned issues is required. These two challenges are overcome by the first three novelties (Section 1.4) respectively and the work described in this thesis (Chapters 2 and 3).
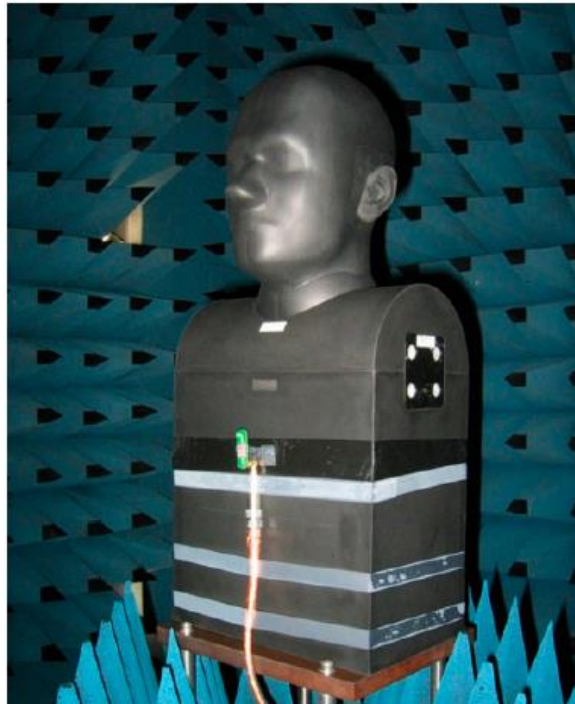
Fig. 1- 2 Experimental setup for pattern measurements of a wearable antenna with a head and torso solid anthropomorphic phantom [55]

1.3 Research challenges of feeding and interconnecting wearable textile antennas and transmission lines

The connection between the wearable antenna and the electronics is arguably the greater weakness in wearable electronics [4]. This includes the feeding of wearable antennas and the transmission lines interconnecting way. The majorities of published papers do not consider this and use an SMA connector and a coaxial cable [4]. Having a rigid connector negates some of the advantages of having a textile antenna (Fig. 1-3 [61]). Some papers though proposed different and wearable possible ways of feeding and interconnecting of antennas and TLs. In [62] a U.FL low profile connector in combination with a flexible cable has been proposed and could be a possible solution for wearable textile patch antennas feeding. Also, the use of metallic Snap-on buttons, as an easily detachable wearable solution, has been successfully proposed for RF connectors to feed/connect a wearable textile antenna [63], [64]. Recently, RF measurements have demonstrated the feasibility of using conductive Hook and Loop (Velcro) as an RF interconnection mechanism at the low GHz frequency

range [65] (Fig. 1-4). This has the advantage that the antennas can be disconnected from the electronics and/or clothing to allow washing or for the electronics to be placed in a different item of clothing. However, considerable work is needed to find the optimal solution to this challenge. By optimal it is meant that the interconnection between wearable antennas and transmission lines or electronics will be fully textile, practical, flexible and efficient (novelties (4) and (5) – Section 1.4, Chapters 4 and 5).
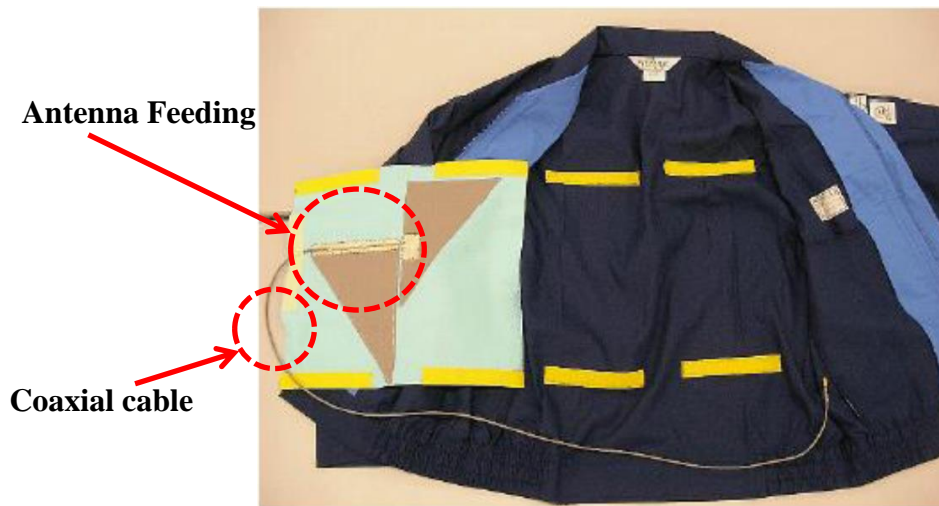
Fig. 1- 3 Fabric wideband wearable antenna with a jacket [61]
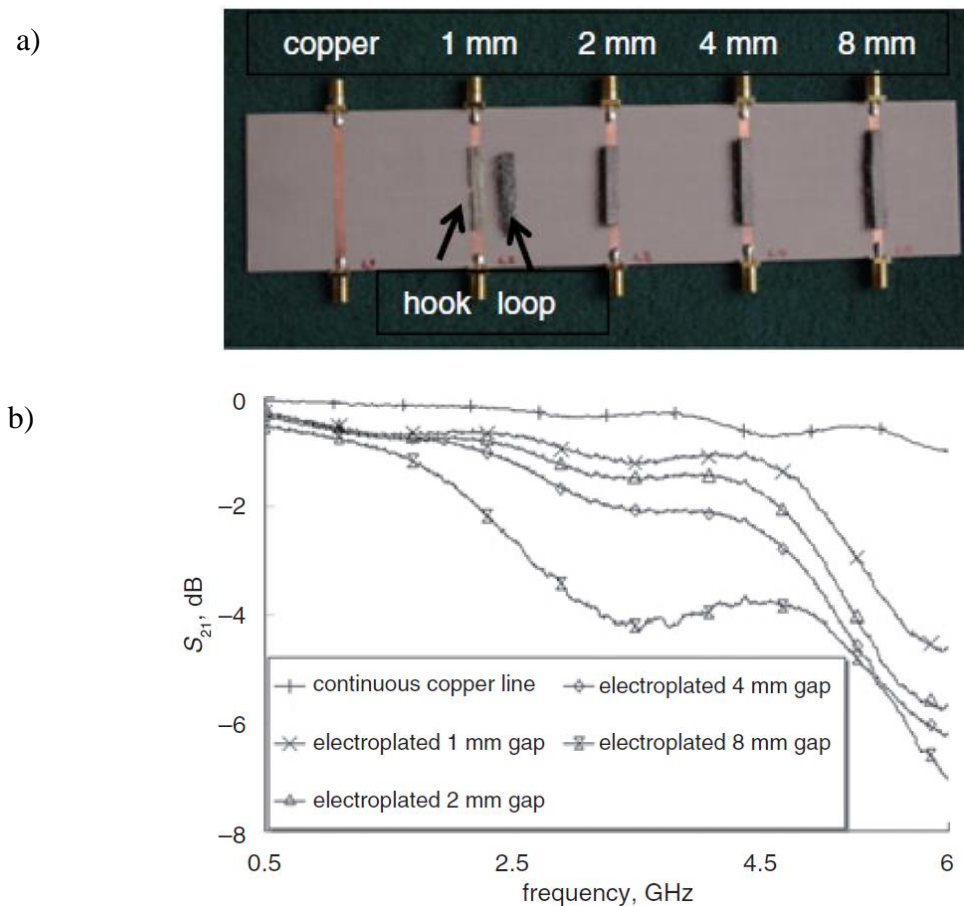
Fig. 1- 4 a) Hook and loop measurement setup, b) S_{21} measurement results for electroplated hook and loop "switches" [65]

1.4   Novel contributions in this thesis

The novelties of this thesis are:

(1)   The design, realization and evaluation of a new, low cost and lightweight, liquid hollow oval cross-section torso phantom appropriate for wearable antenna performance assessment, including reflection coefficient (S_{11}), near field (E-field), on-body communication link budget (S_{21}) and far field [66],[67].

(2)   An evaluation technique of a cylindrical near field test site appropriate for wearable antenna measurements on a torso phantom [68].

(3)   A methodology for wearable antennas performance evaluation by using the cylindrical near field measurement technique on a torso phantom.

(4)   Two new methods for interconnecting textile transmission lines (striplines) have been designed and fabricated [69]. The most, power transfer (S_{21}), efficient method has been fabricated with purely textile (all-textile), practical and flexible materials [70] so as to meet the "wearable textile" criteria.

(5)   The "all-textile" (novelty no. (4)) method has been used to flexibly feed a microstrip fed patch antenna with a textile stripline, introducing by this way a new "practical and flexible connector" for microstrip fed textile patch antennas.

1.5   Overview of this thesis

Chapter 2 will present a novel liquid hollow oval cross-section (HOCS) torso phantom appropriate for wearable antenna performance assessment. The design, realization and evaluation of the proposed phantom are described. The phantom is compared with a corresponding full liquid torso phantom and a numerical heterogeneous anthropomorphic voxel phantom via simulations. Measurements with the realized phantom are compared with real human bodies and a realistic homogeneous anthropomorphic solid phantom. The simulations and measurements include reflection coefficient, near field, on-body communication link budget and far field.

Chapter 3 will introduce the geometry of the HOCS torso phantom in a cylindrical near field (CNF) test site. A new evaluation technique, which is targeted for the CNF test site / measurement system appropriate for wearable antenna measurements mounted on a torso phantom, is described. The evaluation technique is assessed by comparing the CNF measurement results with simulations and with direct far field measurements carried out inside a full wave anechoic chamber. Then the new methodology for wearable antennas performance evaluation by using the CNF measurement technique is presented. The CNF measurement results are compared with simulations so as to validate the proposed methodology.

Chapter 4 will introduce the textile stripline TL theory, geometry and wearable criteria. The selection of the textile materials (conductive and dielectric cloth) for the all-textile stripline fabrication will be explained. Emphasis will be given in the use of the adhesive ways so as to assembly the TL. Two novel methods for interconnecting stripline TLs will be presented. These methods are evaluated via simulations and measurements in terms of insertion losses and reflection coefficient. The most efficient method realization with purely textile and flexible materials (all-textile) is presented. Finally, the practical and flexible (using Velcro) implementation, of the most efficient "all-textile" TL interconnection method is investigated.

Chapter 5 will investigate the use of the interconnecting methods presented in chapter 4 so as to feed / interconnect a stripline with a microstrip and a probe fed wearable textile patch antennas. The stripline and probe fed patch antenna investigation will be limited on simulations. The stripline and microstrip fed patch antenna scenario (the most efficient method from chapter 4) is described in terms of design, fabrication and measurement results (S_{11}, radiation patterns). Finally, the practical and flexible interconnection technique introduced in chapter 4 will be presented when applied in the scenario of: stripline and microstrip fed patch antenna interconnection and a possible real life wearable scenario of this will be demonstrated via measurements.

Chapter 6 will summarize the use of the research achievements/novelties and draw the main conclusions of this thesis. Recommendations for future work will be included in this final chapter.

References

[1]   C. A. Balanis, *Modern Antenna Handbook*. John Wiley & Sons, 2008.

[2]   C. A. Balanis, *Antenna Theory Analysis and Design*, 3rd ed. New Jersey: John Wiley & Sons, 2005.

[3]   P. Hall and Y. Hao, *Antennas and Propagation for Body-Centric Wireless Communications*, 2nd ed. London / Boston: Artech House, 2012.

[4]   A. Tsolis, W. Whittow, A. Alexandridis, and J. Vardaxoglou, "Embroidery and Related Manufacturing Techniques for Wearable Antennas: Challenges and Opportunities," *Electronics*, vol. 3, no. 2, pp. 314–338, May 2014.

[5]   R. Waterhouse, D. Novak, and G. Burnie, "Small uni-planar antenna suitable for body wearable applications," *Military Communications Conference*, pp. 1–6, 2006.

[6]   G. Pettitt, J. C. G. Matthews, A. J. Tyler, and B. P. Pirollo, "Wide-Band Body Wearable Antennas," *BAE Systems & Defence Science and Technology Laboratory*, 2008.

[7]   N. Noury, P. Barralon, and D. Flammarion, "Preliminary Results on the Study of Smart Wearable Antennas," *Conference proceedings : 27th Annual International Conference of the IEEE Engineering in Medicine and Biology Society. IEEE Engineering in Medicine and Biology Society. Conference*, vol. 4, pp. 3814–7, Jan. 2005.

[8]   P. Salonen, L. Sydänheimo, M. Keskilammi, and M. Kivikoski, "A Small Planar Inverted-F Antenna for Wearable Applications," *Proc. of the 3rd International Symposium on Wearable Computers*, pp. 95–100, 1999.

[9]   C.-H. Lin, Z. Li, K. Ito, M. Takahashi, and K. Saito, "Dual-mode antenna for on-/off-body communications (10 MHz/2.45 GHz)," *Electronics Letters*, vol. 48, no. 22, pp. 1383 – 1384, 2012.

[10] B. Huang, G. Yan, and Q. Li, "A four spiral slots microstrip patch antenna for radiotelemetry capsules based on FDTD," *Journal of Zhejiang University SCIENCE A*, vol. 8, no. 10, pp. 1560–1567, Oct. 2007.

[11] A. R. Chandran and W. G. Scanlon, "Reduced Groundplane Shorted Patch Antenna for On-Body Communications," in *Loughborough Antennas & Propagation Conference*, 2009, pp. 409–412.

[12] T. Alves, B. Poussot, and J. Laheurte, "PIFA – Top-Loaded-Monopole Antenna With Diversity Features for WBAN Applications," *IEEE Antennas and Propagation Letters*, vol. 10, pp. 693–696, 2011.

[13] S. Kim, S. Lee, K. Kwon, H. Park, and J. Choi, "Miniaturized and High-Isolation Diversity Antenna for WBAN Applications," *Proceedings of ISAP2012, Nagoya, Japan*, pp. 979–982.

[14] S. Manzari, S. Pettinari, and G. Marrocco, "Miniaturised wearable UHF-RFID tag with tuning capability," *Electronics Letters*, vol. 48, no. 21, pp. 1325 – 1326, 2012.

[15] S. Manzari, S. Pettinari, and G. Marrocco, "Miniaturized and Tunable Wearable RFID Tag for Body-Centric Applications," *IEEE International Conference on RFID-Technologies and Applications (RFID-TA)*, vol. 2, no. 1, pp. 239–243, Nov. 2012.

[16] C. Hertleer, H. Rogier, and L. Van Langenhove, "A Textile Anetnna for Protective Clothing," *Antennas and Propagation for Body-Centric Wireless Communications, IET*, pp. 44–46, 2007.

[17] P. Salonen, M. Keskilammi, J. Rantanen, and L. Sydanheimo, "A novel Bluetooth antenna on flexible substrate for smart clothing," in *IEEE International Conference on Systems, Man and Cybernetics. e-Systems and e-Man for Cybernetics in Cyberspace*, 2001, vol. 2, pp. 789–794.

[18] P. Salonen and L. Sydanheimo, "Development of an S-Band Antenna for Smart Clothing," *International Symposium on Antennas and Propagation*, pp. 6–9, 2002.

[19] J. Carter, J. Saberin, T. Shah, and S. P. R. Ananthanarayanan, "Inexpensive Fabric Antenna for Off-Body Wireless Sensor Communication," in *Antennas and Propagation Society International Symposium (APSURSI)*, 2010, pp. 1–4.

[20] P. Salonen, J. Kim, and Y. Rahmat-Samii, "Dual-Band E-Shaped Patch Wearable Textile Antenna," in *Antennas Propag. Soc. Int. Symp. IEEE*, 2005, vol. 1A, pp. 466–469.

[21] P. Salonen, Y. Rahmat-Samii, H. Hurme, and M. Kivikoski, "Dual-Band Wearable Textile Antenna," in *IEEE Antennas and Propagation Society International Symposium*, 2004, vol. 1, pp. 463–466.

[22] E. K. Kaivanto, M. Berg, E. Salonen, and P. de Maagt, "Wearable Circularly Polarized Antenna for Personal Satellite Communication and Navigation," *IEEE Transactions on Antennas and Propagation*, vol. 59, no. 12, pp. 4490–4496, 2011.

[23] T. F. Kennedy, P. W. Fink, A. W. Chu, N. J. Champagne, G. Y. Lin, and M. A. Khayat, "Body-Worn E-Textile Antennas : The Good , the Low-Mass , and the Conformal," *IEEE Transactions on Antennas and Propagation*, vol. 57, no. 4, pp. 910–918, 2009.

[24] J. A. Dobbins, A. W. Chu, P. W. Fink, T. F. Kennedy, G. Y. Lin, M. A. Khayat, and R. C. Scully, "Fabric Equiangular Spiral Antenna," in *IEEE Antennas and Propagation Society International Symposium*, 2006, pp. 2113–2116.

[25] F. Declercq and H. Rogier, "Active Integrated Wearable Textile Antenna With Optimized Noise Characteristics," *IEEE Transactions on Antennas and Propagation*, vol. 58, no. 9, pp. 3050–3054, Sep. 2010.

[26] A. Dierck, F. Declercq, and H. Rogier, "Review of active textile antenna co-design and optimization strategies," in *IEEE International Conference on RFID-Technologies and Applications*, 2011, pp. 194–201.

[27] S. Zhu and R. Langley, "Dual-band wearable antennas over EBG substrate," *Electronic Letters*, vol. 43, no. 3, pp. 141–142, 2007.

[28] R. Langley, S. Zhu, and L. Liu, "Dual Band Body Worn Antenna," in *European Conference on Antennas and Propagation (EuCAP)*, 2007, pp. 137–140.

[29] P. J. Soh, G. A. E. Vandenbosch, and J. Higuera-Oro, "Design and Evaluation of Flexible CPW-fed UltraWide Band (UWB) Textile Antennas," in *IEEE Int. RF Microw. Conf. (RFM 2011), Seremban, Malaysia*, 2011, pp. 133–136.

[30] B. Sanz-Izquierdo, L. Wu, J. Batchelor, and P. Yound, "Textile Integrated Waveguide Slot Antenna," in *IEEE Antennas and Propagation Society International Symposium (APSURSI)*, 2010, pp. 1–4.

[31] R. Moro, S. Agneessens, H. Rogier, and M. Bozzi, "Wearable textile antenna in substrate integrated waveguide technology," *Electronics Letters*, vol. 48, no. 16, pp. 985–987, Aug. 2012.

[32] R. D. Seager, A. Chauraya, J. C. Vardaxoglou, and P. de Maagt, "Towards a compact low frequency woven antenna," in *Antennas and Propagation Society International Symposium (APSURSI)*, 2009, pp. 1–4.

[33] J.-S. Roh, Y.-S. Chi, J.-H. Lee, Y. Tak, S. Nam, and T. J. Kang, "Embroidered Wearable Multiresonant Folded Dipole Antenna for FM Reception," *IEEE Antennas and Wireless Propagation Letters*, vol. 9, pp. 803–806, 2010.

[34] R. Shobana and S. Radha, "Ultra Wideband Wearable Textile Antenna," in *International Conference on Computing and Control Engineering (ICCCR 2012), 12 & 13 April*, 2012, pp. 7–10.

[35] Z. Wang, L. Zhang, D. Psychoudakis, and J. L. Volakis, "GSM and Wi-Fi textile antenna for high data rate communications," *Proceedings of the 2012 IEEE International Symposium on Antennas and Propagation*, pp. 1–2, Jul. 2012.

[36] E. Moradi, T. Björninen, L. Ukkonen, and Y. Rahmat-Samii, "Characterization of Embroidered Dipole-type RFID Tag Antennas," in *IEEE International Conference on RFID-Technologies and Applications (RFID-TA)*, 2012, pp. 248–253.

[37] M.A.R. Osman, M. K. A. Rahim, M. Azfar, N. A. Samsuri, F. Zubir, and K. Kamardin, "Design, Implementation and Performance of Ultra-Wideband Textile Antenna," *Progress In Electromagnetics Research B*, vol. 27, pp. 307–325, 2011.

[38] P. Salonen and Y. Rahmat-Samii, "Textile Antennas : Effects of Antenna Bending on Input Matching and Impedance Bandwidth," *IEEE Aerospace and Electronic Systems Magazine*, vol. 22, no. 3, pp. 10–14, 2007.

[39] F. Boeykens, L. Vallozzi, and H. Rogier, "Cylindrical Bending of Deformable Textile Rectangular Patch Antennas," *International Journal of Antennas and Propagation*, vol. 2012, no. 170420, pp. 1–11, 2012.

[40] H. Shimasaki and M. Tanaka, "Measurement of the Roundly Bending Characteistics of a Cavity Slot Antenna Made of Conductive Textile," in *Proceedings of the Asia-Pacific Conference*, 2011, pp. 1598–1601.

[41] M. Tanaka and J. H. Jang, "Wearable Microstrip Antenna," in *IEEE Antennas and Propagation Society International Symposium*, 2003, vol. 2, pp. 704–707.

[42] Q. Bai and R. Langley, "Crumpling of PIFA Textile Antenna," *IEEE Transactions on Antennas and Propagation*, vol. 60, no. 1, pp. 63–70, Jan. 2012.

[43] Q. Bai and R. Langley, "Crumpled textile antennas," *Electronics Letters*, vol. 45, no. 9, pp. 436–437, 2009.

[44] J. Lilja, P. Salonen, T. Kaija, and P. de Maagt, "Design and Manufacturing of Robust Textile Antennas for Harsh Environments," *IEEE Transactions on Antennas and Propagation*, vol. 60, no. 9, pp. 4130–4140, Sep. 2012.

[45] C. Hertleer, A. Van Laere, H. Rogier, and L. Van Langenhove, "Influence of Relative Humidity on Textile Antenna Performance," *Textile Research Journal*, vol. 80, no. 2, pp. 177–183, Sep. 2009.

[46] K. Koski, E. Moradi, A. A. Babar, T. Björninen, L. Sydänheimo, and L. Ukkonen, "Durability of Embroidered Antennas in Wireless Body-Centric Healthcare Applications," in *7th European Conference on Antennas and Propagation (EuCAP)*, 2013, pp. 565–569.

[47] S. Zhang, A. Chauraya, W. Whittow, R. Seager, T. Acti, T. Dias, and Y. Vardaxoglou, "Repeatability of Embroidered Patch Antennas," in *Loughborough Antennas & Propagation Conference (LAPC)*, 2013, pp. 140–144.

[48]   K. Koski, E. Koski, T. Björninen, A. Babar, L. Ukkonen, and L. Sydänheimo, "Practical Read Range Evaluation of Wearable Embroidered UHF RFID Tag," in *Antennas and Propagation Society International Symposium (APS-URSI), IEEE*, 2012, pp. 1–2.

[49]   S. J. Boyes, P. J. Soh, Y. Huang, G. A. E. Vandenbosch, and N. Khiabani, "Measurement and Performance of Textile Antenna Efficiency on a Human Body in a Reverberation Chamber," *IEEE Transactions on Antennas and Propagation*, vol. 61, no. 2, pp. 871–881, 2013.

[50]   D. Psychoudakis, G. Lee, C. Chen, and J. L. Volakis, "Military UHF Body-Worn Antennas for Armored Vests," in *European Conference on Antennas and Propagation (EuCAP)*, 2010, pp. 1–4.

[51]   L. Zhang, Z. Wang, D. Psychoudakis, and J. L. Volakis, "E-fiber electronics for body-worn devices," in *6th European Conference on Antennas and Propagation (EUCAP)*, 2012, pp. 760–761.

[52]   J. G. Santas and A. Alomainy, "Textile antennas for on-body communications: techniques and properties," in *European Conference on Antennas and Propagation (EuCAP)*, 2007, pp. 1–4.

[53]   M. Hasani, A. Vena, L. Sydänheimo, L. Ukkonen, and M. M. Tentzeris, "Implementation of a Dual-Interrogation-Mode Embroidered RFID-Enabled Strain Sensor," *IEEE Antennas and Wireless Propagation Letters*, vol. 12, pp. 1272–1275, 2013.

[54]   H. R. Raad, A. I. Abbosh, H. M. Al-Rizzo, and D. G. Rucker, "Flexible and Compact AMC Based Antenna for Telemedicine Applications," *IEEE Transactions on Antennas and Propagation*, vol. 61, no. 2, pp. 524–531, 2013.

[55]   T. H. Loh, D. Cheadle, and L. Rosenfeld, "Radiation Pattern Measurement of a Low-Profile Wearable Antenna Using an Optical Fibre and a Solid Anthropomorphic Phantom," *Electronics*, vol. 3, no. 3, pp. 462–473, 2014.

[56] T. Salim and P. S. Hall, "Efficiency measurement of antennas for on-body communications," *Microwave and Optical Technology Letters*, vol. 48, no. 11, pp. 2256–2259, 2006.

[57] C. Parini, S. Gregson, J. Mccormick, and D. Janse van Rensburg, *Theory and Practice of Modern Antenna Range Measurements*. London, UK: IET, 2014.

[58] I. J. Mohd, F. J. Mohd, J. Muzammil, S. Thennarasan, R. K. Muhammad, R. B. Ahmad, P. J. Soh, G. A. E. Vandenbosch, L. K. N. Ishak, I. E. Azmi, and A. Azremi, "A Novel 2.45GHz Switchable Beam Textile Antenna (SBTA) for Outdoor Wireless Body Area Network (WBAN) Aapplications," *Progress In Electromagnetics Research*, vol. 138, pp. 613–627, 2013.

[59] "http://www.speag.com/", accessed September 2016

[60] IEEE, *IEEE Recommended Practice for Near-Field Antenna Measurements*, December. 2012.

[61] A. Kuramoto and Y. Furuya, "Wideband Wearable Antenna," in *Proceedings of ISAP, Niigata, Japan*, 2007, pp. 1086–1089.

[62] S. Zhang, "Design Advances of Embroidered Fabric Antennas", PhD Thesis Loughborough, 2014.

[63] T. Kellomaki and W. G. Whittow, "Bendable plaster antenna for 2.45 GHz applications," in *Loughborough Antennas & Propagation Conference (LAPC)*, 2009, no. March, pp. 453–456.

[64] S. J. Chen, C. Fumeaux, D. C. Ranasinghe, and T. Kaufmann, "Paired Snap-On Buttons Connections for Balanced Antennas in Wearable Systems," *IEEE Antennas and Propagation Letters*, vol. 14, pp. 1498–1501, 2015.

[65] R. D. Seager, W. Whittow, Y. Vardaxoglou, A. Chauraya, and S. Zhang, "Flexible radio frequency connectors for textile electronics," *Electronics Letters*, vol. 49, no. 22, pp. 1371–1373, Oct. 2013.

[66] A. Tsolis, W. G. Whittow, A. A. Alexandridis, and J. C. Vardaxoglou, "Evaluation of a Human Body Phantom for Wearable Antenna Measurements at the 5.8GHz Band," in *Loughborough Antennas & Propagation Conference (LAPC), 11-12 November, Loughborough, UK*, 2013, pp. 414–419.

[67] A. Tsolis, W. G. Whittow, A. Chauraya, A. A. Alexandridis, and J. Y. C. Vardaxoglou, "Evaluation of a Realized Hollow Torso Phantom for Wearable Antenna Measurements," in *Loughborough Antennas & Propagation Conference (LAPC)*, 2014, no. November, pp. 560–561.

[68] A. Tsolis, W. G. Whittow, A. Chauraya, A. A. Alexandridis, and J. Y. C. Vardaxoglou, "A Calibration of a Cylindrical Near Field Test Site Appropriate for Wearable Antenna Measurements on a Liquid Torso Phantom at 2GHz," in *Loughborough Antennas & Propagation Conference (LAPC)*, 2015, pp. 1–5.

[69] A. Tsolis, A. A. Alexandridis, W. G. Whittow, and J. C. Vardaxoglou, "Investigation of Textile Striplines Connectivity for Feeding and Connecting Wearable Antennas," in *European Conference on Antennas and Propagation (EuCAP)*, 2015, pp. 1–5.

[70] A. Tsolis, A. A. Alexandridis, W. G. Whittow, and J. C. Vardaxoglou, "Connecting wearable textile transmission lines: all-textile fabrication solutions and design techniques," *Electronics Letters*, vol. 51, no. 15, pp. 1136–1138, Jul. 2015.

CHAPTER 2

HOLLOW OVAL CROSS-SECTION

LIQUID TORSO PHANTOM:

DESIGN, REALIZATION AND EVALUATION

Abstract

This chapter presents the design, realization and evaluation of a low cost and lightweight hollow oval cross-section torso phantom appropriate for wearable antenna performance assessment. The phantom consists of an empty inner space (hollow) surrounded by a shell with double plastic walls between which there is a tissue emulating liquid. The shell is made of a low loss cast acrylic and the liquid is a commercially available one with properties calibrated for the frequency range of 2-6GHz. The phantom's liquid volume is reduced by at least 60% compared with the respective full liquid phantom. The phantom is validated with the respective full liquid torso phantom and a numerical heterogeneous anthropomorphic voxel phantom via simulations. Measurements with the realized phantom are compared with human subjects and a realistic homogeneous anthropomorphic solid phantom. The phantom performance is tested in terms of simulated electric field distribution of a wearable antenna on its surface and of simulated path loss between two wearable antennas, on either side of the phantom. It is proved that the hollow phantom performance approximates the full liquid phantom when a simulated RF absorbing material is placed in its central hollow region. The phantom performance in terms of S_{11} wearable antenna measurements is evaluated and found in good agreement with real human bodies in the examined frequency range (2-6GHz). In terms of far field wearable antenna performance the proposed phantom yields almost same performance with the full liquid phantom and maximum deviation less than 2.5dB, 1.5dB and 6.6% in gain, directivity and efficiency values respectively compared with an anthropomorphic simulated phantom. Also, the maximum deviation compared with a measured anthropomorphic phantom is less than 1.2dB, 0.5dB and 4% in terms of gain, directivity and efficiency values respectively. The proposed phantom is

evaluated as good candidate for wearable antenna performance assessment including reflection coefficient, near field (E-field), on-body communication link budget and far field.

2.1 Introduction

2.1.1 Phantoms for wearable antennas

Test and evaluation of antenna systems mounted on a person (wearable antennas and electronics) can be a really challenging procedure. Due to ethics, safety and repeatability issues it is not appropriate and always possible to use a real person inside an anechoic chamber for wearable antennas performance evaluation. This requires the design, the realization and the use of an equivalent phantom which represents the human body shape and electrical properties. The use of phantoms for wearable antenna measurements can provide a stable and controllable propagation environment that cannot be easily realized with alive human subjects[1]. Such measurements exclude the dynamic nature of real human bodies and give an ideal and stable wearable antenna performance.

A phantom can be defined as a simulated biological body or as a physical model emulating the characteristics of the biological tissues of the human body. The goal of such a phantom is to be used to investigate the interaction between the human tissues and the electromagnetic fields, produced by a wearable antenna. This means that phantoms are capable of being a tool in the study of radio wave and microwave propagation around and inside the human body [1]. The phantoms can be categorized from several different points of view such as the frequency range, the type of tissues the phantom represents and the state of the phantom structure which can be a) liquid, b) semisolid (gel), or c) solid (dry) [1]. The liquid phantom is a container filled with a liquid that emulates the electrical properties of the tissues of the body in a specific range of frequencies. These phantoms have a thin shell usually made from fiberglass or plastic. The shell has small relative permittivity ($\varepsilon_r < 5$), the loss tangent should be less than 0.05 and the thickness should be 2±0.2mm in the frequency range of 0.8 to 3GHz [2]. Depending on the requirements of the application under test, the phantom shell has a shape of the whole body, or torso, or human head [1]. A simple square shaped liquid phantom has been already presented in [3] (Fig. 2-1a) and an anthropomorphic whole human body liquid phantom used for measurements in [4] (Fig. 2-1b). Ogawa et al. proposed in [5] (Fig. 2-1c) a multi-postural realistic human-torso liquid phantom, which is

composed of a shell filled with liquid. The evolution of liquid phantoms so as to get rid of the outer shell is the semisolid (gel) phantoms. A solidifying agent has been used to make materials of jelly-like consistency that are capable of self-shaping (gel phantoms) [1]. Semi-solid phantom structures and recipes were presented in [6]. The durability of the phantom structure has been improved by the introduction of the solid phantoms[1]. Recipes for solid phantoms have been proposed in [7],[8],[9]. More examples of all the types of phantoms are extensively described in [1]. These three categories of phantoms have some advantages and disadvantages or they have some specific tradeoffs:

Liquid: easily fabricated; cheap; the human body/part is not represented accurately, as the internal structure is replaced with a homogeneous liquid; limited range of frequencies over which the liquid can have the required dielectric properties; difficulty of handling the container in the test environment, the container (shell) itself has electrical properties that should be taken into account; lifespan: liquid to be checked and maybe changed every year.

Semi-solid: easy to be constructed (but not easier than the liquid ones); no need for outer shell, jelly-like which makes them capable of self-shaping (flexible to be reshaped); most of them are suitable for emulating high water content tissues (e.g. muscle, skin, brain, lungs) [1]; limited control of the electrical characteristic over a wide frequency range; lifespan: forever if maintained at room conditions.

Solid: no outer shell, stable structure (long lasting); the best suited type of phantoms for studying the propagation around and inside the body (accurately represents the inhomogeneous structure of the human body); excellent mechanical and dielectric properties which make the fabrication difficult and expensive compared to the other types of phantoms; lifespan: forever.

a)

b)   c)
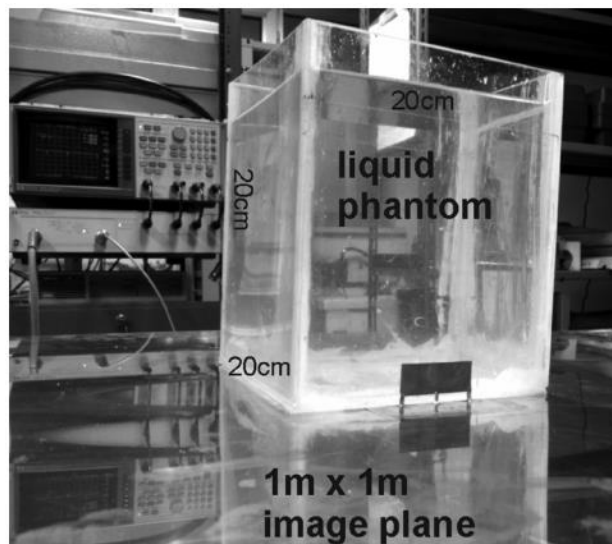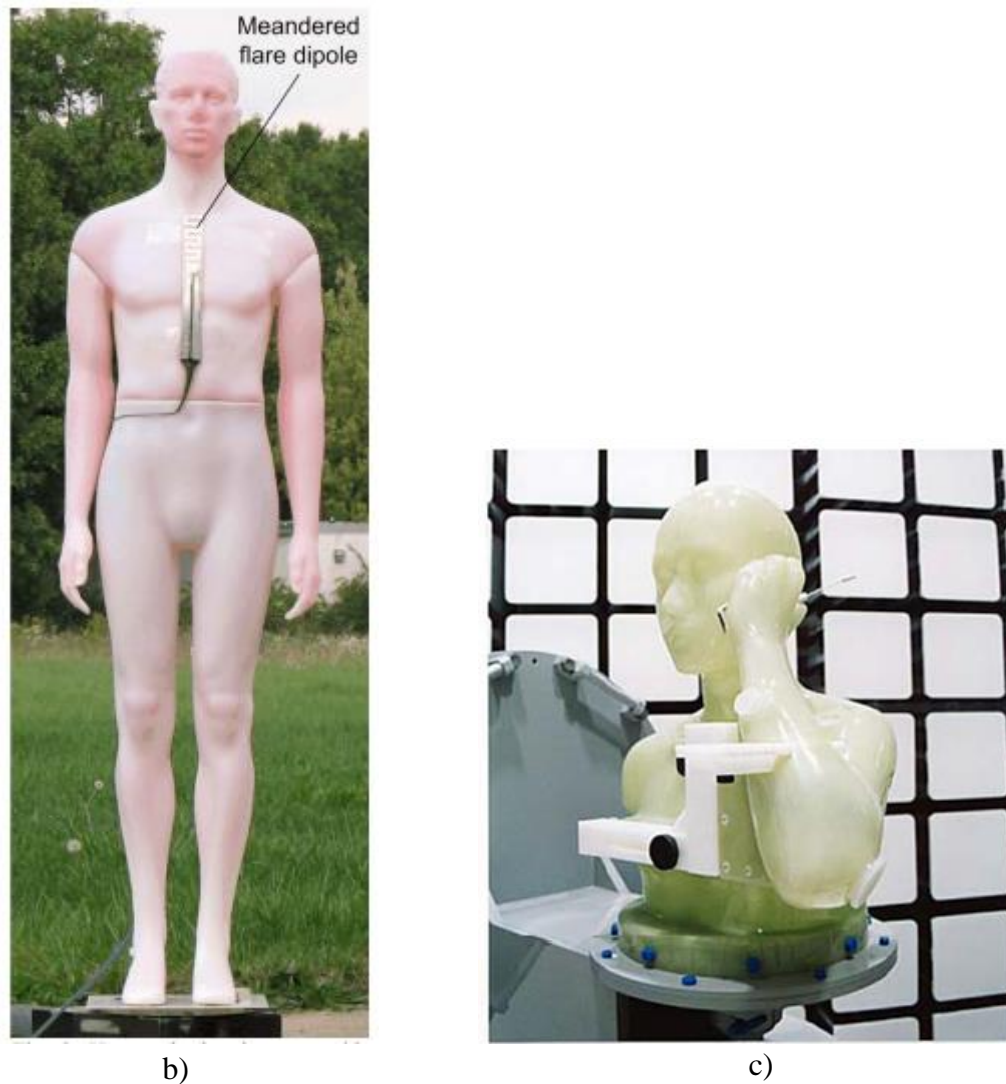
Fig. 2- 1 a) Perspex cubic phantom filled with tissue-equivalent solution made of deionized water, saccharose and sodium chloride [3], b) Whole body phantom [4], c) Torso phantom [5]

Phantoms are also used in simulation softwares and they are called as numerical (digital) phantoms. The numerical phantoms are categorized in: a) theoretical phantoms which are simple shaped phantoms and b) voxel phantoms which are more realistic numerical phantoms composed of many voxels, to better calculate the characteristics of wearable antennas close to the human body. It is understandable that numerical phantoms are used for theoretical analysis and computational simulations, giving an estimate or a standard of a wearable antenna performance and saving time before proceeding to the more realistic measurements with physical phantoms. More extensively:

Theoretical phantoms: Homogeneous or layered flat phantoms are the simplest theoretical models (commonly used to evaluate EM dosimetry). Spherical models are mainly

used for EM dosimetry inside the human head and for dosimetry in the eyes [10], [11], [12], [13]. Cylindrical phantoms are used for whole body models [14], [15]. These models can be used for simplified and less complex simulation analysis of wearable antennas in terms of time and data space.

Voxel phantoms: Detailed human head models are proposed in [16]. A widely used detailed whole body voxel phantom, in terms of numerical simulations, is presented in [17] (Fig. 2-2). *This phantom has been used for the needs of simulations for this chapter in the far field analysis.* Finally Nagaoka in [18] developed a high-resolution whole body Japanese human voxel models, classifying 51 different types of tissues, in advance of the 40 types of tissues proposed in [17], based on images of males and females. These models [18] enable numerical evaluation of EM dosimetry and propagation up to 3GHz.
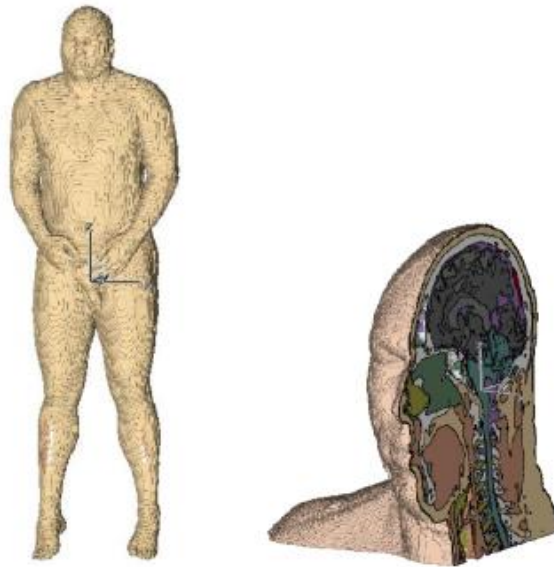
Fig. 2- 2 High spatial resolution whole body human voxel phantom and detailed cross-sectional view of head [17]

In this chapter a novel design of a liquid torso phantom with a hollow oval cross – section (HOCS) structure [19] is proposed, characterized and evaluated in terms of wearable antenna performance. This phantom has all the drawbacks that liquid phantoms have. The goal of the proposed HOCS phantom is to reduce the liquid volume by at least 60% compared with the respective full liquid phantom and to give similar and comparable results with the full liquid phantom and with human bodies and anthropomorphic phantoms respectively. This phantom has the main following advantages: *lower fabrication cost and lighter than full liquid phantoms.* The procedure followed for the evaluation of HOCS phantom is proposed as a method for evaluating phantoms which are appropriate for wearable antenna performance assessment.

2.1.2 Outline of this chapter

This chapter is structured as follows: in section 2.2 the hollow torso phantom is classified and compared with other liquid phantoms that have already been proposed and used by other researchers. The geometry of the phantom and the electrical and geometrical characteristics of its components are described. In Section 2.3 the E-field distribution on, in and around the hollow torso phantom is examined and compared with a full liquid phantom via simulations. Additionally, wearable antenna reflection coefficient (S_{11}) measurements on the realized hollow torso phantom and on different volunteers are presented and compared in order to study the validity of the phantom for such type of measurements. Also, the simulated path loss (S_{21}) for on-body communication links on the phantom is examined and compared with the corresponding results on a full liquid phantom. Finally, the far field behavior of the hollow torso phantom is investigated and compared with other phantoms (full liquid and anthropomorphic), via simulations and measurements. In Section 2.4 conclusions are drawn from this chapter.

2.2 Phantom classification, geometry and components

2.2.1 Classification and geometry

The geometry of HOCS phantom in 3D is shown in Fig. 2-3 and on the YZ-plane (Y-axis: width, Z-axis: depth) is shown in Fig. 2-4. The height of the phantom (X-axis), is equal to 485mm (Fig. 2-3). These dimensions approximate the average anthropomorphic phantom torso [20]. The phantom has an oval cross-section geometry which has a more accurate shape to that of a real human torso compared with a cylindrical one presented in [21]. The idea for the structure of the phantom was derived from [22] where an oval cross-section phantom was proposed and successfully used for wearable antenna measurements. That phantom was fully filled with liquid. So, the design of a hollow phantom will simplify the measurement setup compared with a heavier full liquid phantom. Note the HOCS phantom does not have arms, legs and head. There is a variety of wearable antenna applications which could be developed on the human torso [1] . So, in terms of a realistic study the human torso is part of the body which has the biggest surface and the chances of integrating wearable devices on the torso are bigger compared to other parts of the human body.
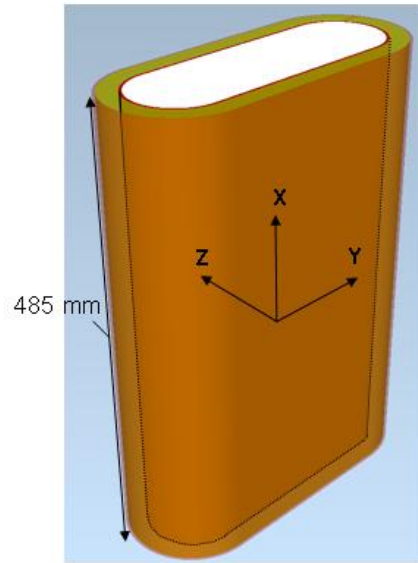
Fig. 2- 3 HOCS phantom 3D geometry
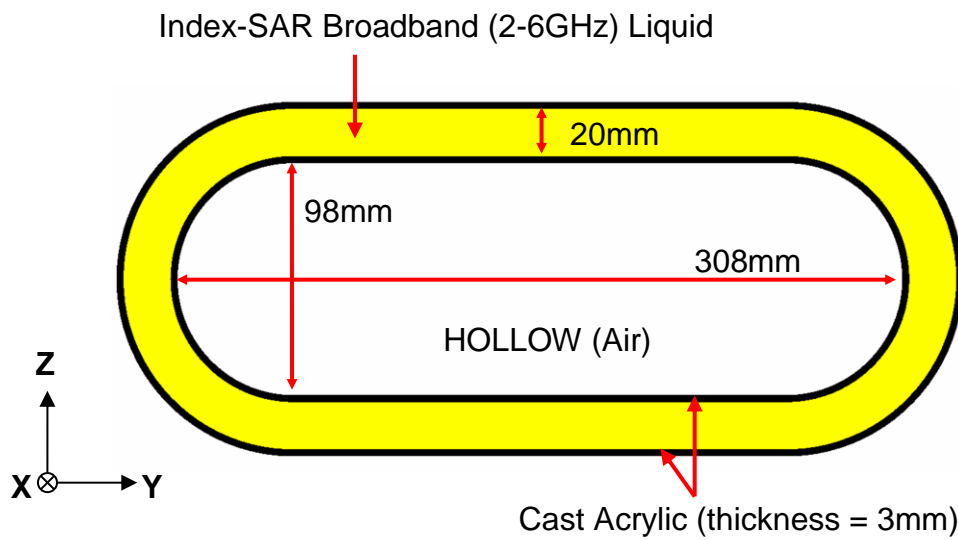
Fig. 2- 4 Geometry of the proposed HOCS torso phantom on the YZ-plane

2.2.2 Phantom structural components

The proposed HOCS phantom has two parts: a) the outer shell which is a low loss cast acrylic and b) the liquid emulating the average human body dielectric properties calibrated for the frequency range of 2 up to 6GHz which was produced by Index-SAR [23] (Table 2-1) following the IEEE 1528-2013 standard for the liquid dielectric properties.

Table 2 - 1 Properties of tissue simulating liquid (given by Index-SAR) [23]

f_c (GHz)	ε_r	$tan\delta$	σ (S/m)
2.00	43.90	0.2681	1.31
2.45	42.47	0.3023	1.75
3.00	40.78	0.3452	2.35
4.00	37.53	0.3688	3.08
5.00	34.38	0.4402	4.21
5.80	31.95	0.5112	5.27
6.00	31.41	0.5125	5.32

The dielectric properties of the used cast acrylic material were unknown. For this reason prior to the design and construction of the phantom, the dielectric properties of cast acrylic were measured by using three different split post dielectric resonators at 1.10GHz; 1.92GHz and 2.47GHz (Fig. 2-6b) [24], [25], [26], [27]. The procedure and concept of this measurement is shown in the flowchart depicted in Fig. 2-5. The measurement setup is shown in Fig. 2-6a. Two samples of cast acrylic were used so as to determine the dielectric properties of this material. The first sample is 2.75mm thick and the second 1.6mm. For each sample and for each split post dielectric resonator (frequency) three measurements were carried out. The aim was to assess the repeatability of the results. This was done because the cast acrylic properties were not known. As an example and a proof of these measurements Tables no. 1and no. 2 (Fig. 2-5) for the case of the 2.47GHz split post dielectric resonator are shown in Tables 2-2 and 2-3 respectively. The measured and calculated properties of cast acrylic (Table 2-4) were used in simulations, in order to design and evaluate the phantom (following sections). The properties of cast acrylic material for higher frequencies (e.g. 6GHz) have been estimated by applying the linear [28] least square fitting method, via MatLab or MS-Office Excel.
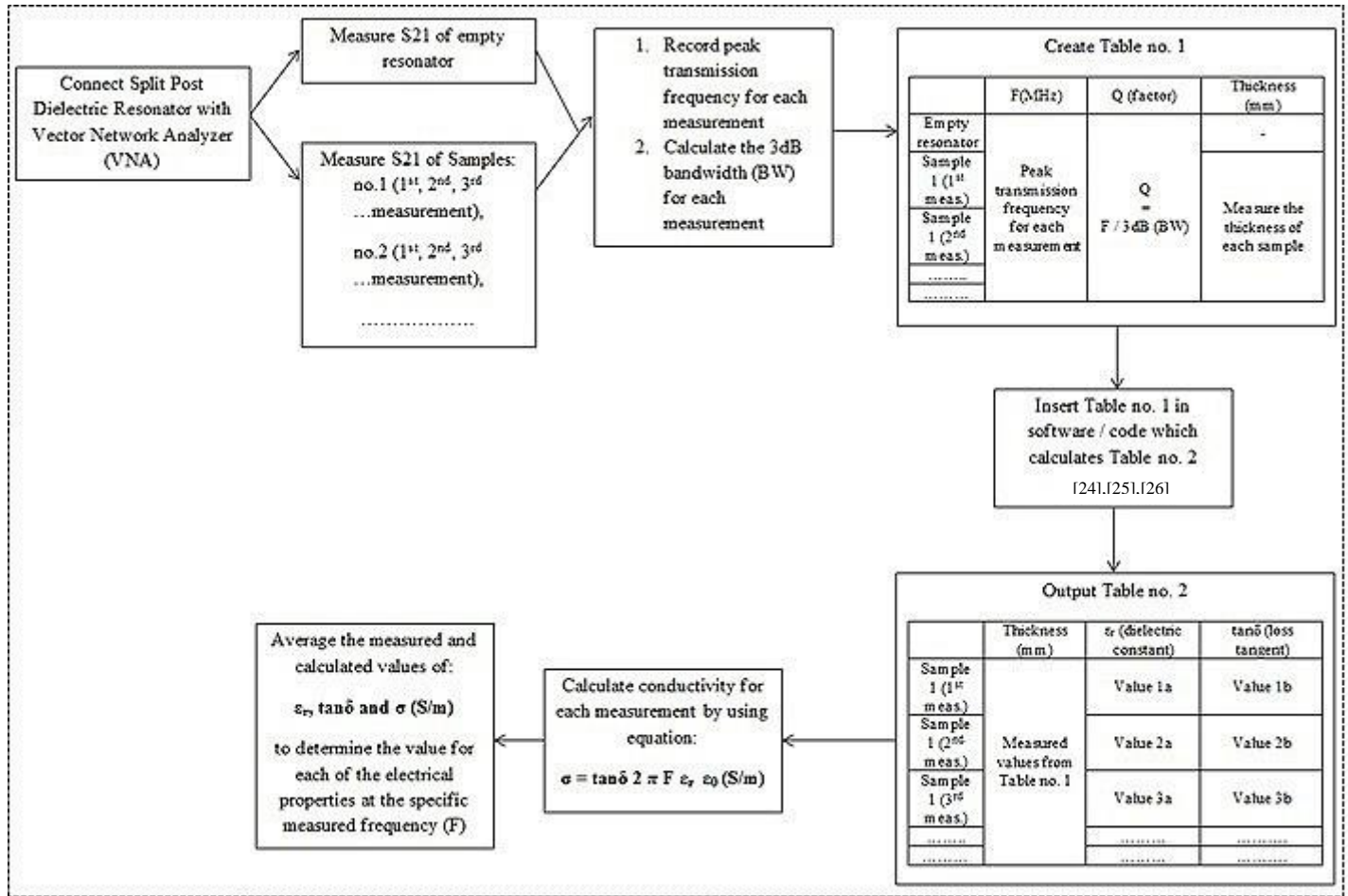
Fig. 2- 5 Procedure for measuring the dielectric properties of a material by using the method of split post dielectric resonators

Table 2 - 2 Input table (Table no.1 – Fig. 2-5) for dielectric properties calculation using the 2.47GHz split post resonator

	F (MHz)	Q (factor)	Thickness (mm)
Empty resonator	2470.106250	14074.679490	-
Sample 1 (1st measurement)	2444.681250	3039.230769	
Sample 1 (2nd measurement)	2444.737500	3069.350282	2.75
Sample 1 (3rd measurement)	2444.737500	3086.789773	
Sample 2 (1st measurement)	2455.453125	4585.346639	
Sample 2 (2nd measurement)	2455.396875	4828.705752	1.60
Sample 2 (3rd measurement)	2455.396875	4663.621795	

Table 2 - 3 Output table (Table no.2 – Fig. 2-5), calculated dielectric properties of cast acrylic at 2.44GHz

	Thickness (mm)	ε_r (dielectric constant)	tanδ (loss tangent)
Sample 1 (1st measurement)	2.75	2.672868	0.00774330
Sample 1 (2nd measurement)		2.679158	0.00765770
Sample 1 (3rd measurement)		2.679158	0.00760270
Sample 2 (1st measurement)	1.60	2.652387	0.00764380
Sample 2 (2nd measurement)		2.658710	0.00745940
Sample 2 (3rd measurement)		2.658710	0.00743700

Table 2 - 4 Measured properties of the phantom shell material (cast acrylic)

f_c *(GHz)*	ε_r	*tanδ*	*σ (S/m)*
1.09	2.70	0.0075	0.0012
1.91	2.68	0.0076	0.0021
2.44	2.67	0.0076	0.0027

As can be seen from Table 2-4 cast acrylic is a low loss material and this property could characterize it as a good candidate for an approximate representation of the garments, surrounding the tissue emulating liquid, in terms of dielectric losses [29]. However, the values of the permittivity are higher compared with garments [29]. This is easily understandable considering that cast acrylic is plastic and denser than woven or knitted etc. garments. The thickness of the cast acrylic was chosen to be equal to 3mm so as to provide good mechanical stability of the structure, which is comparable with other phantoms (Table 2-5). HOCS phantom construction has been undertaken in a specialized oven where the orthogonal sheets of cast acrylic (inner and outer oval cross section sheets) were bent to form HOCS structure. The sheets where attached together using a special glue for plastics.

a)

b)

1.1 GHz

1.91 GHz
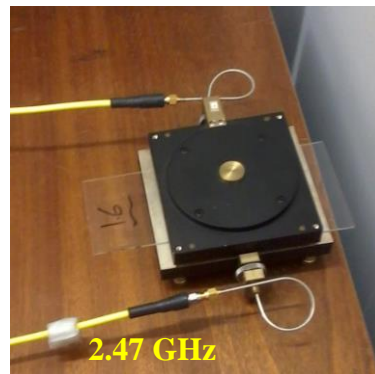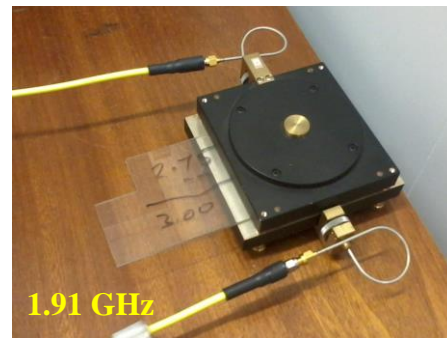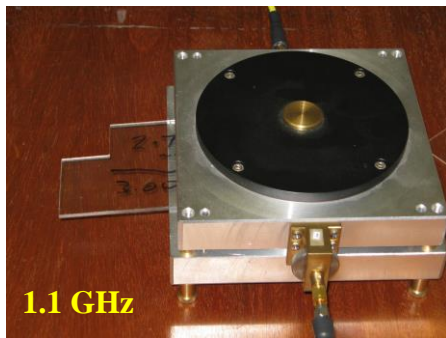
2.47 GHz

**Fig. 2- 6 a) 1.1GHz split post resonator connected with an Anritsu VNA for S_{21} measurements,
b) cast acrylic samples placed inside 1.1; 1.91 and 2.47GHz split post ring resonators respectively [25], [26]**

2.2.3 Phantom comparison with other liquid phantoms

The HOCS phantom is compared with liquid phantoms proposed by other researchers in Table 2-5. The parameters used to compare the liquid phantoms are: shape of the phantom, dielectric constant, thickness of the shell and the frequency where the referred phantoms were used for wearable antennas measurements.

Table 2 - 5 HOCS torso phantom comparison with other liquid phantoms

Shape	Shell		Frequency (GHz)	Reference
	ε_r	Thickness(mm)		
HOCS	2.70	3	1.09	Table 2-4
Oval cross-section	3.40	2	2.45	[22]
Cubic	2.10	5	0.90	[3]
Anthropomorphic (Mannequin)	2.00	3-8	0.30	[4]
Anthropomorphic (Multi Postural)	NA	3-5	0.90	[5]

2.3 Phantom characterization and evaluation

2.3.1 Simulated electric field distribution and attenuation on and in the phantom

2.3.1.1 Attenuation in the phantom

In this sub subsection the effect of the liquid thickness on the electric field attenuation has been analyzed. The aim was to reduce the liquid volume by at least 60%, and subsequently the weight, compared with the full liquid phantom which would result in a reduction of the cost by approximately two thirds. It is described why the 20mm liquid thickness (Fig. 2-4) was selected instead of making the phantom non-hollow (full liquid) or choosing another liquid thickness. A cylindrical dipole antenna (Appendix A) of length equal to 62mm was designed to operate at 2GHz which is the largest wavelength [27], [30] that the liquid is calibrated for (Section-2.2). This is the worst case as the attenuation per distance of the field in the lower frequency is less compared to the higher frequencies. The dipole was placed 10mm away from the phantom surface which is a common separation distance for a wearable antenna [31]. At this distance the dipole antenna suffers less dielectric loading and frequency detuning from the phantom compared to the 0mm distance. This simplifies the analysis followed in this subsection and excludes the parameter of HOCS phantom frequency detuning effect (S_{11}) (see subsection-2.3.2). This antenna has electric field propagation normal to the phantom surface. The analysis was based on the simulation results of the electric field attenuation from the front side (where the antenna was mounted) to the back side of the

phantom. The basic concept is that the electric field attenuation should be comparable with the results derived from the simulations with the full liquid phantom.

The simulation analysis was carried out in Empire-XPU, a Finite-Difference Time-Domain (FDTD) 3D electromagnetic field simulator. An E-field line monitor simulation was used in order to observe the E-field attenuation in the phantom for the case of full liquid and various liquid thicknesses of the HOCS phantom. The setup of the simulation models followed for this analysis can be seen in Fig. 2-7. Point 1 is the position on the front side of HOCS and point 2 is the position on the opposite surface, back side of HOCS. These points are marked in the electric field results to facilitate the comparison of the attenuation of the E-field for all the phantoms simulated.

The E-field attenuation (A) in dB for all the liquid thickness cases and the full liquid case is shown in Table 2-6. The E-field attenuates similarly, between points 1 and 2, for the case of full liquid and for liquid thicknesses 45mm and above. Hence, it can be derived that the liquid thickness 45mm should be the best solution approximating the performance of the full liquid case. However, another criterion which led to the final choice for 20mm liquid thickness is the liquid volume reduction of the hollow phantom compared with the full liquid phantom's volume. The aim of HOCS volume was set to be equal or less than 40% of the full liquid phantom volume. The percentage of the volume for each liquid thickness compared with the full liquid one is shown in Table 2-6.
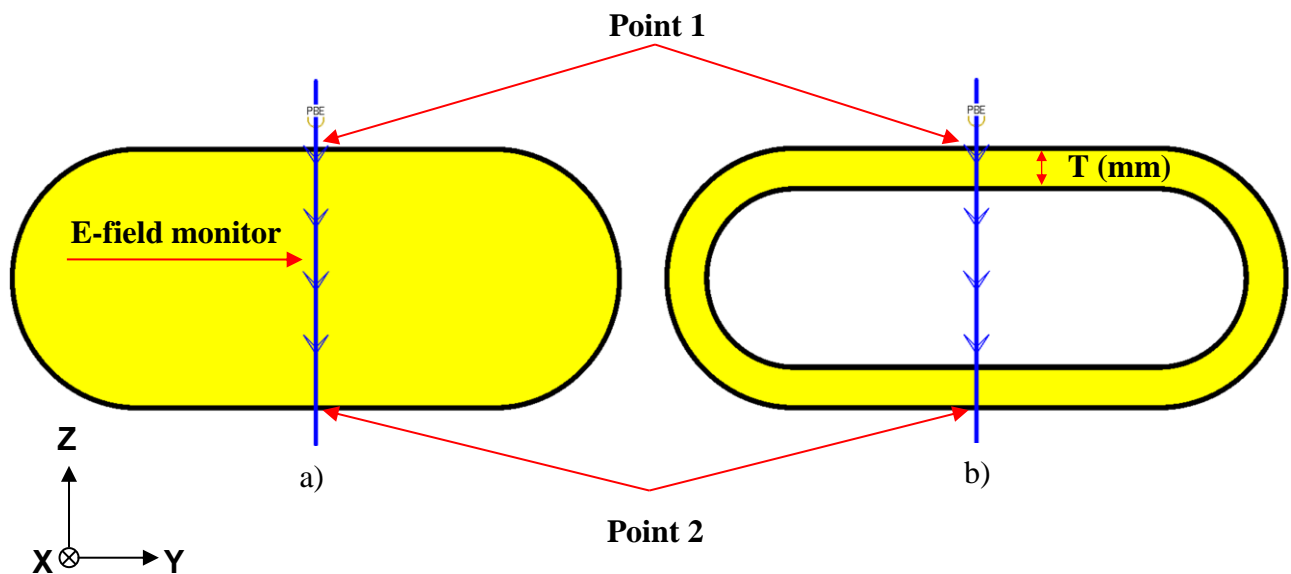

Fig. 2- 7 E-field line monitors simulation analysis model setup:

a) Full liquid and b) HOCS with variable thickness

Table 2 - 6 Electric field attenuation (dB) from point 1 to 2 at 2GHz and HOCS phantom volume comparison with the full liquid phantom for various liquid thicknesses

T (mm)	V_{HOCS} / V_{FULL}	A (dB)
Full Liquid	100.00%	78.42
15	26.59%	45.39
20	34.79%	55.62
25	42.64%	58.06
30	50.17%	62.57
35	57.35%	68.08
40	64.18%	70.88
45	70.70%	76.91
50	76.86%	77.06
55	82.71%	77.84

In order to examine the behavior of the 20mm liquid thickness in the calibrated liquid frequency range, respective simulations (Fig. 2-7) for the full liquid and the 20mm HOCS phantoms, for dipoles resonating at 2.5 ; 3.5 and 5.5GHz (Appendix A) were performed. The E-field attenuation in dB for the 20mm liquid thickness case and the full liquid case are shown in Table 2-7.

Table 2 - 7 E-field attenuation (A) from point 1 to point 2 at 2.5; 3.5 and 5.5GHz for the full liquid phantom and for the HOCS phantom with 20mm liquid thickness

Frequency (GHz)	A (dB)	
	Full liquid	**HOCS (20mm)**
2.5	84.16	64.02
3.5	96.78	72.71
5.5	111.71	110.93

As can be seen from Table 2-7 at higher frequencies close to the upper calibrated liquid frequency limit the electric field attenuation increases. More specifically at 2.5GHz the total electric field attenuation of the HOCS (20mm) phantom is less than the full liquid one, but it is higher than the attenuation at 2GHz. The total electric field attenuation at 3.5GHz for the case of the HOCS (20mm) deviates from the full liquid one, but it is higher than it is at the 2 and 2.5GHz. Finally the E-field attenuation of HOCS (20mm) at the 5.5GHz is quite close with the full liquid one and it is significantly larger than the lower frequencies.

The analysis followed in this sub subsection showed than the 20mm liquid thickness HOCS phantom design led to a more than 60% decreased liquid volume compared with the the liquid volume of the full liquid phantom. Additionally, the electric field attenuation simulation analysis showed that the attenuation taking place from the front to the back side of the HOCS (20mm) phantom deviates from the full liquid phantom at 2; 2.5 and 3.5GHz. This attenuation at the 5.5GHz in the case of the HOCS (20mm) phantom is quite close with the full liquid one. This deviation could lead to a divergence (between HOCS and the full liquid phantom) on the On-phantom electric field distribution (see sub subsection 2.3.1.3) and to the On-phantom communication link budget (see subsection 2.3.3). A solution, via simulations, to improve this deviation is proposed in the next sub subsection.

2.3.1.2 Absorber modification

Sub subsection 2.3.1.1 conclusion is for using a 20mm liquid thickness HOCS phantom which would reduce the volume by 60%. This is the liquid thickness of the proposed and realized phantom. So, in the following of this study, the 20mm liquid thickness HOCS phantom will be referred as "HOCS phantom". As a solution to the attenuation issue presented in the previous analysis, a modification to the HOCS phantom is proposed. This modification has an RF absorbing material [32] in the middle of HOCS, instead of being hollow. Three different RF absorbing materials were simulated. All the absorbing materials had a simulated (using Empire-XPU) target absorption equal to 1dB / mm. They differ in terms of dielectric constant value. The dielectric constant values of the absorbing materials simulated were equal to 15 (ferrite tile), 5, 1 (foam). The electromagnetic properties of these three RF absorbing materials, using the absorption rate and the dielectric constant values, can be easily calculated from the formulas of equation (2.1), given by Empire-XPU. These properties are the ones used by the simulation software, Empire-XPU. The simulated normalized to the maximum value, at point 1, E-field attenuation for the cases of HOCS, HOCS with RF absorbing materials and the full liquid phantoms are shown in Fig.2-8; 2-9; 2-10 and 2-11 for the 2; 2.5; 3.5 and 5.5GHz respectively. The E-field attenuation, from point 1 to point 2, of HOCS with all the absorbing materials simulated is closer to the full liquid compared with the HOCS without the absorbing materials for the frequencies of 2; 2.5 and 3.5GHz. From Fig. 2-11 the conclusion that at 5.5GHz the HOCS phantom electric field attenuation from point 1 to point 2 is quite close with the full liquid one is verified. So, for the

case of 5.5GHz no RF absorbing material is required to modify HOCS phantom in order to achieve similar electric field attenuation (between point 1 and 2) with the full liquid phantom. From all the absorbers simulated, as long as it was found that all of them improve the electric field attenuation performance, the foam-absorber with dielectric constant equal to 1 is proposed to be used. This is proposed because in terms of a real life scenario a foam absorber ($\varepsilon_r = 1$) would be lighter than a ferrite tile absorber ($\varepsilon_r = 15$) and an absorber with dielectric constant equal to 5.

$\varepsilon r = \varepsilon r2$ (εr: Dielectric constant of absorber)

$\mu r = \varepsilon r2/\varepsilon r1$ (μr: Relative permeability of absorber, εr1:Dielectric constant of HOCS shell)

$ZF = ZF0/sqrt(\varepsilon r2)$ (ZF: Impedance of absorber, ZF0: Free space impedance=377Ohm)   **(2.1)**

$\sigma e = $ ZF $\ast$ (abs $\ast$ 1000.0)/8.68 (σe: Electric conductivity of absorber, abs: absorption rate)

$\sigma m = 1./$ZF $\ast$ (abs $\ast$ 1000.0)/8.68 (σm: Magnetic conductivity of absorber)

Fig. 2- 8 Simulated E$_{field}$ vs position of the E-field line monitor between points 1 & 2 at 2GHz

Fig. 2- 9 Simulated E$_{field}$ vs position of the E-field line monitor between points 1 & 2 at 2.5GHz
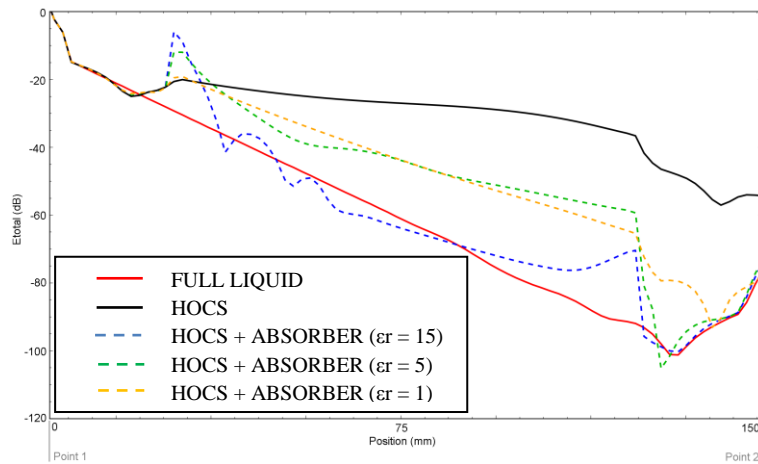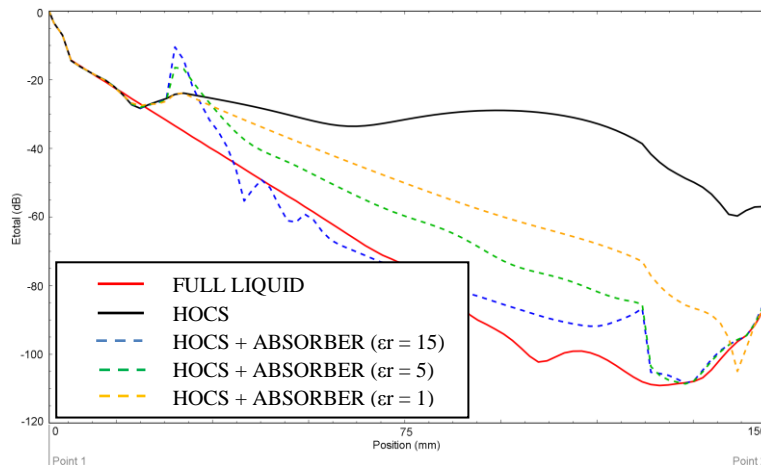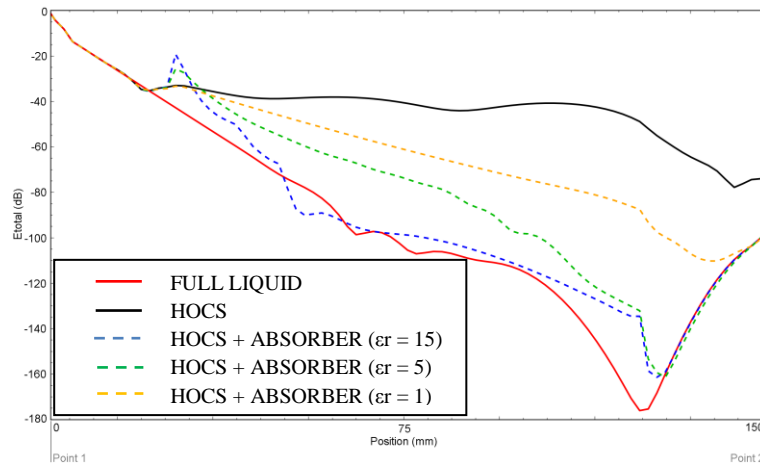
Fig. 2- 10 Simulated E$_{field}$ vs position of the E-field line monitor between points 1 & 2 at 3.5GHz
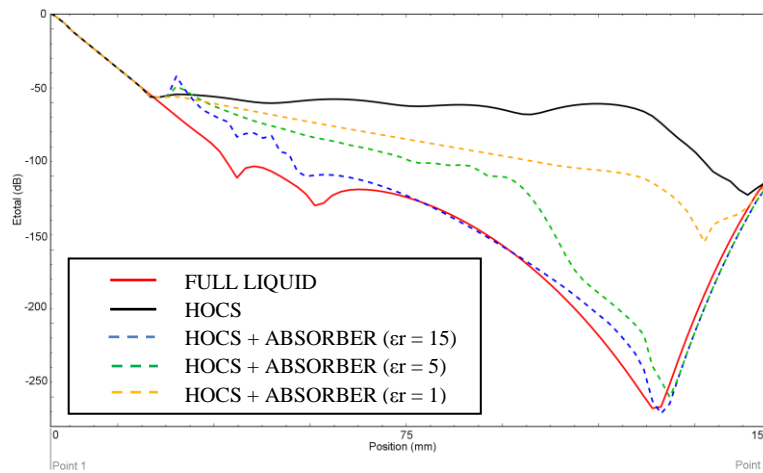
Fig. 2- 11 Simulated E$_{field}$ vs position of the E-field line monitor between points 1 & 2 at 5.5GHz

2.3.1.3 Electric field distribution on the phantom

In order to give a full image of the effect of the RF absorbing materials addition on the electric field distribution in and around the phantom compared with the full liquid and HOCS phantom versions (with and without the RF absorbing materials), the simulated 2; 2.5; 3.5 and 5.5GHz dipoles' (sub subsection 2.3.1.1) E-field distributions are plotted. The dipoles' examined polarizations were vertical (X-axis) and horizontal (Y-axis). These two polarization scenarios express two common wearable antenna polarization cases were the polarization of the antenna is parallel to the height of the phantom or parallel to the width of the phantom [1]. The XZ and YZ plane cuts, of the normalized to the maximum value, E-field distribution are shown in Fig. 2-12; 2-13; 2-14; 2-15; 2-16; 2-17; 2-18 and 2-19. In all these figures the grey

"shadow" is the phantom and it is used to mark the limits of the external dimensions of the phantom in order to focus the study on the electric field distribution on the phantoms external surface or around the phantoms.

Generally, in terms of the electric field distribution on or around the phantom, the addition of the RF absorbing materials brings the HOCS phantom's performance closer to the full liquid phantom. This comes to verify and extend the results of the previous sub subsection about the absorber effect (improvement) on the electric field attenuation performance. The effect on the electric field distribution from all the absorbing materials at all the examined frequencies (2; 2.5; 3.5 and 5.5GHz) for both polarizations (Vertical and Horizontal) is summarized in Table 2-8. Considering the E-field distribution simulation results of all studied HOCS phantom cases, this table presents how close to the reference full liquid phantom is each one of these cases. The notations used in this table are: NC: "Not Close to full liquid phantom performance", C: "Close to full liquid phantom performance" and S: "Similar (almost the same) to full liquid phantom performance". From Table 2-8 it could be said that for the 2GHz for both polarizations examined that HOCS modification with the absorbers of dielectric constant equal to 15 and 5 yield E-field distribution on or around phantom similar to that of the full liquid phantom. From the measurement setup facilitation point of view it would be preferable to use the second absorber with the lower dielectric constant as it will be lighter than the other absorber with the higher dielectric constant. Similar, with the 2GHz, conclusions are derived for the 2.5GHz band for both polarizations. At the 3.5GHz for vertical polarization the E-field distribution on HOCS phantom is similar to that of the full liquid one. At the same frequency, in terms of horizontal polarizations, the RF absorbing material is required to achieve E-field distribution similar with the full liquid phantom. It is proposed that the foam absorber should be used because it will be lighter than the other two. The 5.5GHz frequency results yield that no RF absorbing material is required.

Concluding, it could be said that for near field measurements (which could approximate the E-field distribution recording) using the HOCS phantom, RF absorbing material is not required (to achieve E-field distribution similar to the full liquid one) at 5.5GHz for any polarization and at 3.5GHz for Vertical polarization only. For measurements at 3.5GHz for Horizontal polarization, as well as at 2.5 and 2GHz frequency bands RF absorbing material is required to achieve near field amplitude (E-field) distribution similar with that of the full liquid phantom one. From the near field measurement facilitation point of view, HOCS phantom and wearable antenna on it should be set up first and secondly the RF

absorbing material should be placed in the hollow region. This should be the case due to increased weight of the HOCS phantom with the absorbers, which could complicate the measurement setup.

Table 2 - 8 HOCS phantom with and without RF absorbing materials comparison with full liquid phantom (NC: "Not Close", C: "Close" and S: "Similar")

Frequency (GHz)	2				2.5				3.5				5.5			
Polarization	Vertical		Horizontal		Vertical		Horizontal		Vertical		Horizontal		Vertical		Horizontal	
Plane	YZ	XZ	YZ	XZ	YZ	XZ	YZ	XZ	YZ	XZ	YZ	XZ	YZ	XZ	YZ	XZ
HOCS	NC	NC	NC	NC	NC	NC	NC	NC	S	S	C	C	S	S	S	S
HOCS & ABSORBER (εr=15)	S	S	S	S	S	S	S	S	S	S	S	S	S	S	S	S
HOCS & ABSORBER (εr=5)	S	S	S	S	S	S	S	S	S	S	S	S	S	S	S	S
HOCS & ABSORBER (εr=1)	S	C	C	C	S	C	S	C	S	S	S	S	S	S	S	S

2.3.1.4 Electric field propagation at HOCS phantom

Due to HOCS phantom variation of dielectric mediums (Perspex – Liquid – Perspex – Air – Perspex – Liquid – Perspex) in its structure, there have been occurred various E-field propagation phenomena. Such phenomena are: *a) smaller E-field attenuation in HOCS phantom compared with the full liquid phantom and with the HOCS phantom with the RF absorbers; b) reflection of the E/M wave due to different mediums propagation; c) standing waves and d) wave guidance through the liquid thickness (high dielectric (liquid) surrounded by low dielectric (Perspex).* About: a) it is clear from the E-field attenuation and distribution figures (Fig. 2-8 – 2-19); b) it is clear from the E-field distribution plots (Fig. 2-12 – 2-19) and cam be seen as the field propagates through HOCS phantom (especially at the point where the field passes from the liquid to the lower dielectrics (Perspex and Air); c) it is clear from the E-field attenuation plots (abrupt attenuation of the E-field) (Fig. 2-8 – 2-11) and d) it can be seen from the E-field distribution plots (Fig. 2-12 – 2-19).

Fig. 2- 12 Simulated YZ and XZ plane cuts of the normalized to the maximum value E$_{total}$ field distribution of a Vertical polarized dipole at 2GHz for: a) full liquid, b)HOCS, c) HOCS & Absorber (εr =15), d) HOCS & Absorber (εr =5), e) HOCS & Absorber (εr =1) phantoms

Fig. 2- 13 Simulated YZ and XZ plane cuts of the of the normalized to the maximum value E_total field distribution of a Horizontal polarized dipole at 2GHz for: a) full liquid, b)HOCS, c) HOCS & Absorber (εr =15), d) HOCS & Absorber (εr =5), e) HOCS & Absorber (εr =1) phantoms
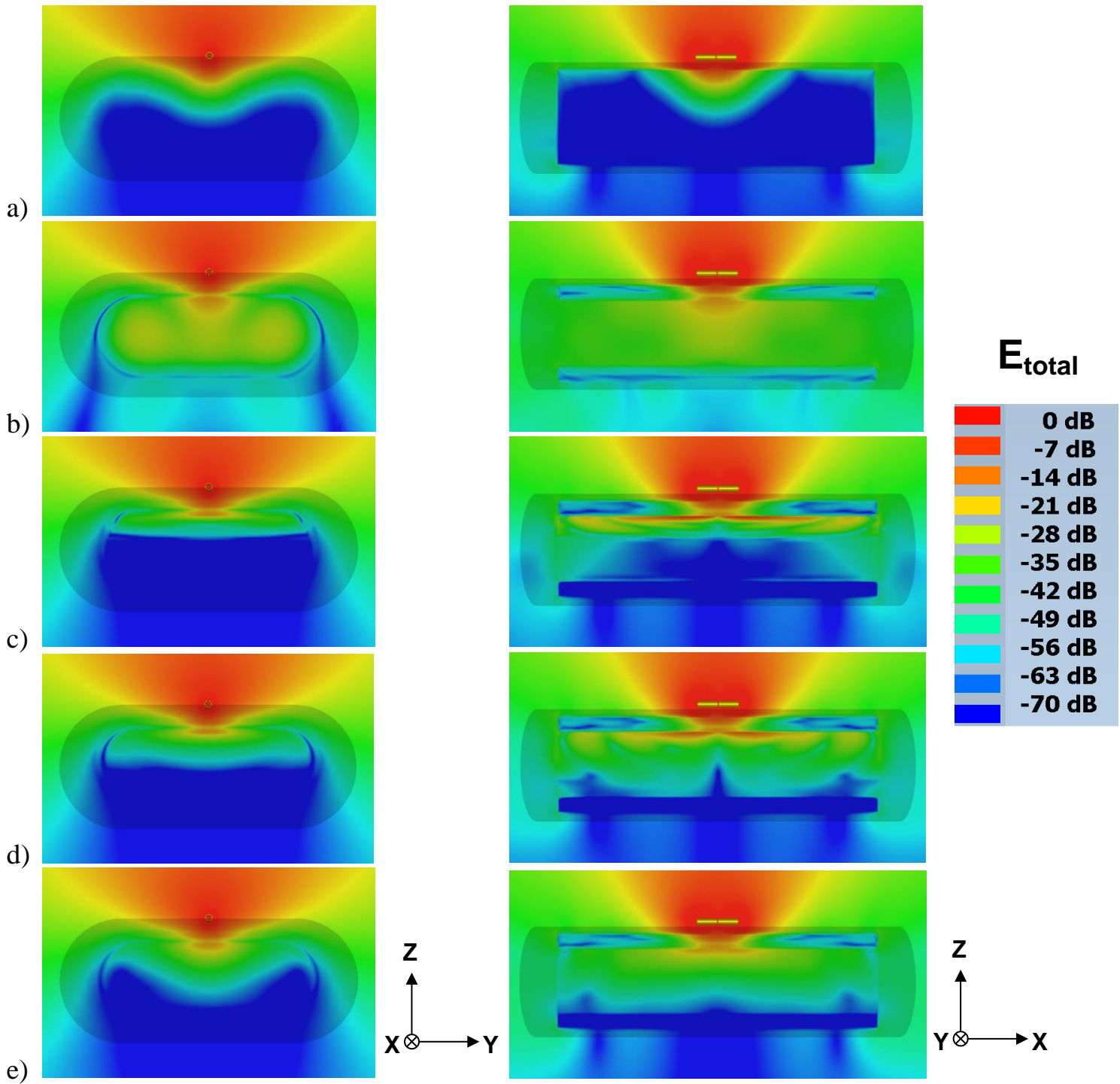
Fig. 2- 14 Simulated YZ and XZ plane cuts of the of the normalized to the maximum value E_{total} field distribution of a Vertical polarized dipole at 2.5GHz for: a) full liquid, b)HOCS, c) HOCS & Absorber (εr =15), d) HOCS & Absorber (εr =5), e) HOCS & Absorber (εr =1) phantoms

Fig. 2- 15 Simulated YZ and XZ plane cuts of the of the normalized to the maximum value E$_{total}$ field distribution of a Horizontal polarized dipole at 2.5GHz for: a) full liquid, b)HOCS, c) HOCS & Absorber (εr =15), d) HOCS & Absorber (εr =5), e) HOCS & Absorber (εr =1) phantoms
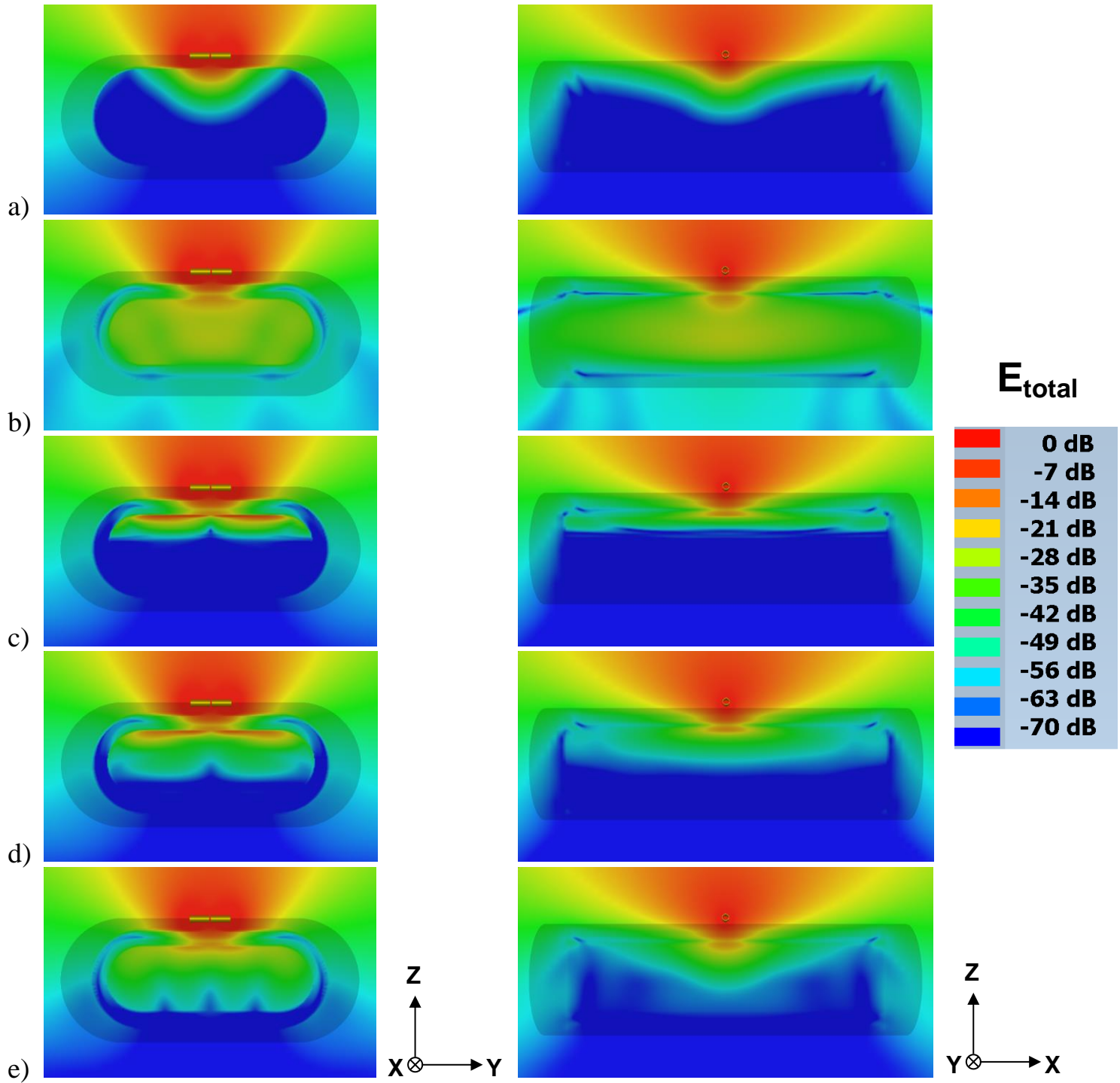
Fig. 2- 16 Simulated YZ and XZ plane cuts of the of the normalized to the maximum value E$_{total}$ field distribution of a Vertical polarized dipole at 3.5GHz for: a) full liquid, b)HOCS, c) HOCS & Absorber (εr =15), d) HOCS & Absorber (εr =5), e) HOCS & Absorber (εr =1) phantoms

Fig. 2- 17 Simulated YZ and XZ plane cuts of the of the normalized to the maximum value E$_{total}$ field distribution of a Horizontal polarized dipole at 3.5GHz for: a) full liquid, b)HOCS, c) HOCS & Absorber (εr =15), d) HOCS & Absorber (εr =5), e) HOCS & Absorber (εr =1) phantoms
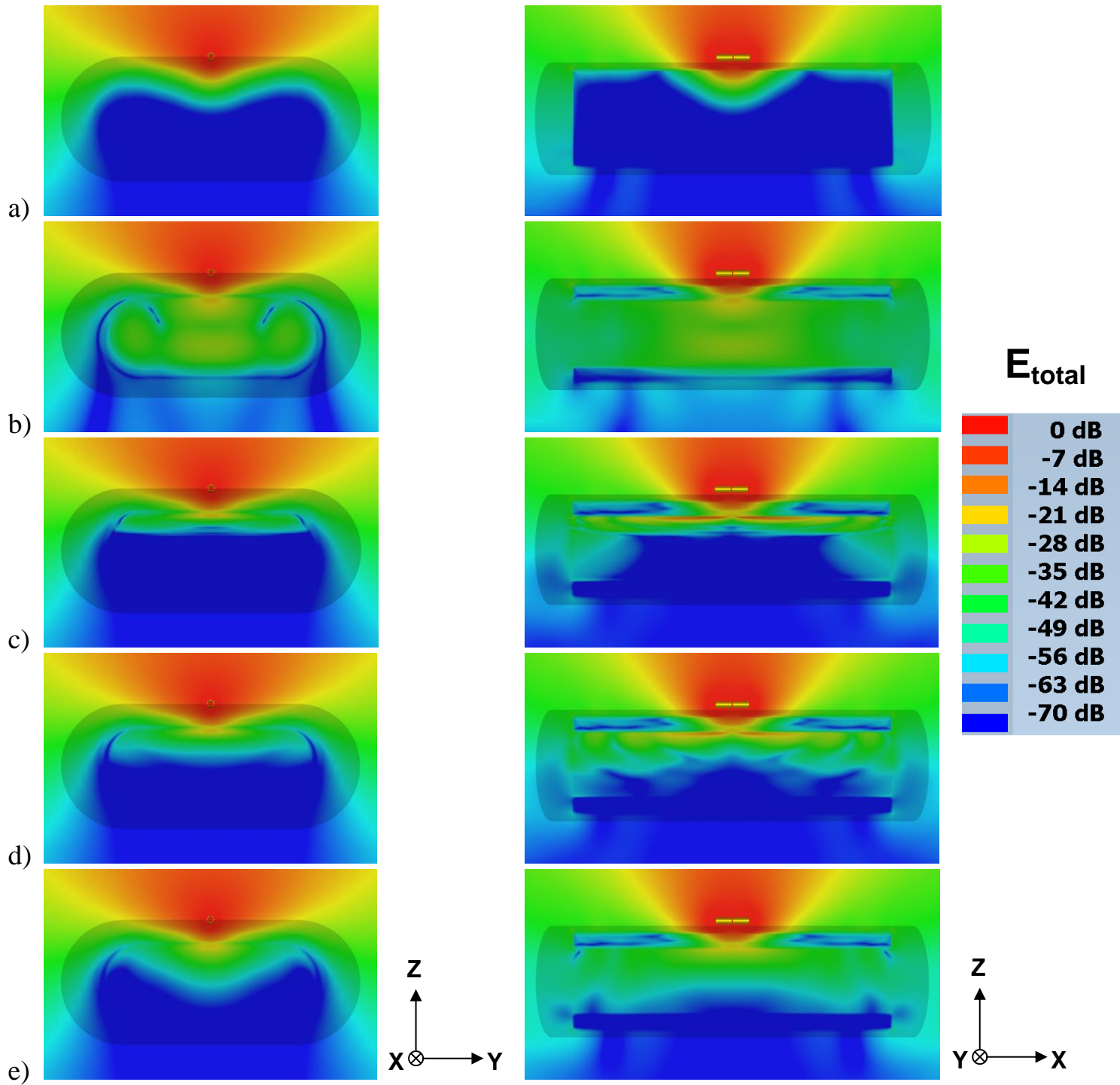
Fig. 2- 18 Simulated YZ and XZ plane cuts of the of the normalized to the maximum value E$_{total}$ field distribution of a Vertical polarized dipole at 5.5GHz for: a) full liquid, b)HOCS, c) HOCS & Absorber (ε$_r$ =15), d) HOCS & Absorber (ε$_r$ =5), e) HOCS & Absorber (ε$_r$ =1) phantoms
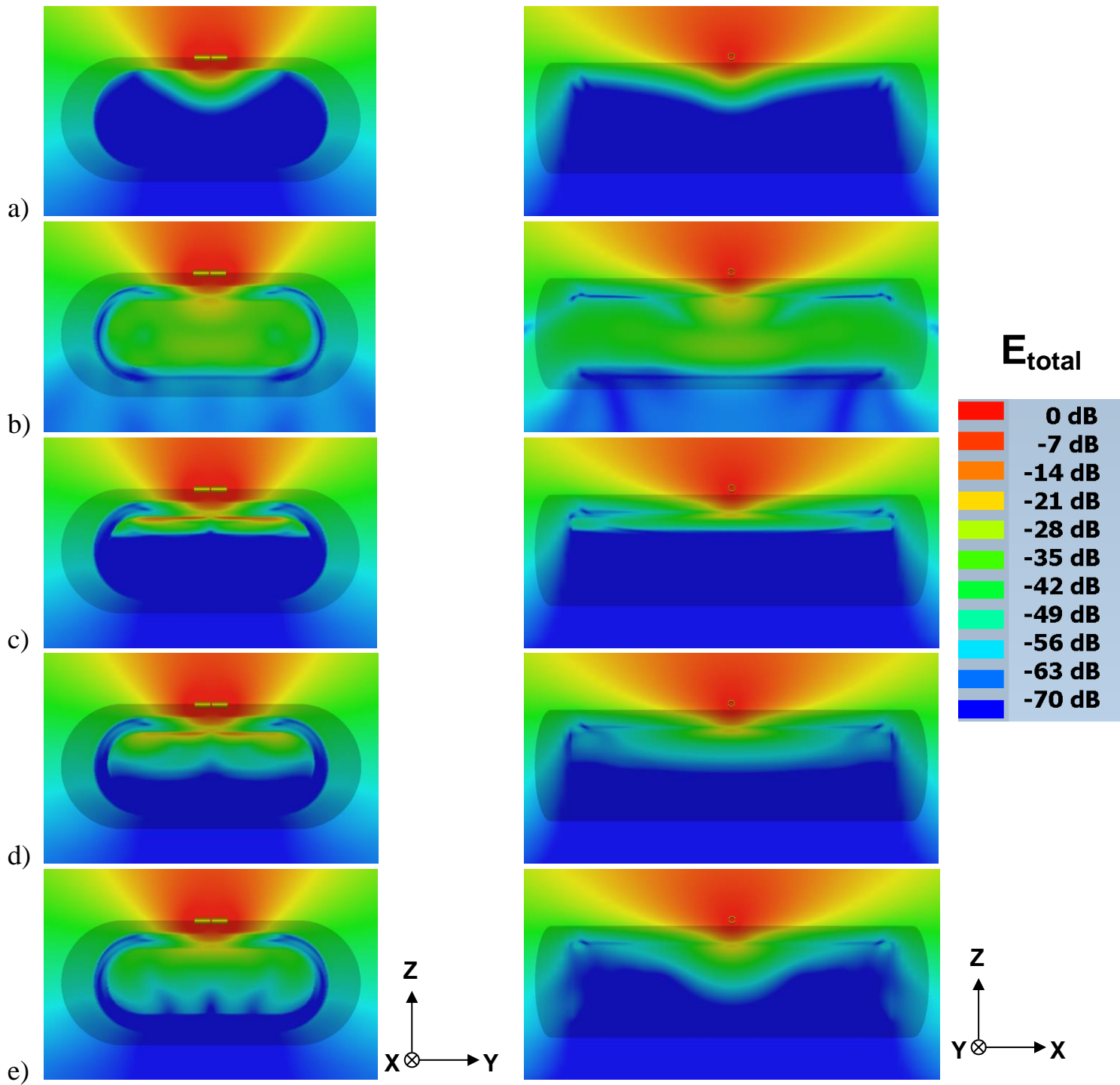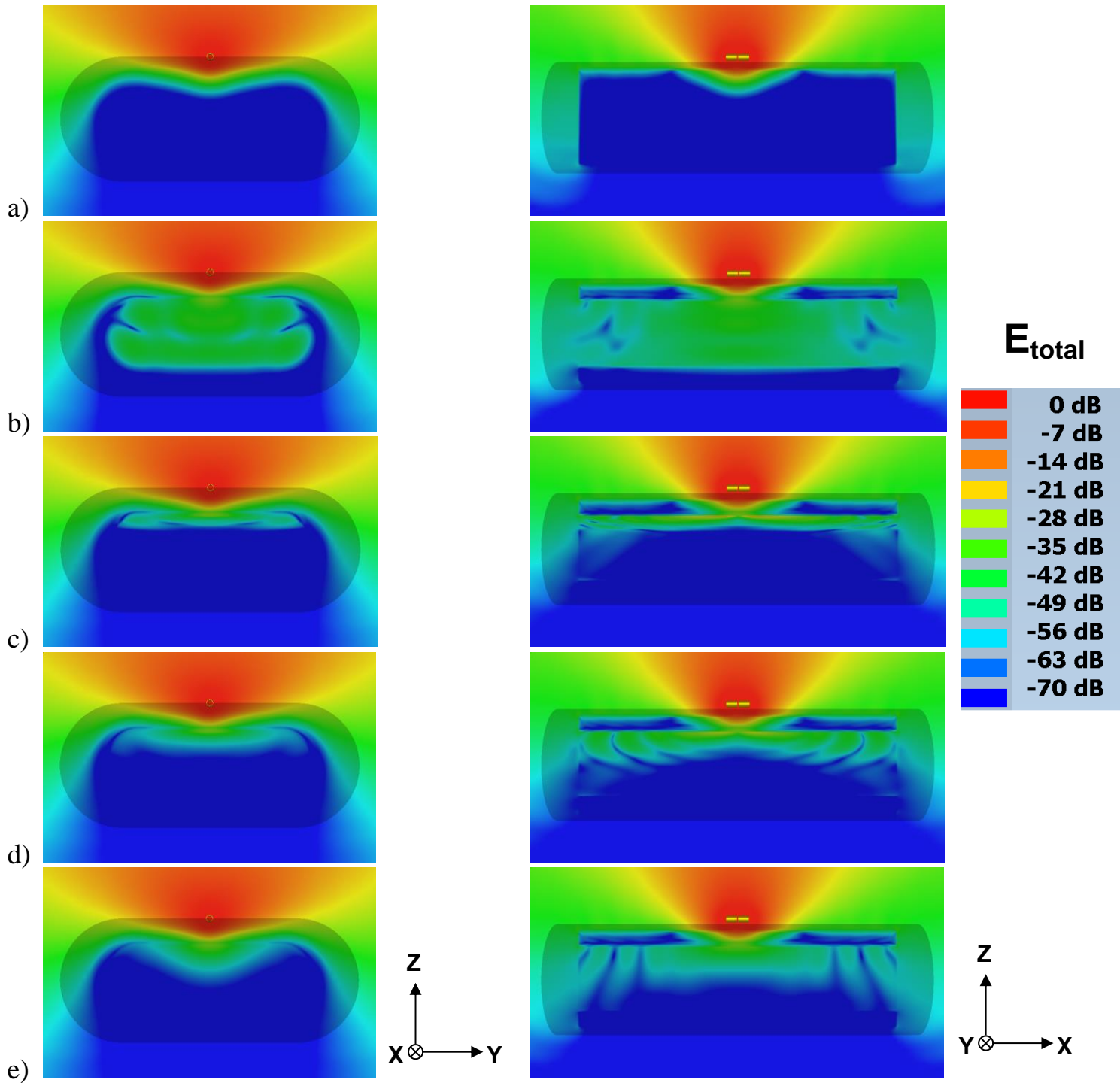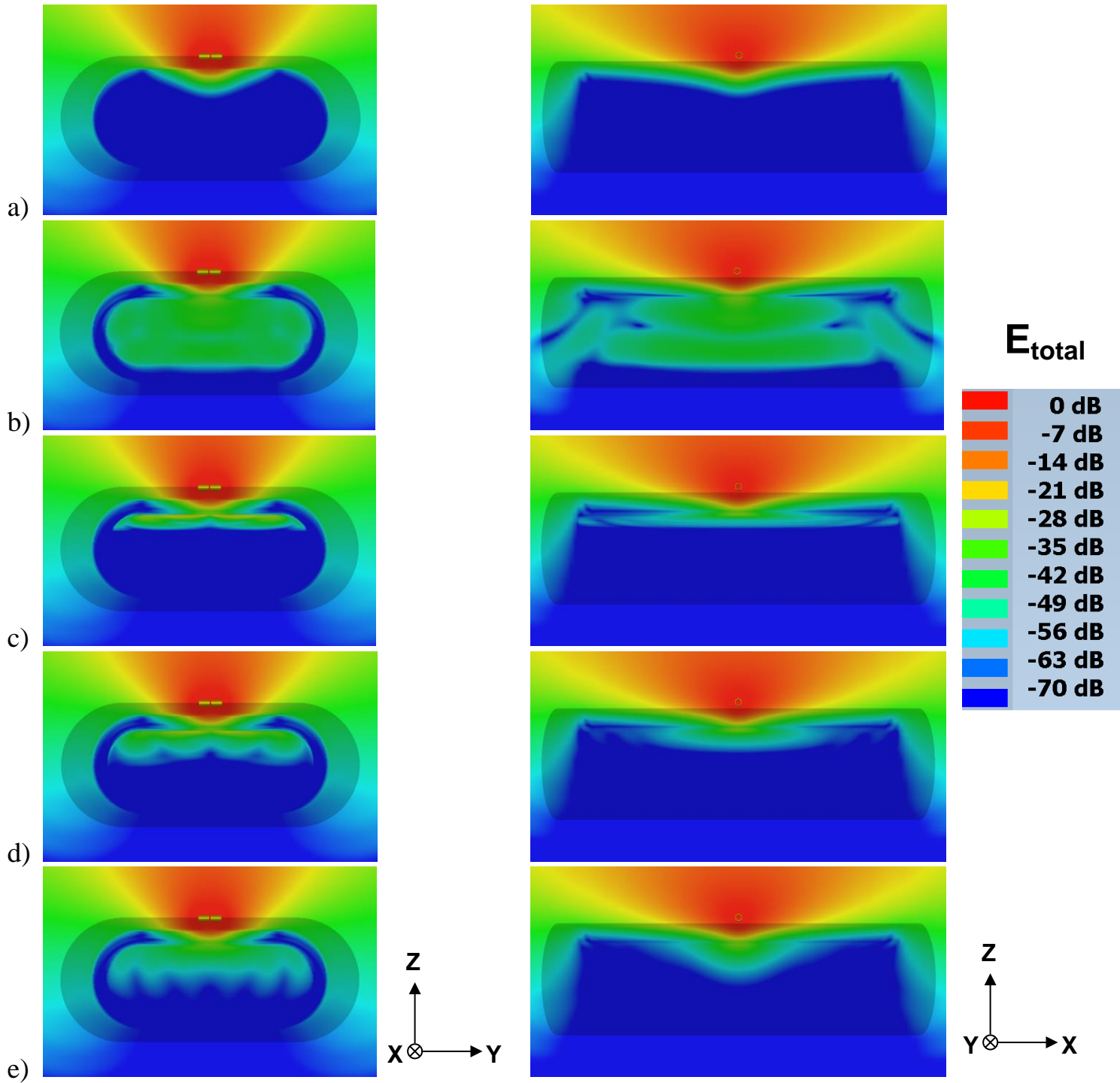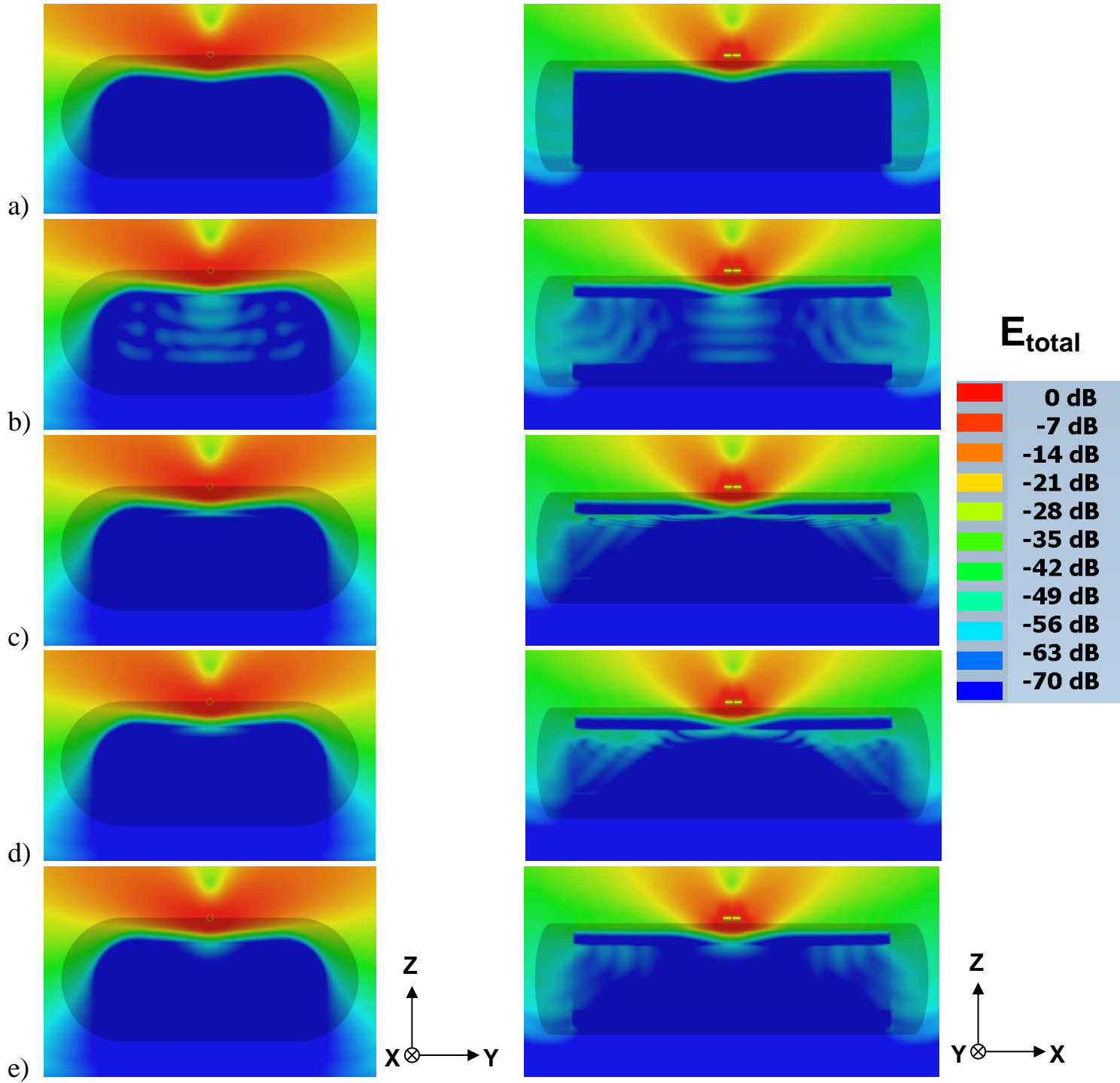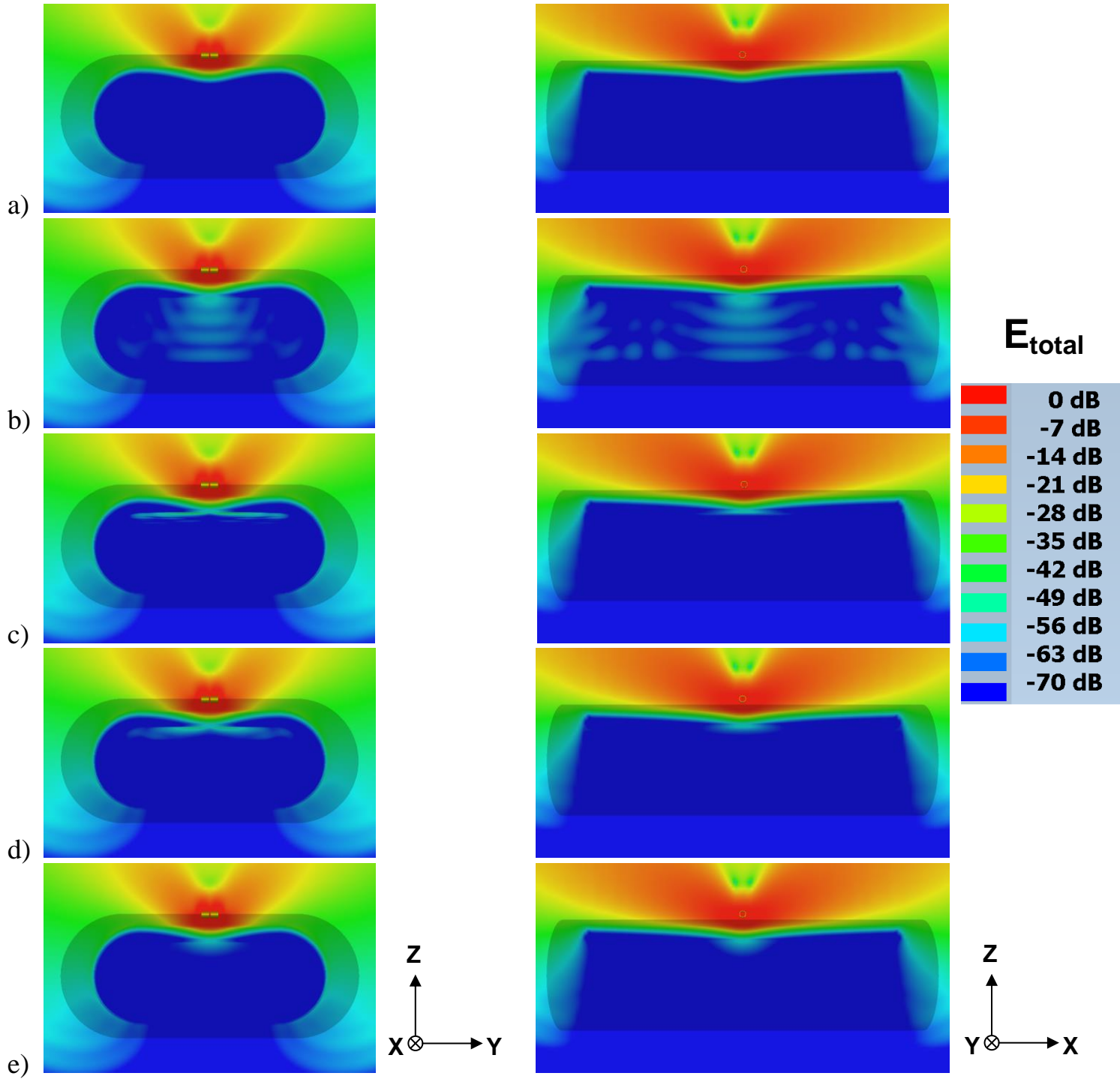
Fig. 2- 19 Simulated YZ and XZ plane cuts of the of the normalized to the maximum value E_{total} field distribution of a Horizontal polarized dipole at 5.5GHz for: a) full liquid, b)HOCS, c) HOCS & Absorber (εr =15), d) HOCS & Absorber (εr =5), e) HOCS & Absorber (εr =1) phantoms

2.3.2 Phantom influence on the reflection coefficient of a wearable antenna

The reflection coefficient (S_{11}) [1] of a wearable antenna is related to the input impedance (Z_{in}) which is affected by the presence of the body/phantom [33]. The wearable antenna is dielectrically loaded by the human tissues. It is important that the phantom is evaluated for S_{11} wearable antenna measurements. Various S_{11} measurements were carried out on HOCS and compared with respective ones which were obtained from three different volunteers (Fig. 2-20). For the S_{11} measurements three antennas were used: two sleeved balanced dipoles (subsection 2.3.1) [34] and a printed monopole antenna [30],[35] (the antennas geometry and free space performance are described in Appendix A). The antennas were mounted directly against the plastic shell (HOCS) and the clothes (volunteers) (0mm distance away from phantom and bodies). The dipole antennas have no ground plane and the printed monopole antenna has a short ground plane. This means that their S_{11} performance is highly affected by the presence of the human body/phantom. That is why these antennas were selected for the wearable antenna reflection coefficient measurements evaluation of the phantom. These antennas resonate at 2, 2.5 (subsection 2.3.1) and 5.8 GHz respectively. This gives the chance to evaluate the phantom at the lower calibrated frequency limit of the liquid (2GHz), the higher frequency limit (close to 6GHz) and the ISM band (2.5GHz).

Fig. 2- 20 Measurement setup of the 2GHz sleeved balanced dipole antenna mounted on three volunteers and on HOCS torso phantom

The S_{11} measurements (12 measurements, 4 in each location, carried out on each subject and they were repeatable for each one at each location) on each volunteer and on HOCS phantom results for the three examined frequencies and for the respective locations (Fig. 2-20) are shown in Fig. 2-21. It can be noticed from Fig. 2-21a that the effect of three

different bodies (volunteers) is similar to that of the phantom and reduce the resonant frequency (2GHz) of the dipole antenna. The downshift in the resonant frequency of volunteers 2 and 3 is equal to 0.1GHz whilst that of volunteer 1 is 0.2GHz and finally HOCS phantom gives a downshift of 0.3GHz. A parameter sweep analysis (for the 2GHz dipole antenna) for various values of the dielectric constant of the phantom shell was performed and the results are shown in Fig. 2-22. It can be seen that the value of the dielectric constant of the phantom shell affects the downshift of the resonant frequency. Therefore, the deviation between phantom and human bodies is due to the value of the dielectric constant (Table 2-4) of the phantom shell (Cast Acrylic). A phantom shell with a dielectric constant equal to 1.3 will give a better approximation of clothes. The S_{11} measurement results with the dipole (2.5GHz) and the printed monopole (5.8GHz) are shown in Fig. 2-21b and Fig. 2-21c respectively. Fig. 2-21b (2.5GHz) shows that the HOCS phantom frequency downshift and detuning is between the respective downshift and detuning caused by the volunteers. It can be noticed from Fig. 2-21c (5.8GHz) that there is a good agreement, in terms of frequency downshift and detuning, between real human bodies and the HOCS phantom effect on the S_{11} at the high frequency range ($5 - 6$GHz) that the liquid dielectric properties are calibrated for.
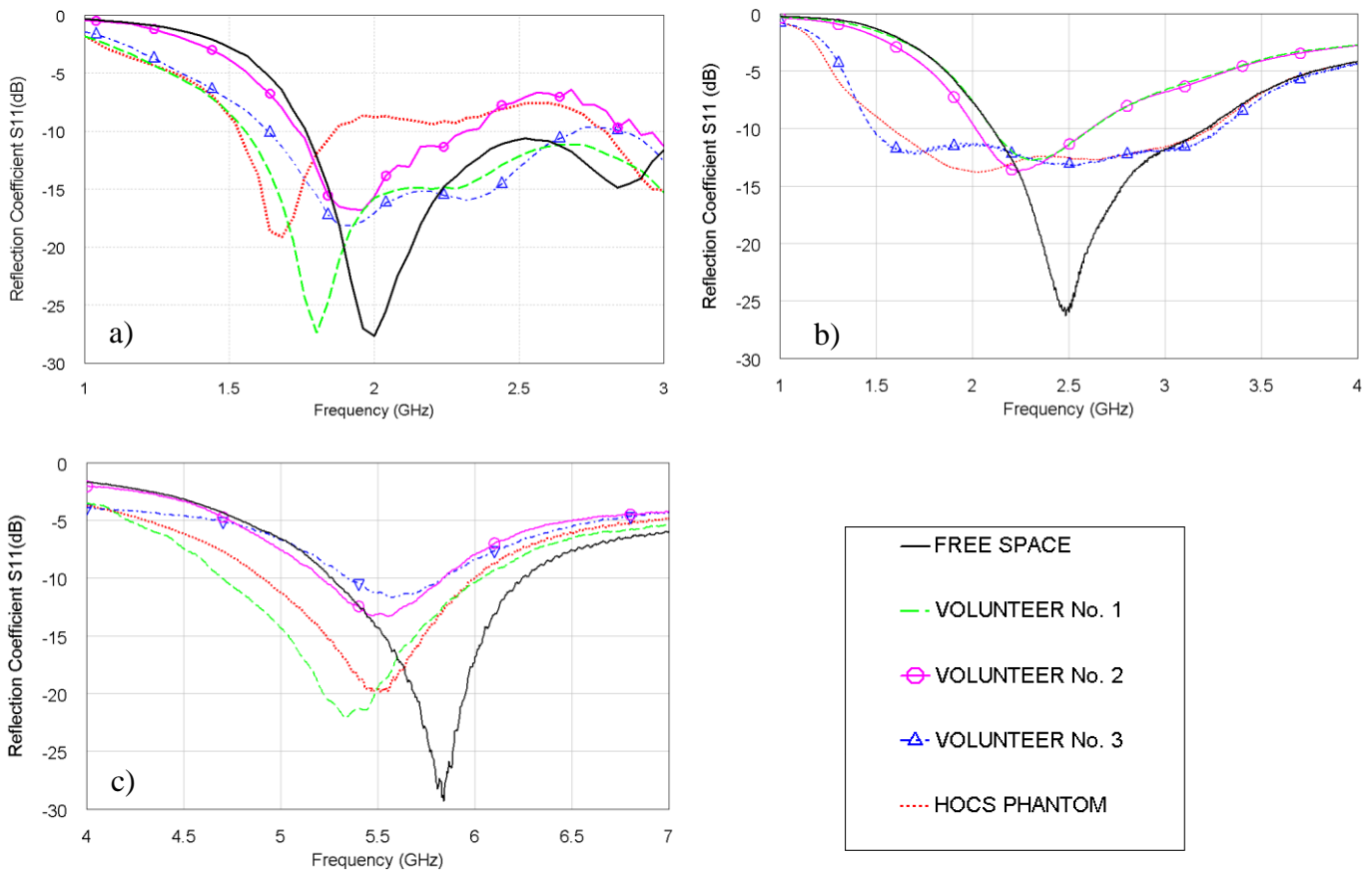

Fig. 2- 21 Measured S11 of sleeved balanced dipole antennas operating at: a) 2GHz and b) 2.5GHz and c) a printed monopole antenna resonating at 5.8GHz in: Free Space, on three volunteers and on HOCS phantom
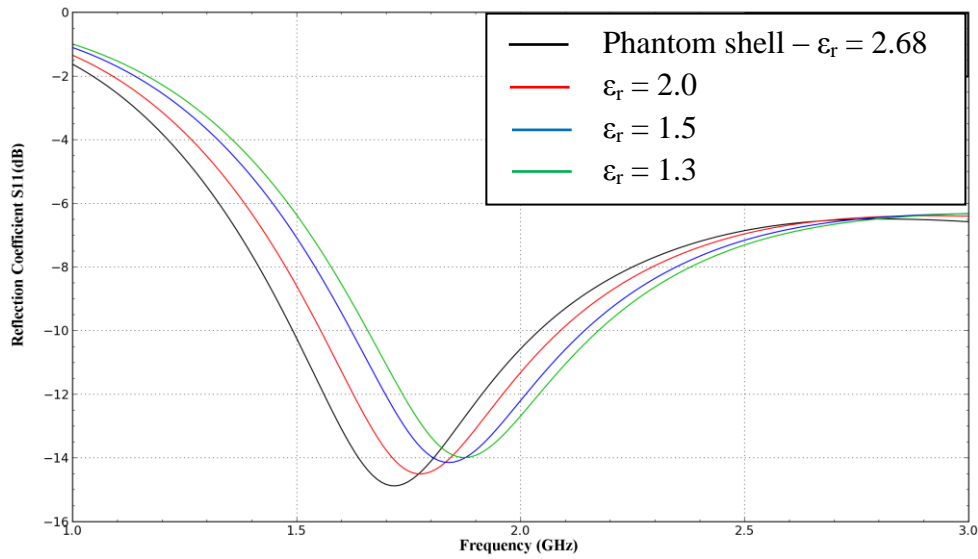
Fig. 2- 22 Simulated S11 results of a sleeved balanced dipole antenna for various values of the dielectric constant of the phantom shell

As the liquid properties are calibrated for the frequency range 2-6GHz the HOCS phantom performance presents better agreement with real human bodies for frequencies higher than the lower frequency limit (2GHz). A phantom made from plastic shell with lower dielectric constant would give better agreement with real human bodies in terms of S_{11} at the lower calibrated liquid frequency limit of the 2GHz band.

2.3.3 Simulated phantom influence on path loss for On-body communication links

Wearable communication systems may include two or more communicating antennas. The signal transmission between two antennas, mounted on the phantom, was examined, through simulations, in order to evaluate the performance of the HOCS phantom under these conditions compared with the full liquid phantom and with the HOCS phantom filled with the RF absorbing materials. The simulation scenario followed for this evaluation is illustrated in Fig. 2-23. Two dipole antennas mounted at a distance of 10mm from the phantom surface on the front and the back side of the phantom respectively. The reason for selecting such types of antennas (dipoles) and this separation distance between each antenna and phantom is the same with the one is subsection 2.3.1. The S_{21} was examined when both dipoles were vertically (X-

axis) and horizontally (Y-axis) polarized. The S_{21} was examined for the case of the full liquid, HOCS and HOCS with the RF absorbing materials phantoms. The normalized S_{21} results for all five phantoms and for dipole antennas operating at 2; 2.5; 3.5 and 5.5GHz (Appendix A) are shown in Fig. 2-24; 2-25; 2-26 and 2-27 respectively.

It can be noticed from the simulation results that the use of the RF absorbing materials decrease the S_{21} deviation in the case of the HOCS phantom compared with the full liquid phantom. More specifically at 2GHz for both polarization scenarios the RF absorbing materials with dielectric constant equal to 15 and 5 result in a path loss quite close with the full liquid one. Similar conclusions are derived of the 2.5GHz for the Vertical polarization scenario. At 2.5GHz for the Horizontal polarization scenario the same RF absorbing materials yield the closest S_{21} to the full liquid phantom with the foam absorber in the HOCS phantom. At 3.5GHz similar, with the 2GHz, conclusions can be derived. At 5.5GHz for the Vertical polarization scenario all the absorbers yield path loss similar to the full liquid one. At the same frequency for Horizontal polarization all the absorbers yield path loss close to the full liquid phantom.

For all the frequencies simulated, the use of these specific RF absorbing materials is proven as a good solution. From measurement setup facilitation point of view the RF absorbers with the lowest dielectric constant are proposed to be used, since they are the lighter ones. More specifically the HOCS phantom would give similar and more realistic path loss at 2; 2.5 and 3.5GHz by the addition of an absorber with a dielectric constant equal to 5. This could be achieved, at the 5.5GHz, with the addition of a foam RF absorber (εr = 1). Additionally to this, and in terms of measurements setup, HOCS phantom and wearable antennas on it should be set up first and secondly the RF absorbing material should be placed in the hollow region. This should be the case due to increased weight of the HOCS phantom with the absorbers, which could complicate the measurement setup.
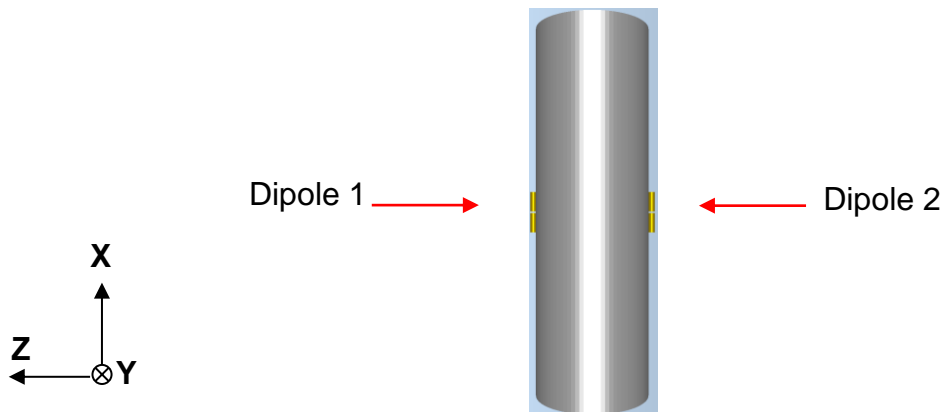
Fig. 2- 23 Simulation model of two vertically polarized dipole antennas mounted on either side of the phantom
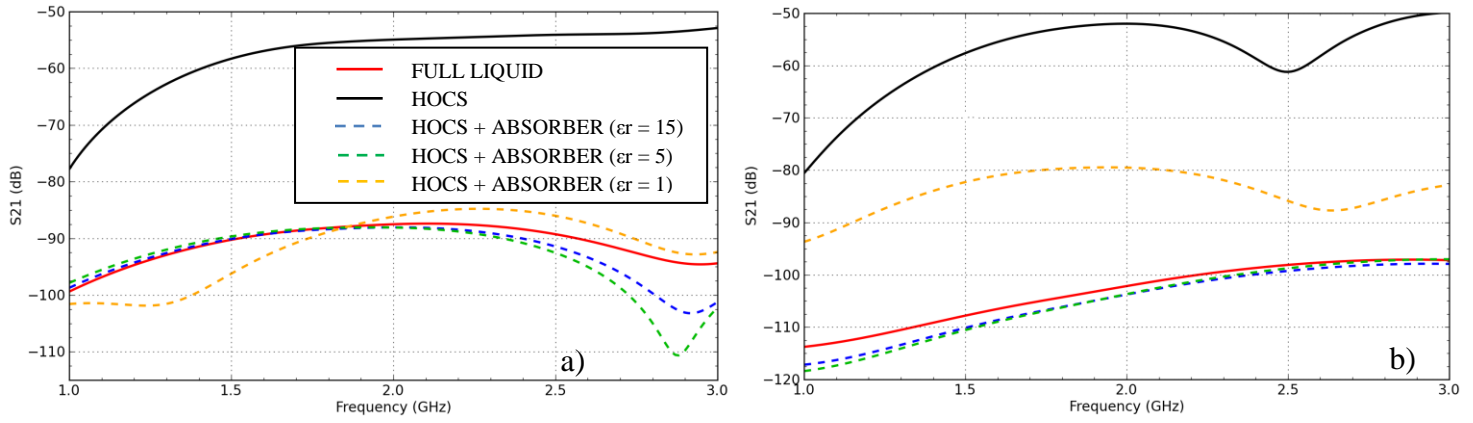
Fig. 2- 24 Simulated path loss (S21) normalized results for the full liquid, HOCS and HOCS with RF absorbing materials phantom for: a) Vertical and b) Horizontal polarizations for dipole antennas resonating at 2GHz
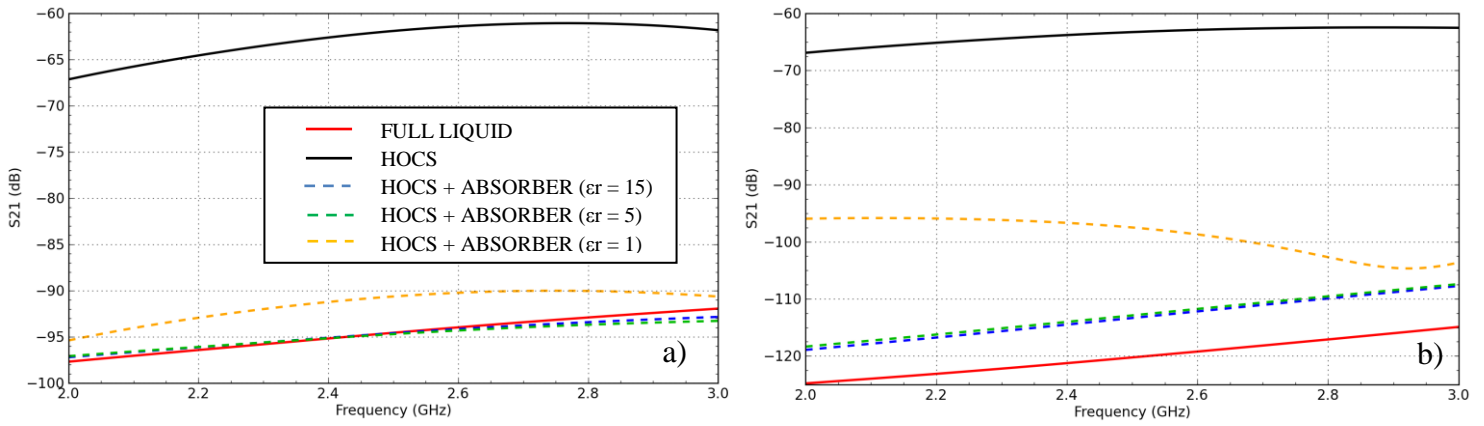
Fig. 2- 25 Simulated path loss (S21) normalized results for the full liquid, HOCS and HOCS with RF absorbing materials phantom for: a) Vertical and b) Horizontal polarizations for dipole antennas resonating at 2.5GHz
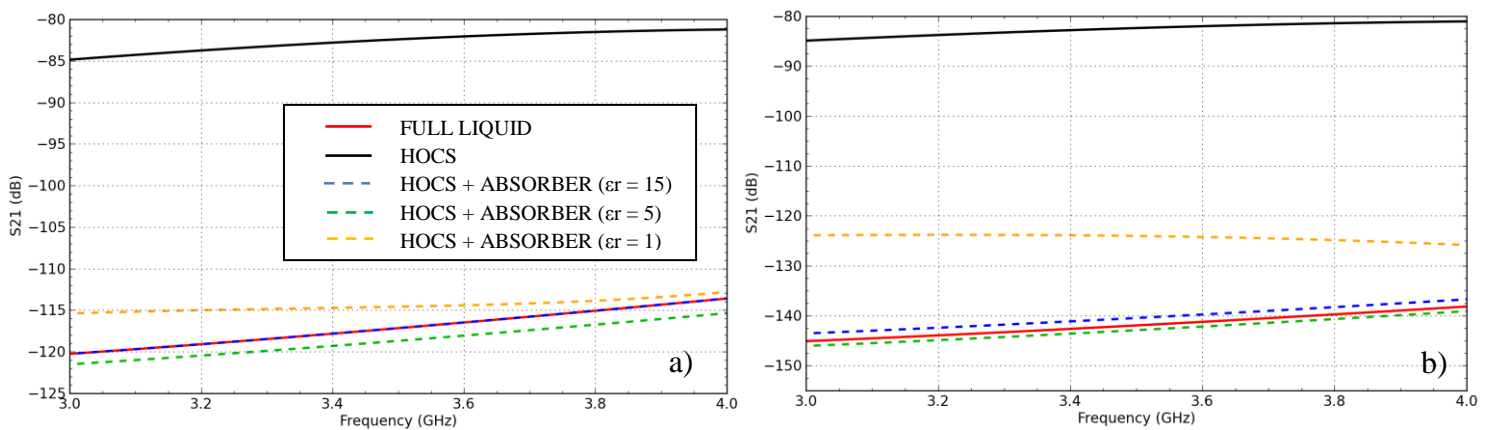
Fig. 2- 26 Simulated path loss (S21) normalized results for the full liquid, HOCS and HOCS with RF absorbing materials phantom for: a) Vertical and b) Horizontal polarizations for dipole antennas resonating at 3.5GHz
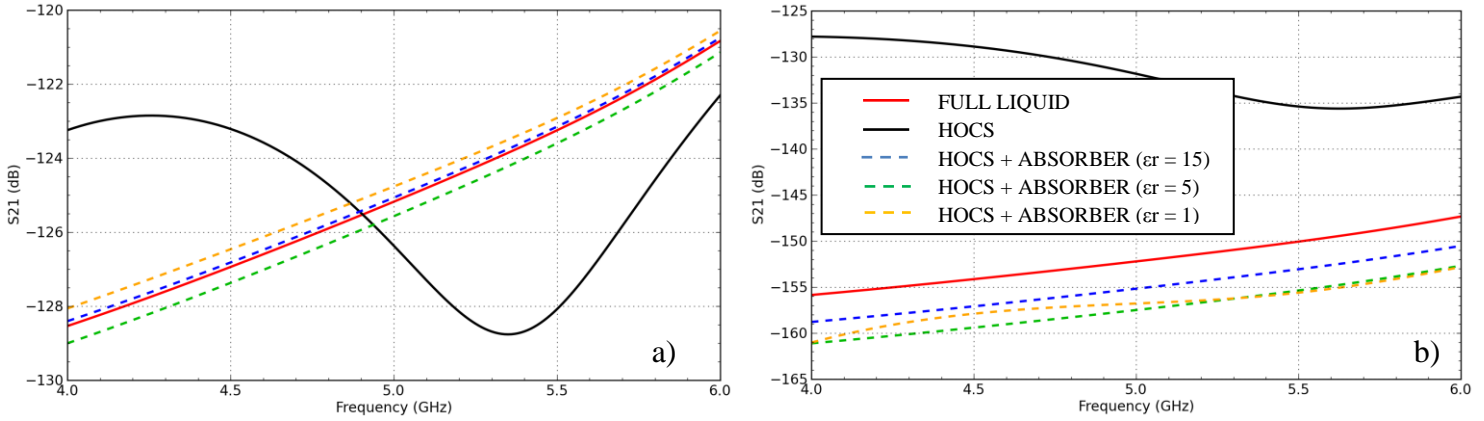
Fig. 2- 27 Simulated path loss (S21) normalized results for the full liquid, HOCS and HOCS with RF absorbing materials phantom for: a) Vertical and b) Horizontal polarizations for dipole antennas resonating at 5.5GHz

2.3.4 Far-field phantom evaluation

2.3.4.1 Simulations

For the purposes of the far field evaluation of the HOCS phantom three printed monopole antennas operating at 2.5, 3.5, 5.5GHz (geometry shown in Appendix A) were designed and simulated for Vertical (X-axis) and Horizontal (Y-axis) polarization orientations. These two polarization scenarios express two common and possible wearable antenna polarization cases were the polarization of the antenna is parallel to the height of the phantom or parallel to the width of the phantom (subsection 2.3.1). These antennas were selected because: a) they are highly affected by the presence of the lossy phantom at 0mm distance and b) they operate at thee bands where the phantom is examined. These give a complete far field HOCS phantom evaluation in the examined frequency range (2-6GHz). The far field results derived from HOCS phantom for all the three frequency bands were compared with the full liquid phantom and a heterogeneous voxel anthropomorphic phantom available at [36] for simulation in Empire-XPU (Fig. 2-28). The far field parameters results are presented in Tables 2-9, 2-10, 2-11. The orientation of the phantoms in the radiation patterns is depicted in Fig. 2-29 and the normalized to the maximum value radiation patterns are presented in Fig. 2-30, 2-31, 2-32, 2-33, 2-34, 2-35 (at Fig.2-30b, 2-32b and 2-34b the HOCS and full liquid phantoms cross-polar component are not depicted because they are negligible, the simulation software yielded maximum cross-polar component values equal to -150dB).

Fig. 2- 28 Simulation setups for far field evaluation-2.5GHz printed monopole antenna with vertical polarization mounted on: a) HOCS, b) Full Liquid and c) heterogeneous anthropomorphic voxel phantoms

The simulated far field results for all frequencies and polarization scenarios show that the HOCS and the full liquid phantoms are in very good agreement in terms of far field anal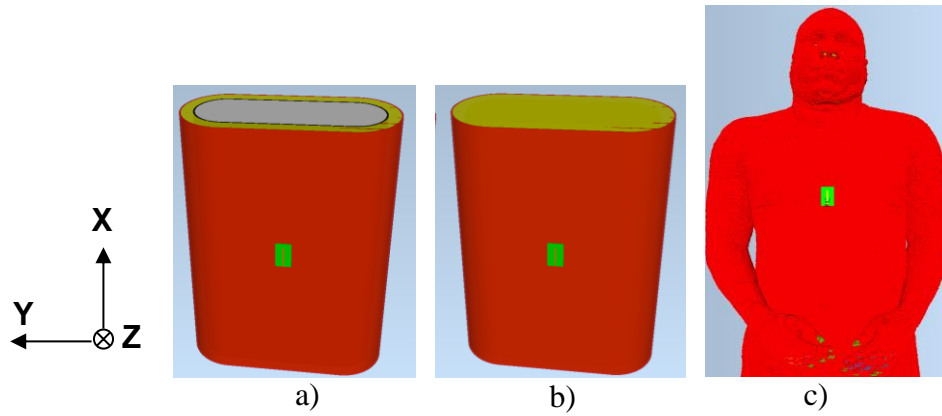ysis. This means that the idea of removing part of the liquid and transforming the full liquid phantom into a hollow one with 20mm liquid thickness is effective in terms of far field wearable antenna performance. More specifically and in terms of far field wearable antenna parameters, gain; directivity and efficiency, the HOCS and the full liquid phantoms for the 2.5GHz monopole antenna (Table 2-9) are quite close and for the 3.5GHz (Table 2-10) and the 5.5GHz (Table 2-11) monopoles they are almost the same. These are valid for both polarization scenarios examined. In terms of radiation patterns at the 2.5GHz dipole for both polarization scenarios (Fig. 2-30 and 2-31) the co-polar components, at azimuth and elevation planes, are quite close with a small difference at the back lobe (180°). In this case the power radiated at the back lobe when the monopole antenna is placed on the full liquid phantom is larger than it is in the case of the HOCS phantom. Additionally, the cross-polar components are almost the same (Fig. 2-30 and 2-31). For the case of the 3.5GHz monopole antenna and for both polarization scenarios (Fig. 2-32 and 2-33) the co-polar components at azimuth and elevation planes are almost the same. Also, the difference in the back lobe noticed at the 2.5GHz case is decreased in the case of the 3.5GHz. Additionally, the cross-polar components are almost the same (Fig. 2-32 and 2-33). Finally, at the 5.5GHz the radiation patterns derived from the HOCS and the full liquid phantoms are similar, for both polarization scenarios (Fig. 2-34 and 2-35).

The heterogeneous anthropomorphic voxel Phantom, which is a very good representation of the real human body, deviates in the far field parameters (gain, efficiency and directivity) compared with the HOCS phantom. Noticeable differences between the

HOCS and the anthropomorphic phantoms are derived from the radiation patterns. One difference is the effect of the hands in the case of the anthropomorphic, which results into less power radiated, in some cases at the angle of the hands, compared with the HOCS phantom. Another difference which is noticeable is the reduced back lobe (180°) radiated power in the case of the anthropomorphic phantom compared with the HOCS phantom. The effect of the existence of the head (elevation angle 90°) in the case of the anthropomorphic phantom where in some cases resulted into an increased radiated power and in some other cases into a decreased radiated power compared with the HOCS phantom. Additionally another noticeable fact is that the heterogeneity and non-uniformity of the anthropomorphic phantom increases the cross-polar components of the radiation patterns compared with those of the HOCS Phantom [19]. More specifically and in terms of far field parameters (gain, directivity and efficiency) at the case of the 2.5GHz monopole antenna for the vertical polarization scenario there is a deviation between HOCS and anthropomorphic about 1.84dB , 3.18% and 0.47dB for the gain, efficiency and directivity respectively (Table 2-9). For the case of horizontal polarization scenario the deviation is about 2.38dB, 4.33% and 0.64dB for the gain, efficiency and directivity respectively (Table 2-9). For the case of the 3.5GHz monopole antenna, for the vertical polarization scenario, the deviation between HOCS and anthropomorphic phantom are 1.33dB, 1.42% and 0.93dB for the gain, efficiency and directivity respectively (Table 2-10). For the horizontal polarization scenario the deviation lies at 2.43dB, 6.59% and 0.87dB for the gain, efficiency and directivity respectively (Table 2-10). For the case of the 5.5GHz monopole antenna and for the vertical polarization scenario the deviation between HOCS and anthropomorphic phantoms is about 0.54dB, 5.53% and 0.51dB (Table 2-11) for the gain, efficiency and directivity respectively. For the horizontal polarization scenario the deviation is about 1.08dB, 0.87% and 1.22dB for the gain, efficiency and directivity (Table 2-11).The differences, between HOCS and anthropomorphic phantoms, derived from the radiation patterns are summarized as follows:

- For the case of the 2.5GHz monopole antenna, for the vertical polarization scenario: the azimuth co-polar components of HOCS and anthropomorphic differ in the back lobe (180°), which shows that less power is radiated in the case of the anthropomorphic phantom. Similar effect (back lobe) is noticed in the elevation plane with an addition effect of the head (at the side of 90° less power is radiated) in the case of the anthropomorphic phantom compared with the HOCS. The respective cross-polar components reveal that they are

increased in the case of the anthropomorphic phantom compared with the HOCS phantom, for azimuth and elevation planes. At the 2.5GHz case and for the horizontal polarization scenario, in terms of co-polar components: similar effect with the vertical polarization is noticed in the azimuth plane (back lobe) and the effect of a narrower beam due to the hands is also noticed. Similar effect (vertical polarization) is noticed in the elevation plane with the difference that in the side of the head (90°) more power is radiated and less power in the side of the belly (270°). The cross-polar components, of this scenario, reveal that in the azimuth plane the cross-polar power is increased in the case of the anthropomorphic phantom and in the elevation plane the cross-polar power of the anthropomorphic phantom is similar with the HOCS phantom.

- For the case of the 3.5GHz monopole antenna and for the vertical polarization scenario similar effects with the respective 2.5GHz scenario are noticed. In addition less radiated power in the elevation plane at the side of the belly (270° – co-polar component) compared with the respective 2.5GHz scenario. In the case of the horizontal case the effects are similar with those of the 2.5GHz case for co and cross-polar components in the azimuth and elevation plane. For this polarization scenario, a noticeable difference between the 3.5GHz and the 2.5GHz is the beam narrowing in the co-polar component at the azimuth plane. The beam of the anthropomorphic phantom is narrower in the case of the 3.5GHz revealing that the effect of the hands in the radiated power is increased by the frequency. This could be due to shorter wavelength.

- For the case of the 5.5GHz monopole antenna for both vertical and horizontal polarization scenarios the differences noticed between the HOCS and the anthropomorphic phantoms are similar with those of the 3.5GHz. The effect of the hands (anthropomorphic phantom), according to which the beam (for horizontal polarization) in the azimuth plane is narrower at higher frequencies, is verified.

Taking into account the above simulation results, HOCS phantom is estimated as an acceptable one for far field wearable antenna performance assessment. By acceptable it is meant that HOCS phantom far field performance is quite close with the full liquid phantom,

satisfying the idea of removing part of the liquid, and differences will be expected to occur compared with an anthropomorphic phantom, as described above.

Table 2 - 9 Simulated 2.5GHz printed monopole antenna on different types of phantoms

Parameters	*Free Space*	*HOCS*		*Full Liquid*		*Voxel*	
		Vertical	*Horizontal*	*Vertical*	*Horizontal*	*Vertical*	*Horizontal*
f_0 (GHz)	2.50	2.10		2.10		2.36	2.39
S11 (dB)	-21.81	-14.13		-14.42		-16.80	-18.32
BW (GHz)	0.42	0.35		0.36		0.39	0.40
e_{rad} (%)	86.7	8.70	8.83	8.52	8.71	11.88	13.16
Gain (dBi)	+1.53	-3.86	-4.05	-3.74	-4.24	-2.02	-1.67
Directivity (dBi)	+1.86	+6.76	+6.49	+6.95	+6.35	+7.23	+7.13

Table 2 - 10 Simulated 3.5GHz printed monopole antenna on different types of phantoms

Parameters	*Free Space*	*HOCS*		*Full Liquid*		*Voxel*	
		Vertical	*Horizontal*	*Vertical*	*Horizontal*	*Vertical*	*Horizontal*
f_0 (GHz)	3.47	3.10		3.10		3.33	3.35
S11 (dB)	-20.00	-12.35		-12.33		-15.05	-15.56
BW (GHz)	0.735	0.48		0.48		0.64	0.66
e_{rad} (%)	85.28	14.97	15.25	15.00	15.25	16.39	21.84
Gain (dBi)	+1.74	-1.33	-1.17	-1.32	-1.17	-0.00	+1.26
Directivity (dBi)	+2.43	+6.92	+7.00	+6.92	+6.99	+7.85	+7.87

Table 2 - 11 Simulated 5.5GHz printed monopole antenna on different types of phantoms

Parameters	*Free Space*	*HOCS*		*Full Liquid*		*Voxel*	
		Vertical	*Horizontal*	*Vertical*	*Horizontal*	*Vertical*	*Horizontal*
f_0 (GHz)	5.50	4.90		4.90		5.32	5.15
S11 (dB)	-30.73	-19.07		-19.07		-16.04	-14.03
BW (GHz)	1.875	1.515		1.515		1.275	0.93
e_{rad} (%)	80.89	25.66	26.04	25.66	26.04	20.13	25.17
Gain (dBi)	+2.37	+1.72	+1.57	+1.74	+1.58	+1.18	+2.65
Directivity (dBi)	+3.29	+7.63	+7.42	+7.65	+7.43	+8.14	+8.64
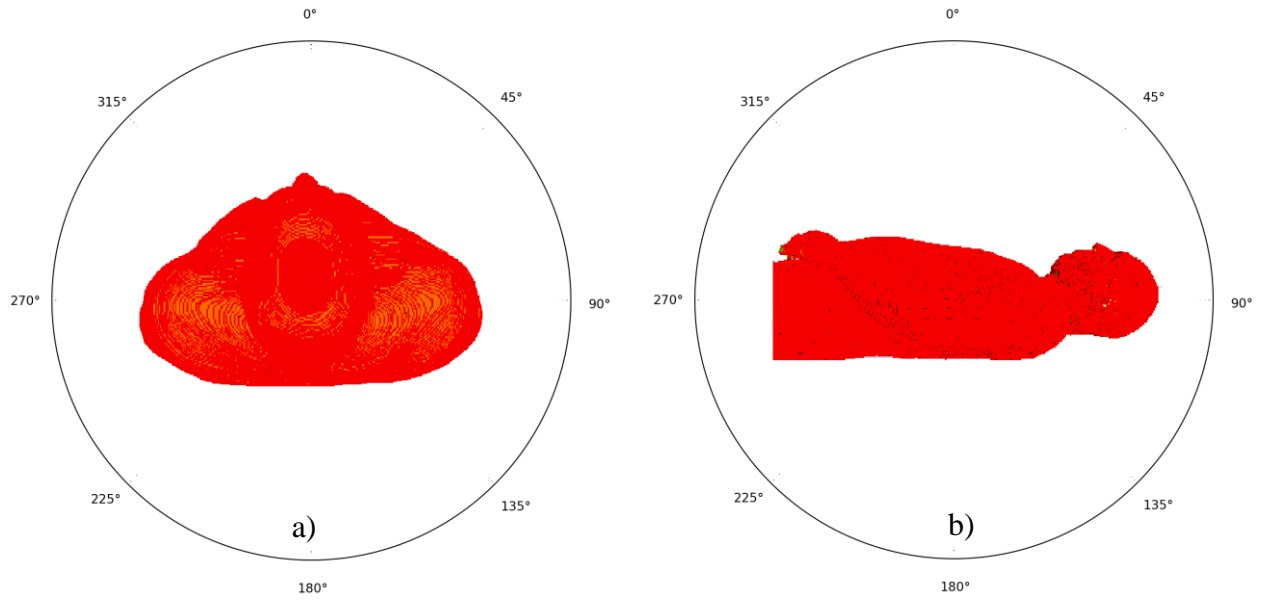
Fig. 2- 29 Phantoms orientation in the radiation patterns: a) Azimuth and b) Elevation

Co-polar   Cross-polar

Fig. 2- 30 simulated normalized radiation patterns for a 2.5GHz printed monopole antenna vertically polarized mounted at HOCS (2.1GHz), full liquid (2.1GHz) and heterogeneous anthropomorphic voxel (2.36GHz) phantoms at: a) Azimuth, b) Elevation planes

Co-polar   Cross-polar

Fig. 2- 31 simulated normalized radiation patterns for a 2.5GHz printed monopole antenna horizontally polarized mounted at HOCS (2.1GHz), full liquid (2.1GHz) and heterogeneous anthropomorphic voxel (2.39GHz) phantoms at: a) Azimuth, b) Elevation planes

Co-polar   Cross-polar
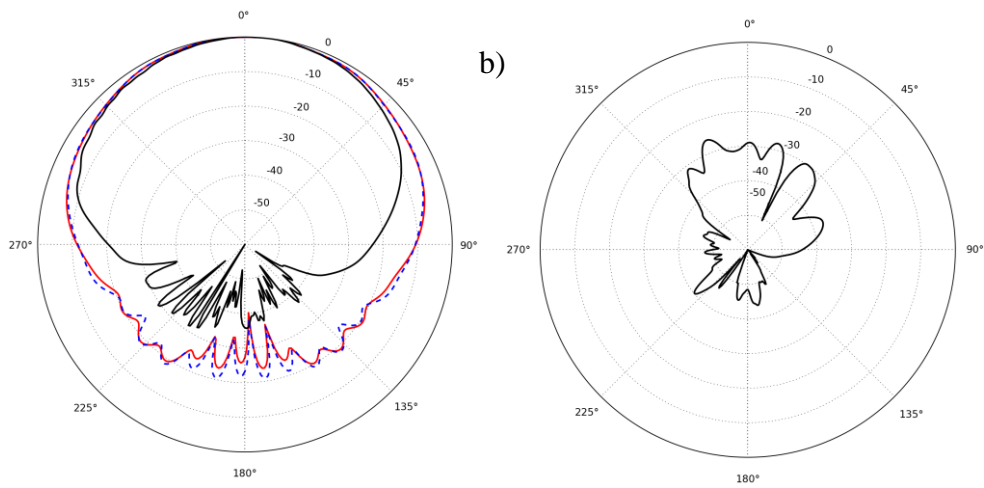
Fig. 2- 32 simulated normalized radiation patterns for a 3.5GHz printed monopole antenna vertically polarized mounted at HOCS (3.1GHz), full liquid (3.1GHz) and heterogeneous anthropomorphic voxel (3.33GHz) phantoms at: a) Azimuth, b) Elevation planes

Co-polar   Cross-polar
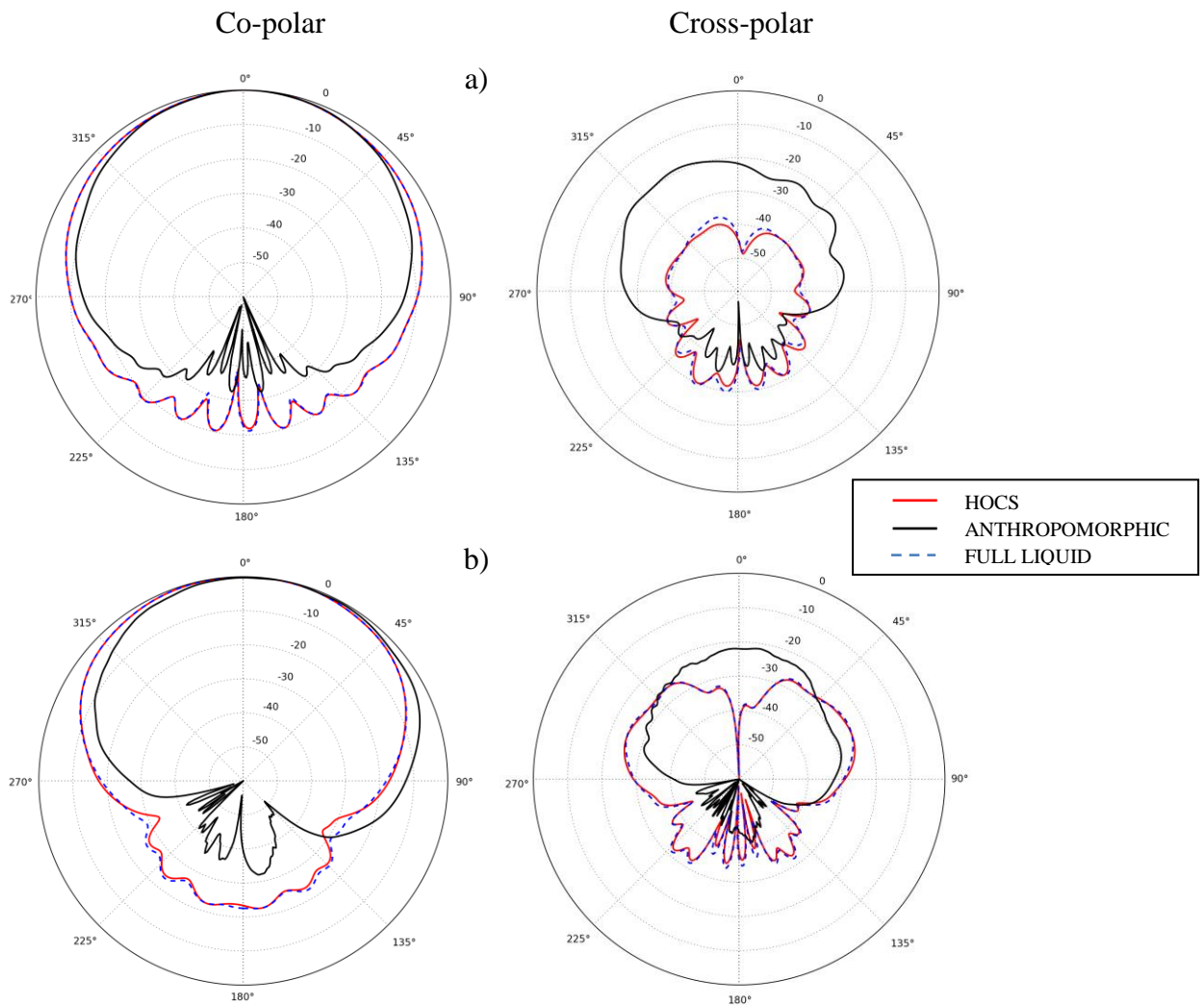
Fig. 2- 33 simulated normalized radiation patterns for a 3.5GHz printed monopole antenna horizontally polarized mounted at HOCS (3.1GHz), full liquid (3.1GHz) and heterogeneous anthropomorphic voxel (3.35GHz) phantoms at: a) Azimuth, b) Elevation planes

Co-polar   Cross-polar

a)

b)
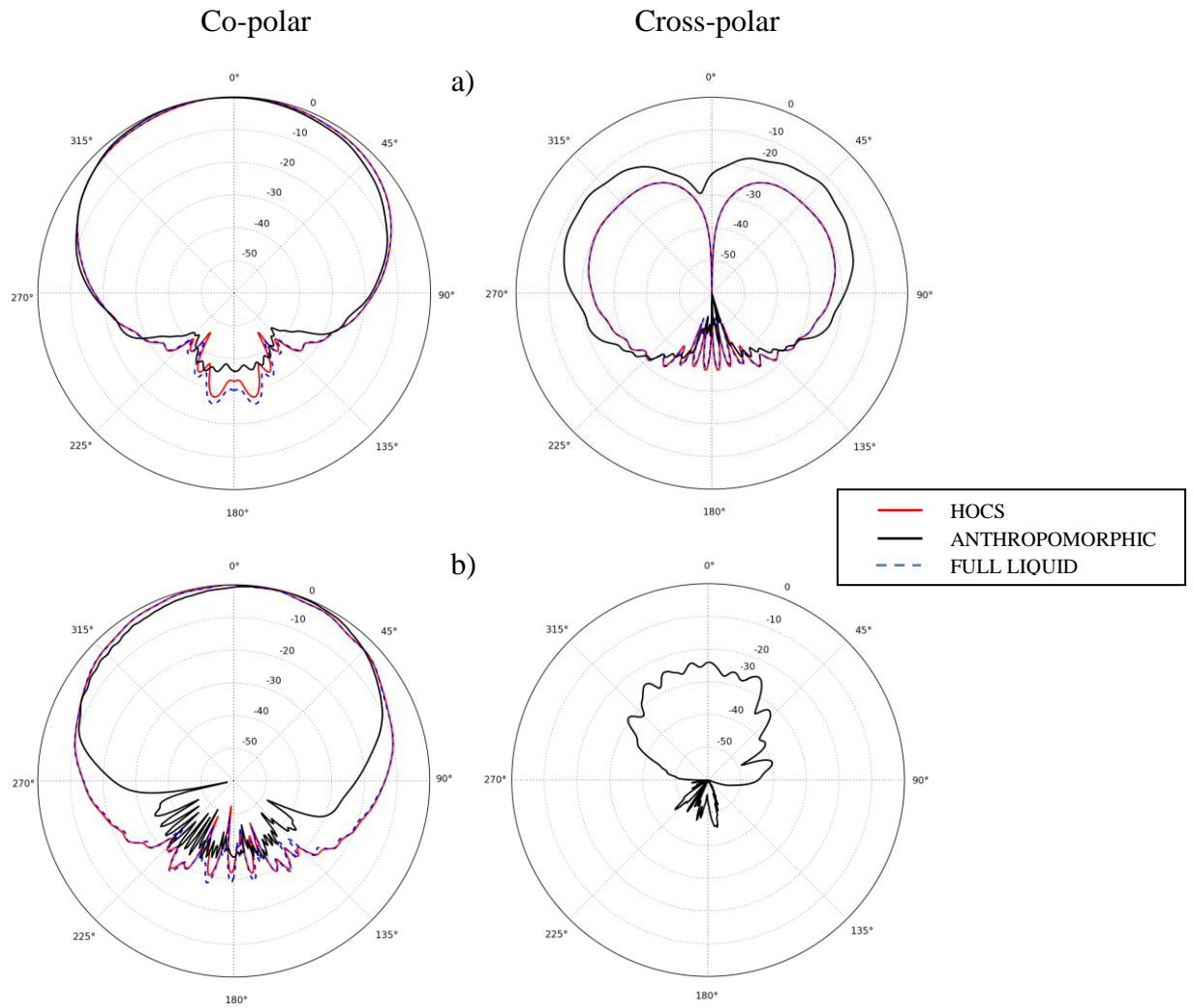
Fig. 2- 34 simulated normalized radiation patterns for a 5.5GHz printed monopole antenna vertically polarized mounted at HOCS (4.9GHz), full liquid (4.9GHz) and heterogeneous anthropomorphic voxel (5.32GHz) phantoms at: a) Azimuth, b) Elevation planes

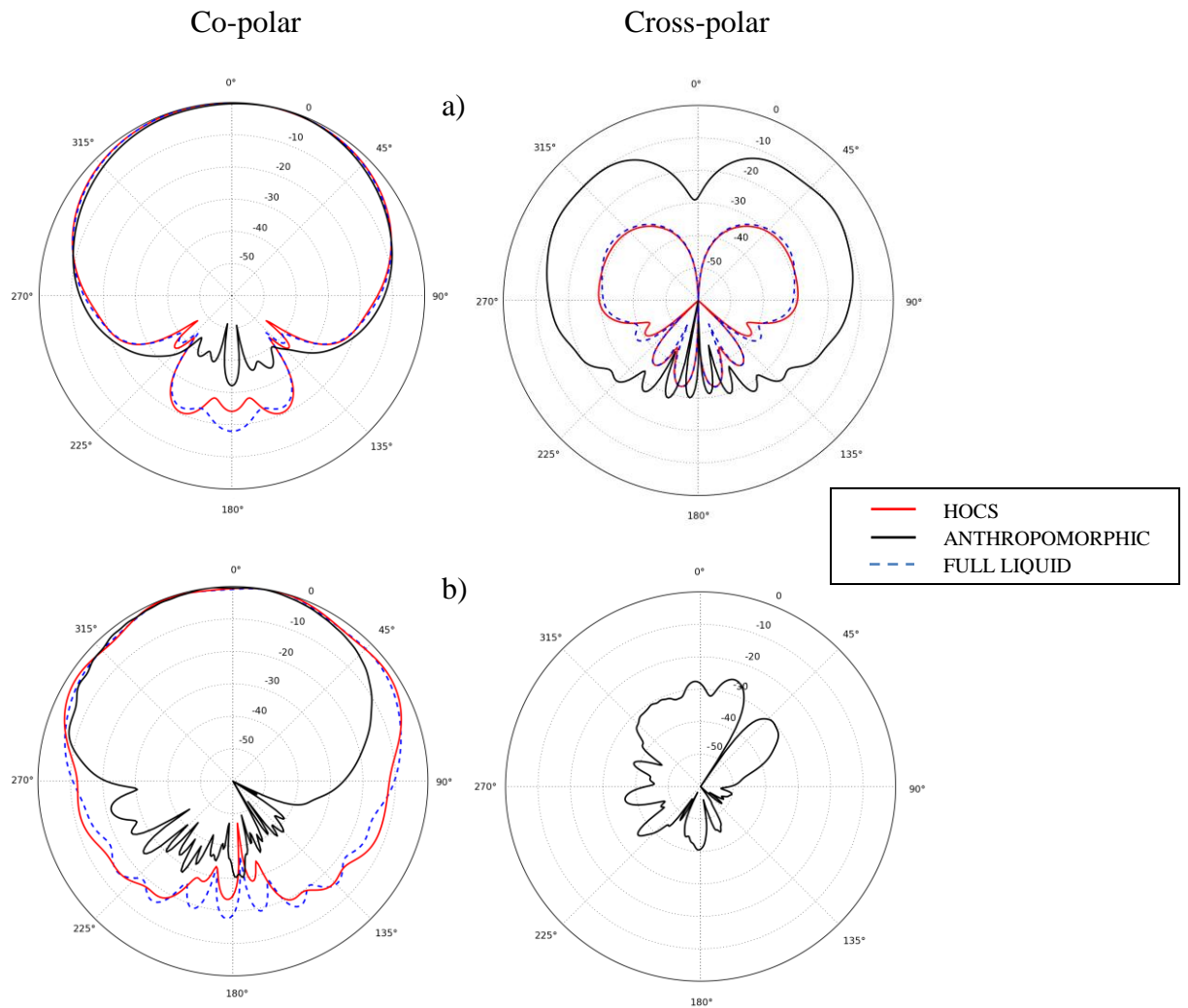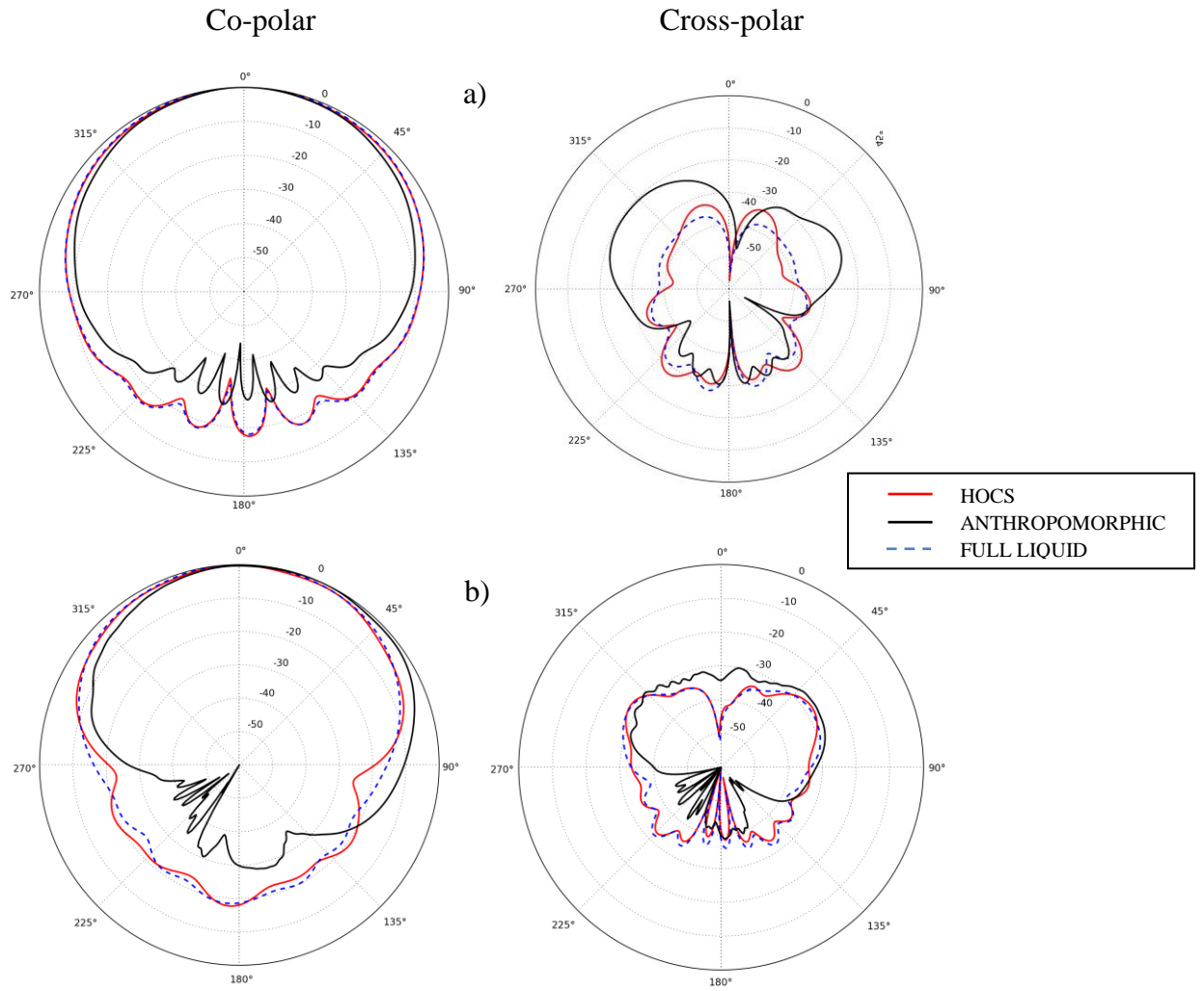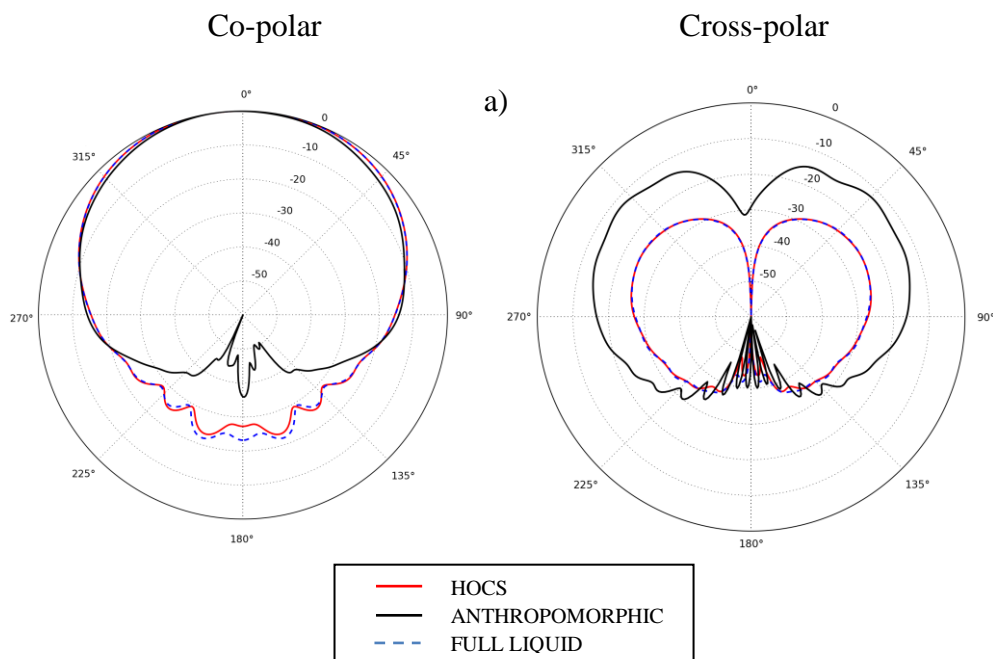Co-polar   Cross-polar

a)
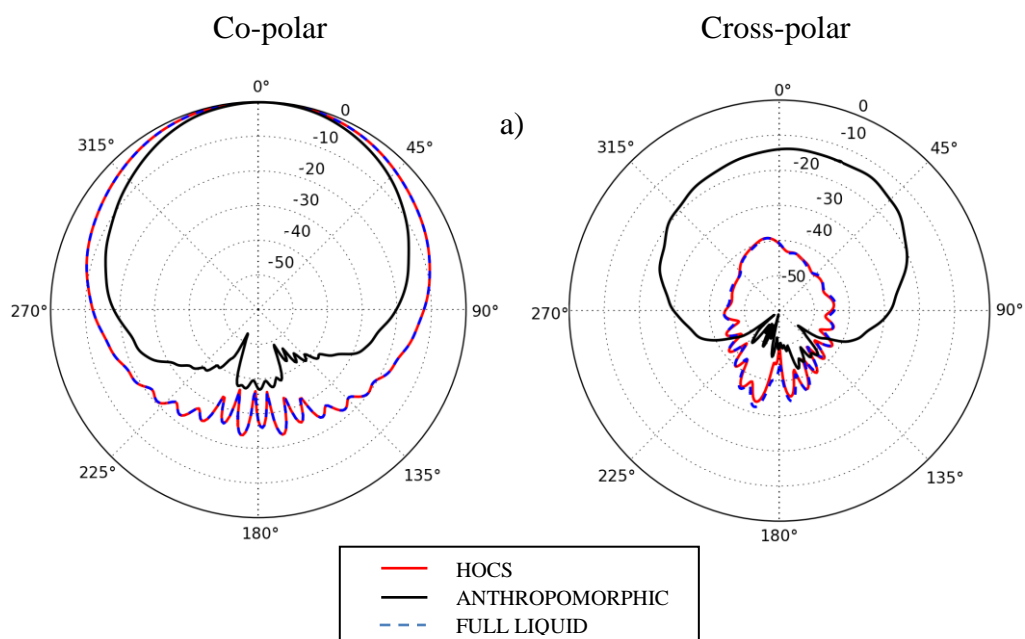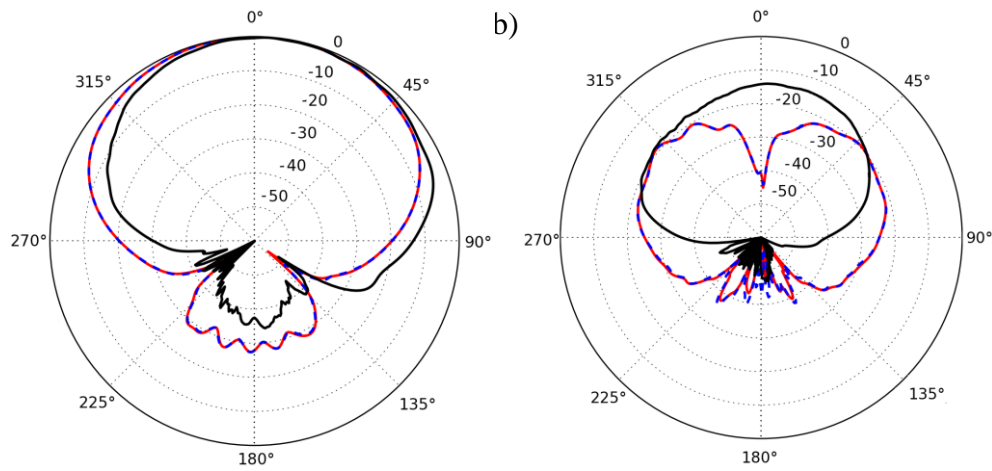
Fig. 2- 35 simulated normalized radiation patterns for a 5.5GHz printed monopole antenna horizontally polarized mounted at HOCS (4.9GHz), full liquid (4.9GHz) and heterogeneous anthropomorphic voxel (5.15GHz) phantoms at: a) Azimuth, b) Elevation planes

2.3.4.2 Measurements

In order to verify the simulated far field behavior of an antenna mounted on the HOCS phantom, measurements were carried out. These measurements used a printed dipole antenna mounted on the HOCS and on a homogeneous solid anthropomorphic phantom [37] (no arms were available) (Fig. 2-36). This antenna was selected: a) to verify the far field simulation behavior for the HOCS phantom for similar type antennas (dipole or monopole) and b) to notice the difference in the far field behavior between the HOCS and anthropomorphic phantoms. The selected antenna operates at the 2.45GHz ISM-band. The dipole antenna was measured for: vertical (X-axis) and horizontal (Y-axis) polarization orientation.
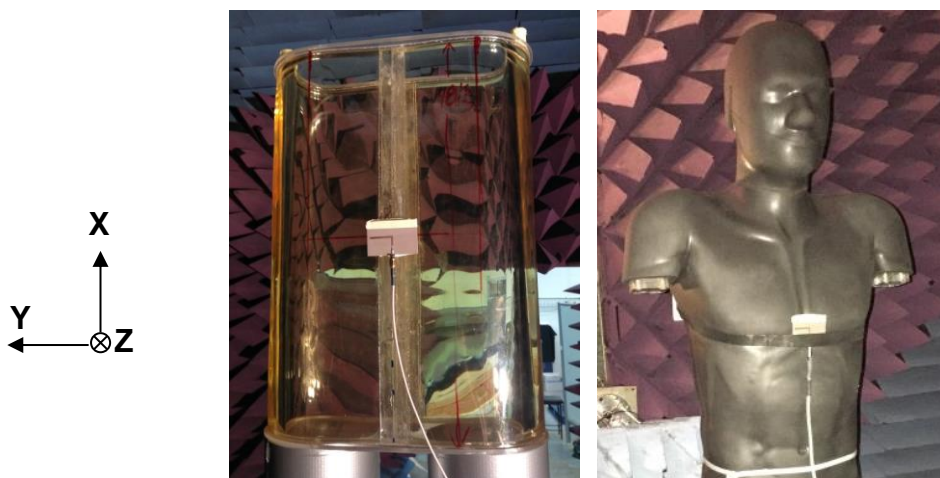
Fig. 2- 36 Measurement setups for far field evaluation of a 2.5GHz printed dipole antenna horizontally polarized mounted on HOCS and on a solid homogeneous anthropomorphic torso phantom

The normalized, to the maximum value, far field radiation patterns for the dipole antenna are shown in Fig. 2-37 for vertical polarization and in Fig. 2-38 for horizontal polarization. The phantoms orientation in the radiation patterns is the same as the one depicted in Fig.2-29. Additionally, the measured far field parameters (gain, directivity, radiation efficiency) are shown in Table 2-12. From the radiation patterns it can be said that generally there is an acceptable agreement between the realized HOCS phantom and the anthropomorphic torso phantom. Though, there are noticeable differences which need to be commented upon. More specifically in the case where the dipole is mounted vertically on the phantoms the gain at the back side lobe is higher in the case of HOCS phantom. This means that the anthropomorphic phantom yields less radiated power at the back side (180°) than the HOCS phantom. Additionally from Fig. 2-37b (elevation plane) the co-polar results reveal the effect of the head presence in the case of the anthropomorphic phantom. The radiated power is reduced from 0°-90° in the case of the anthropomorphic phantom compared with HOCS. For the case of horizontal polarization likewise conclusions can be made. Additionally, due to the lack of hands the effect of them in the radiated power, as noticed in simulations is not visible in measurements. Finally, the measured far field parameters (Table 2-12) yielded comparable differences noticed in simulations. The maximum deviation is less than 1.2dB, 0.5dB and 4% for gain, directivity and efficiency respectively.
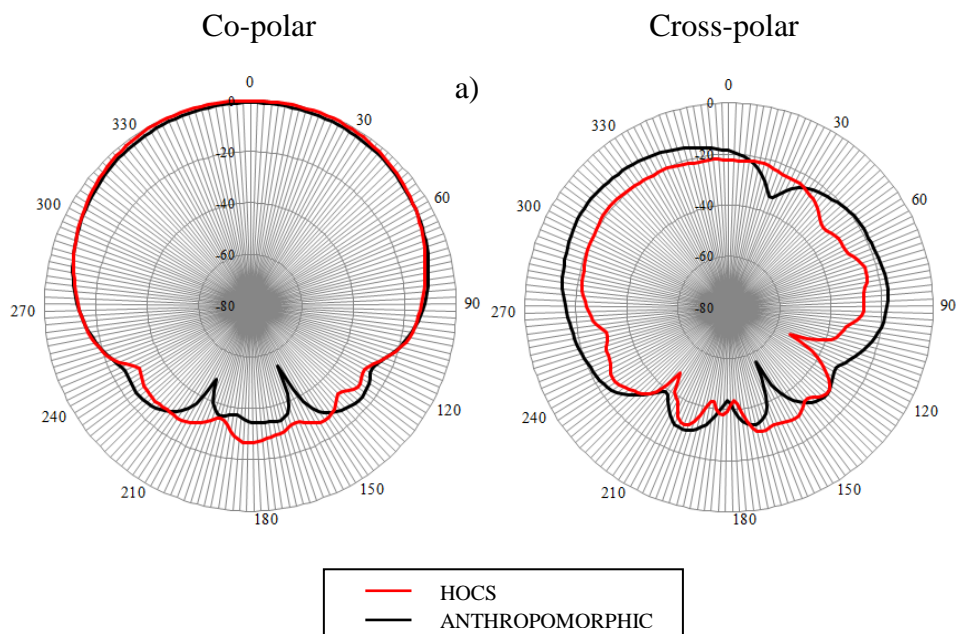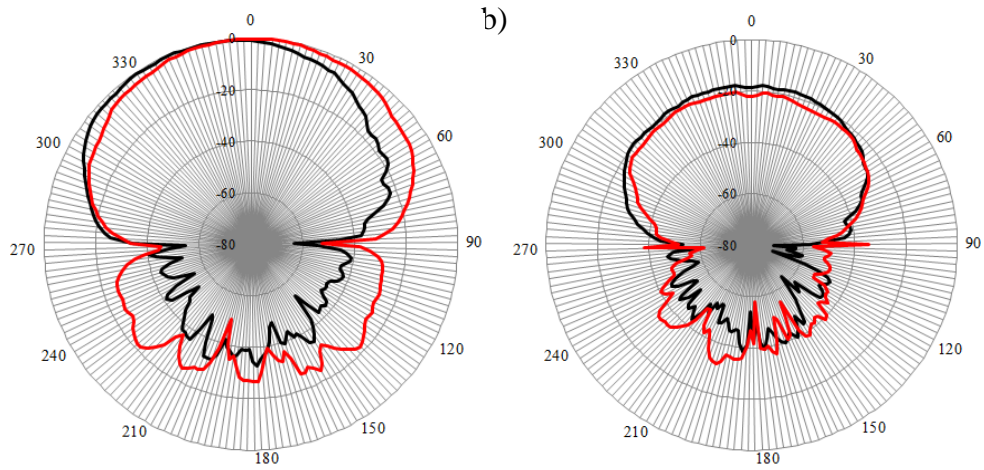
Fig. 2- 37 Measured normalized radiation patterns of dipole antenna mounted, with vertical polarization, on HOCS (2.4GHz) and anthropomorphic (2.38GHz) phantoms on: a) Azimuth and b) Elevation planes

Co-polar   Cross-polar
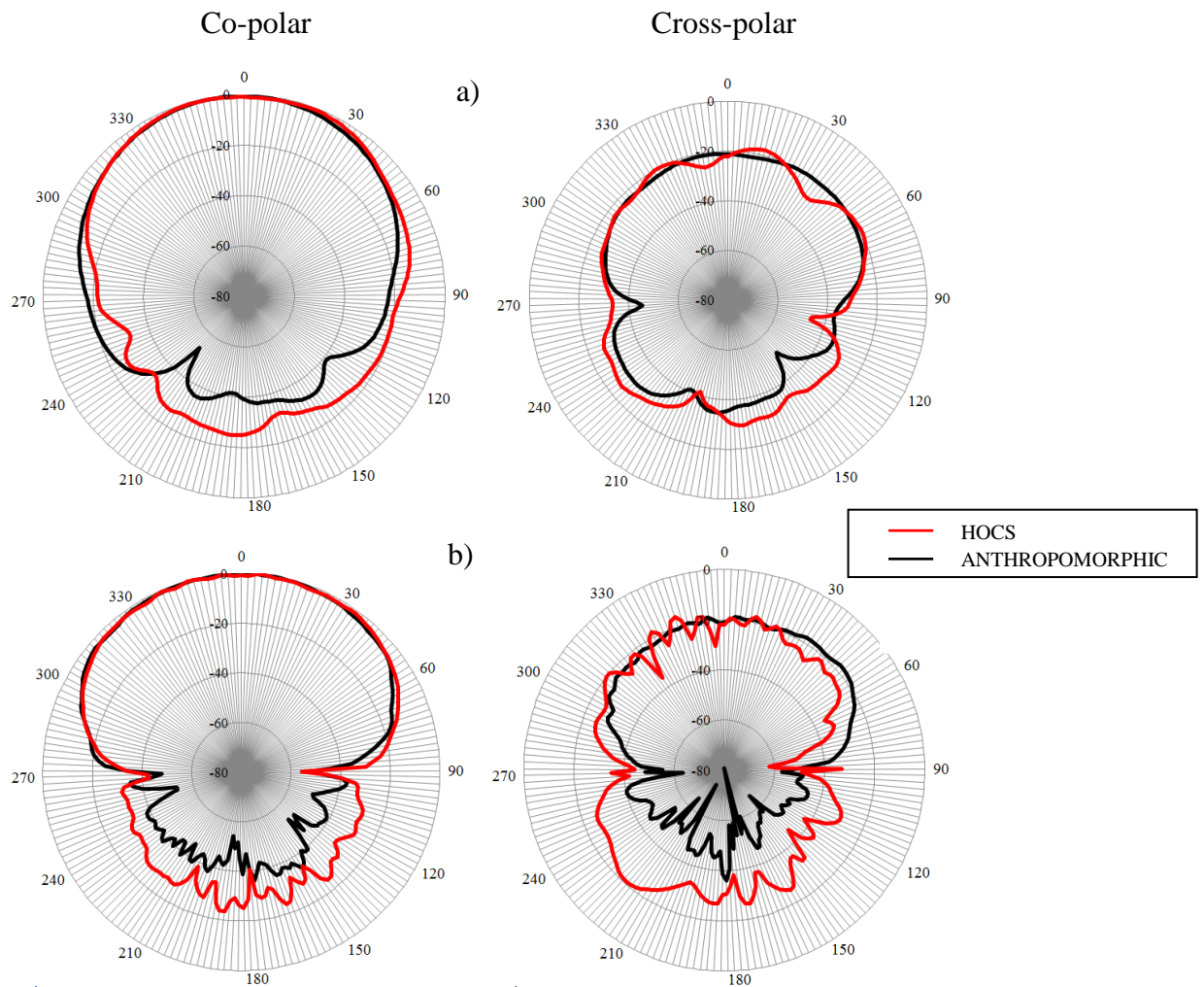
Fig. 2- 38 Measured normalized radiation patterns of dipole antenna mounted, with horizontal polarization, on HOCS (2.4GHz) and anthropomorphic (2.38GHz) phantoms on: a) Azimuth and b) Elevation planes

Table 2 - 12 Measured far field parameters of a 2.45GHz printed dipole antenna mounted on HOCS and on a solid anthropomorphic phantoms

Parameters	*HOCS phantom*		*Anthropomorphic phantom*	
	Vertical	*Horizontal*	*Vertical*	*Horizontal*
f_0 **(GHz)**	2.30		2.38	
S_{11} **(dB)**	-12.05		-14.58	
Directivity (dBi)	7.9	7.8	8.1	8.3
Gain (dBi)	-0.6	-0.5	-1.8	-1.1
e_{rad} **(%)**	14.1	14.8	10.2	11.5

Having recorded and taking into account the deviations between HOCS and the simulated and measured anthropomorphic phantoms, in terms of far field wearable antenna performance evaluation, it could be said that HOCS torso phantom is an acceptable candidate for such measurements.

2.4 Conclusions

This chapter has presented the design, realization and evaluation of a low cost and lightweight hollow oval cross-section (HOCS) torso phantom appropriate for wearable antenna performance assessment. The cost and the liquid volume of the HOCS phantom is reduced by 2/3 and 60% respectively, compared to the respective full liquid phantom. The structural components of the HOCS phantom (phantom shell and liquid tissue simulating) in terms of properties and dimensions are comparable with other liquid anthropomorphic phantoms.

The main advantage of the proposed phantom is that its performance in terms of wearable antenna performance evaluation is comparable with full liquid, anthropomorphic phantoms and real human bodies.

In terms of S_{11} wearable antenna performance HOCS is in better agreement with real human bodies for frequencies higher than the lower liquid calibrated frequency limit, of 2GHz. It was demonstrated, via simulations, that a phantom shell with a lower dielectric constant could bring the HOCS phantom in better agreement with real human bodies at 2GHz.

In terms of simulated electric field distribution and penetration, the HOCS phantom deviates from the full liquid, at lower frequencies close to 2GHz and it is close with the full liquid at frequencies close to 6GHz (e.g. 5.5GHz). The electric field penetration and distribution of HOCS phantom are improved and brought closer with the full liquid phantom by the addition of a simulated RF absorbing material, having a dielectric constant equal 5 or 1 having a simulated (using Empire-XPU) target absorption rate = 1dB/mm.

Additionally, the simulated path loss performance, when considering two antennas on either side of the HOCS phantom, differs from the full liquid phantom. The path loss performance of the HOCS phantom was brought closer with the full liquid one by the addition of an RF absorbing material with: dielectric constant = 5, simulated target absorption rate = 1dB/mm at 2; 2.5 and 3.5GHz and dielectric constant = 1(foam), simulated target absorption rate = 1dB/mm at 5.5GHz.

In terms of simulated far field wearable antenna performance the HOCS phantom yielded almost same performance with the full liquid phantom. Additionally the HOCS phantom yielded maximum deviation less than 2.5dB, 1.3dB and 6.6% in terms of gain, directivity and efficiency respectively compared with a simulated anthropomorphic phantom. Also, the maximum deviation compared with a measured anthropomorphic phantom was less than 1.2dB, 0.5dB and 4% in terms of gain, directivity and efficiency respectively. It was noticed that the radiated power at the back side of the HOCS phantom is higher than the respective simulated and measured anthropomorphic phantoms at all frequencies examined. The heterogeneity and the non-uniformity of the anthropomorphic phantom resulted into an increased cross –polar components compared with the HOCS phantom. Finally, the existence of the head and arms in the case of the anthropomorphic phantom differentiate the radiation patterns compared with the respective ones derived from HOCS phantom measurements and simulations.

References

[1]   P. Hall and Y. Hao, *Antennas and Propagation for Body-Centric Wireless Communications*, 2nd ed. London / Boston: Artech House, 2012.

[2] M. Y. Kanda, M. Ballen, S. Salins, C.-K. Chou, and Q. Balzano, "Formulation and Characterization of Tissue Equivalent Liquids Used for RF Densitometry and Dosimetry Measurements," *IEEE Transactions on Microwave Theory and Techniques*, vol. 52, no. 8, pp. 2046–2056, Aug. 2004.

[3] G. Marrocco, "RFID Antennas for the UHF Remote Monitoring of Human Subjects," *IEEE Transactions on Antennas and Propagation*, vol. 55, no. 6, pp. 1862–1870, Jun. 2007.

[4] D. Psychoudakis, C. Chen, and J. L. Volakis, "Wearable UHF Antenna for Squad Area Networks (SAN)," in *Antennas and Propagation Society International Symposium, AP-S, IEEE*, 2008, pp. 1–4.

[5] K. Ogawa, T. Matsuyoshi, H. Iwai, and N. Hatakenaka, "A High-Precision Real Human Phantom for EM Evaluation of Handheld Terminals in a Talk Situation," *IEEE Antennas and Propagation Society International Symposium. 2001*, vol. 2, pp. 68–71.

[6] K. Ito, "Human Body Phantoms for Evaluation of Wearable and Implantable Antennas," in *Antennas and Propagation, EuCAP*, 2007, pp. 1–6.

[7] H. Tamura, Y. Ishikawa, T. Kobayashi, and T. Nojima, "A Dry Phantom Material Composed of Ceramic and Graphite Powder," *IEEE Transactions on Electromagnetic Compatibility*, vol. 39, no. 2, pp. 132–137, May 1997.

[8] Y. Nikawa, M. Chino, and K. Kikuchi, "Soft and Dry Phantom Modeling Material Using Silicone Rubber with Carbon Fiber," *IEEE Transactions on Microwave Theory and Techniques*, vol. 44, no. 10, pp. 1949–1953, 1996.

[9] J. T. Chang, M. W. Fanning, P. M. Meaney, and K. D. Paulsen, "A Conductive Plastic for Simulating Biological Tissue at Microwave Frequencies," *IEEE Transactions on Electromagnetic Compatibility*, vol. 42, no. 1, pp. 76–81, 2000.

[10] N. K. Haralambos and P. S. Herman, "Hot Spots Generated in Conlcuding Spheres by Electromagnetic Waves and Biological Implications," *IEEE transactions on biomedical engineering*, vol. 19, no. 1, pp. 53–58, 1972.

[11]   H. P. Schwan, R. F. Schwartz, and J. Chotfer, "Induced fields and Heating Within a Crabial Structure Irradiated by an Electromagnetic Plane Wave," *IEEE Trans. on Microwave Theory and Techniques*, vol. 19, no. 2, pp. 187–196, 1971.

[12]   T. William and R. J. Spiegel, "Resonance Absorption of Microwaves by the Human Skull," *IEEE transactions on bio-medical engineering*, vol. 21, no. 1, January, pp. 46–48, 1974.

[13]   C. M. Weil, "Absorption characteristics of multilayered sphere models exposed to UHF/microwave radiation.," *IEEE transactions on bio-medical engineering*, vol. 22, no. 6, pp. 468–76, Nov. 1975.

[14]   H. Massoudi, "Electromagnetic Absorption in Multilayered Cylindrical Models of Man," *IEEE Trans. on Microwave Theory and Techniques*, vol. 27, no. 10, pp. 825–830, 1979.

[15]   S. Nishizawa and O. Hashimoto, "Effectiveness Analysis of Lossy Dielectric Shields for a Three-Layered Human Model," *IEEE Trans. on Microwave Theory and Techniques*, vol. 47, no. 3, pp. 277–283, 1999.

[16]   M. Okoniewski and M. A. Stuchly, "A study of the handset antenna and human body interaction," *IEEE Transactions on Microwave Theory and Techniques*, vol. 44, no. 10, pp. 1855–1864, 1996.

[17]   X. G. Xu, T. C. Chao, and a Bozkurt, "VIP-Man: an image-based whole-body adult male model constructed from color photographs of the Visible Human Project for multi-particle Monte Carlo calculations.," *Health physics*, vol. 78, no. 5, pp. 476–86, May 2000.

[18]   T. Nagaoka, S. Watanabe, K. Sakurai, E. Kunieda, S. Watanabe, M. Taki, and Y. Yamanaka, "Development of realistic high-resolution whole-body voxel models of Japanese adult males and females of average height and weight, and application of models to radio-frequency electromagnetic-field dosimetry," *Physics in Medicine and Biology*, vol. 49, no. 1, pp. 1–15, Jan. 2004.

[19] A. Tsolis, W. G. Whittow, A. A. Alexandridis, and J. C. Vardaxoglou, "Evaluation of a Human Body Phantom for Wearable Antenna Measurements at the 5.8GHz Band," in *Loughborough Antennas & Propagation Conference (LAPC), 11-12 November, Loughborough, UK*, 2013, pp. 414–419.

[20] SPEAG, *EM-Phantom User Manual V 4 . 3*. 2015, found in "http://www.speag.com/, accessed September 2016

[21] "ETSI technical report : Electromagnetic compatibility and Radio spectrum Matters (ERM); Improvement of radiated methods of measurement (using test sites) and evaluation of the corresponding measurement uncertainties ; Part 7 : Artificial human beings," 1998.

[22] G. A. Conway and W. G. Scanlon, "Antennas for Over-Body-Surface Communication at 2.45GHz," *IEEE Transactions on Antennas and Propagation*, vol. 57, no. 4, pp. 844–855, 2009.

[23] "http://www.indexsar.com/.", accessed September 2016

[24] S. Zhang, "Design Advances of Embroidered Fabric Antennas", PhD Thesis, Loughborough, 2014.

[25] J. Krupka, R. G. Geyer, J. Baker-Jarvis, and J. Ceremuga, "Measurements of the Complex Permittivity of Microwave Circuit Board Substrates Using Split Dielectric Resonator and Reentrant Cavity Techniques," in *Seventh International Conference on Dielectric Materials Measurements & Applications, 23-26 September*, 1996, no. 430, pp. 21–24.

[26] J. Krupka, a. P. Gregory, O. C. Rochard, R. N. Clarke, B. Riddle, and J. Baker-Jarvis, "Uncertainty of complex permittivity measurements by split-post dielectric resonator technique," *Journal of the European Ceramic Society*, vol. 21, no. 15, pp. 2673–2676, Jan. 2001.

[27] C. A. Balanis, *Advanced Engineering Electromagnetics*, 2nd ed. John Wiley & Sons, 2012.

[28]   G. T. Pawlikowski, "Effects of Polymer Material Variations on High Frequency Dielectric Properties," in *MRS Spring Meeting*, 2009, vol. 1156, pp. 1–7.

[29]   A. Tsolis, W. Whittow, A. Alexandridis, and J. Vardaxoglou, "Embroidery and Related Manufacturing Techniques for Wearable Antennas: Challenges and Opportunities," *Electronics*, vol. 3, no. 2, pp. 314–338, May 2014.

[30]   C. A. Balanis, *Antenna Theory Analysis and Design*, 3rd ed. New Jersey: John Wiley & Sons, 2005.

[31]   A. Paraskevopoulos, A. Alexandridis, F. Lazarakis, and J. C. Vardaxoglou, "Modelling of Dynamic On-Body Waist-Foot Channel," in *Loughborough Antennas & Propagation Conference (LAPC)*, 2013, pp. 155–160.

[32]   "http://www.ets-lindgren.com/emcabsorbers.", accessed September 2016

[33]   C. Parini, S. Gregson, J. Mccormick, and D. Janse van Rensburg, *Theory and Practice of Modern Antenna Range Measurements*. IET, London, UK, 2015.

[34]   A. Chauraya, "Photoconductive Switching using Silicon and its Applications in Antennas and Reconfigurable Metallodielectric Electromagnetic Band Gap (EBG)", PhD Thesis, Loughborough University, 2004.

[35]   C. A. Balanis, *Modern Antenna Handbook*. John Wiley & Sons, 2008.

[36]   "http://www.empire.de/cat63.html.", accessed September 2016

[37]   "http://www.speag.com/.", accessed September 2016

CHAPTER 3

CYLINDRICAL NEAR FIELD MEASUREMENT TECHNIQUE FOR WEARABLE ANTENNAS MOUNTED ON HOCS TORSO PHANTOM

Abstract

In this Chapter a new methodology, which uses the cylindrical near field (CNF) measurement technique, to evaluate wearable antennas performance parameters is described. For this methodology the proposed HOCS phantom (Chapter 2) and three patch antennas operating at 2; 2.5 and 5GHz frequency bands are used. The patch antennas are mostly suitable for Off-body communication link. The main advantage of this methodology is that a smaller measurement space is required compared to a conventional far field test site and the use of a heavy duty roll axis, so as to rotate the phantom for 3D pattern coverage is excluded (this is a lab requirement) compared to a conventional spherical near field test site. These advantages could significantly reduce the cost and the complexity of the measurement.

Chapter 3 introduces the geometry of HOCS torso phantom in a CNF test site. Limitations and restrictions of finding an optimum cylindrical volume (*measurement CNF volume which would result into transformed far field parameters as accurately as possible (closest) to the simulation far field parameters*) for the near field measurements are described. The need for evaluating the CNF test site, so as to define the optimum volume, of the measurements is described. Subsequently an evaluation technique, which is targeted for the CNF test site appropriate for wearable antenna measurements mounted on HOCS phantom, is proposed and described. The goal of the evaluation technique is to find the optimum CNF measurement volume which would result into transformed far field parameters which will be closest to the simulation far field results. Additionally, the evaluation technique is an attempt

to get the measurement system (CNF) measuring as accurately as possible. The evaluation technique uses a 2mm thick ConDucting Plate (CDP) whose dimensions (height and width) are equal to the cross sectional dimensions of the HOCS phantom. It is shown that this technique is effective and useful as an evaluation for CNF wearable antenna measurements and removes the necessity of using the phantom during the measurement preparation procedure (define optimum CNF volume). The evaluation technique is assessed by comparing the far field performance parameters (gain, directivity and efficiency), derived from the CNF measurements, with simulations and with direct far field measurements carried out inside a full wave chamber. Validation of the evaluation technique is carried out by applying the derived optimum CNF volumes on the HOCS phantom, for the three antennas, and then measuring and comparing the results with simulations.

Then the new methodology for evaluating wearable antennas performance, mounted on HOCS torso phantom, by using the CNF measurement technique is presented. The wearable patch antennas (as previously referred) are mounted in different locations on the HOCS phantom. The steps of the new methodology can be listed as follows: *1) The image of the E-field distribution (near field amplitude) in the near field region, for each antenna in each location is recorded; 2) From the near field results, assumptionss for the maximum direction of radiation, for the radiation at the main geometrical planes and for the directivity are derived. 3) Finally, the far field parameters (gain, directivity and efficiency) and the radiation patterns are produced from the near field results, validating the assumptions made from the near field results (step 2).*

3.1 Introduction

3.1.1 Wearable antennas performance assessment

  In recent years there has been significant interest in wearable antenna technology [1]. Wearable antenna design and implementation demand manufacturing and characterization of the antenna. This involves measuring and studying the wearable antenna performance under various conditions. Its performance must be characterized in free space but the most important consideration in terms of "wearability" of the antenna is its performance under the influence of a real human body. Important performance parameters for wearable antennas are: **reflection coefficient; E-field distribution in the near field region; radiation efficiency;**

gain; directivity; radiation patterns.

Many procedures have been so far proposed for wearable antenna performance evaluation. The first procedure (methodology) that is used before manufacturing the wearable antenna and evaluating it on body/phantom is simulating the design of the wearable antenna. Then by using numerical phantoms [1],[2],[3],[4],[5],[6],[7],[8],[9],[10] (arm, head, whole body, homogeneous, layered, flat phantoms etc. – depending on the application) wearable antenna's performance is estimated for what it is made for, to be worn. Simulations are really important because they save time in terms of optimizing the performance of the antenna before proceeding to measuring the antenna on body/phantom. Measurements are an important and the final step to characterize an antenna system. All practical applications require measurements results rather than only simulations [11].

The question for all the measurement methodologies used so far is: *what their contribution was to the evaluation of wearable antennas performance and influence by the body/phantom?* It is useful to address one by one all the wearable antenna performance parameters (as referred in the first paragraph of this section) and notice for each one of them the difficulties that exist so as to evaluate them.

The reflection coefficient (S_{11}) of a wearable antenna expresses the input impedance (Z_{in}) of the wearable antenna which is affected by the presence of the human body. So it is necessary that S_{11} will be measured on-body. It is necessary to know where the antenna resonates on body. Many papers so far have successfully presented S_{11} measurements on body/phantom in various locations on and various postures of it [12], [13], [14], [15], [16], [17]. It is important to check the repeatability of the S_{11} results by measuring on different human bodies and phantoms. This will give an average estimation of the reflection coefficient. This would be useful for antennas which are highly affected in terms of impedance matching by the presence of the body/phantom. Such antennas are dipoles or monopoles where there is no ground plane to shield the radiator from the human body[18].

The radiation efficiency, gain, directivity, radiation patterns are parameters which can be directly measured in a far field test site. Measurement setups with phantoms introduce difficulties in far field test sites such as requiring specific equipment (positioner) to rotate the phantom in the roll and azimuth axis so as to obtain 3D radiation patterns. If the phantom is liquid or semi-solid (gel) [19] there is a risk of breaking or spilling the liquid of the phantom while rotating (scanning) it on the roll axis. In case that the phantom is solid, there is a better chance of rotating the phantom on the roll axis. There are two concerns for the solid phantom: a) it is very expensive compared to the other types of phantoms and b) it is a heavy one so a

heavy duty positioner is required [20]. This concludes to the fact that in far field test sites the easiest and the most feasible solution is to rotate and scan the phantom on the azimuth plane only [2],[21],[22] (Fig. 3-1a),[23],[24] (Fig. 3-1b),[25]. This leads to get the far field parameters only on the 2D plane around the phantom [26] . The above restriction is mostly valid in case of torso, or whole body phantoms [20]. In case of having only an arm or head phantom it is easier to rotate the phantom on the roll axis so as to get a second plane and to finally obtain a 3D radiation pattern.

a)
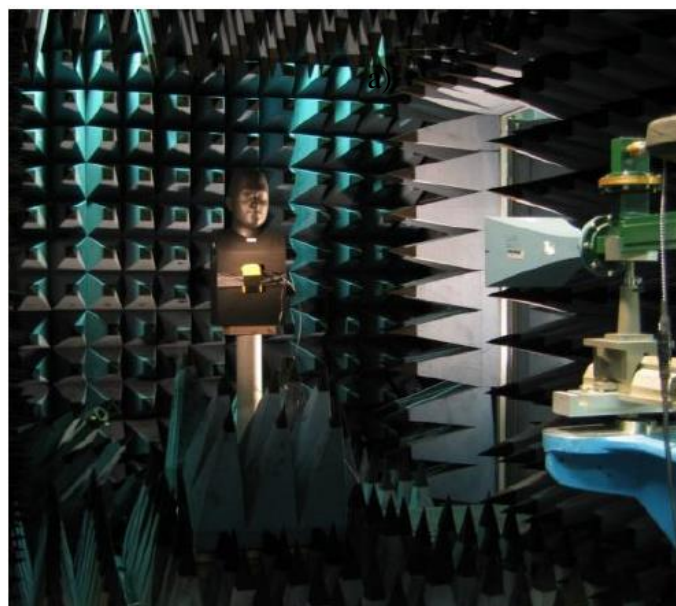
b)

Fig. 3- 1 a) Azimuth plane measurement environment at [22], b) Phantom in anechoic room with transmit horn antenna [24]

3 - 4

Radiation efficiency is proven that can be measured with a good accuracy in a reverberation chamber (RC), with the antenna mounted on body [27] (Fig. 3-2a),[28],[29] (Fig. 3-2b),[30],[31],[32]. So the reverberation chamber is one solution for wearable antenna efficiency measurement. This solves the problem of producing 3D radiation patterns to calculate the efficiency on a body/phantom. But this technique lacks in providing the image of the E-field distribution in the near field region, gain, directivity and the radiation patterns of the wearable antenna. Additionally the wearable antenna radiation efficiency has also been successfully measured by a modified Wheeler cap [33] (Fig. 3-2c).

In the last couple of decades the near field measurement technique, found in spherical (STARGATE SG-62) [34](Fig. 3-2d) and in [35](RAMS)(Fig. 3-2e) have been successfully used as an alternative method for assessing the far-field radiation of antennas in close proximity to the human body (handset antennas). There is a growing interest in using the near field measurement technique for wearable antennas performance evaluation [36],[37],[38].

In this chapter it is proposed (new methodology), that the CNF technique applied to a wearable antenna mounted on a liquid torso phantom (HOCS) will cross over the above difficulties. The CNF advantages can be listed as follows: *1.) less physical space is needed compared to the far field measurement, 2.) the phantom needs to be mounted on a turntable which rotates only on the azimuth axis, excluding rotation on the roll axis (as it will be done when using the Spherical Near Field measurement technique), 3.) information about the image of the E-field distribution, in the near field region, of the phantom by the antenna is acquired by the near field scan which could be important for best position selection of the wearable antenna which could lead to a better design of a wearable antenna system and 4.) far field results (gain, directivity, efficiency, radiation patterns) can be produced by transforming the near field ones.* Summarizing, the measurement value of the CNF technique for evaluating wearable antennas is that it can capture many (the CNF measurement technique lacks in capturing sampling data at the top and bottom of the AUTs elevation plane) possible antenna positions with a single scan due to the approximate cylindrical shape of the HOCS torso phantom. This can reduce the measurement time and the required volume of the test site.

The CNF technique is applied on HOCS torso phantom. Three wearable patch antennas (2; 2.5 and 5GHz frequency bands – Appendix B) are used. Antenna different locations scenarios are examined. The image of the E-field in the near field region is measured and examined (assumptions for the radiation and directivity are made). The far field performance parameters for the patch antennas are produced from the near field ones, verifying the assumptions made

from the image of the E-field. Before this an evaluation of the CNF scan volume is done. From the evaluation the optimum CNF scanning volume is defined, which will give far field (produced from near field) results closest to the simulation ones. This evaluation technique excludes the use of the HOCS phantom for the the measurement preparation procedure (define optimum CNF volume) and uses a ConDucting Plate (CDP) whose cross-sectional dimensions (height and width) are the same with the HOCS phantom's one.

a)

b)
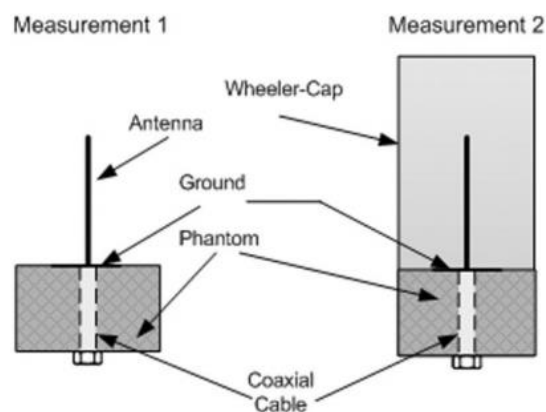
c)

d)
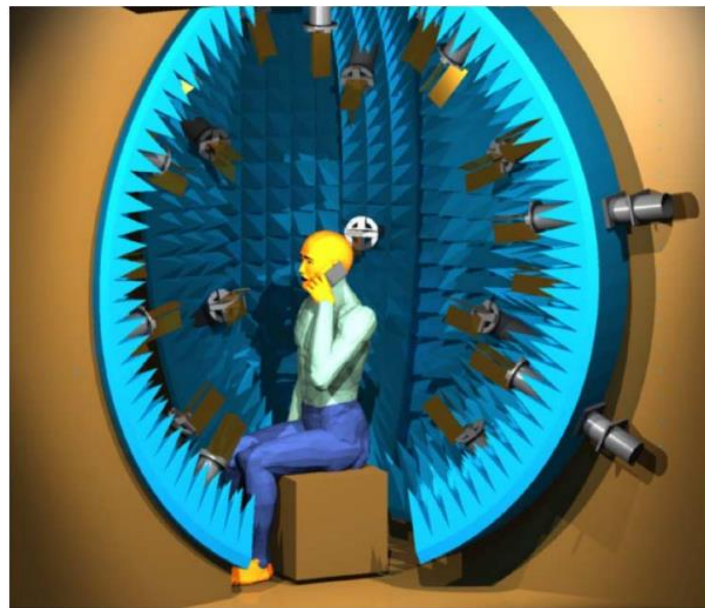
e)

Fig. 3- 2 a) The RC at the university of Liverpool [27], b) RC measurement setup [29], c) Monopole antenna with body phantom in free space and in Wheeler cap [33], d) STARGATE-64 with user – mobile measurement setup [34], e) Measurement setup with the RAMS [35]

3.1.2 Outline of this chapter

In Section 3.2 the geometry, setup measurement, errors and limitations of HOCS phantom in the CNF test site are described. In Section 3.3 a new evaluation technique so as to prepare (find optimum CNF volume) the CNF test site and overcome HOCS phantom limitations is presented. The evaluation technique tool is a ConDucting Plate (CDP), whose

dimensions are equal to the cross-sectional dimensions of the HOCS phantom, excluding the use of HOCS phantom for this purpose. The evaluation technique is based on the comparison of near field measurements (NFtoFF transformation); on direct far field measurements and simulations. The evaluated geometrical setup parameters (EGSP) (these define the optimum CNF scanning volume) for all the three wearable patch antennas (2; 2.5 and 5GHz) are found. Additionally, the evaluation technique is validated by applying the EGSP on the HOCS torso phantom and comparing the far field parameters (gain, directivity and efficiency) derived from NFtoFF transformation with simulations **(for the ease of use in this Chapter: radiation efficiency will be referred as efficiency)**. In Section 3.4 the new methodology which includes the implementation of the CNF technique for evaluating wearable patch antennas (appropriate for Off-body communication links) mounted on HOCS torso phantom by using the image of the E-field amplitude in the near field region (**near field amplitude**) results and the NFtoFF parameters, is presented. In Section 3.5 the conclusions drawn from this chapter are presented.

3.2 Geometry, setup and limitations of HOCS phantom in the cylindrical near field test site

The CNF measurement is primarily used to produce the 3D far field antenna radiation pattern. This is done by taking two orthogonal measurements of the E-field amplitude and phase on the desired cylindrical grid in the near field range of the AUT, and after transformation, the far field radiation of the antenna is obtained.

3.2.1 Geometry and setup

The geometry, setup and basic principles followed are the ones used in the classic CNF measurements [39],[40] (Fig.3-3). The CNF measurement system inside an anechoic chamber includes a linear vertical scanning axis (Y-slide) and an azimuth turntable rotating the AUT (antenna under test) at theta (θ^o) Azimuth angle (Fig. 3-3, 3-4). Regarding the specific (Fig. 3-4) CNF geometry and measurement, the AUT is the HOCS phantom + wearable patch antenna. The wearable patch antenna together with the phantom comprise an effective AUT or super antenna [41]. The point (0, 0, 0) is on the axis of rotation in the

middle and on the side of the AUT (see Fig. 3-7). An open ended waveguide probe [42],[43] (the WR-430 for the 2 and 2.5GHz patch antennas or the WR-187 for the 5GHz patch antenna) was connected at the Tx port of a VNA that scans along linear axis (Y-slide) and the AUT was connected at the Rx port of the VNA which was rotated on Azimuth (θ^o). The VNA was configured with a frequency span of 250MHz for all the wearable antennas used. A 100Hz IF BW and 0dBm (1mW) Tx-power were settled, while a dynamic range of more than 80dB, 89dB and 90dB for the 2GHz, 2.5GHz and 5GHz respectively, has been provided. By rotating the Tx probe antenna from its initial vertical polarization at 0° by 90°, two orthogonal components (A_V and A_H) were measured, in amplitude and phase, in the propagation near-field range of the AUT [39]. The full control of the VNA and the synchronization of the linear and azimuth axis positioners is achieved by using the acquisition software called MiDAS 6.0 provided from ORBIT-FR (installed at Loughborough University tapered anechoic chamber measurement facility) [44] to capture the near field in a cylindrical surface around the AUT. After the completion of the near field measurement, a near field to far field (NFtoFF) transformation is applied by using the MiDAS software's code. The transformation code is based on a fast Fourier transform (FFT) which uses the theoretical or measured probe antenna radiation patterns to apply a correction to the acquired near field data. After, the transformation the 3D far field radiation patterns of the AUT are obtained by using MiDAS software as well. Finally, the far field parameters (gain, directivity and efficiency) are calculated by MiDAS software as well. The workflow which has been followed for the specific CNF setup, measurement, transformation and analysis of results is depicted in Fig. 3-5.
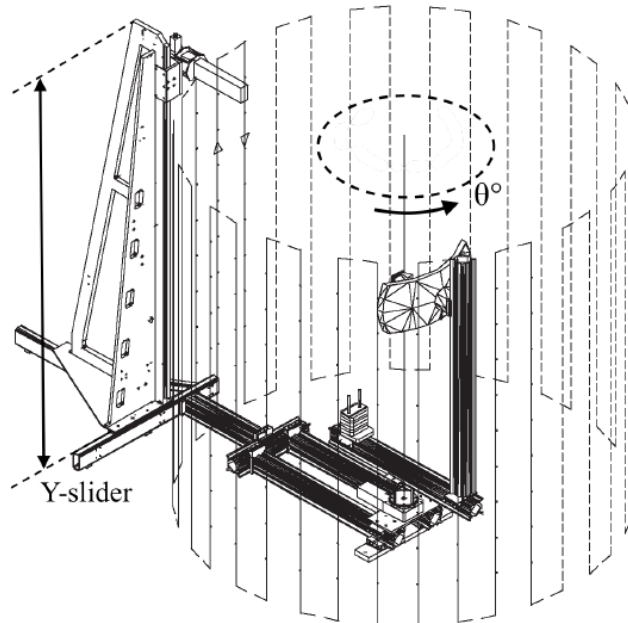
Fig. 3- 3 General schematic of the cylindrical near field measurement configuration, showing the scanning probe antenna (Tx) and the AUT (Rx) [39]

a)

b)
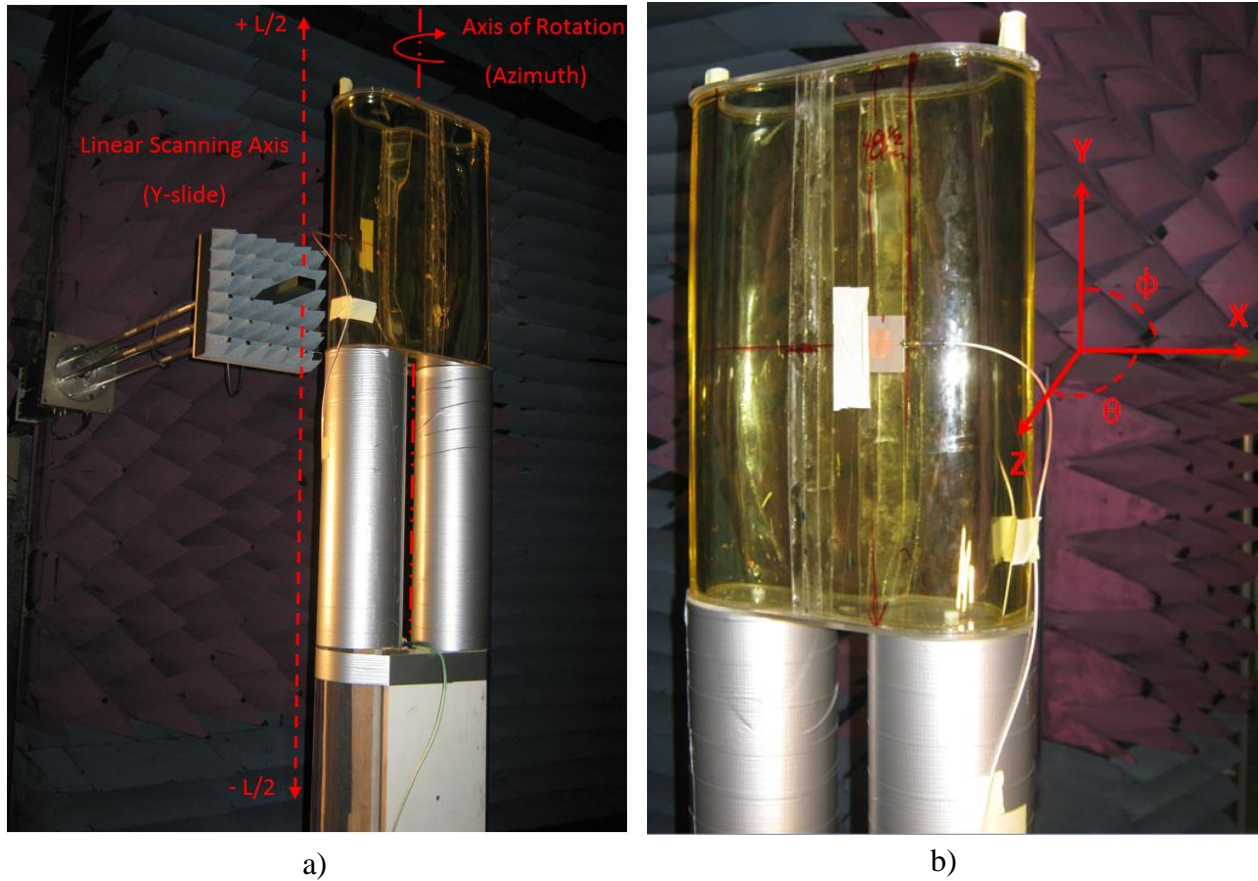
Fig. 3- 4 a) Cylindrical near field measurement setup of AUT = HOCS phantom + wearable patch antenna, b) Coordinate system of AUT in the CNF measurement system

| 1. AUT and Probe antenna setup |
| 2. Alingment of probe and AUT |
| 3. CNF geometrical parameters setup |
| 4. Receiver configuration |
| 5. MiDAS calibration parameters |
| 6. Scan setup and run |
| 7. Obtain near field results |
| 8. Near field to far field transform |
| 9. Obtain far field results |

Fig. 3- 5 Workflow of CNF measurement

3.2.1.1 AUT and probe antenna setup

The mechanical setup of the near field test site for the HOCS torso phantom follows the steps below: *1. mounting the plastic feet supporting structure (positioners) on the turntable, 2. Mounting the torso phantom on the supporting structure (the phantom needs to be empty without the liquid so as to avoid the danger of spilling or breaking the phantom due to in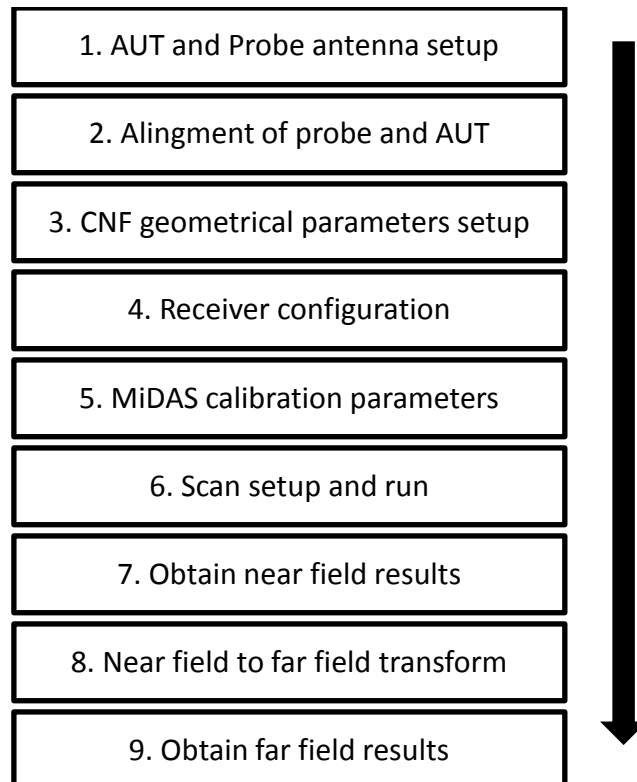creased weight), 3. Fill the phantom with the liquid, 4. Select the appropriate near field probe and mount it on the near field positioner with the appropriate absorbers mounted at the back of the probe antenna [40]* (For steps 1,2 and 3 a spirit level should and has been used for AUT alignment). From Fig. 3-4 and in terms of HOCS phantom mechanical setting up inside the anechoic chamber it was assumed that the plastic feet supporting structure (positioners) don't have a big effect in the near field data because they are low loss and low conductive (3mm thick cast acrylic), without significantly reflecting the electromagnetic wave as it would be reflected by a highly conducting material. As for the supporting structure a cubic box of Styrofoam or wooden cylindrical legs could be used as well.

The wearable antennas were placed directly on the HOCS phantom (0mm distance from the surface of the phantom). This was examined as the worst case scenario for a wearable antenna. Worst case in terms of maximum phantom influence on the antennas performance parameters when placed at the minimum possible separation distance from HOCS phantom [1] .

3.2.1.2 Alignment of probe and AUT

The probe and the AUT need to be aligned at the reference point (0, 0, 0) (Fig. 3-6 & 3.7). A perfect alignment so as to minimize and make negligible the error (see sub subsection 3.2.1.10) from it has been achieved in three steps. They are as follows: (a) the probe antenna is a linearly polarized and its electrical polarization has to be aligned with the X' and Y' axis. This has been achieved by using a spirit level; (b) laser tracking alignment of the probe antenna with the AUT's aperture (centre at the middle of the AUT). This is important because with the main co-polar component of the probe the co-polar component of the AUT has to be measured; (c) as a final and important step is to match the X'Y' plane of the probe with the AUT's respective XY (Fig. 3-6). This means that the Y=0mm needs to match with the AUTs middle. This has been achieved by using the laser trackers. This step is important to ensure CNF scanning symmetry. After this three step procedure an alignment recheck is suggested

and it follows the steps: (i) Check that the probe antenna at Y=0mm position is aligned with the middle of the AUT (HOCS) at azimuth = 0°; (ii) at Y=0mm check that at azimuth angles (AUT) 90° and 180° the AUT's middle is aligned with the probe antenna's middle; (iii) Rotate the AUT around the azimuth axis and check if it is stable (doesn't tremble) and (iv) Check again with a spirit level the probe and the AUT alignment.
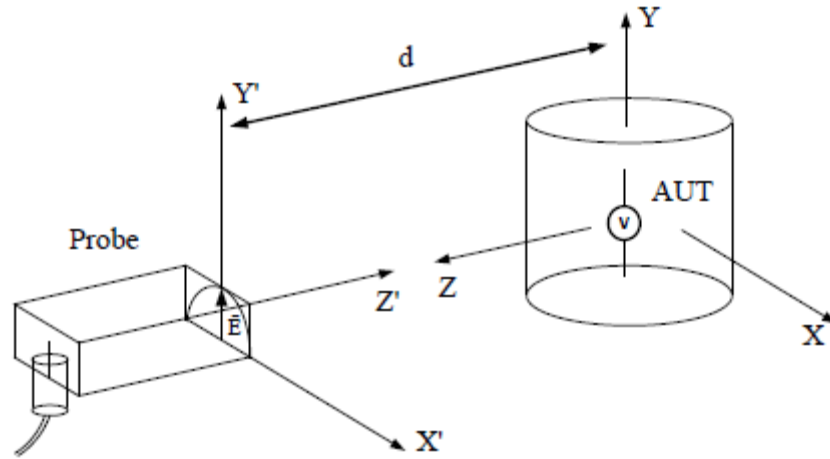

Fig. 3- 6 Schematic of the desirable alignment between probe antenna and AUT

3.2.1.3 Cylindrical near field geometrical parameters setup

When using MiDAS for CNF measurement during the setup the geometrical parameters need to be setup before the scan. These include: defining the probe antenna used and the dimensions of it (it is suggested that the setup dimensions need to be checked with the real ones); defining the AUT dimensions (for the specific measurement they have been defined as height=0.485m and width=0.360m) and polarization orientation (Vertical or Horizontal); defining the polarization of the probe antenna (for all the measurements undertaken in this chapter: Vertical = 0° and Horizontal = 90°) and finally, defining the geometrical parameters such as *the separation distance (d = AUT axis of rotation to probe- see next subsection),minimum radius enclosing the AUT which is constant for all measurements carried out and equal to 0.180m and the far field valid angle (see equation 3.7).* All these parameters affect the scan setup and sampling (see equations 3.1, 3.2 and 3.7) and determine the CNF scanning volume.

3.2.1.4 Receiver configuration

At this measurement setup step MiDAS help us to determine and define the output power (it has been setup to 0dBm); the ports numbering; the IF bandwidth and the frequency span recorded at each measurement. It is suggested and has been done, that before setting up those parameters to physically check which ports of the VNA are connected with the AUT and with the probe antenna (e.g. check that port 1 is the one ending to the probe antenna and port 2 the port connected with the AUT).

3.2.1.5 MiDAS calibration parameters

In this step the parameters that will be used from MiDAS software during the NF toFF transform to calculate the Gain (sub subsection 3.2.1.8) of the AUT must and have been measured and inserted, as txt files, to MiDAS calibration tab. Such parameters are:

(i)   The cable loss, which is the losses of the cables involved in the measurement measured with bypass (through) connection. The losses of the cables connected at port 1, connected through bypass and end up connected at port 2 of the VNA [40]

(ii)   AUT return loss (the clear with no cables involved reflection coefficient of the AUT) [40]

(iii)   Probe return loss (the clear with no cables involved reflection coefficient of the probe antenna) [40]

(iv)   AUT inserted return loss (the reflection coefficient of the AUT with the cable that connects it with the VNA) [40]

(v)   Probe inserted return loss (the reflection coefficient of the probe antenna with the cable that connects it with the VNA) [40]

(vi)   Gain of the probe antenna (WR-430 or WR-187)

Parameters (i) up to (v) have been measured in the tampered anechoic chamber where the CNF measurements carried out as well. It must be noted that when measuring each of these parameters (i-v) the power level of the VNA must be the same as the one that has been set up in the previous step (0dBm). The gain of the probe antennas at the desired frequency bands (2; 2.5 and 5GHz) has been measured in a characterized orthogonal far field anechoic chamber (Fig. 3-14a). The measurement involved measuring at 4 meters (which is a far field distance range for all examined frequencies and probe antennas) the S21 between the probe antennas

and a characterized horn antenna, on boresight of the probe, where the maximum gain is directed. Then by using Friis equation the Gain of the probe antennas has been calculated. For the WR-430 probe antenna at the 2GHz band the gain was between 4-4.5dBi and the 2.5GHz band the gain was between 4.7-5.1dBi. For the WR-187 probe antenna at the 5GHz band the gain was between 5.8-6.3dBi. Those calculated gain values are similar with the theoretical ones provided from ORBIT-FR.

The equation 3.4 that these parameters are added to by MiDAS code for Gain calculation is explained in sub subsection 3.2.1.8.

3.2.1.6 Scan setup and run

This is the final step before scanning the AUT with the probe antenna to obtain the near field measurement results. In this step linear (Y-scan) length (*L* - see equation 3.7), the span of the azimuth rotation angles (for all measurements carried out in this chapter it has been set from -180° - $+180^o$), the sampling on the Y and azimuth axis (ΔY, $\Delta\theta$) described in equations 3.1 and 3.2 [40]) and the values of the probe antenna polarization which are two (0° and 90°) for all measurements carried out in this chapter, are determined. After the setup of the scan parameters, scan time estimation is calculated by MiDAS. The scanning time was: 49 min. for the 2GHz, 57min. for the 2.5GHz and 1hr. and 15min. for the 5GHz.

$$\Delta Y \leq \frac{\lambda}{2} \ (mm) \tag{3.1}$$

$$\Delta\theta \leq \frac{\lambda}{2r} \ (^o), \text{ where } r \text{ is the radius of the minimum cylinder that is centred on the axis}$$
$$\text{of rotation (azimuth) and encloses the AUT} \tag{3.2}$$

3.2.1.7 Obtain near field results

After the scan is finished the cylindrical near field results can and have been obtained and inspected for revealing sources of possible measurement errors (see sub subsection 3.2.1.10). The near field results in amplitude and phase can be normalized to maximum values and 0dB. The near field data (E-field image) can be transformed to far field (see next step).

3.2.1.8 Near field to far field transform

In this step the NFtoFF transform is and have been done by using MiDAS application tab where the Fourier points (see in sub subsection 3.2.1.10 the importance of them), the radiation patterns geometrical transformation (Roll/Az was selected for all measurements), the normalization of the radiation patterns (to maximum value, directivity or gain) and the method of the AUT gain calculation (the direct method was selected for all measurements – see equation 3.4), must be determined.

The directivity is calculated by MiDAS using equation 3.3. It is understandable that directivity calculation by MiDAS requires only the near field raw (scan) data. MiDAS code finds the maximum measured power and divides it with the average (it is calculated by MiDAS) measured power.

$$D = \frac{P_{rm}}{\{P_{rm}\}} \tag{3.3}$$

Where:

P_{rm}: the maximum power measured at the AUT during the AUT scan

$\{P_{rm}\}$: the all over directions average power measured at the AUT during the AUT scan

The Gain is calculated by MiDAS using equation 3.4. Gain measurement using near field technique differs from that in far field measurements, since it does not depend on the distance between the two antennas involved. Direct gain near field measurements requires knowledge of the probe antenna's gain and a measurement that represent the computed far field peak. The maximum near field value, measured over the CNF scanning surface, surrounding the AUT, is used from which the peak value of the far field plane wave is computed by MiDAS. The computation includes also a correction for the effect of the probe's pattern. However, normalization is required to relate the far field peak value of the AUT to the input power at the probe antenna. This normalization is done by connecting the probe antenna's cable directly with the AUT's cable, to bypass the probe and the AUT. Thus, the computed far field peak value and bypass measurements represent a measured power ratio *(Pr-Pt) = (FFpeak-Bypass).* The bypass power measurement is the cable loss measurement as referred in 3.2.1.5.

$$G = (P_r - P_t) - G_P + M \qquad \text{(3.4)}$$

Where:

(Pr-Pt) = (FFpeak-Bypass): is the far field peak ratio of the received power at the AUT aperture to the input power at the probe antenna calculated by MiDAS.

GP: is the measured Gain of the probe (described in 3.2.1.5)

M: is the mismatch losses factor of the probe antenna and the AUT

The mismatch factor (*M*) is derived from the following equation (3.5):

$$M = \frac{|1 - \Gamma_s \Gamma_a|^2 \ |1 - \Gamma_p \Gamma_x|^2}{|1 - \Gamma_s \Gamma_x|^2 \ (1 - |\Gamma_a|^2) \ \left(1 - |\Gamma_p|^2\right)} \qquad \text{(3.5)}$$

Where:

Γ_s: is the source return loss or probe antenna inserted return loss as described in 3.2.1.5

Γ_a: is the AUT return loss as described in 3.2.1.5

Γ_p: is the probe antenna return loss as described in 3.2.1.5

Γ_x: is receiver return loss or the AUT inserted loss as described in 3.2.1.5

The radiation efficiency is calculated by the basic formula described in equation 3.6.

$$e = \frac{G}{D} \qquad \text{(3.6)}$$

Finally, the 3D radiation patterns of the AUT are produced by MiDAS by applying probe correction to the calculated near field data. The theoretical probe antenna's radiation patterns provided in MiDAS databasse are and have been used to apply a correction to the acquired near field data. The correction uses the near field peak value (from which the far field peak value is derived from) as the reference value.

3.2.1.9 Obtain far field results

After the near field to far field transform the radiation patterns, gain, directivity and efficiency of the AUT can and have been obtained so as to be compared with other measurements and simulations and to be used for research and commercial reasons.

3.2.1.10 Possible measurement errors, uncertainty and their sources

For every antenna measurement there are sources that will add to the measurement error and uncertainty. These sources are of mechanical, computational, and electromagnetic nature. It must be noted that no antenna measurement is "shielded" from error and uncertainty as long as they are not ideal like the simulations are.

More specifically, for the CNF measurement methodology for wearable antennas mounted on HOCS torso phantom, described in this chapter, the possible sources that could add to the measurement error and uncertainty are listed as follows:

- The structure of the AUT (HOCS phantom + wearable antenna) is oval cross section and not cylindrical. It could be said that it approximates the cylindrical. The distance between the probe (Tx antenna) and the AUT is not the same at every azimuth angle. This could result into deviation of the attenuated E-field at various azimuth angles between measurement and simulation. It is assumed that this physical weakness of the CNF measurement system adds to the error and deviation between measurements and simulations. This source of measurement error in combination with the following doesn't increase significantly the deviation between measurements and simulations. As it is proved from the following section (3.3) the maximum recorded difference between measurements and simulations is less than ±0.95dB when assuming that a ±1dB difference is always expected and so called *difference within the measurement error* [40].

- Absorbers quality is of crucial importance so as to create free space signal transmission and reception and to avoid unwanted multipath transmission and reflection which could distort measuring free space ("clear") radiation of the AUT, adding to the measurement error. The confidence that such an error doesn't exist in the measurements undertaken in this chapter is revealed from the near field plots and proven by the datasheet characterization of the specific anechoic chamber used

(Loughborough University). Additionally, it needs to be commented that the absorbers used in the probe antenna follow the standards in terms of dimensions and position on the probe described in [40]. The absorbers used in the probe are very important so as to remove side lobe transmission of the probe antenna so that its main radiation lobe is used for transmission avoiding multipath transmission. This is important for the probe correction stage as well. Finally, the metallic parts of the positioners of the AUT have been covered with absorbers and the plastic legs don't reflect signal back to the probe antenna altering by this way the measurements. This is clear from all near field plots.

- Proper alignment of the AUT'S aperture with the scanning probe antenna's (Tx) aperture is crucial in near field measurements. Positioning tolerances are stricter than in far field measurements. As a common practice, the positioning accuracy should be on the order of lamda/50 to achieve ±1dB accuracy for a side lobe of a -35dB. To ensure positioning accuracy, crossed laser tracking for centring the probe antenna's aperture with the AUT's aperture has been used (see sub subsection 3.2.1.2).

- The sampling points in the Azimuth and the Y-scan axis could affect the transformed far field results. The ones used in this chapter are the least required. It was found that by doubling the sample points the deviation between measurements and simulations decreased by 0.2dB in magnitude. But the measurement time was doubled as well. It has been judged by the author that this small improvement is not worth doubling the time for each measurement, considering the great number of the scans undertaken and the fact that the proposed methodology of this chapter can be described without this.

- The directivity values that are produced from NFtoFF transformation have some unavoidable truncation errors [39]. These predominantly comprise of the lack of sampling data over a portion of the radiating near field area (finite cylindrical surface area). The lack of sampling area is the one above and below the phantom on the Y-axis (top and bottom of elevation plane, in the arcs defined by: phi=90°-θ_{FF} and phi=-90°-(- θ_{FF})). Also, even if having an infinite cylindrical surface and ideally no lack of sampling, still this error would occur because in the transformation process the Hankel functions (which are used for the NFtoFF transform so as to produce the radiation patterns) are not defined at phi=90° and phi=-90°. The lack of sampling results into missing information for calculating the directivity as accurate as possible. This cannot be avoided when using the CNF measurement system. This factor is expected to add more, than the other described in this list, in the measurement error.

- The more accurate as possible measurement and definition of all MiDAS calibration parameters (3.2.1.5) are of crucial importance for calculating the AUT's gain (3.2.1.8) by NFtoFF. It is assumed that the probe gain, for both probe antennas, the mismatch factors, the FFpeak (from near field peak) and the Bypass loss (cable loss) used at all examined frequencies, have been measured as accurately as possible with repeatable measurements for each parameter showing almost same results.

- During the NFtoFF setup transformation when using the MiDAS software, the points of the Fast Fourier Transform must be defined. The increase of these points significantly increases the disk memory required for the transformed far field data. Additionally the increase of these points increases the accuracy of the transformed far field pattern. It was found that the set of 1024x1024 points resulted into similar far field transformed results with the set of 2048x2048. Obviously, the first set was used for saving memory disk. Finally, it was found that the set of 512x512 points resulted into an increased, by 1dB in magnitude, deviation between measurements and simulations , when compared with the set of 1024x1024 points.

3.2.2 Limitations

The AUTs basic geometrical parameters (*L* and *d*), which determine the CNF scanning volume, are shown in Fig. 3-7. Where *L* and *d* are: the CNF linear (Y-axis) scan length and the separation distance between probe and AUT respectively. These parameters should be evaluated in terms of AUT measurement performance compared with simulations. The goal of evaluating these geometrical parameters must be, to find for which pair of *d* and *L* the measurement results show closer agreement with simulations. For such an evaluation of the CNF test site lots of measurements will be required. This could endanger the phantom's safety and also the liquid's properties (which have an expiry date [45]). These are the limitations of the HOCS torso phantom, in terms of evaluating the CNF scanning volume (finding the ECGP which define the optimum CNF scanning volume). It was proposed that instead of using the HOCS liquid phantom, to use a CDP, so as to evaluate the CNF test site. This removed the necessity of using the HOCS liquid phantom itself. The proposed evaluation technique is described in details in Section 3.3.
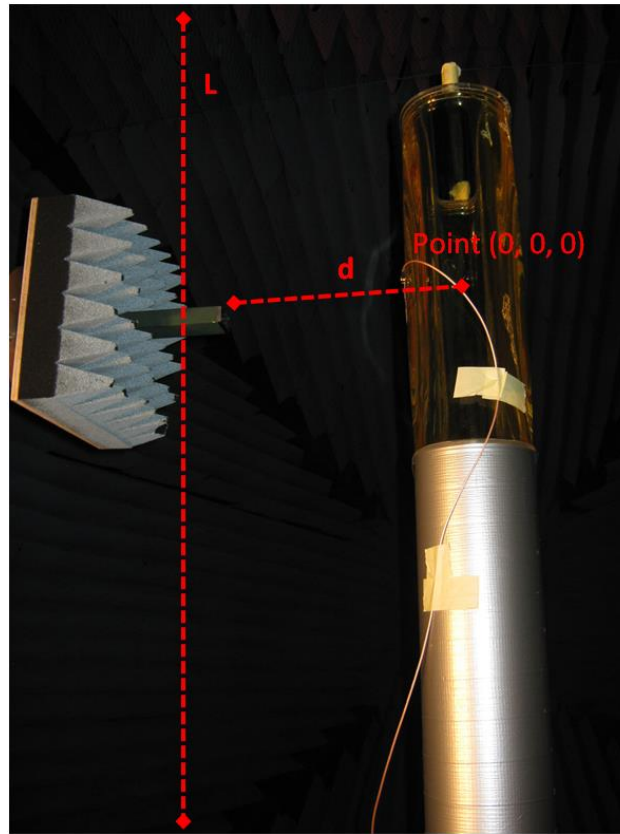
Fig. 3- 7 Basic geometrical parameters (*L* and *d*) which determine the cylindrical near field scanning volume

3.3 Cylindrical near field test site evaluation technique

3.3.1 Evaluation technique tool

As outlined in Section 3.2 the evaluation technique will be based on the use of a CDP instead of the HOCS liquid phantom. The wearable patch antennas were mounted on the CDP as they would be mounted on HOCS phantom (Fig. 3-8). The dimensions of the CDP on the XY plane were selected to be equal with the HOCS phantom dimensions. These dimensions are those which affect the *d* and *L* parameters, defining the CNF scanning volume (ECGP parameters). This ensured that the CNF geometry, which must be defined at the CNF measurement setup [5], will be the same when using as an AUT the CDP + wearable patch antenna and when the AUT is the HOCS phantom + wearable patch antenna. The parameters and criteria of the evaluation technique are described in the next subsection.
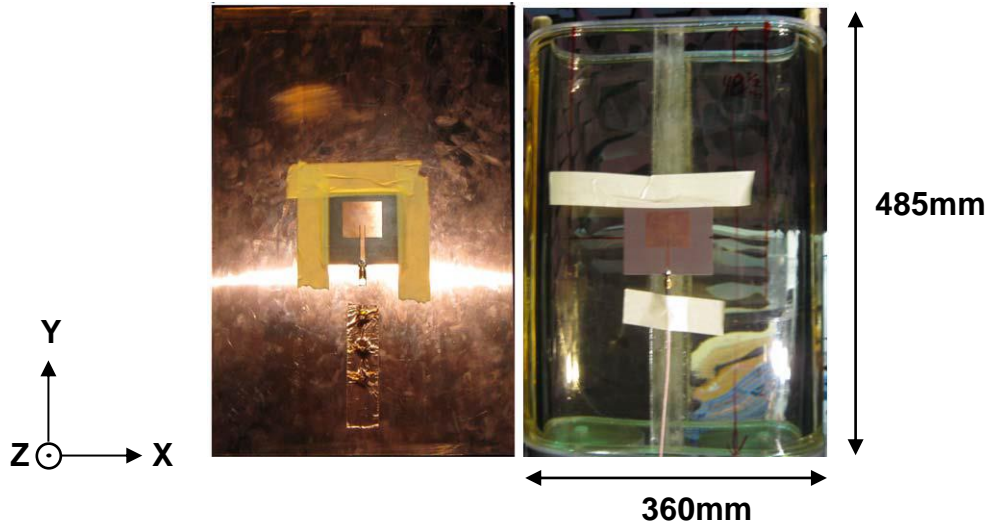
Fig. 3- 8 The 2.5GHz patch antenna mounted on CDP and on HOCS phantom

3.3.2 Parameters and criteria of evaluation technique

As referred in subsection 3.2.2 the geometrical parameters that were investigated and optimized (evaluated) are *d* and *L*. The criteria of evaluation are based on the comparison between the NFtoFF derived results, which correspond to specific *d* and *L*, with the simulated and directly measured FF results. Equation 3.7 connects the far field valid angle *(θ_{FF})*, the scan range (*L*) and the separation distance between AUT and probe (*d*) [46]. The geometry, according to theory, that corresponds to equation 3.7 is shown in Fig. 3-9. Each parameter (*d* or *L*) was investigated separately, so as to show the effect of each parameter in determining the optimum CNF scanning volume for each AUT (2; 2.5 and 5GHz).

$$\theta_{FF} = arctan(\frac{L-a}{2d}) \tag{3.7}$$

Where:

L: total scan length

d: separation distance between AUT axis of rotation (Azimuth) and probe (Y-scan plane)
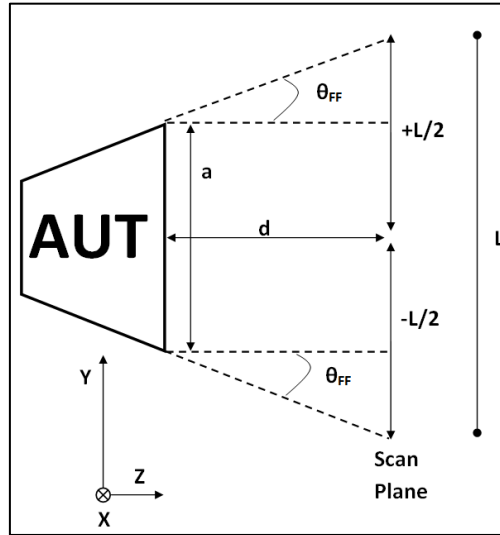
a: height of the AUT

Fig. 3- 9 Geometry of the cylindrical near field YZ scan plane

3.3.2.1 Varying the total scan length (*L*)

In the case of the 2GHz AUT for the evaluation of the scan length (*L*) parameter the separation distance (*d*) parameter was assumed constant (d = 0.97cm). Applying a constant *d* in equation 3.7 the varying parameters *L* and θ_{FF} resulted into transformed far field (NF to FF) results which are shown in Table 3-1. The recorded frequencies are those for which the AUT yielded S_{11} lower than -10dB. It is understandable from Table 3-1 that while the total scan length increased the gain and especially the directivity were improved in comparison with simulations (Fig.3-15). This means that the increase of Y-scan increases the chance of full pattern coverage [46]. More specifically and according to theory, to achieve full pattern coverage, the difference between the near field peak amplitude with the near field amplitude on the Y-slide scan edges must be at least 30dB (Fig. 3-10). The Y scan length with range: ±1473.66mm is close to the physical maximum range of the WR-430 probe in the specific anechoic chamber of Loughborough University. This is a limitation of the specific CNF test site. For the similar reason the evaluated scan length found for the case of the 2.5GHz AUT yielded range: ±1457.37. For the case of the 5GHz AUT, the physical maximum range of WR-187 probe is the range of: ±1521.37mm which met the 30dB criteria for full pattern coverage. Though the least Y-scan range which resulted into almost the same far field parameters (Fig. 3-17), met the 30dB criteria, was: ± 1154.15mm. This was the evaluated Y-scan selected for the 5GHz AUT. This selection saved measurement time without excluding near field information for full pattern coverage. For all three examined AUTs (2; 2.5 and 5GHz) these evaluated *L* parameters were used for the second parameter (*d*) evaluation.

Table 3- 1 Total scan length variation vs the NFtoFF parameters for the 2GHz AUT (CDP+patch antenna)

Frequency (GHz)		1.977		1.982		1.987		1.992	
θ_{FF} (^{O})	Y-scan range (mm)	Gain (dBi)	Dir (dBi)	Gain (dBi)	Dir (dBi)	Gain (dBi)	Dir (dBi)	Gain (dBi)	Dir (dBi)
5	[±352.3]	8.33	13.08	8.24	13.13	8.31	13.08	8.09	13.09
10	[±448.5]	8.07	12.01	8.02	12.10	7.97	11.95	7.84	12.05
15	[±512]	7.53	11.11	7.49	11.22	7.43	11.05	7.27	11.12
20	[±608]	7.61	10.72	7.49	10.73	7.49	10.63	7.34	10.72
25	[±704]	7.32	10.07	7.16	10.06	7.21	10.00	7.02	10.07
30	[±832.9]	7.32	9.71	7.34	9.88	7.28	9.71	7.14	9.84
35	[±929]	7.28	9.48	7.12	9.47	7.16	9.40	7.09	9.58
40	[±1089]	7.13	9.06	7.11	9.18	7.04	9.01	6.93	9.17
45	[±1217]	6.96	8.74	6.86	8.77	6.90	8.71	6.84	8.92
47.5	[±1313]	6.92	8.68	6.83	8.69	6.97	8.68	6.81	8.76
50	[±1409]	6.91	8.56	6.86	8.62	6.82	8.44	6.85	8.72
51	[±1473.66]	6.89	8.43	6.82	8.54	6.84	8.42	6.69	8.57

3.3.2.2 Varying the separation distance (*d*) between the AUT and probe

Having found the optimum (evaluated) scan length (*L*), in this sub subsection the evaluation of the separation distance (*d*) between the probe and the AUT is presented. According to theory [39] *d* must be three wavelengths or greater in order to avoid unwanted multiple reflections between probe and AUT that could create undesired ripples and distortion on the derived near field (E-field) and subsequently to the transformed far field radiation patterns. Additionally, the separation distance for a near field measurement is required to be within the radiating near field region of the AUT. This means that *d* is required to be between the reactive near field and the far field limit [46]. For all the AUTs measured in this work, no measurement took place within the reactive near field. According to [40] the far field limit distance is at: $2D^2/\lambda$ or 10λ or $10D$ (where D is the largest dimension of the radiating element of the AUT). For all AUTs examined the far field limit was theoretically assumed at 10λ. All the measurements for all AUTs examined were carried out at separation distance (*d*) within the radiating near field range (region).

For the evaluation of the separation distance effect on the measurement results different test cases (TC) were considered. These test cases and their distance in wavelengths (λ) are shown in Table 3-2 and 3-3 for the 2GHz and 2.5GHz AUTs respectively. The TC1 case for the 2GHz and the TC1 case for the 2.5GHz AUT, separation distances, which are close, were the closest achievable ones. This was due to positioner with the probe crashing danger. For the case of 5GHz AUT, the closest achievable separation distance, due to mechanical limitation, was equal to 35.3cm = 5.88λ. This was the only test case which was performed for the 5GHz AUT. For each test case (TC) the AUT was measured. For each measurement the scan length (*L*) which was used is the evaluated one from the previous sub subsection.

Table 3- 2 2GHz AUT separation distance for various test cases

Test Cases	d	θ_{FF}
TC1	55.5cm, 3.7λ	64°
TC2	63cm, 4.2λ	62.8^o
TC3	97cm, 6.46λ	51°
TC4	102cm, 6.8λ	50°
TC5	107cm, 7.13λ	48.5^o
TC6	112cm, 7.46λ	47.5^o
TC7	117cm, 7.8λ	46.2^o

Table 3- 3 2.5GHz AUT separation distance for various test cases

Test Cases	d	θ_{FF}
TC1	54cm, 4.5λ	66.5^o
TC2	58.5cm, 4.875λ	64.8^o
TC3	78cm, 6.5λ	57.9^o
TC4	100cm, 8.33λ	51.2^o

As previously said, in order to obtain full pattern coverage (which would lead to more accurate results) from the CNF measurements, the recorded near field amplitude difference, of the co-polarized with the probe E-field (in the near field area) components (A_V-Vertical or

A_H-Horizontal), between near field peak and the edge of the scan length must be at least 30dB (Fig.3-10) [46]. For all three patch antennas examined when mounted on the CDP the dominant near field (E-field) component is the A_V. For the 2GHz AUT the A_V peak was at (Y = 0mm, Az = 0°) and the edge of the scan length was at (Y = ±1473.66mm, Az = 0°). For the 2.5GHz the A_V peak was at (Y = 0mm, Az = 0°) and the edge of the scan length was at (Y = ±1493.76mm, Az = 0°). For the 5GHz the A_V peak was at (Y = 0mm, Az = 0°) and the edge of the scan length was at (Y = ±1154mm, Az = 0°). The recorded A_V amplitude differences at the main resonance frequency (f_c = 1.982GHz) for the 2GHZ AUT and at the main resonance frequency (f_c = 2.48GHz) for the 2.5GHz, for all the examined separation distance test cases are shown in Tables 3-4 and 3-5, for the 2GHz and 2.5GHz AUTs respectively. Where Δ1 is the A_V amplitude difference between Y=0mm and Y=-scan edge and Δ2 is the A_V amplitude difference between Y=0mm and Y=+scan edge respectively. The results from both Tables (3-4 and 3-5) reveal the effect of decreasing the separation distance between AUT and the Probe. This effect is that the recorded A_V amplitude difference (between near field peak and scan length edge) increased and came closer to the preferred 30dB one. The recorded Δ1 and Δ2 for the 5GHz AUT, at the only separation distance measured (35.3cm), at the resonance frequency (f_c = 4.96GHz) were 30.11dB and 32.60 dB respectively, meeting the full pattern coverage criteria. Additionally, the whole image of the recorded A_V amplitude for test cases: TC1, TC4, and TC7 for the 2GHz AUT and for TC1 and TC4 for the 2.5GHz and for the 5GHz all over the scanning cylinder are shown in Fig. 3-11, 3-12 and 3-13 respectively. It can be said, from the recorded near field patterns, that the attenuation of the amplitude of the A_V component in the case of TC1 for both AUTs (2 and 2.5GHz) was larger and appeared at shorter distance along the Y − axis (scan length). This resulted in increased A_V component amplitude difference between the near field peak and the edge of the scan length. This means that TC1 is closer to full pattern coverage (important for directivity) than the other test cases for the 2 and 2.5GHz. Another conclusion drawn from the above and proven from Fig. 3-15 and 3-16 is that the far field results derived from the near field measurements in the case of TC1 are closer to the simulation ones compared with the other TCs measured in the near field, for the 2 and 2.5GHz. The transformed gain values did not differ significantly for all the measured test cases for the 2 and 2.5GHz AUTs. The 5GHz AUT NFtoFF results derived from the only separation distance point measured were in acceptable agreement with simulations. All the gain values derived from the near field measurements for all test cases showed reasonable agreement with simulations. Finally, for comparison reasons the AUT was measured, for all examined patch antennas (2; 2.5 and 5GHz) in a separate far field test site,

inside a full wave chamber (Fig. 3-14a). The far field measurement results from these measurements are also included in Fig. 3-15, 3-16 and 3-17.
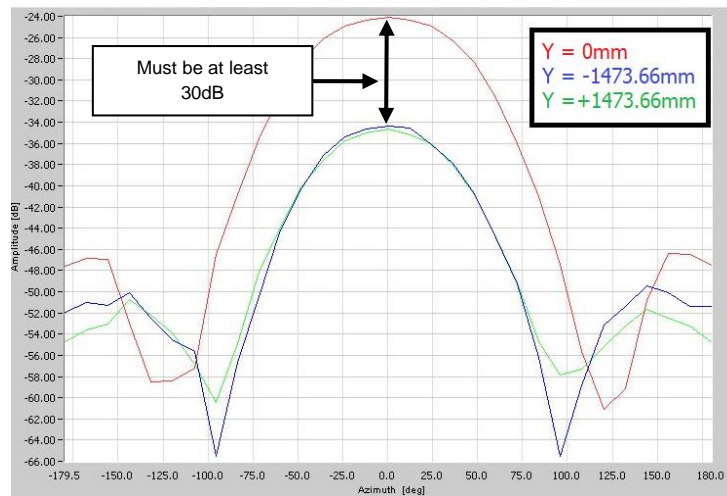

Fig. 3- 10 Measured near field amplitude of Vertical (A_V) component at Y = 0mm, Y = -1473.66mm and Y = +1473.66mm of 2GHz AUT at f_0 = 1.982GHz

Table 3- 4 Measured near field amplitude difference of the Vertical (A_V) component between peak and edges of the CNF scan length of 2GHz AUT (f_0 = 1.982GHz)

Test Cases	Δ1 (dB)	Δ2 (dB)
TC1	21.17	17.35
TC2	18.33	15.97
TC3	12.18	10.33
TC4	11.27	9.62
TC5	10.95	9.48
TC6	10.32	8.90
TC7	9.99	8.36

Table 3- 5 Measured near field amplitude of the Vertical (A_V) component difference between peak and edges of the CNF scan length of 2.5GHz AUT (f_0 = 2.480GHz)

Test Cases	Δ1 (dB)	Δ2 (dB)
TC1	23.45	20.18
TC2	22.05	19.70
TC3	17.84	15.03
TC4	12.61	12.23
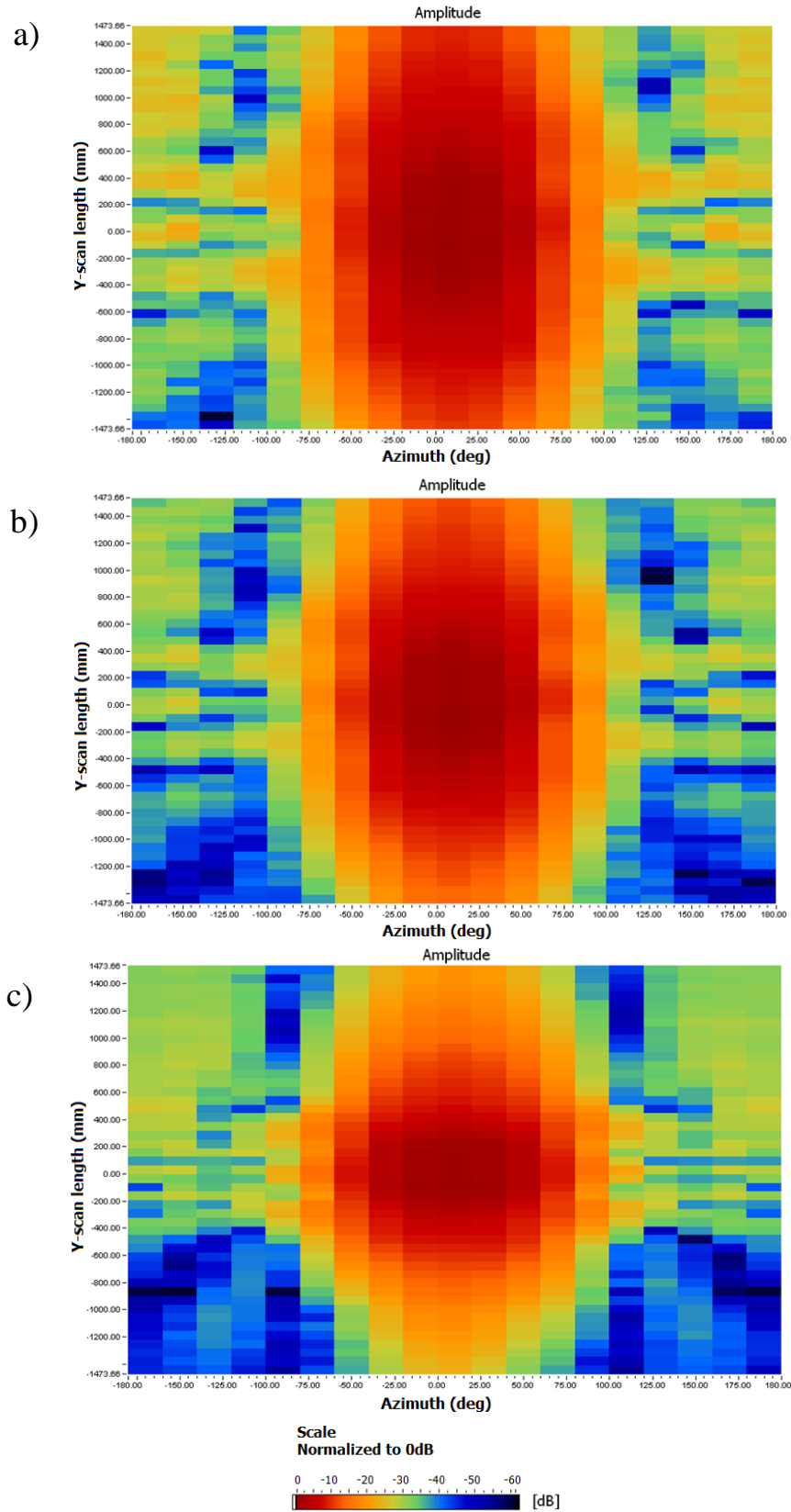
Fig. 3- 11 Measured near field amplitude of vertical (A$_V$) component for test cases: a) TC7, b) TC4 and c) TC1 for the 2GHz AUT, at f$_0$ = 1.982GHz
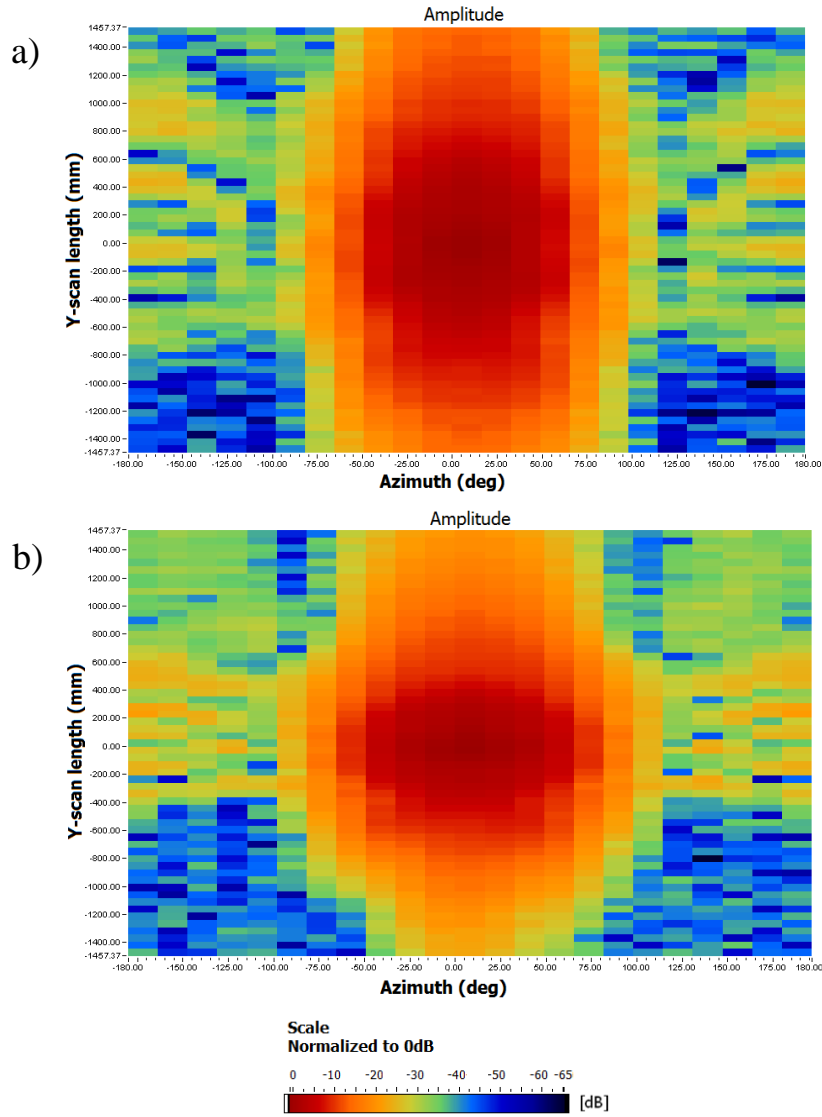
Fig. 3- 12 Measured near field amplitude of vertical (A_V) component for test cases: a) TC4, b) TC1 for the 2.5GHz AUT, at f_0 = 2.48GHz
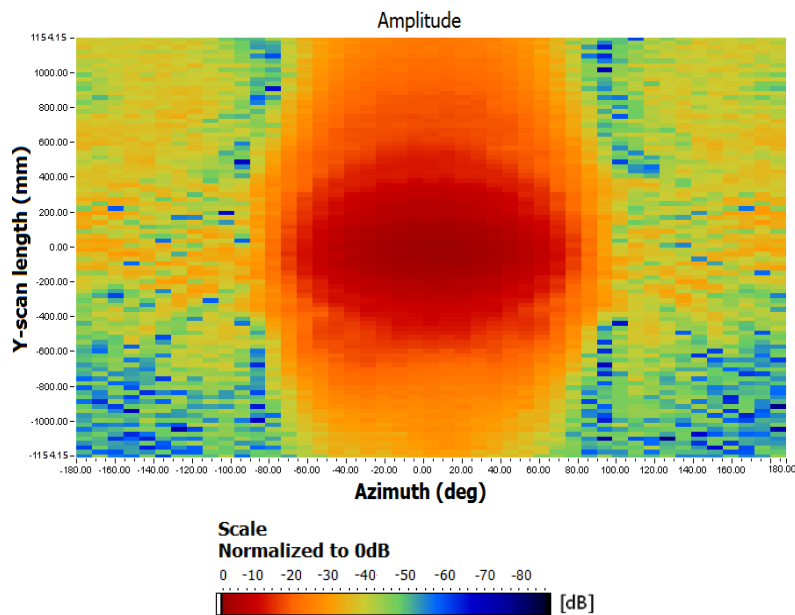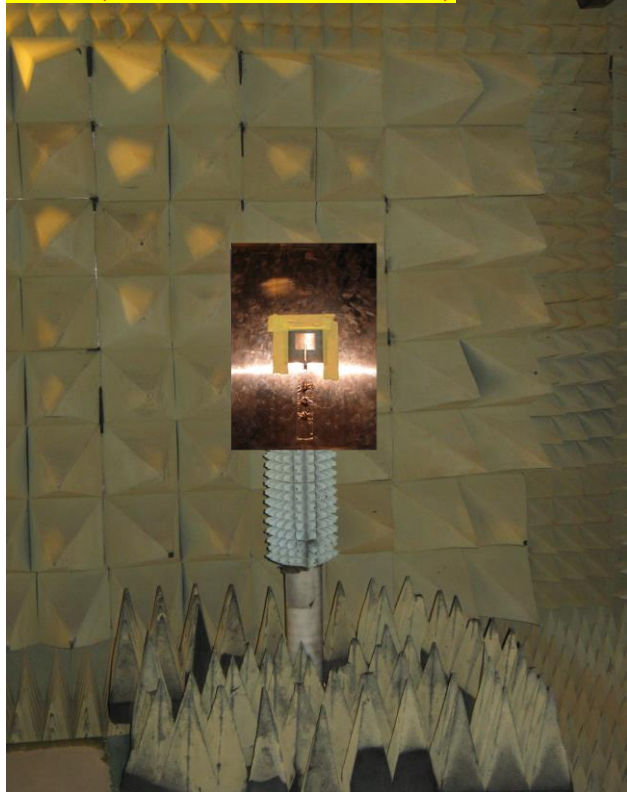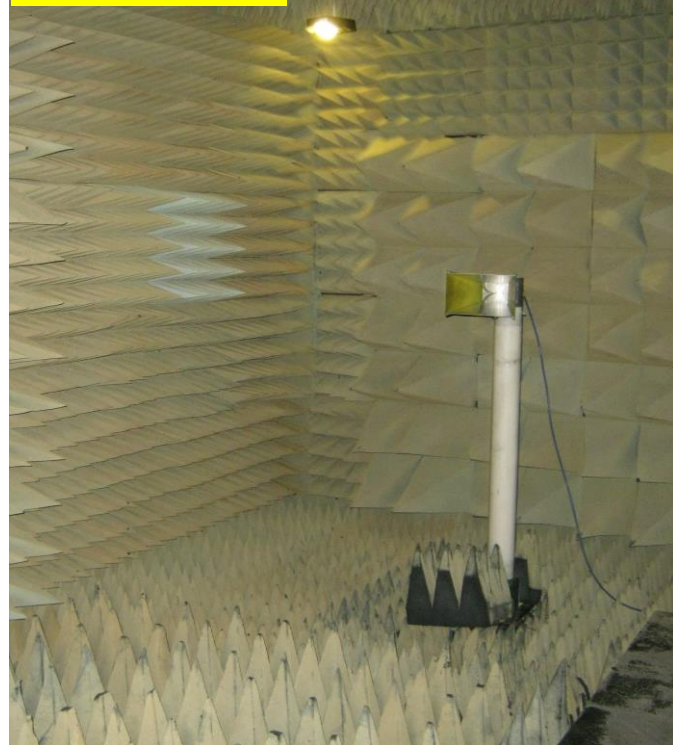

Fig. 3- 13 Measured near field amplitude of vertical (A_V) component for the 5GHz AUT, at f_0 = 4.96GHz

a)

b)

Fig. 3- 14 a) Far field measurement setup of 2.5GHz AUT (CDP+Patch antenna) in a full wave chamber, b) Near field measurement setup of 5GHz AUT (CDP+Patch antenna) in a tapered anechoic chamber
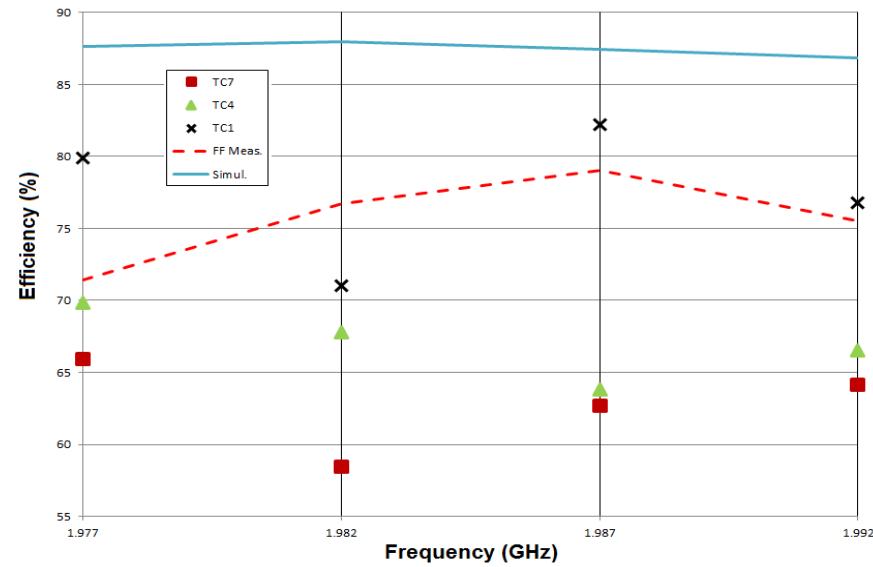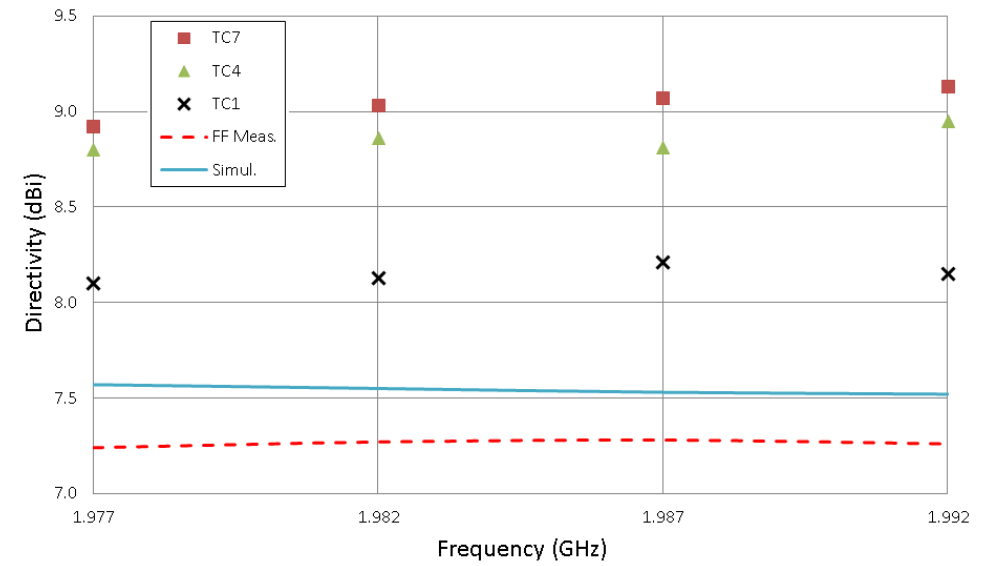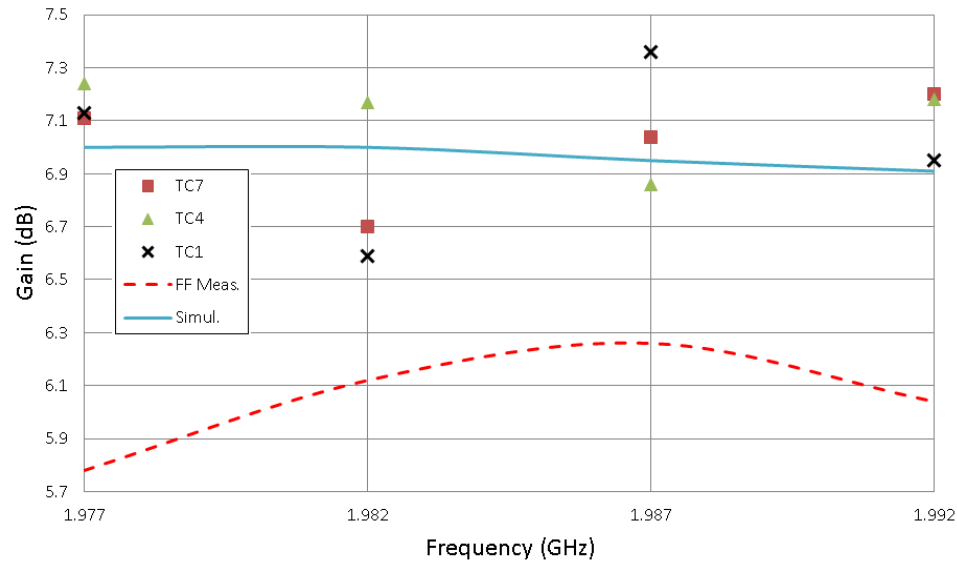
Fig. 3- 15 Gain, Directivity and Efficiency vs. frequency for cases: TC7, TC4, TC1, Simulations and Far Field Measurements for the 2GHz AUT (CDP +wearable patch antenna)
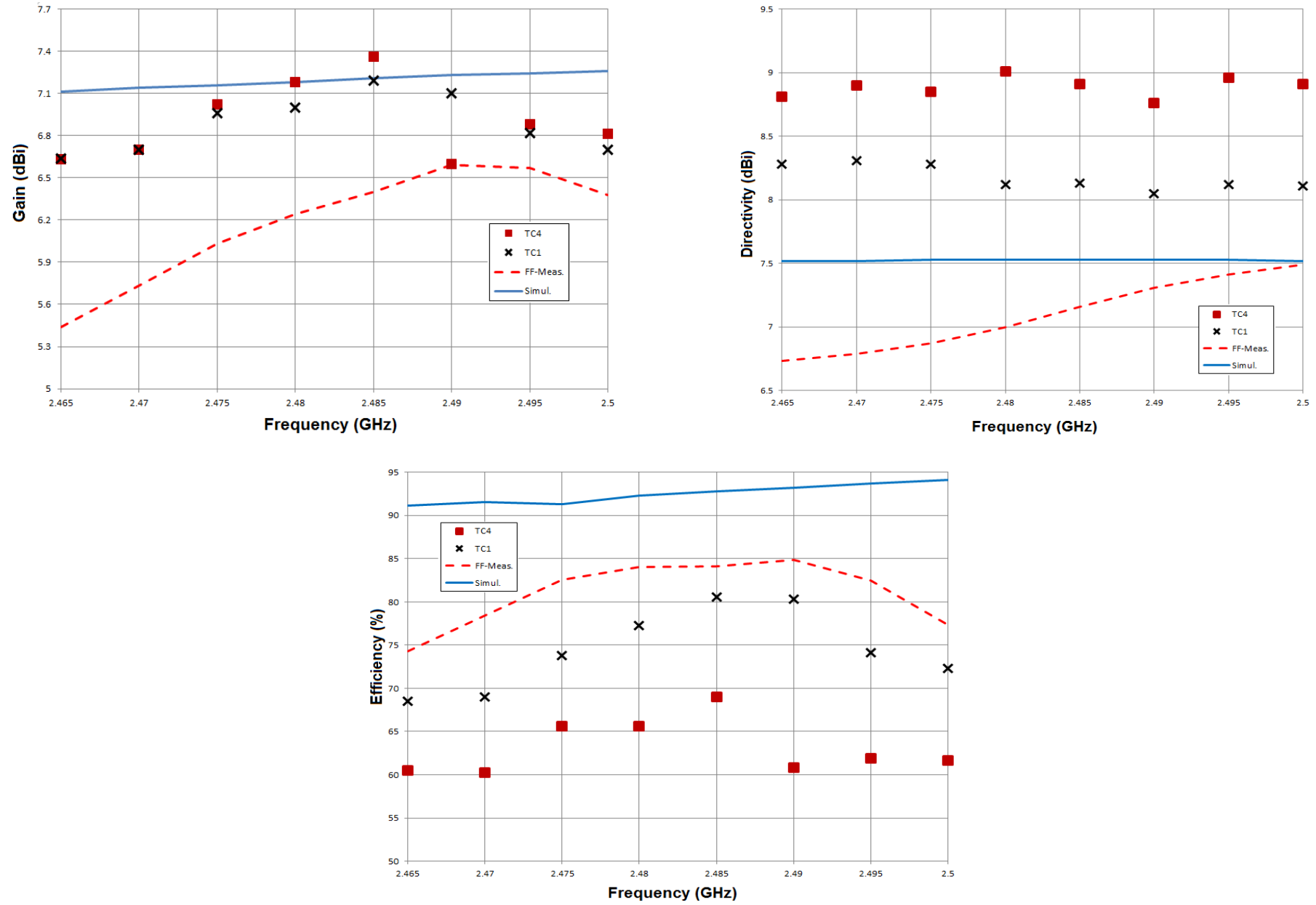
Fig. 3- 16 Gain, Directivity and Efficiency vs. frequency for cases: TC4, TC1, Simulations and Far Field Measurements for the 2.5GHz AUT (CDP + wearable patch antenna)
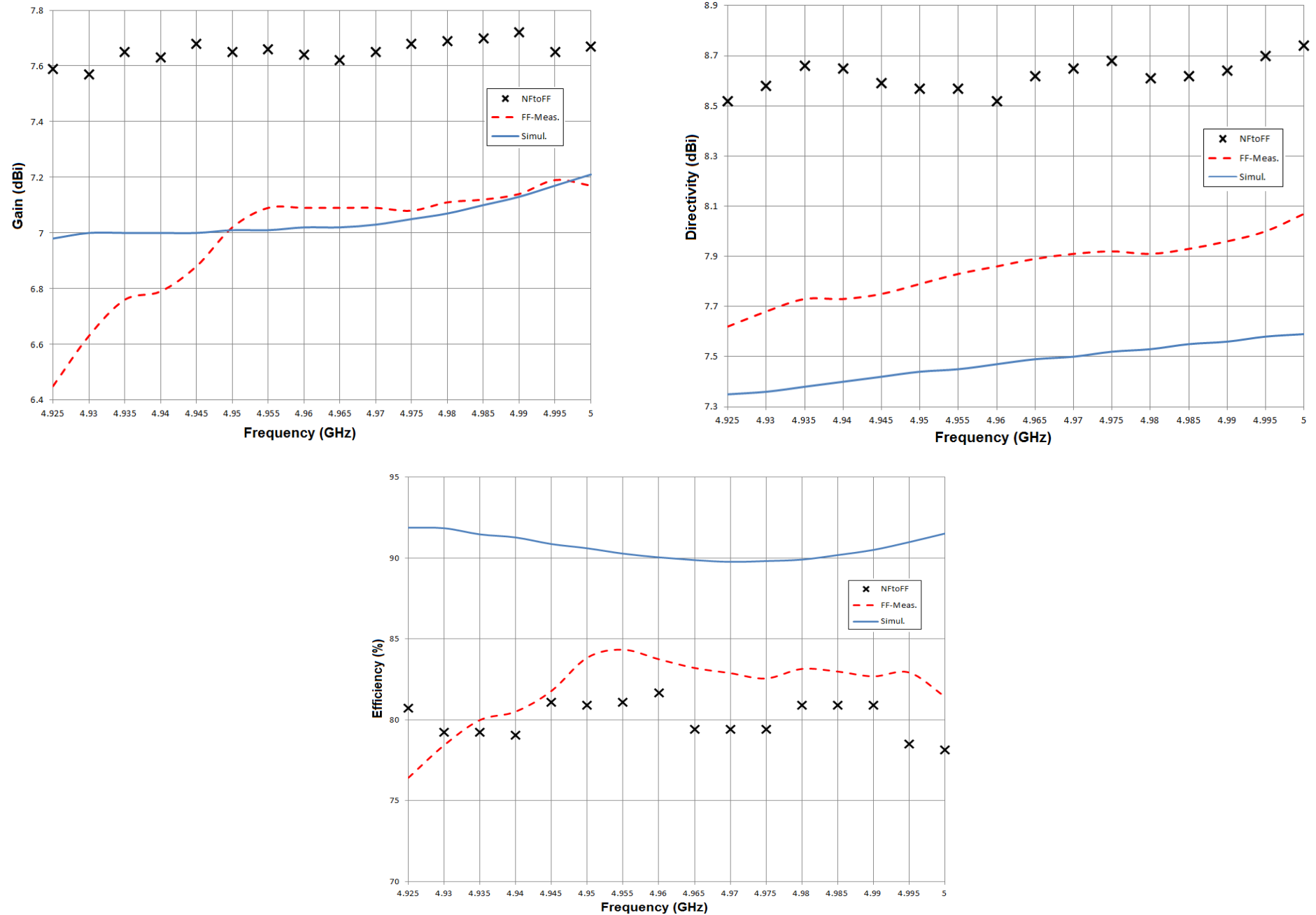
Fig. 3- 17 Gain, Directivity and Efficiency vs. frequency for cases: NFtoFF, Simulations and Far Field Measurements for the 5GHz AUT (CDP + wearable patch antenna)

Concluding from Fig. 3-15, the evaluation technique for the 2GHz AUT inside the CNF test site yielded that TC1 (d = 3.7λ, Y-scan length (*L*) range: (±1473.66mm)) results into a cylindrical near field scanning volume (EGSP parameters) which produced results which show reasonable agreement with the simulations. More specifically, the gain values between TC1 and simulations are within a maximum of 0.41dB and a minimum of 0.04dB deviation. The directivity values are comparable with, a maximum of 0.68dB and a minimum of 0.53dB, deviation. The efficiency values are within a minimum deviation of 5.21% and a maximum deviation of 16.97%. The CNF measurement technique yielded gain values closer to the Simulations than the direct FF measurement technique (Fig. 3-15). Additionally, the direct FF measurement technique yielded directivity values closer to the Simulations than the CNF technique. The efficiency values derived from the direct FF measurement are close to the ones produced from the CNF transformation.

From Fig. 3-16, the evaluation technique for the 2.5GHz AUT inside the CNF test side yielded that TC1 (d = 4.5λ, Y-scan length (*L*) range: (±1457.37mm)) results into CNF scanning volume (EGSP parameters) which produced far field results which show acceptable agreement with simulation. More specifically, the gain values for the TC1 and simulations are within a maximum deviation of and a maximum deviation of 0.56dB and a minimum deviation of 0.02dB. The directivity values deviate in maximum equal to 0.79dB and minimum equal to 0.52dB. The efficiency values are within a maximum deviation of 22.61% and a minimum deviation of 12.23%. The TC1 gain values are closer to simulations than the ones derived from the direct FF measurement. The direct FF measurement yielded directivity values which are comparable with the simulations and deviates from the ones produced from the CNF measurement (deviation: maximum = 1.6dB and minimum = 0.6dB). Finally the efficiency values derived from the FF measurement are closer to the simulations than the ones produced from the CNF measurement.

From Fig. 3-17, for the only separation distance test case (d = 5.88λ, Y-scan length (*L*) range: (±1154.15mm)) carried out for the 5GHz AUT, resulted into a CNF scanning volume (EGSP parameters) whose produced far field results are comparable with simulations. More specifically, the gain values produced from the CNF measurement deviations from the simulations are: maximum of 0.68dB and minimum of 0.46dB. The directivity values yielded maximum deviation equal to 1.28dB and minimum equal to 1.05dB. The efficiency values are within, a maximum deviation of 13.36% and minimum of 8.39%. The gain and directivity values derived from the direct FF measurement are closer to simulations than the CNF ones.

The efficiency derived from the direct FF measurement are close with the efficiency values produced from the CNF measurement.

For all AUTs examined, the directivity values produced from NFtoFF transformation have some unavoidable truncation errors [39]. These predominantly comprise of the lack of sampling data over a portion of the radiating near field area due to finite cylindrical scanning surface. The lack of sampling area is the one above and below the phantom on the Y-axis (top and bottom of the elevation plane). The lack of sampling exists on the elevation plane in the Arcs defined by: phi=90° – θ_{FF} and phi=-90°-(- θ_{FF}). The lack of sampling results into missing information for calculating the directivity as accurate as possible. This happens because the directivity by definition and measurement (eq. 3.3) is the maximum power radiated over the average power radiated. The average power radiated does not include all the information due to the lack of sampling. The effect of the truncation error into directivity values subsequently affects the efficiency values as well. Such truncation error would be minimized if a Spherical Near Field system was used because there would be no lack of sampling over the phantom area. This in combination with the non-satisfactorily full pattern coverage criteria (sub subsection 3.3.2.2 for the 2, 2.5 and 5GHz AUTs) resulted into increased directivity values and into decreased efficiency values for all the AUT cases, for all frequencies measured at the CNF compared with simulations. In terms of Gain limitations it could be said that the deviation between measurement and simulations are within the measurement error [39].

In terms of frequency limitations, from all AUTs examined it can be said that the lower the frequency the larger the CNF Y-scan length required so as to approach full pattern coverage. This is due to the nature of largest wavelength and penetration depth at lower frequencies (2GHz) compared to higher frequencies (5GHz). Though, the larger CNF Y-scan length should be combined with the closer separation distance (*d*) [39] (it should be larger than 3 wavelengths) for approaching full pattern coverage at all CNF scanning volume. For example at the case of 2GHz AUT where $\Delta1$, $\Delta2$ attenuations are lower than the desired 30dB the attenuation in most of the CNF scanning volume edges is more than 40-50dB (Fig. 3-11) in contradiction at the case of 5GHz AUT AUT where $\Delta1$, $\Delta2$ attenuations are close with the desired 30dB the attenuation in most of the CNF scanning volume edges is between 35-45dB (Fig. 3-13). This is due to the closest separation distance [39] in the case of 2GHz compared with the case of 5GHz. The previous point means that the full pattern coverage is more approached when the separation distance is as close as possible when combined with a large Y-scan length. The transformed far field parameters which reveals the pattern coverage is the

directivity. It can be seen that in the case of 2GHz the directivity values are closer to simulations compared with the case of 5GHz.

The concept of the evaluation technique is that these (above) deviations (between measurements and simulations) and limitations will be expected also in the case where the AUT is the HOCS phantom with the wearable patch antenna. More specifically, similar differences (deviations) in the far field parameters (gain, directivity and efficiency) between NFtoFF (CNF) with the Simulations are expected in the case where the AUT is the HOCS torso phantom (instead of the CDP) with the respective wearable patch antennas and measured at the optimum test case of TC1 respective cases for the 2 and 2.5GHz and at the only test case measured for the 5GHz AUT.

3.3.2.3 Evaluated cylindrical near field geometrical measurement setup parameters

The CNF EGSP for the 2, 2.5 and 5GHz AUTs determined from the evaluation technique are shown in Table 3-6. These specific EGSP were implemented in the cases where the AUT is the HOCS phantom with the respective wearable patch antennas (subsection 3.3.3 and section 3.4).

Table 3- 6 Cylindrical near field geometrical setup parameters for the 2, 2.5 and 5GHz AUT

Frequency	2GHz	2.5GHz	5GHz
Y-scan range (±L/2)	±1473.66mm	±1457.37mm	±1154.15mm
Distance Probe – Axis of rotation of AUT (d)	0.555m, 3.7λ	0.54m, 4.5λ	0.353m, 5.88λ
Radius of minimum cylinder enclosing AUT (r)	0.18m	0.18m	0.18m
Sampling step in Azimuth ($\Delta\theta$)	20°	16.36^o	8.18^o
Sampling step in Y-axis (ΔY)	64.07mm	52.05mm	26.23mm
Far field valid angle (θ_{FF})	64°	66.5^o	68.8^o

3.3.3 Evaluation technique validity assessment

In order to assess the validity of the proposed evaluation technique the 2; 2.5 and 5GHz wearable patch antennas were mounted on the HOCS torso phantom [47],[48]. Each

patch antenna was measured in the middle of HOCS phantom, position 1 (Fig. 3-18) for vertical and horizontal polarization (Fig.3-19). The AUT = (HOCS phantom + wearable patch antenna) was measured in the CNF test site for scanning volume corresponding to the EGSP (Table 3-6). The far field results (gain, directivity and efficiency) produced from the CNF measurements transformation were compared with simulations. The comparison between measurements and simulations are shown in Tables 3-7 - 3-12. The frequencies for which the far field parameters are recorded and compared are those which yielded S_{11} lower than -10dB in the CNF measurements.

Table 3- 7 2GHz frequency band AUT (HOCS phantom +wearable patch antenna) far field results for Vertical polarization at Position 1

Frequency (GHz)	FF produced from CNF			Simulations		
	Gain (dBi)	Directivity (dBi)	Efficiency (%)	Gain (dBi)	Directivity (dBi)	Efficiency (%)
1.977	6.75	8.25	70.79	6.50	7.75	74.94
1.982	6.22	8.30	61.94	6.54	7.77	75.44
1.987	6.38	8.28	64.56	6.54	7.78	75.21
1.992	6.00	8.32	58.61	6.54	7.79	75.00
1.997	6.06	8.33	59.29	6.54	7.79	75.00

Table 3- 8 2GHz frequency band AUT (HOCS phantom +wearable patch antenna) far field results for Horizontal polarization at Position 1

Frequency (GHz)	FF produced from CNF			Simulations		
	Gain (dBi)	Directivity (dBi)	Efficiency (%)	Gain (dBi)	Directivity (dBi)	Efficiency (%)
1.977	6.42	7.65	75.33	6.25	7.43	76.18
1.982	5.88	7.68	66.06	6.29	7.44	76.69
1.987	6.13	7.75	68.86	6.28	7.44	76.46
1.992	5.67	7.81	62.08	6.27	7.44	76.24
1.997	5.95	7.92	63.53	6.22	7.45	75.47

Table 3- 9 2.5GHz frequency band AUT (HOCS phantom +wearable patch antenna) far field results for Vertical polarization at Position 1

Frequency (GHz)	FF produced from CNF			Simulations		
	Gain (dBi)	Directivity (dBi)	Efficiency (%)	Gain (dBi)	Directivity (dBi)	Efficiency (%)
2.470	5.79	8.16	57.94	6.74	7.77	79.03
2.475	6.43	8.35	64.26	6.78	7.78	79.47

2.480	6.47	8.46	63.24	6.82	7.80	79.91
2.485	6.78	8.45	68.07	6.86	7.81	80.34
2.490	6.48	8.53	62.37	6.90	7.83	80.77
2.495	6.71	8.56	65.31	6.94	7.84	81.20
2.500	6.75	8.60	65.31	6.98	7.86	81.64

Table 3- 10 2.5GHz frequency band AUT (HOCS phantom +wearable patch antenna) far field results for Horizontal polarization at Position 1

	FF produced from CNF			Simulations		
Frequency	*Gain*	*Directivity*	*Efficiency*	*Gain*	*Directivity*	*Efficiency*
(GHz)	*(dBi)*	*(dBi)*	*(%)*	*(dBi)*	*(dBi)*	*(%)*
2.470	5.60	7.66	62.23	6.58	7.51	80.69
2.475	6.09	7.68	69.34	6.62	7.53	81.13
2.480	6.15	7.80	68.39	6.66	7.54	81.55
2.485	6.51	7.82	73.96	6.70	7.56	81.98
2.490	6.41	7.82	72.27	6.74	7.58	82.40
2.495	6.38	7.86	71.12	6.78	7.59	82.81
2.500	6.37	7.86	70.95	6.81	7.61	83.24

Table 3- 11 5GHz frequency band AUT (HOCS phantom +wearable patch antenna) far field results for Vertical polarization at Position 1

	FF produced from CNF			Simulations		
Frequency	*Gain*	*Directivity*	*Efficiency*	*Gain*	*Directivity*	*Efficiency*
(GHz)	*(dBi)*	*(dBi)*	*(%)*	*(dBi)*	*(dBi)*	*(%)*
4.925	7.15	8.73	69.50	6.64	8.13	70.98
4.930	6.93	8.77	65.43	6.68	8.14	71.42
4.935	7.06	8.66	69.18	6.68	8.15	71.52
4.940	7.03	8.65	68.86	6.72	8.15	71.95
4.945	7.13	8.66	70.30	6.74	8.16	72.07
4.950	7.10	8.52	72.11	6.77	8.17	72.47
4.955	7.28	8.59	73.96	6.78	8.18	72.58
4.960	7.32	8.61	74.30	6.81	8.18	72.93
4.965	7.26	8.59	73.62	6.83	8.19	73.03
4.970	7.01	8.39	72.77	6.85	8.20	73.32
4.975	7.52	8.59	78.16	6.86	8.20	73.41
4.980	7.55	8.47	80.90	6.88	8.21	73.65
4.985	7.10	8.50	72.44	6.90	8.22	73.75

4.990	7.07	8.49	72.11	6.91	8.22	73.96
4.995	7.02	8.42	72.44	6.93	8.23	74.09
5.000	6.92	8.36	71.77	6.95	8.24	74.46

Table 3- 12 5GHz frequency band AUT (HOCS phantom +wearable patch antenna) far field results for Horizontal polarization at Position 1

	FF produced from CNF			Simulations		
Frequency *(GHz)*	*Gain* *(dBi)*	*Directivity* *(dBi)*	*Efficiency* *(%)*	*Gain* *(dBi)*	*Directivity* *(dBi)*	*Efficiency* *(%)*
4.925	7.11	8.37	74.81	6.42	7.81	72.64
4.930	6.81	8.38	69.66	6.45	7.81	73.09
4.935	6.96	8.27	73.96	6.47	7.82	73.20
4.940	6.88	8.33	71.61	6.50	7.83	73.64
4.945	6.85	8.29	71.77	6.51	7.84	73.74
4.950	6.84	8.30	71.44	6.54	7.84	74.15
4.955	7.04	8.33	74.30	6.56	7.85	74.24
4.960	7.01	8.32	73.96	6.59	7.86	74.59
4.965	7.12	8.36	75.16	6.60	7.87	74.68
4.970	7.10	8.41	73.11	6.62	7.88	74.96
4.975	7.16	8.48	73.79	6.64	7.88	75.05
4.980	7.13	8.38	74.98	6.66	7.89	75.29
4.985	7.10	8.47	72.94	6.67	7.90	75.39
4.990	7.88	8.52	86.29	6.69	7.91	75.58
4.995	7.64	8.48	82.41	6.71	7.92	75.71
5.000	7.18	8.45	74.64	6.73	7.93	75.90

Regarding the 2GHz case (Table 3-7 and 3-8) the yielded deviations (between simulations and measurements), for both polarization scenarios examined, are the following:

- **Gain**: Vertical (maximum = 0.54dB, minimum = 0.16dB), Horizontal (maximum = 0.6dB, minimum = 0.17dB)

- **Directivity**: Vertical (maximum = 0.54dB, minimum = 0.5dB), Horizontal (maximum = 0.47dB, minimum = 0.22dB)

- **Efficiency**: Vertical (maximum = 16.39%, minimum = 4.15%), Horizontal (maximum = 14.16%, minimum = 0.85%)

These deviations are in good agreement with those yielded from the evaluation technique (sub subsection 3.2.2.2 – p. 3-33), when the CDP was used instead of the HOCS phantom, for the 2GHz AUT.

Regarding the 2.5GHz case (Table 3-9 and 3-10) the yielded deviations (between simulations and measurements), for both polarization scenarios examined, are the following:

- **Gain**: Vertical (maximum = 0.95dB, minimum = 0.08dB), Horizontal (maximum = 0.98dB, minimum = 0.19dB)

- **Directivity**: Vertical (maximum = 0.74dB, minimum = 0.39dB), Horizontal (maximum = 0.27dB, minimum = 0.15dB)

- **Efficiency**: Vertical (maximum = 22.09%, minimum = 12.27%), Horizontal (maximum = 18.46%, minimum = 8.02%)

These derived deviations are in good agreement with those yielded from the evaluation technique (subsection 3.2.2.2 – p. 3-33), when the CDP was used instead of the HOCS phantom, for the 2.5GHz AUT.

Regarding the 5GHz case (Table 3-11 and 3-12) the yielded deviations, for both polarization scenarios examined, are the following:

- **Gain**: Vertical (maximum = 0.67dB, minimum = 0.03dB), Horizontal (maximum = 1.19dB, minimum = 0.3dB)

- **Directivity**: Vertical (maximum = 0.63dB, minimum = 0.12dB), Horizontal (maximum = 0.61dB, minimum = 0.45dB)

- **Efficiency**: Vertical (maximum = 7.25%, minimum = 0.36%), Horizontal (maximum = 10.71%, minimum = 0.06%)

These deviations are in acceptable agreement with those yielded from the evaluation technique (subsection 3.2.2.2 – p. 3-33), when the CDP was used instead of the HOCS phantom, for the 5GHz AUT.

In conclusion from this section it was proved that a new evaluation technique, appropriate for CNF measurements applied on HOCS torso phantom for wearable antenna performance evaluation, is quite effective and useful as a measurement benchmark aiming to prepare the CNF measurement setup. The advantage of the evaluation technique is that a ConDucting Plate (CDP) is used instead of the HOCS phantom. The use of the CDP resulted into avoiding the risks rising up from the liquid phantom use. Such risks are: (i) the cost of the liquid, in

combination with its expiry date and (ii) possible damage or leakage of the liquid phantom after lots of CNF geometry optimization measurements. The proposed evaluation technique has been assessed and proved valid in order to define an optimized CNF scanning volume (EGSP) for the 2; 2.5 and 5GHz wearable patch antenna mounted on HOCS torso phantom, without using the HOCS torso phantom itself. The EGSP have been applied for all measurement scenarios which are examined at the next section (3.4).

3.4 Evaluation of wearable patch antennas performance parameters for Off-body communication link

In this section the new methodology for evaluating wearable antennas performance, mounted on HOCS torso phantom, by using the CNF measurement technique is presented and described in detail. The wearable patch antennas (2; 2.5 and 5GHz) are mounted in different locations (sub subsection 3.4.1.1) on the HOCS toros phantom. These patch antennas are mostly suitable for an Off-body communication link. So, the new methodology is specialized for evaluating wearable antennas for Off-body mode.

The steps of the new methodology can be listed as follows: *1) The image of the E-field distribution (near field amplitude) in the near field region, for each antenna in each location is recorded; 2) From the near field results, assumptionss for the maximum direction of radiation, for the radiation at the main geometrical planes and for the directivity are derived. 3) Finally, the far field parameters (gain, directivity and efficiency) and the radiation patterns are produced from the near field results, validating the assumptions made from the near field results (step 2).*The first two steps are described in subsection 3.4.1, sub subsection 3.4.1.2 and the third in subsection 3.4.2.

3.4.1 Measurement scenarios and cylindrical near field results

3.4.1.1 Measurement scenarios

The measurement CNF scenarios that were followed for each patch antenna were: 7 different locations on the phantom (Fig. 3-18) and two different polarizations for each position (Fig.3-19). This gave 42 different measurement setups of the AUTs (HOCS phantom + wearable patch antenna). In Fig. 3-18 the different positions were defined as: *1. Middle of Torso, 2. Left Lung, 3. Right Lung, 4. Right Shoulder, 5. Left Shoulder, 6. Left Trunk and 7. Right Trunk (right and left hand side are defined from the phantom's point of view).* In Fig. 3-19 the two polarizations of the measured wearable patch antennas are defined (Fig. 3-19 a. is Vertical – **V** and in Fig. 3-19 b. is Horizontal – **H**).
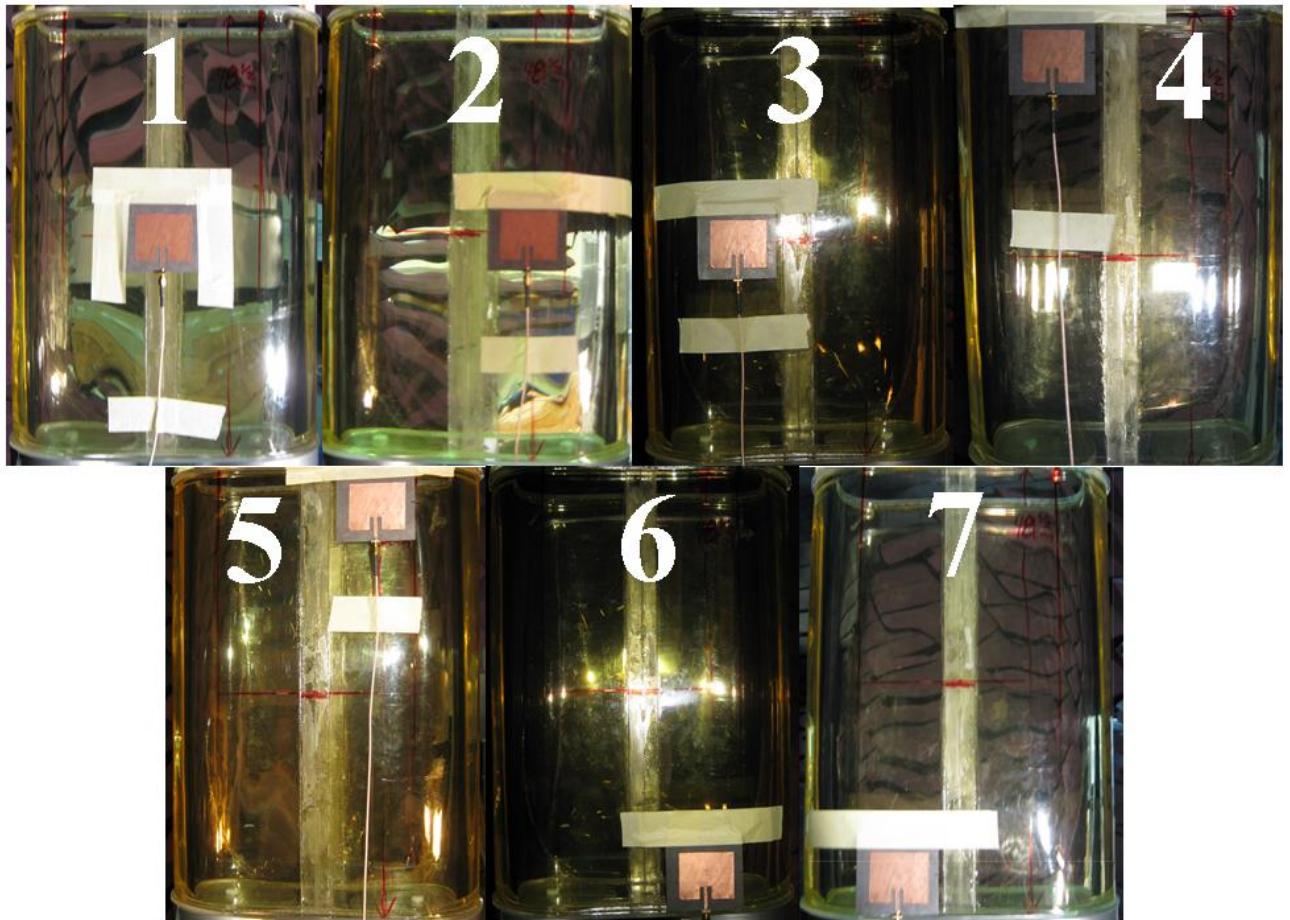
Fig. 3- 18 Wearable patch antenna different on HOCS phantom positions

a)   b)
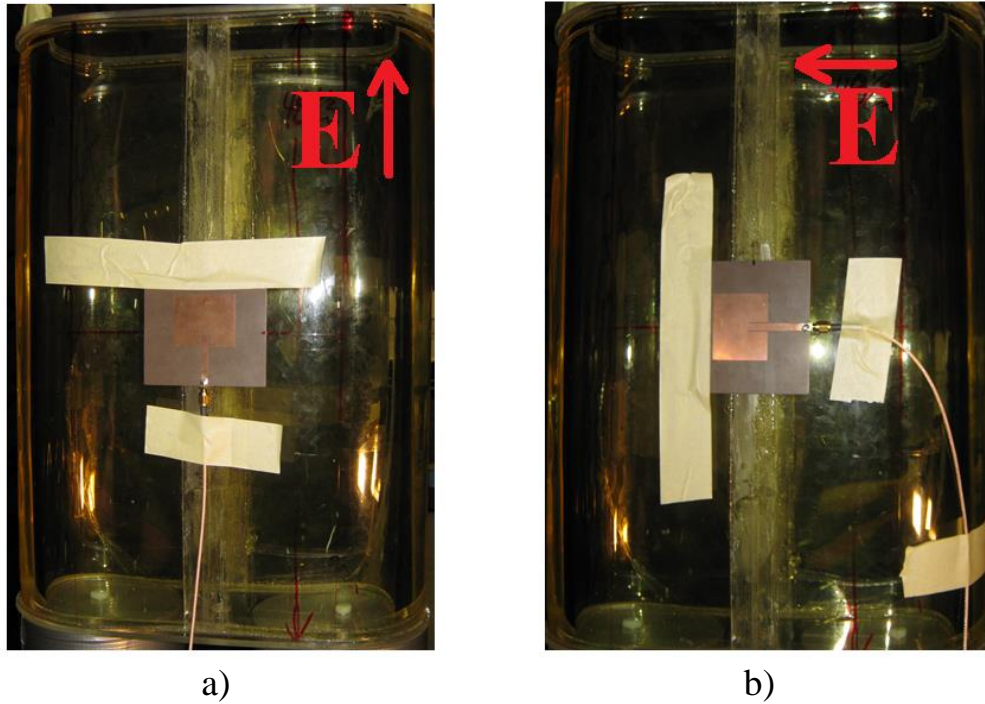
Fig. 3- 19 Polarizations of 2.5GHz Patch Antenna Measured: a) Vertical, b) Horizontal

3.4.1.2 Cylindrical near field measurement results

The near field amplitude contour plots of the CNF measurement results for all three AUTs for both polarization scenarios at all positions are shown in Fig. 3-20 to 3-25. The straight black dashed lines enclose the AUT's height (HOCS phantom's height). For the Vertical polarization scenario the Vertical component (A_V) is recorded and for the horizontal the Horizontal component (A_H) respectively. These components in each polarization scenario were used to produce the main and radiation fundamental co-polar components in the far field by using the MiDAS 6.0 software.
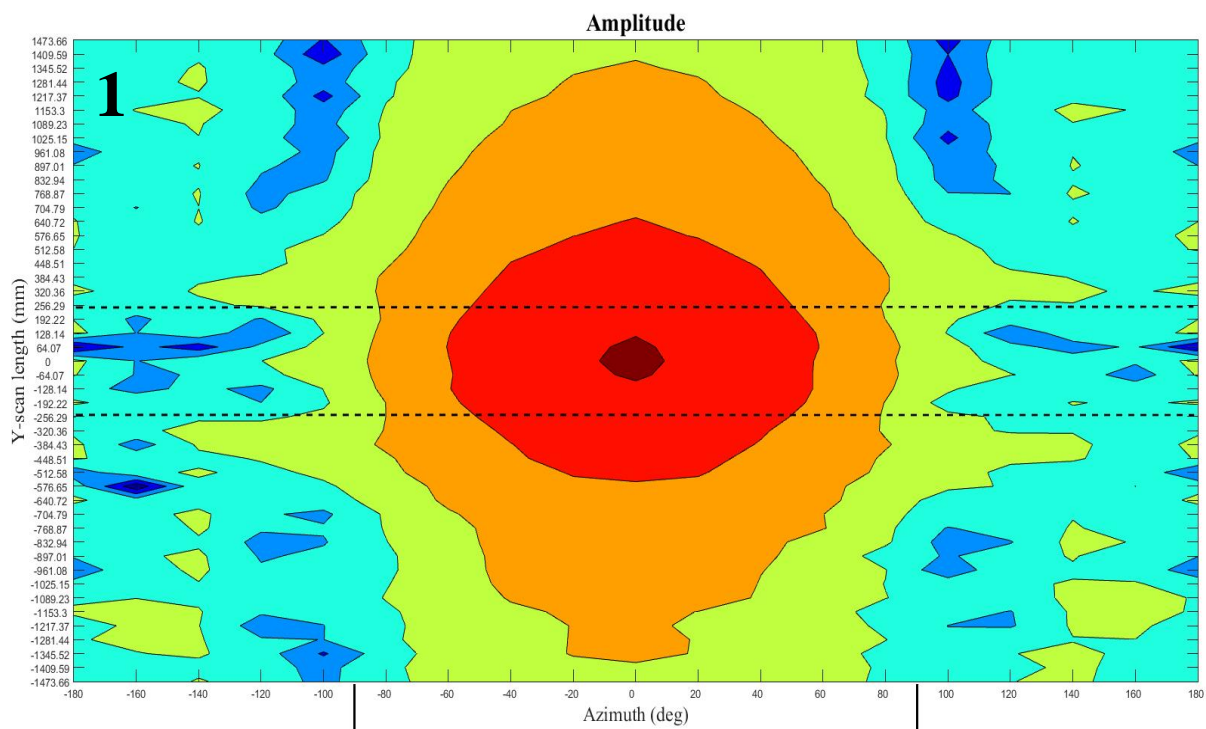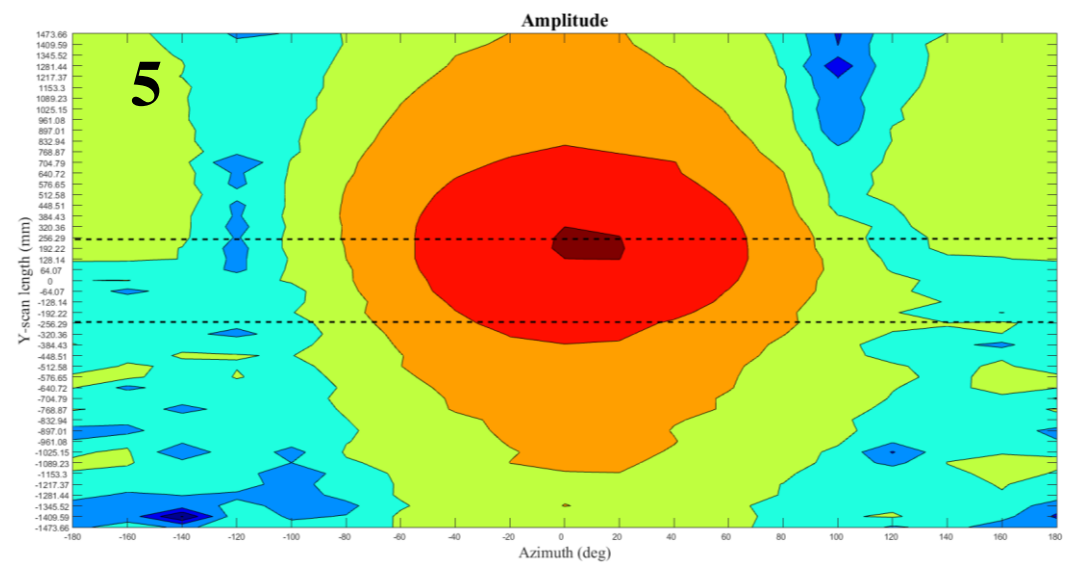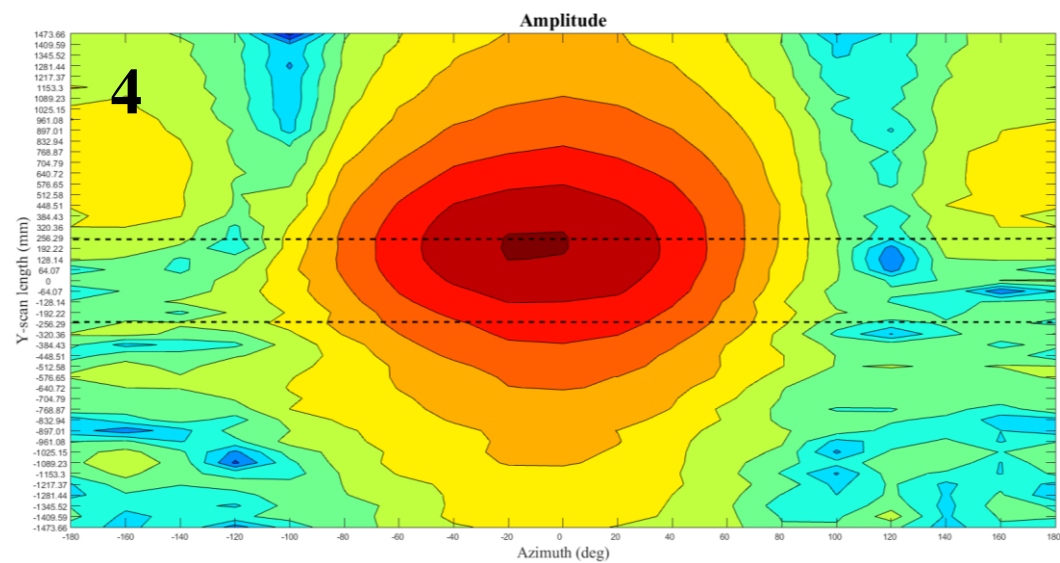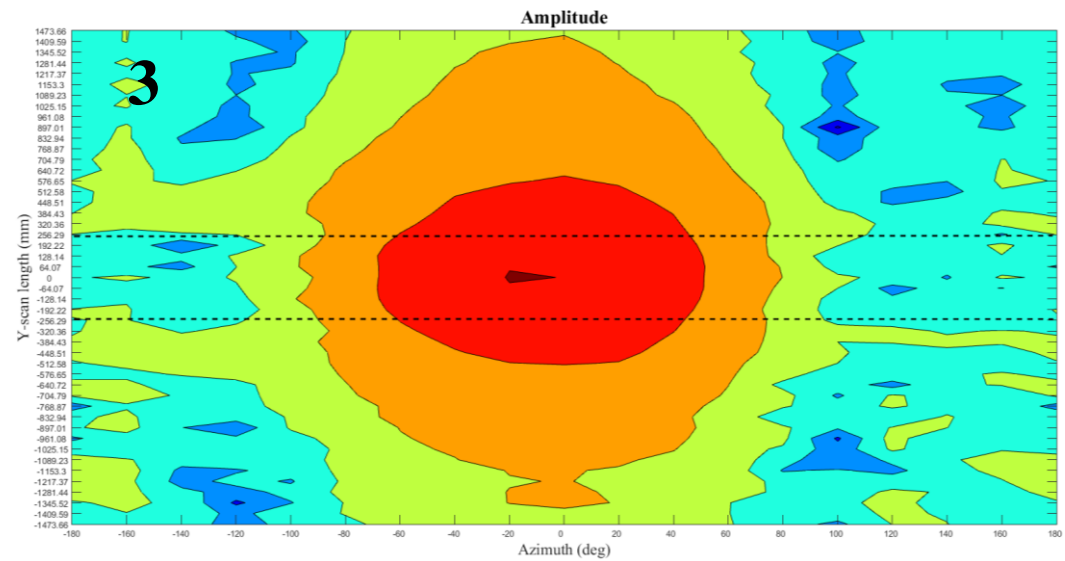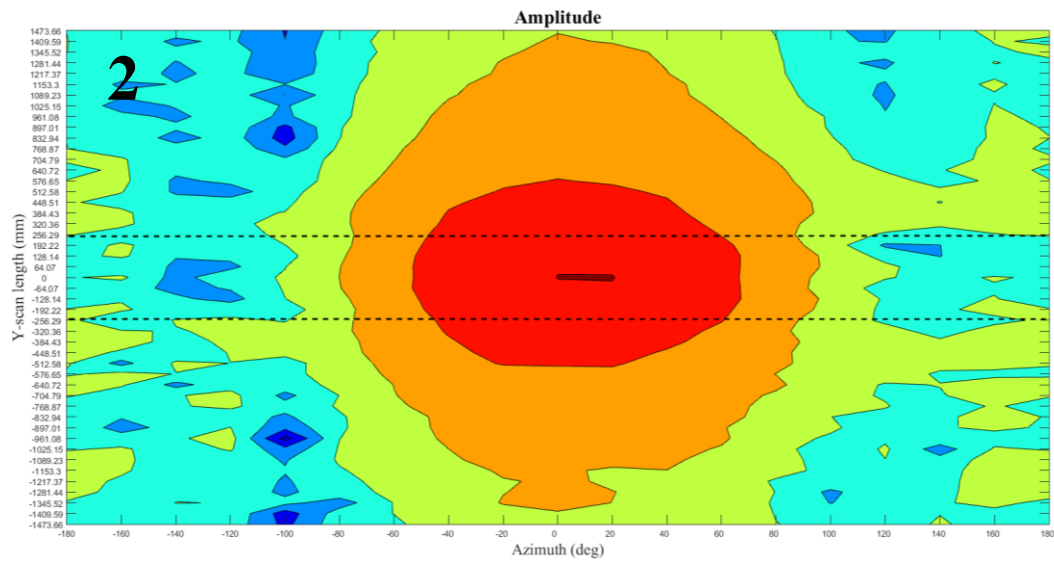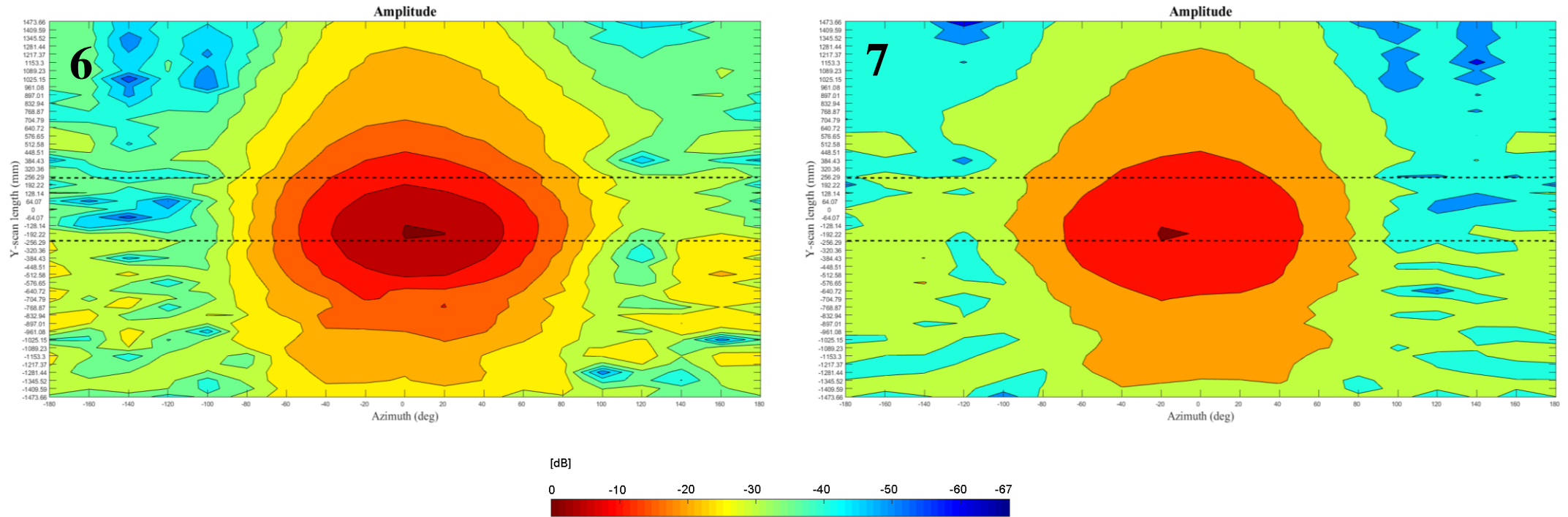
Fig. 3- 20 Measured near field amplitude vertical component (A_V) for the 2GHz vertical polarization scenario at all positions examined at $f_0 = 1.987$GHz
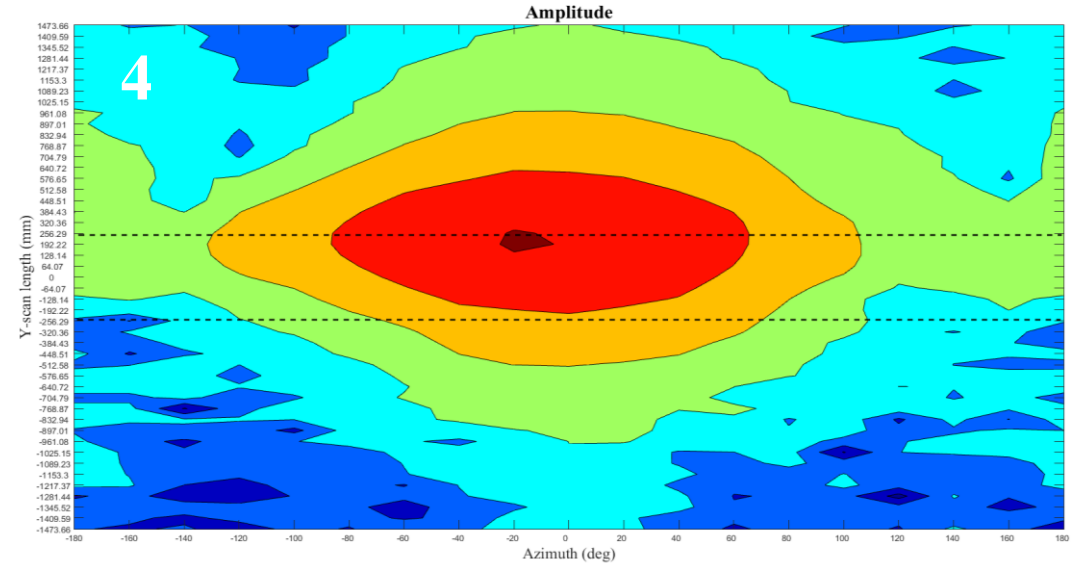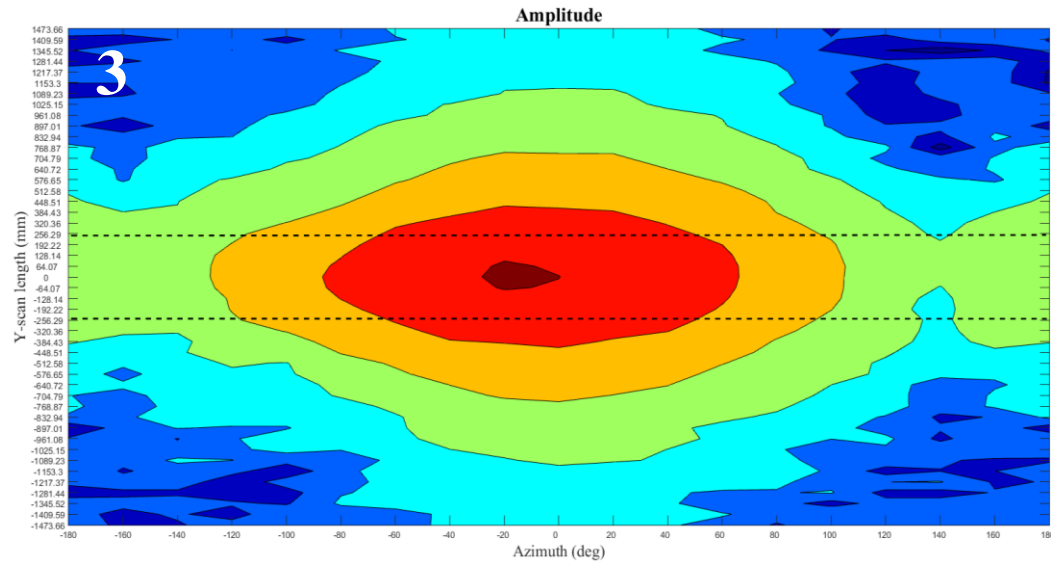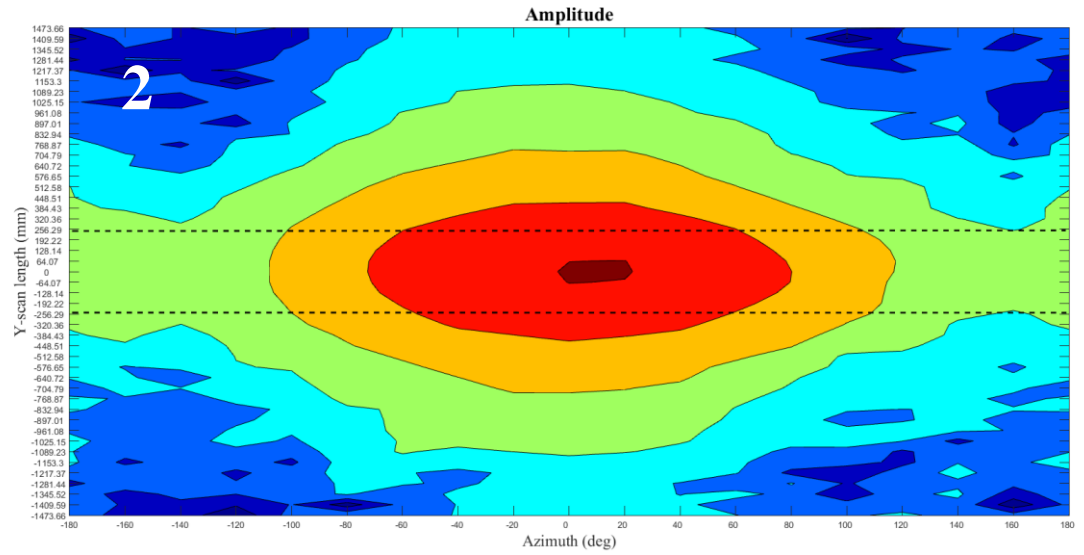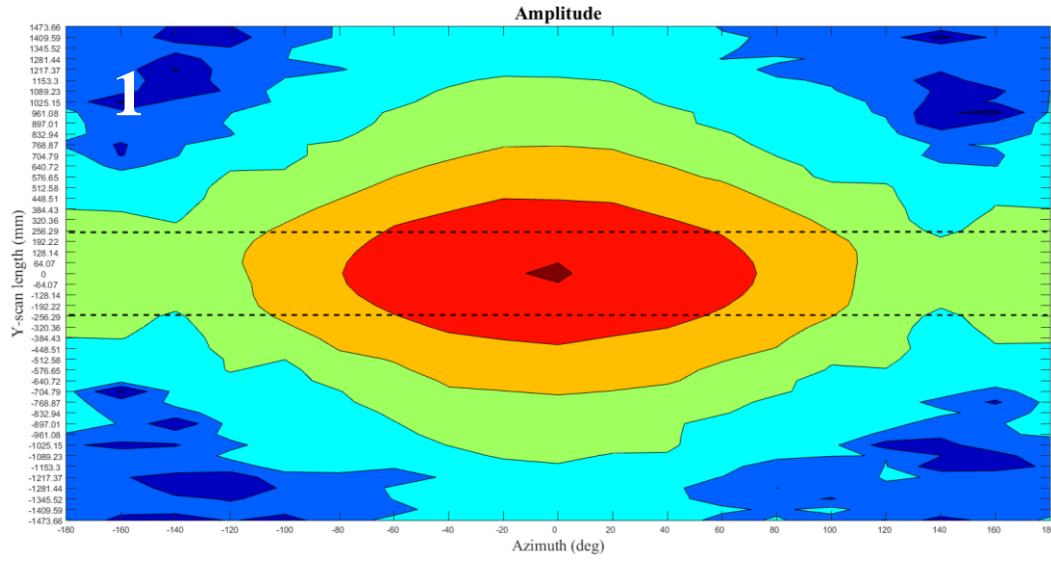
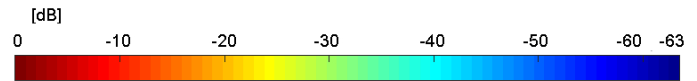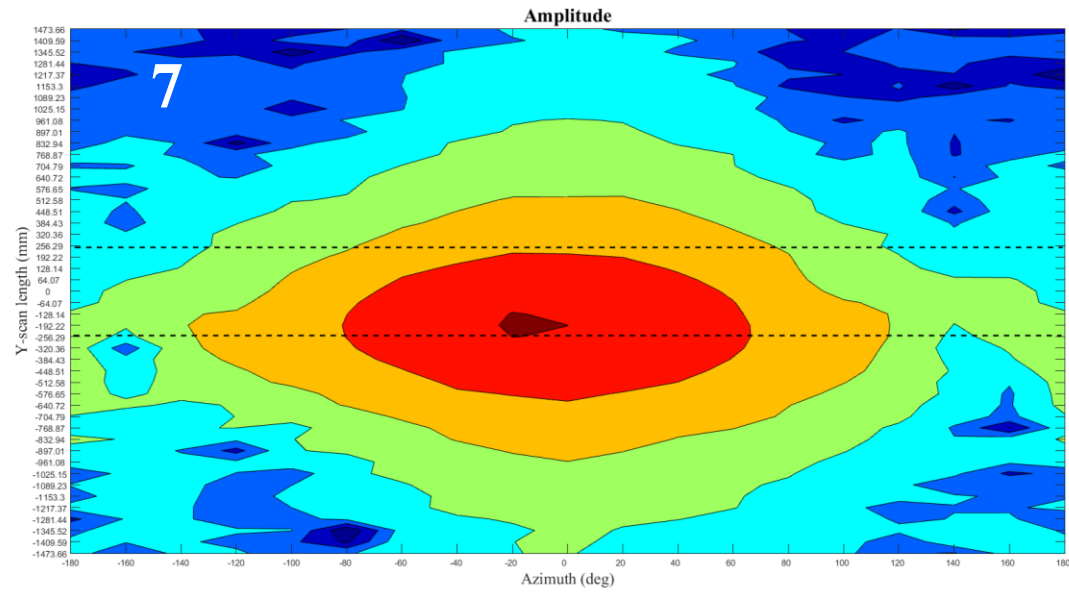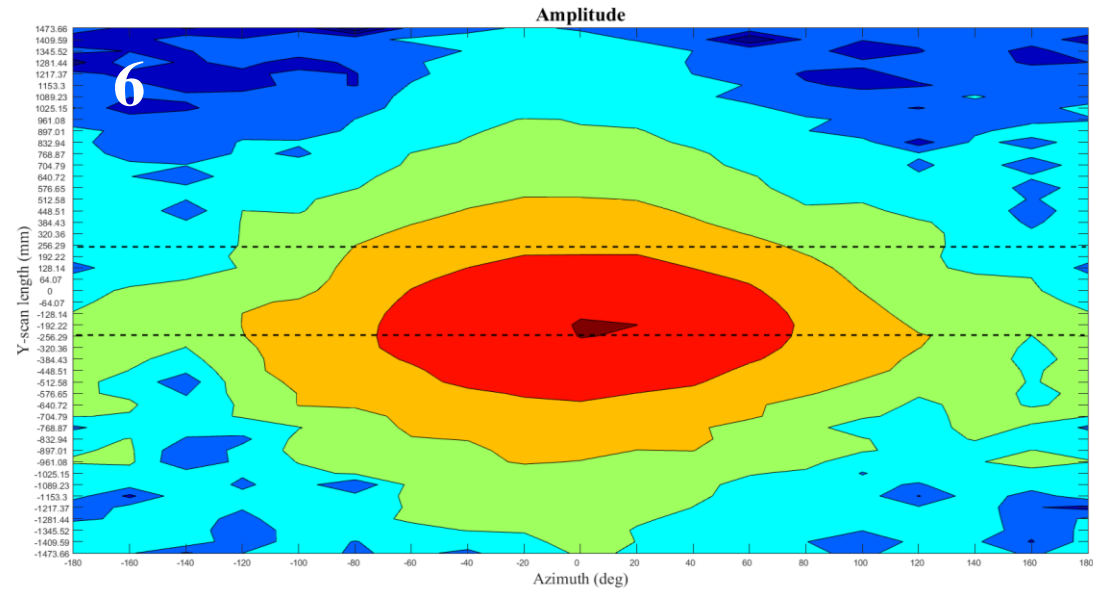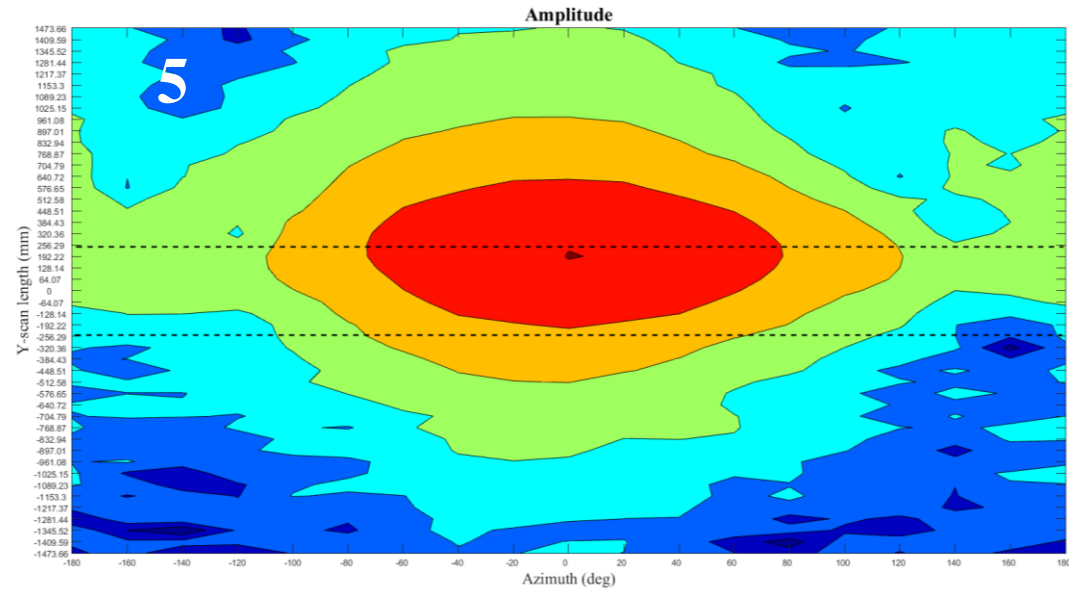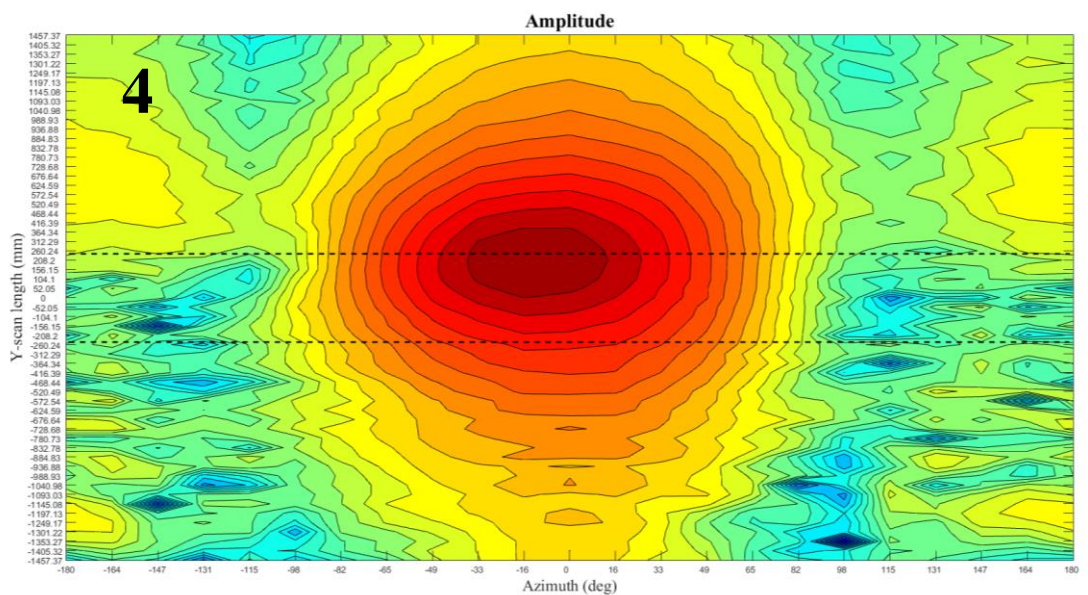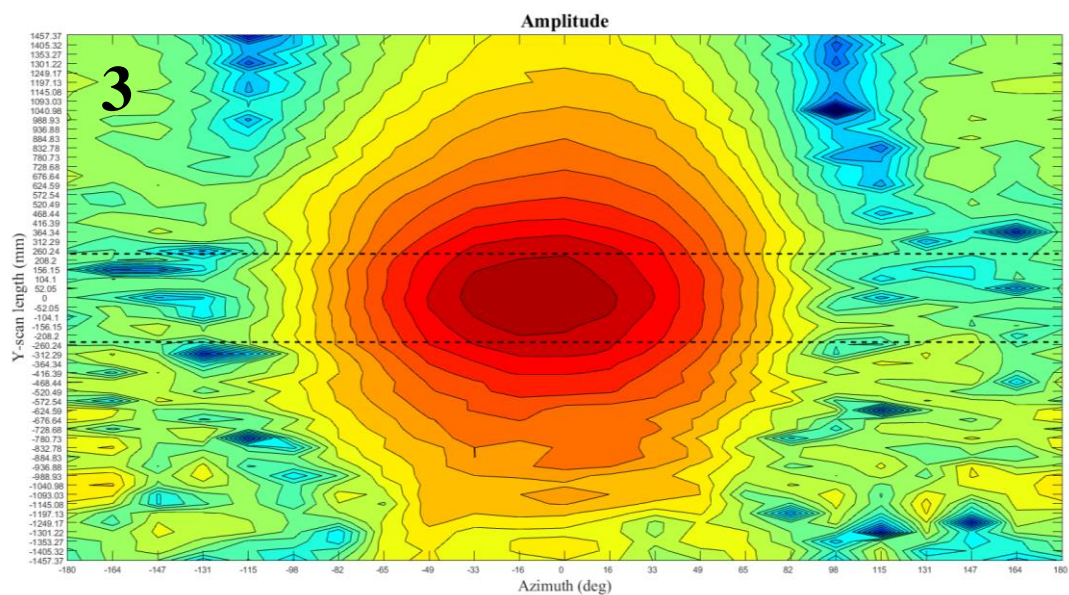**Fig. 3- 21 Measured near field amplitude horizontal component (A_H) for the 2GHz horizontal polarization scenario at all positions examined at f₀ = 1.987GHz**
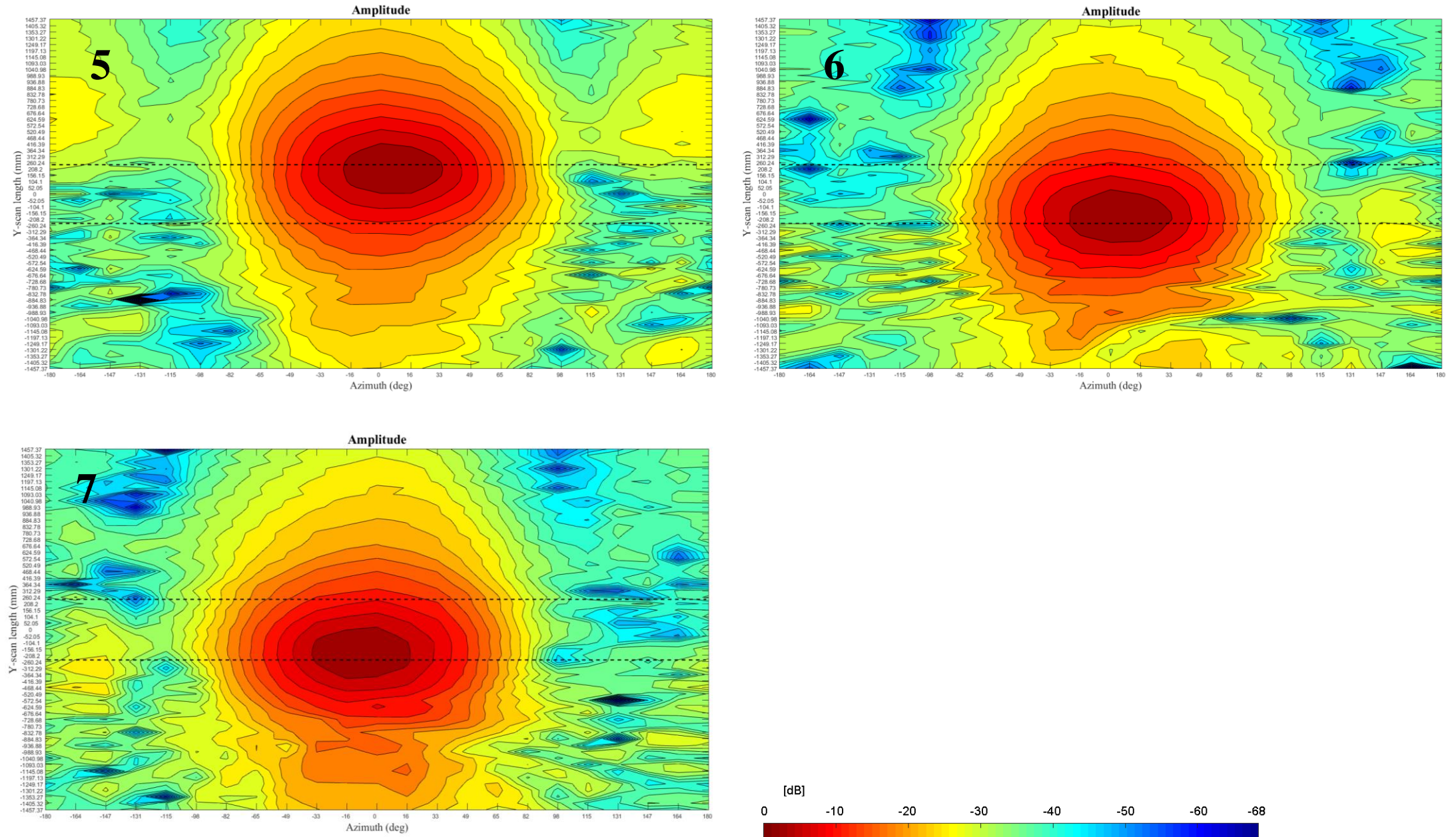
Fig. 3- 22 Measured near field amplitude vertical component (A$_V$) for the 2.5GHz vertical polarization scenario at all positions examined at f$_0$ = 2.485GHz
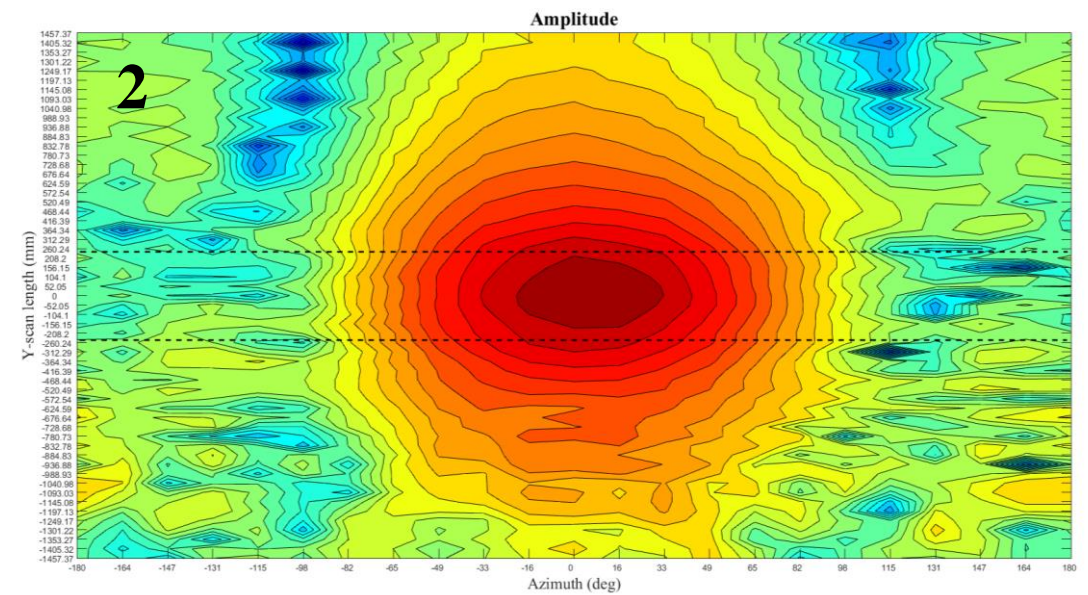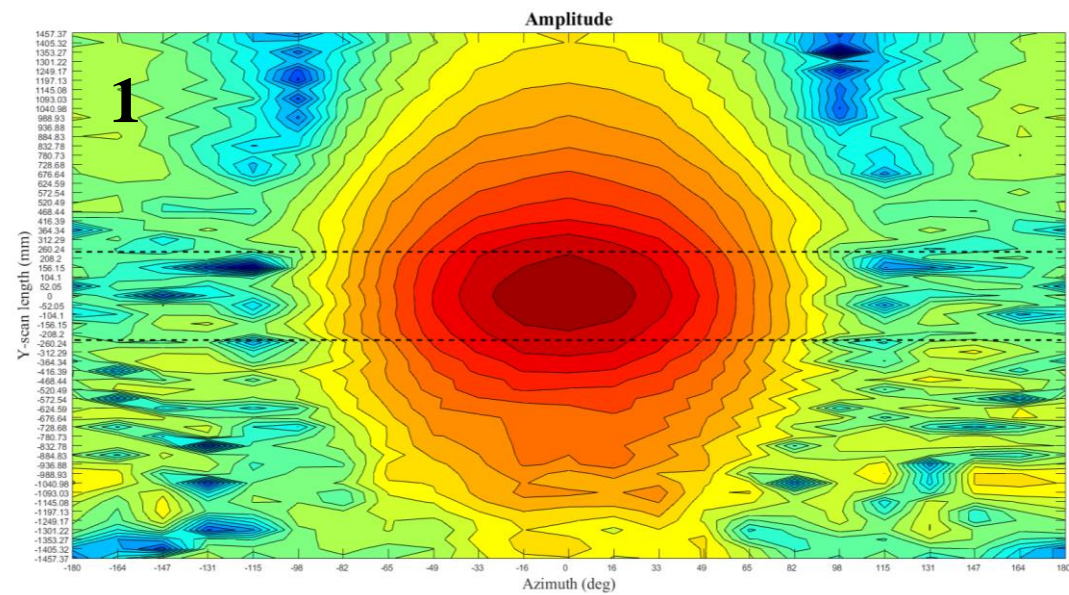
Fig. 3- 23 Measured near field amplitude horizontal component (A$_H$) for the 2.5GHz horizontal polarization scenario at all positions examined at f$_0$ = 2.485GHz

Fig. 3- 24 Measured near field amplitude vertical component (A$_V$) for the 5GHz vertical polarization scenario at all positions examined at f$_0$ = 4.965GHz

Fig. 3- 25 Measured near field amplitude horizontal component (A_H) for the 5GHz horizontal polarization scenario at all positions examined at f_0 = 4.965GHz

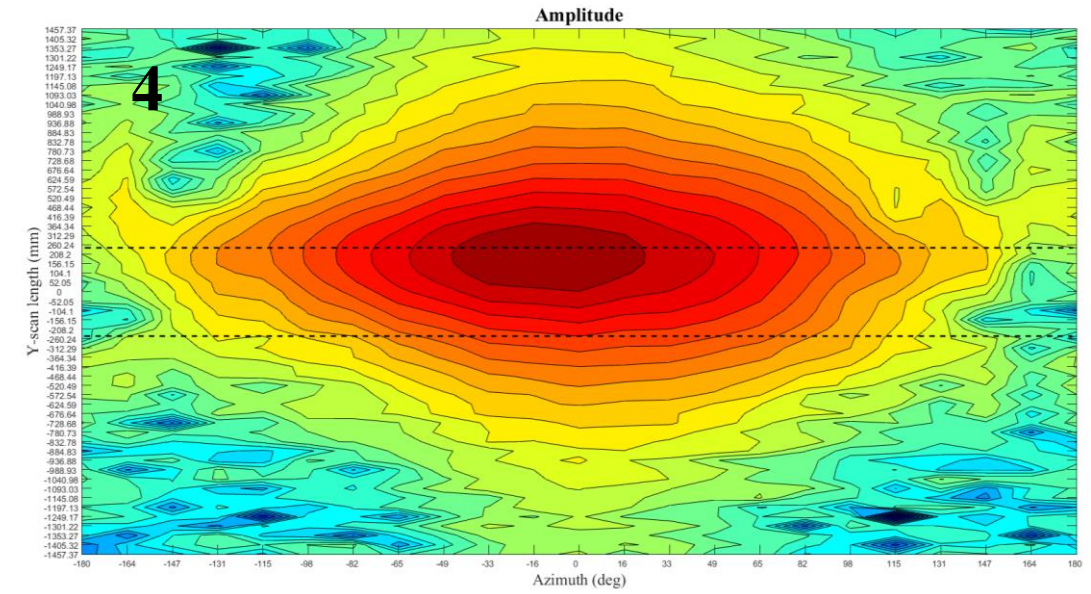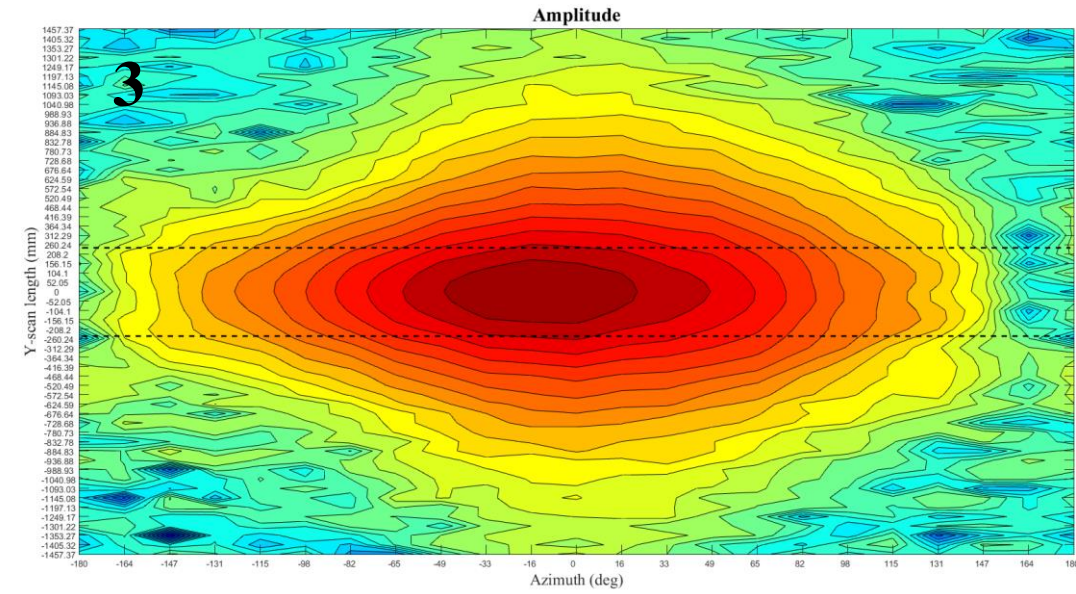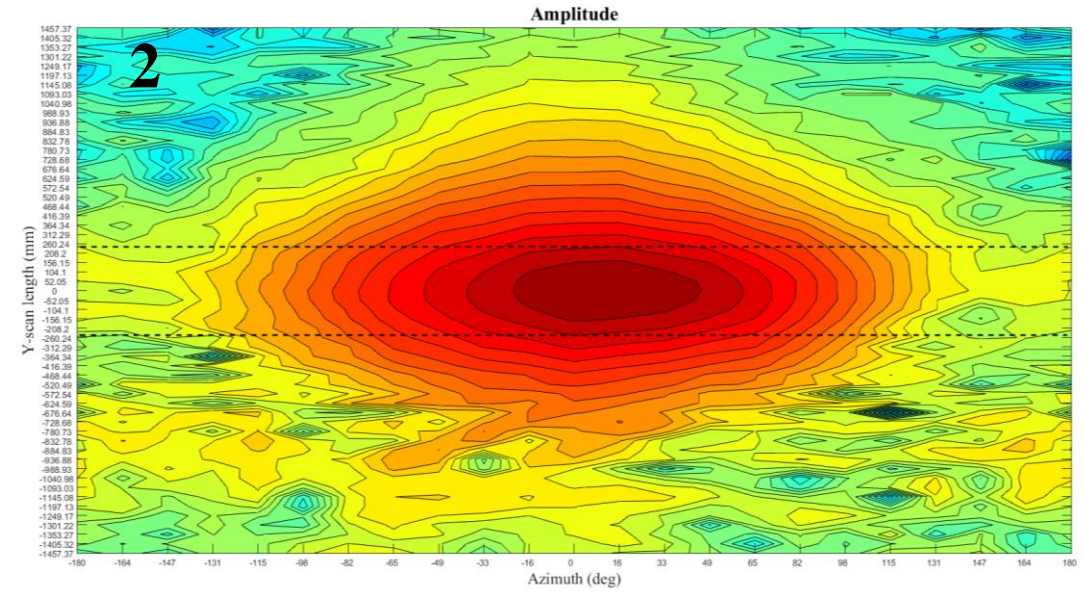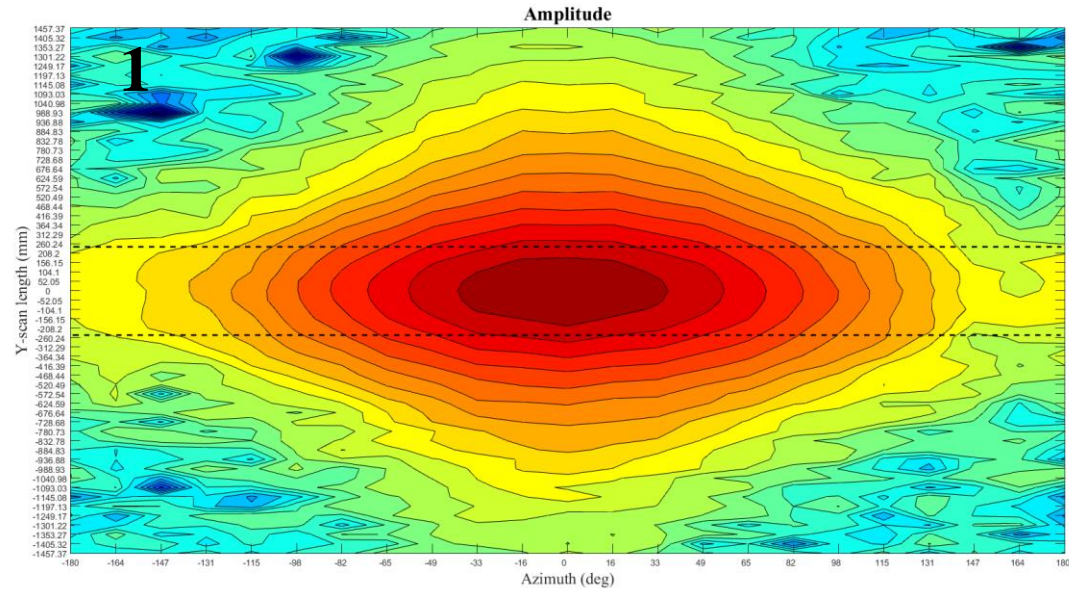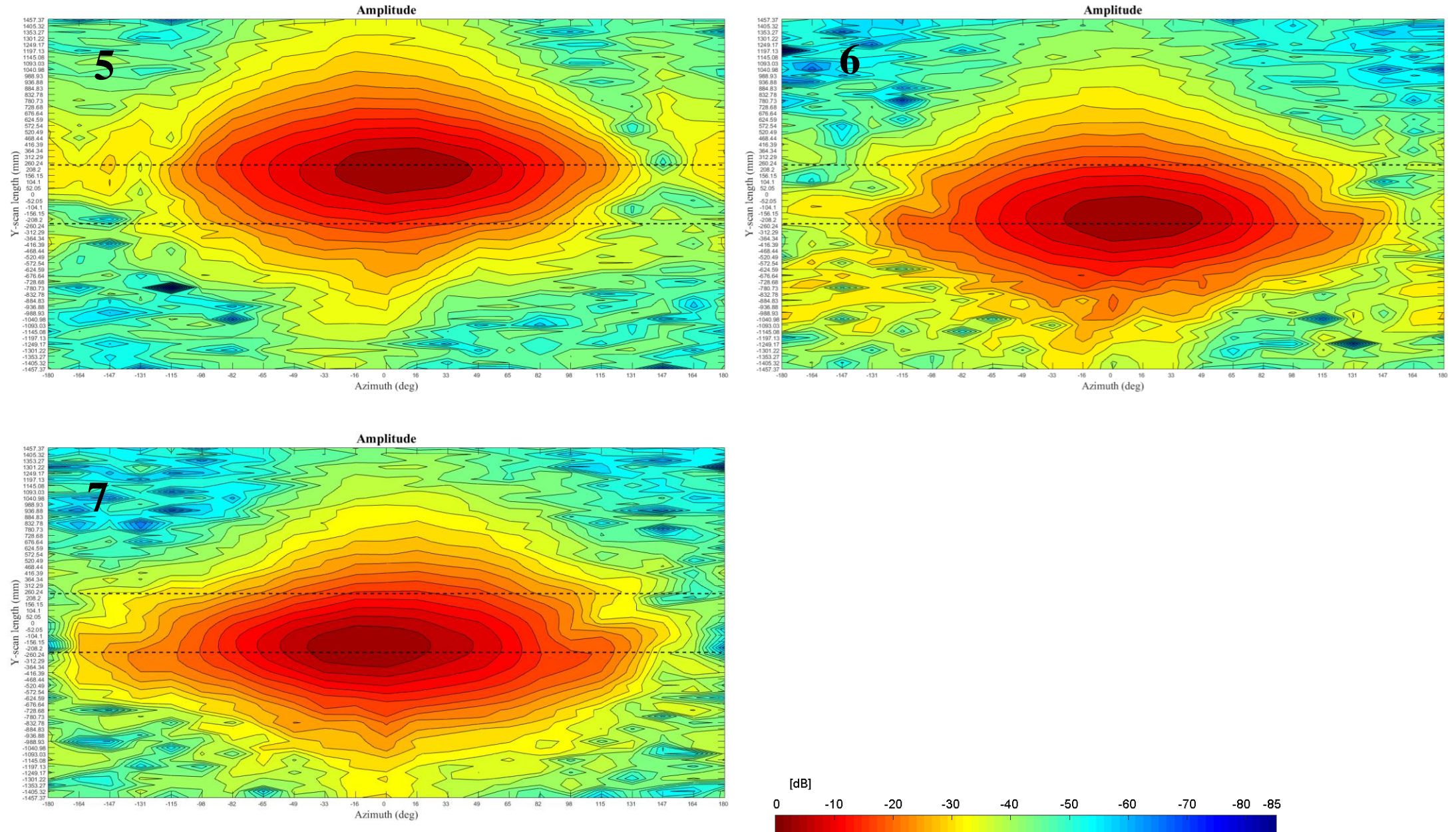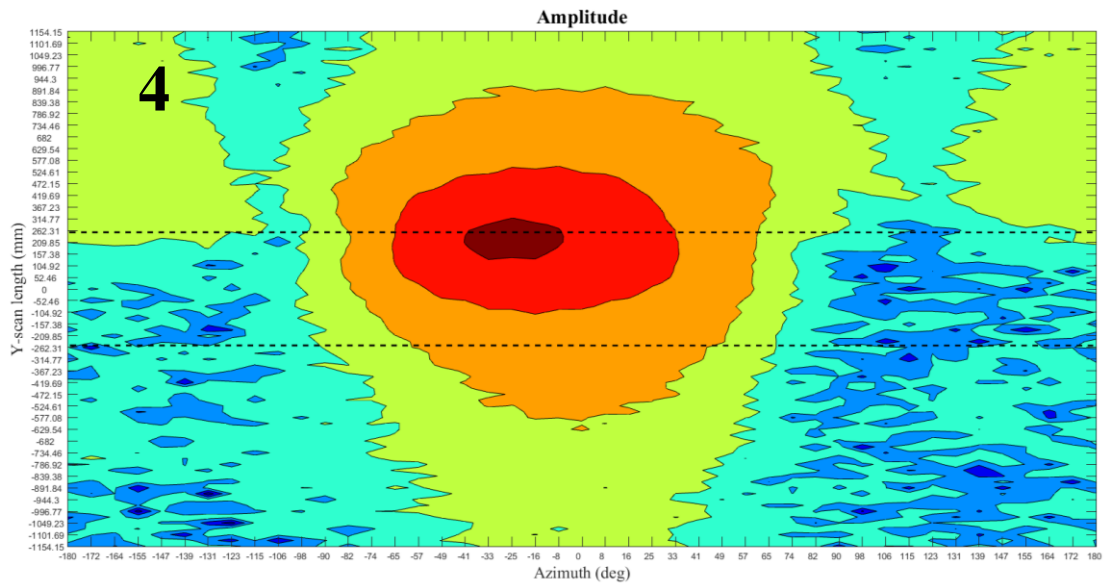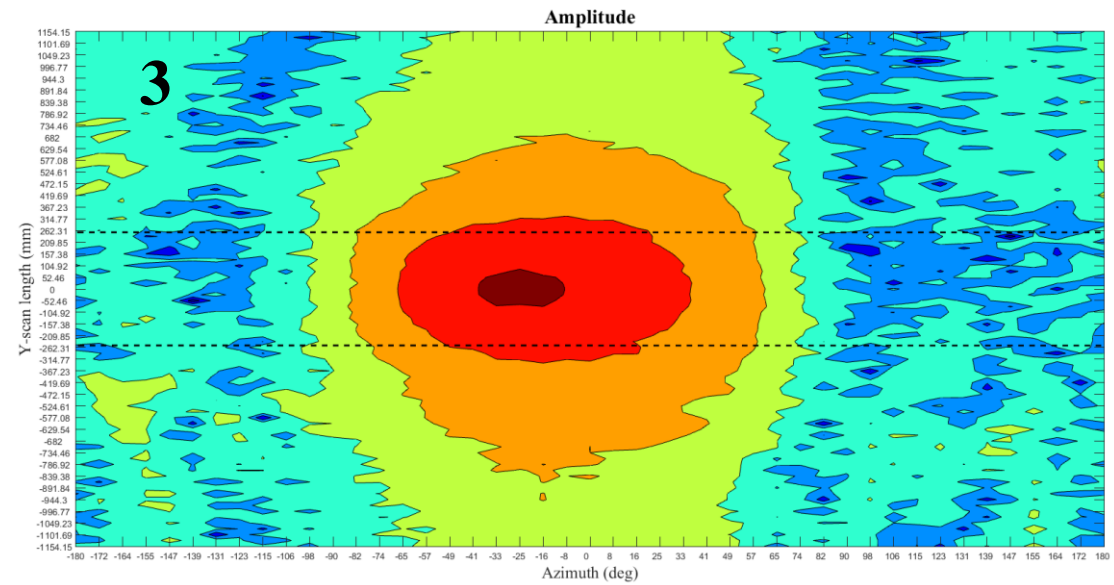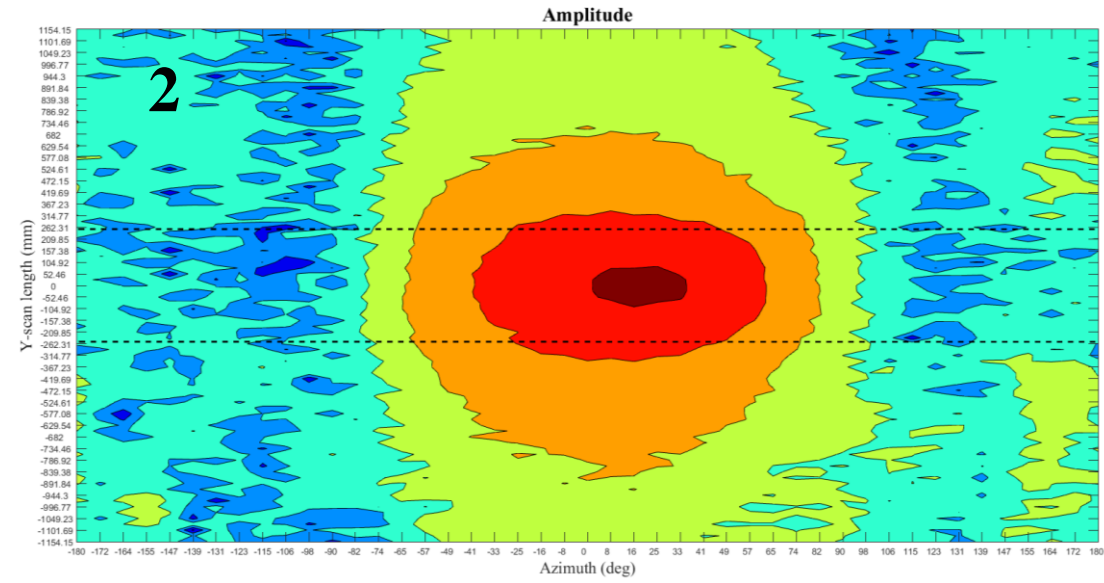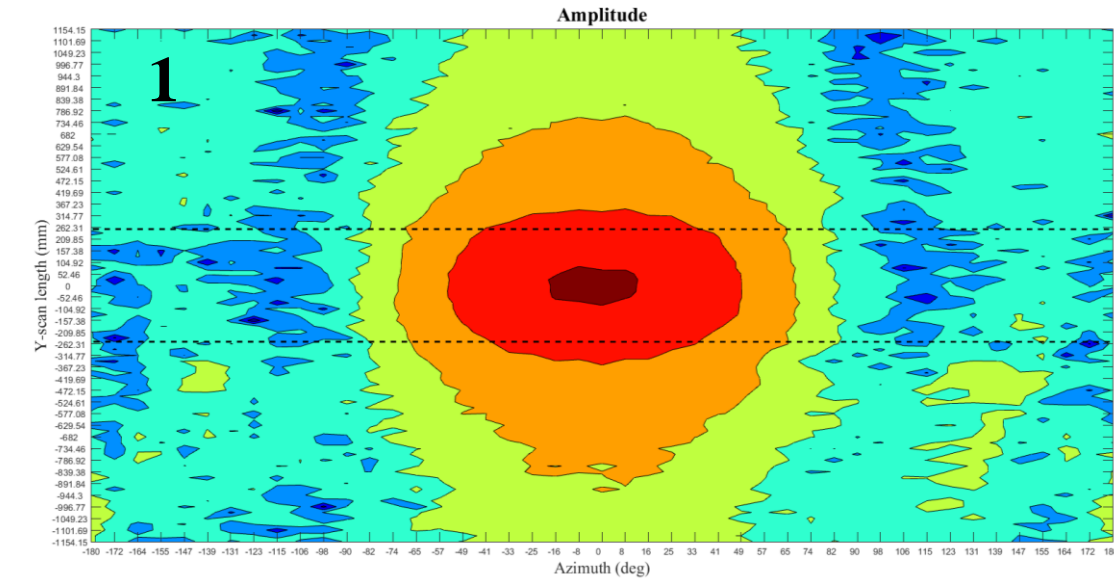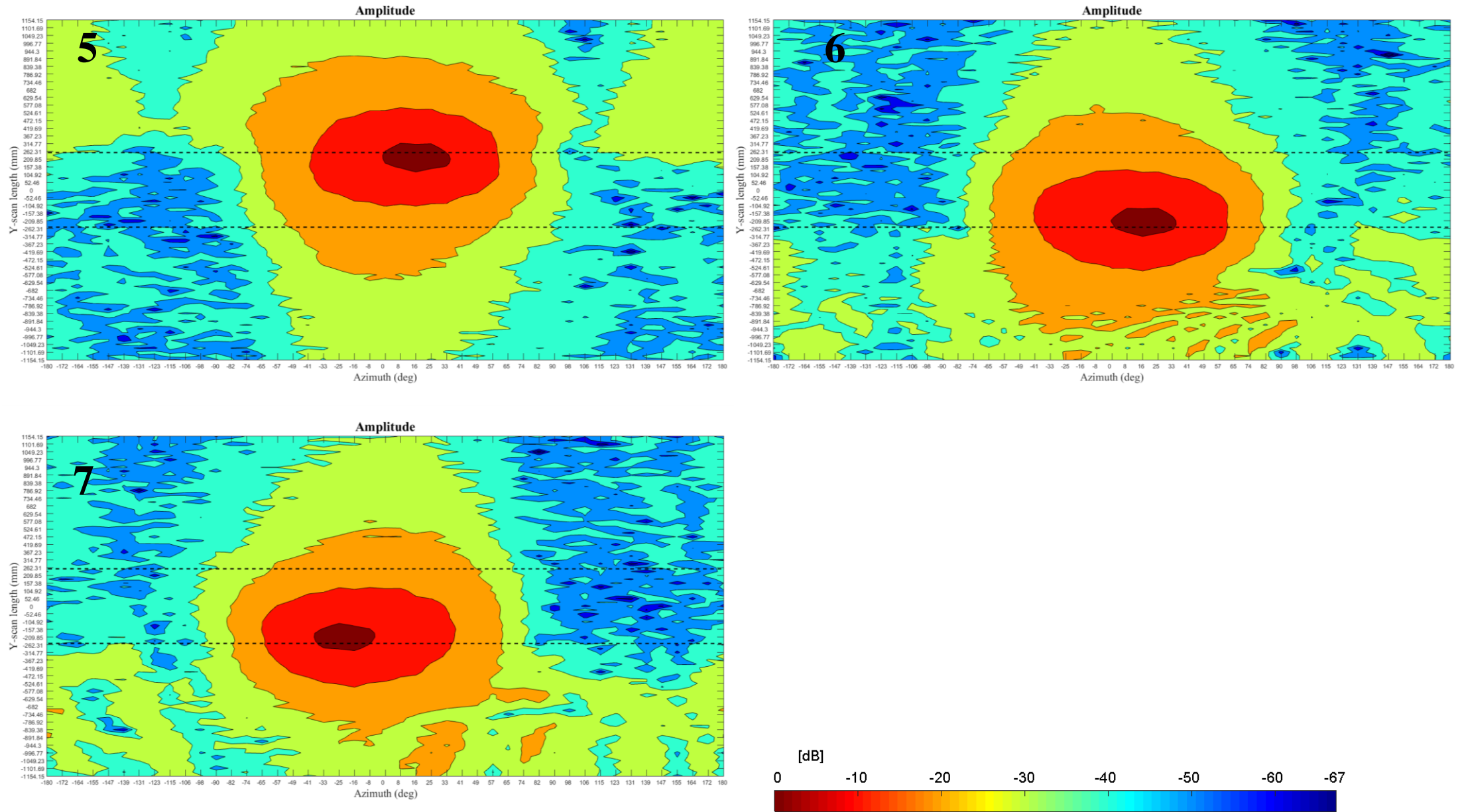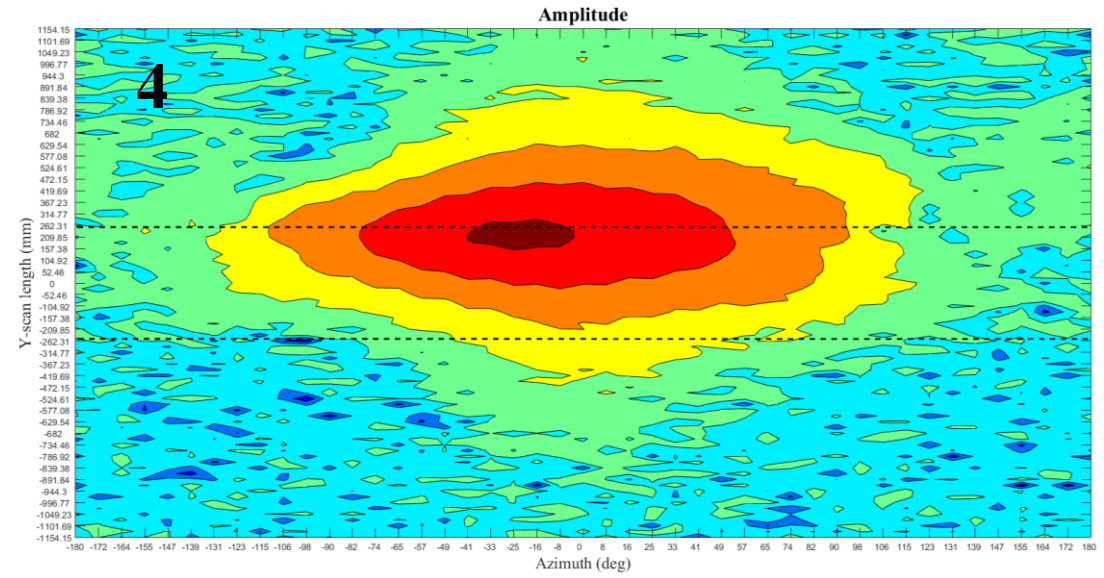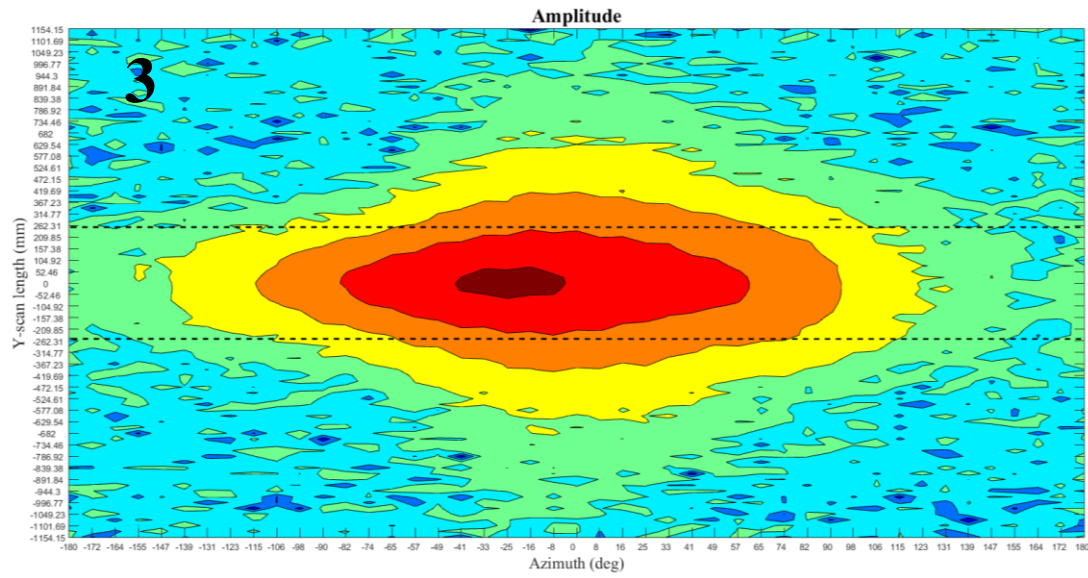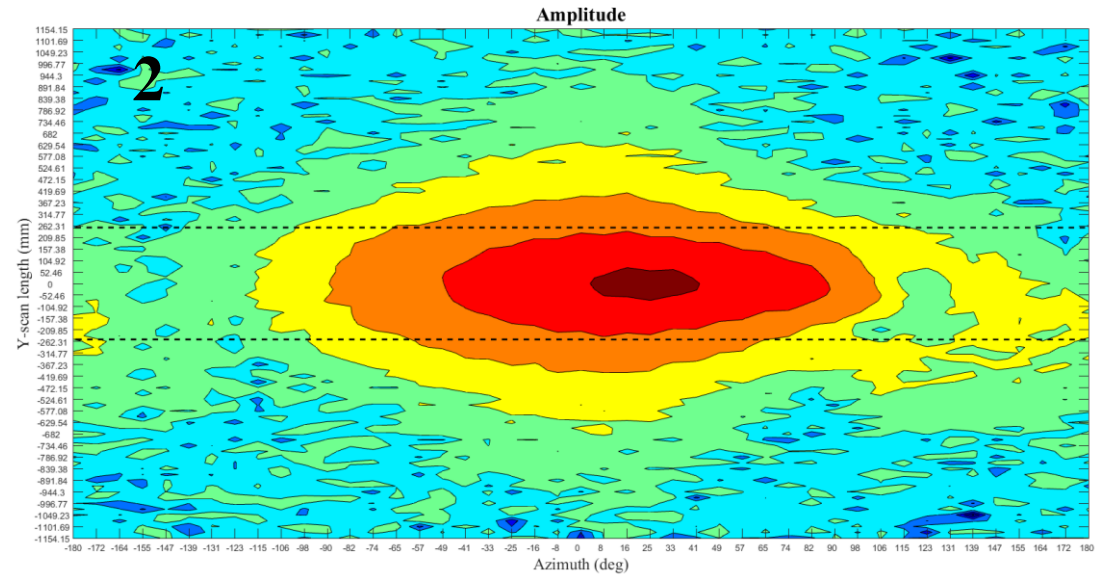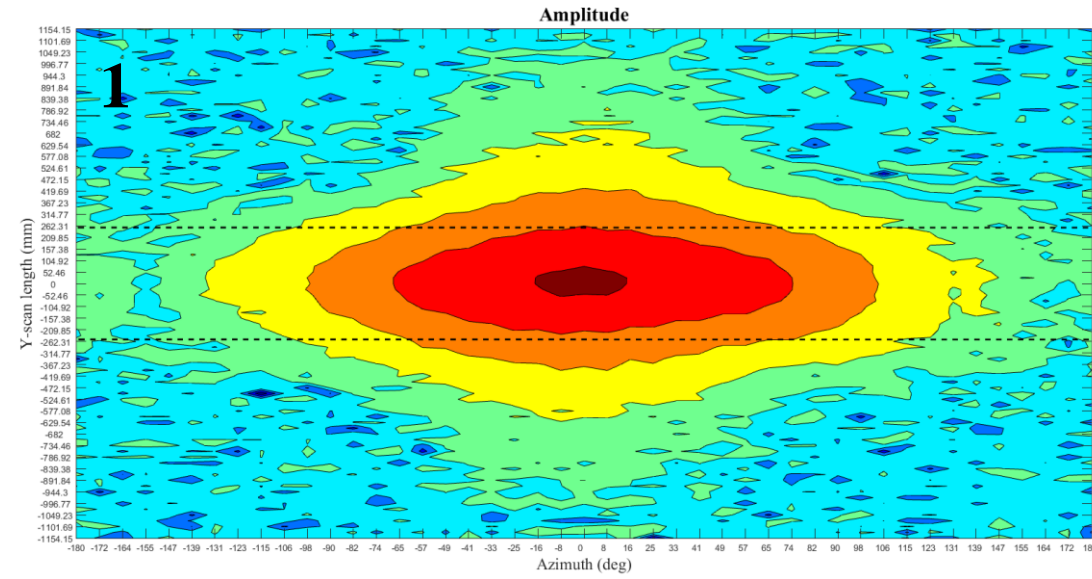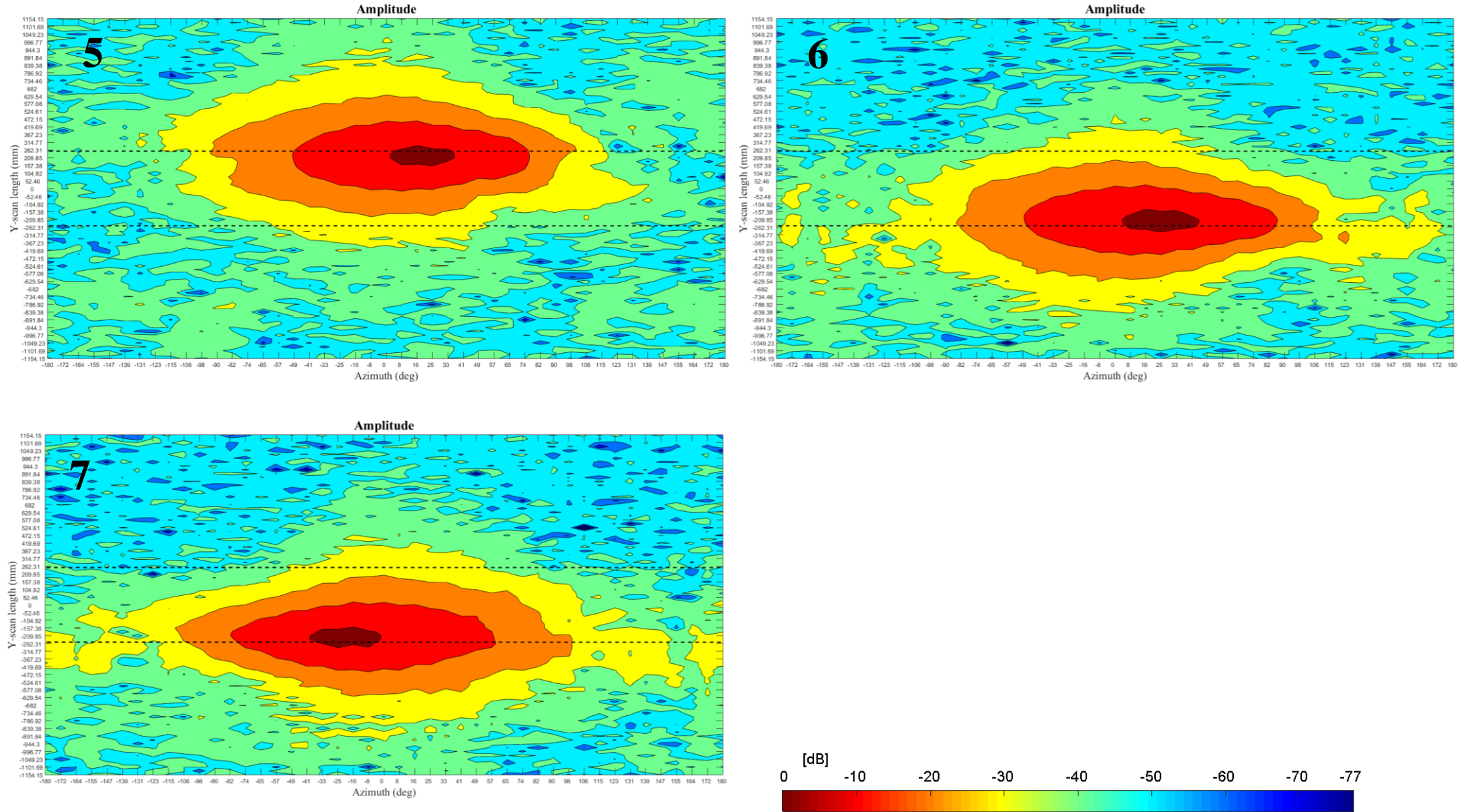From all near field contour plots for all frequencies examined it is noticed that the position of the maximum value of the image of the E-field (near field amplitude) and distribution were shifted depending on the wearable patch antenna on-HOCS phantom position. This is verified by the produced far field radiation patterns shown in the next subsection (3.4.2). This revealed that that the far field maximum radiation direction of the AUT will change and depend on the wearable patch antenna position. The position selection of the wearable patch antenna could determine the required main beam direction, each time.

Additionally, it is noticed that the horizontal polarization scenarios yielded near field amplitude distribution mainly around the HOCS phantom compared with the vertical scenario which yielded near field amplitude distribution mainly along the height of HOCS phantom. This is verified by the produced radiation patterns shown in the next subsection which yield wider beam in azimuth for the horizontal scenario compared with the vertical scenario and the opposite on the elevation plane. This means that the horizontal scenarios could cover more angles around HOCS phantom in terms of off-body communications. The vertical scenarios could better cover off-body links in front of HOCS phantom compared with the horizontal ones.

Additionally, the horizontal scenario seemed to yield a less directive near field amplitude distribution, than the vertical ones, as the E-field distribution is more concentrated at smaller volume (CNF) in the case of the vertical scenario compared with the horizontal one. This is verified by the far field results (subsection 3.4.2) shown in the next subsection which yield directivity higher in the cases of the vertical scenarios than the horizontal one.

Finally, it is obvious that the near field amplitude attenuated in shorter distance at high frequencies (5GHz) compared with lower frequencies (2GHz). For example if there was an application covering Wi-Fi (2.5/5GHz) for an off-body scenario and there was another electronic device, sensitive at both frequencies, mounted at the back side of the torso of a human body. Then in order to minimize the interference between the wearable antenna and this device, the 5GHz patch would be the best option as its near field amplitude attenuates "faster" and is more attenuated at the back side than the 2.5GHz one. Though, the trade-off for this option would be the reduced range link coverage by the 5GHz patch antenna compared to the 2.5GHz one, considering that there is a maximum allowed input power to be used for the wearable patch antennas. In order to justify the last point, assume the two scenarios of the wearable 2.5 and 5GHz patch antennas mounted in the middle of HOCS phantom (position 1-Fig. 3-18) communicating at the Off-body mode in the direct LOS with the free space respective patch antennas (Appendix B- 2.5 and 5GHz). The distance is

5meters and the input power for both cases is 0dbm. Then by applying the gain values from the next subsection (3.4.2) and from Appendix B into Friis-equation, the 2.5GHz and the 5GHz received powers are -39dBm and -45dBm respectively. The reduced received power in the case of the 5GHz compared with the 2.5GHz justifies the reduced link coverage.

3.4.2 Far field parameters results produced from near field measurements

3.4.2.1 Radiation patterns

As previously yielded (NF results), it is expected, that the direction of maximum radiation, in terms of far field, will change by wearable patch antenna position on HOCS phantom. More specifically for positions 1, 2 and 3 it is expected, from the near field results of the vertical polarization scenarios, that the maximum direction and the radiation patterns will be shifted especially on the azimuth plane. These expectations were verified from the normalized co-polar components of the far field radiation patterns for all AUTs examined (2; 2.5 and 5GHz). The orientation of the HOCS phantom in the radiation patterns is depicted in Fig. 3-26. The co-polar components of the radiation patterns are shown in Fig. 3-27, 3-28 and 3-29. Additionally, the unavoidable truncation error due to lack of sampling over and under the AUT on the elevation plane and the not definition of Hankel functions (which are used for the NFtoFF transform so as to produce the radiation patterns) at phi=90° and 270° can be seen at the radiation patterns where on the elevation planes there are abrupt nulls at 90° and 270°, the angles above and below the AUT. These nulls are not realistic and they occur due to truncation error (3.2.1.10). This phenomenon is a weakness of the CNF measurement
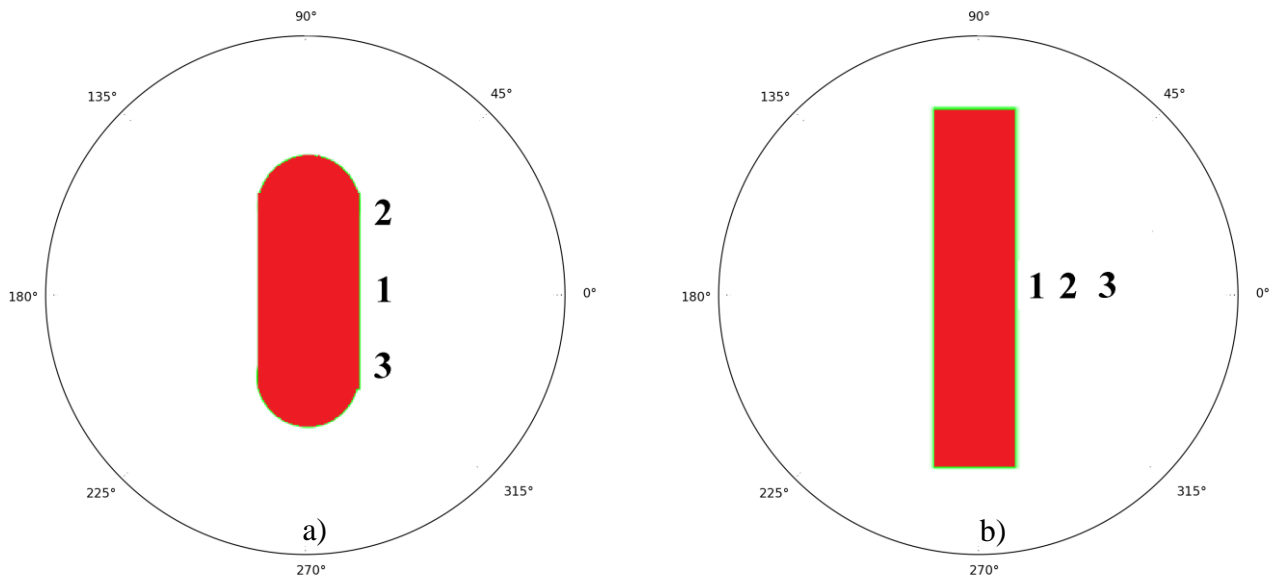
Fig. 3- 26 HOCS phantom orientation in the radiation patterns:
a) Azimuth and b) Elevation
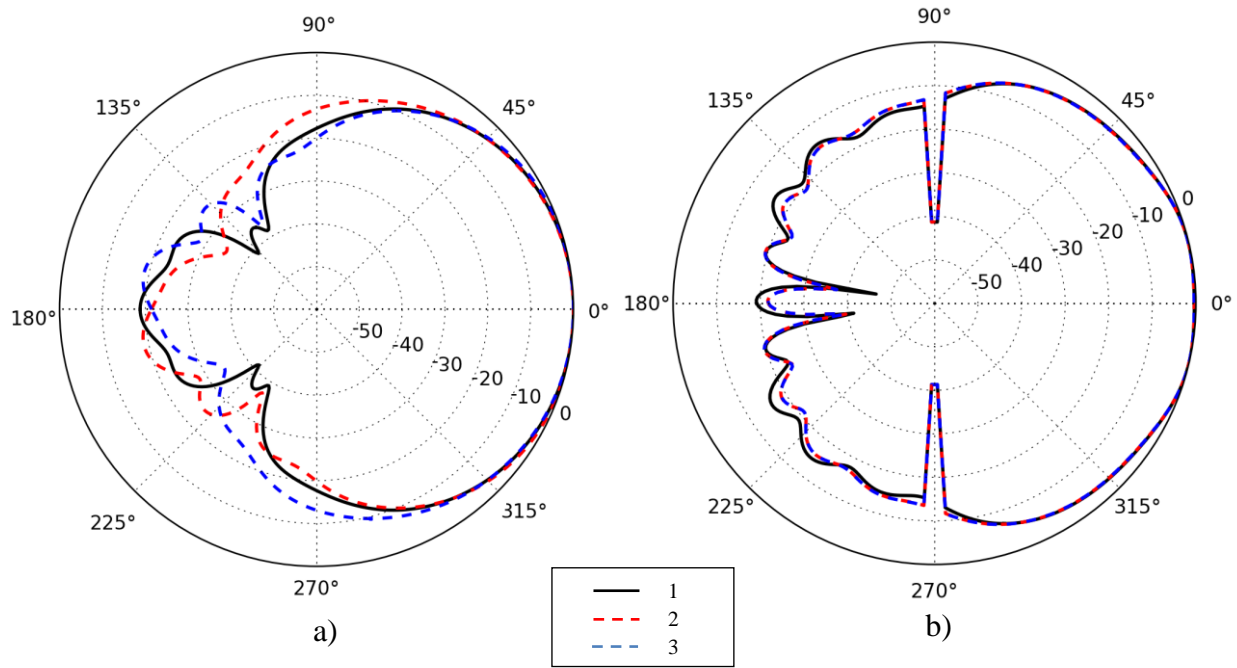
Fig. 3- 27 Measured (transformed) normalized radiation patterns (co-polar components) of vertically polarized 2GHz (f_0=1.987GHz) AUT for 1,2 and 3 wearable patch antenna positions on HOCS phantom at : a) Azimuth, b) Elevation planes
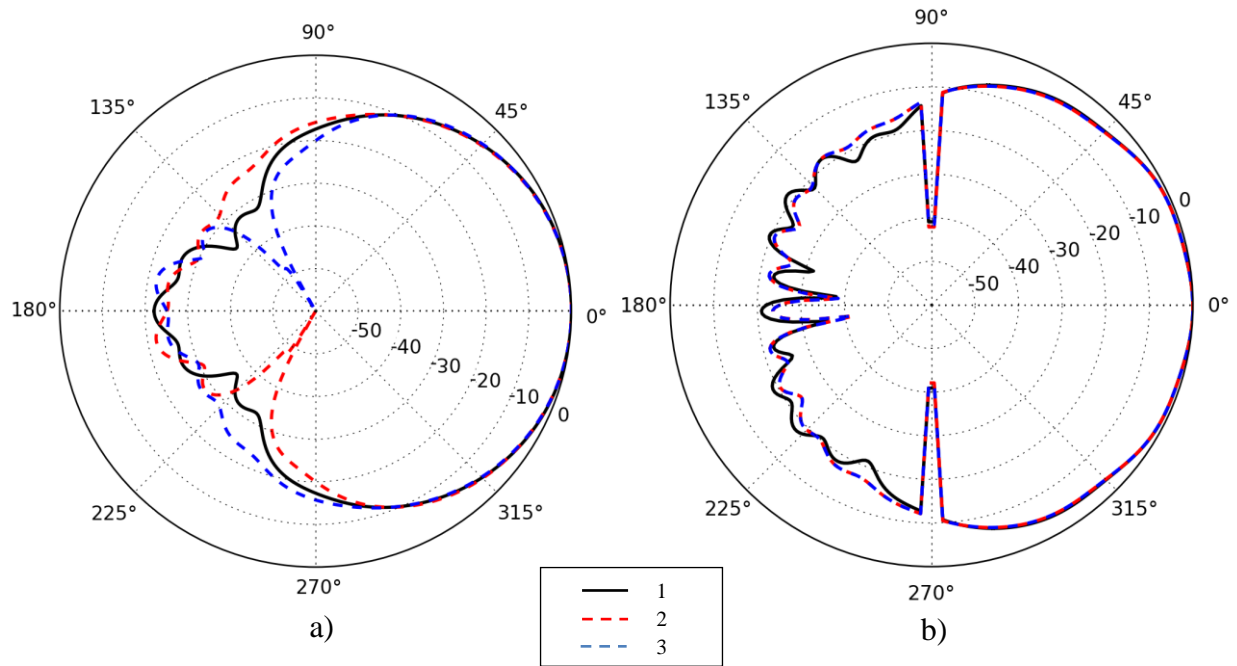
Fig. 3- 28 Measured (transformed) normalized radiation patterns (co-polar components) of vertically polarized 2.5GHz (f_0=2.485GHz) AUT for 1,2 and 3 wearable patch antenna positions on HOCS phantom at : a) Azimuth, b) Elevation planes

Fig. 3- 29 Measured (transformed) normalized radiation patterns (co-polar components) of vertically polarized 5GHz (f$_0$=4.965GHz) AUT for 1,2 and 3 wearable patch antenna positions on HOCS phantom at : a) Azimuth, b) Elevation planes

As previously referred the horizontal polarization scenarios are expected to yield a wider main radiation beam on the azimuth plane and narrower on the elevation plane compared with the vertical scenarios. These expectations are verified by the normalized co-polar components of the far field radiations patterns. The far field radiation patterns comparing vertical and horizontal scenarios for all patch antennas at position 1 are shown in Fig. 3-30, 3-31 and 3-32.
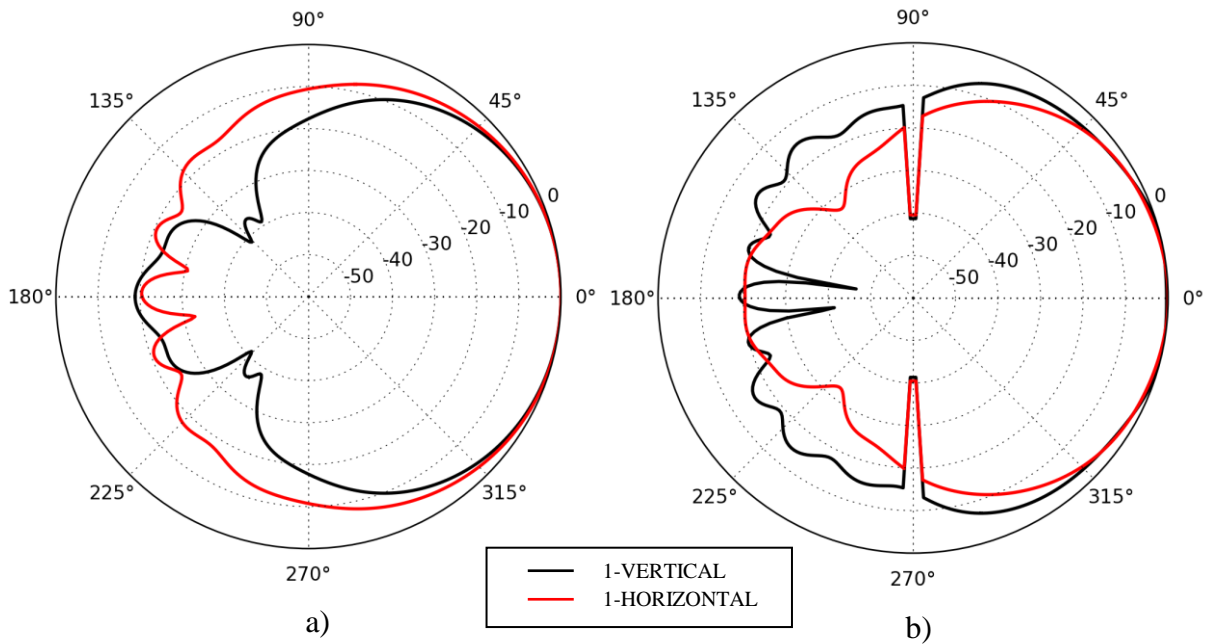
Fig. 3- 30 Measured (transformed) normalized radiation patterns (co-polar components) of 2GHz (f$_0$=1.987GHz) AUT at wearable patch antenna position 1 on HOCS phantom for Vertical and Horizontal polarizations at: a) Azimuth, b) Elevation planes
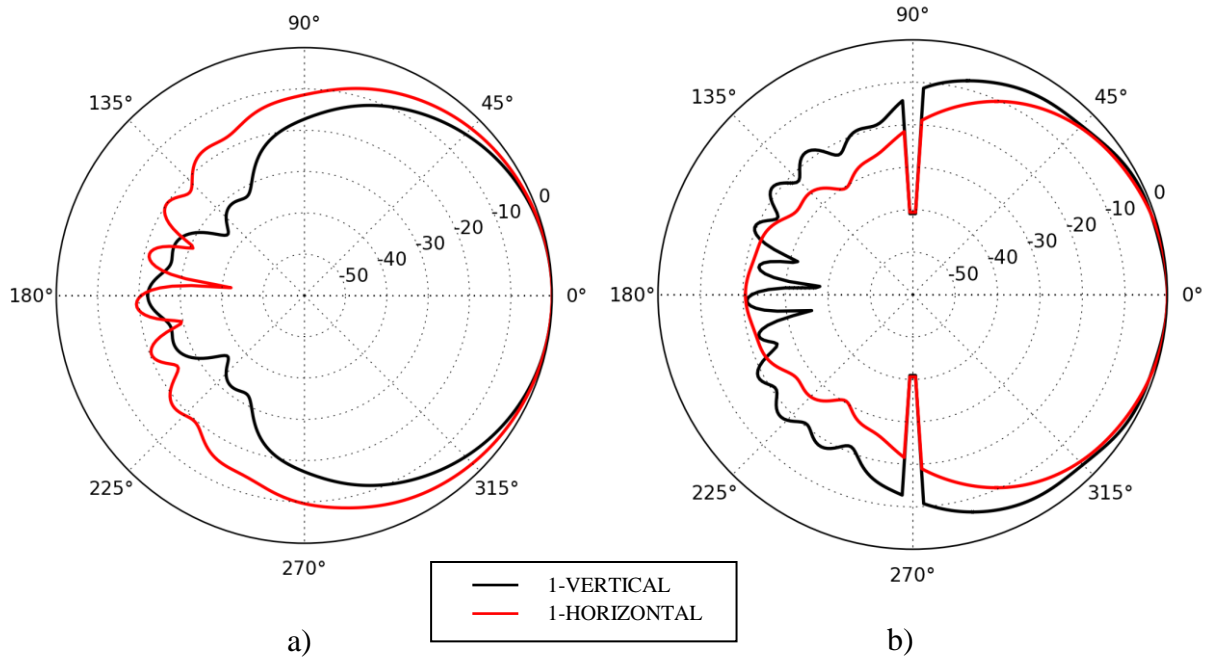
Fig. 3- 31 Measured (transformed) normalized radiation patterns (co-polar components) of 2.5GHz (f_0=2.495GHz) AUT at wearable patch antenna position 1 on HOCS phantom for Vertical and Horizontal polarizations at: a) Azimuth, b) Elevation planes

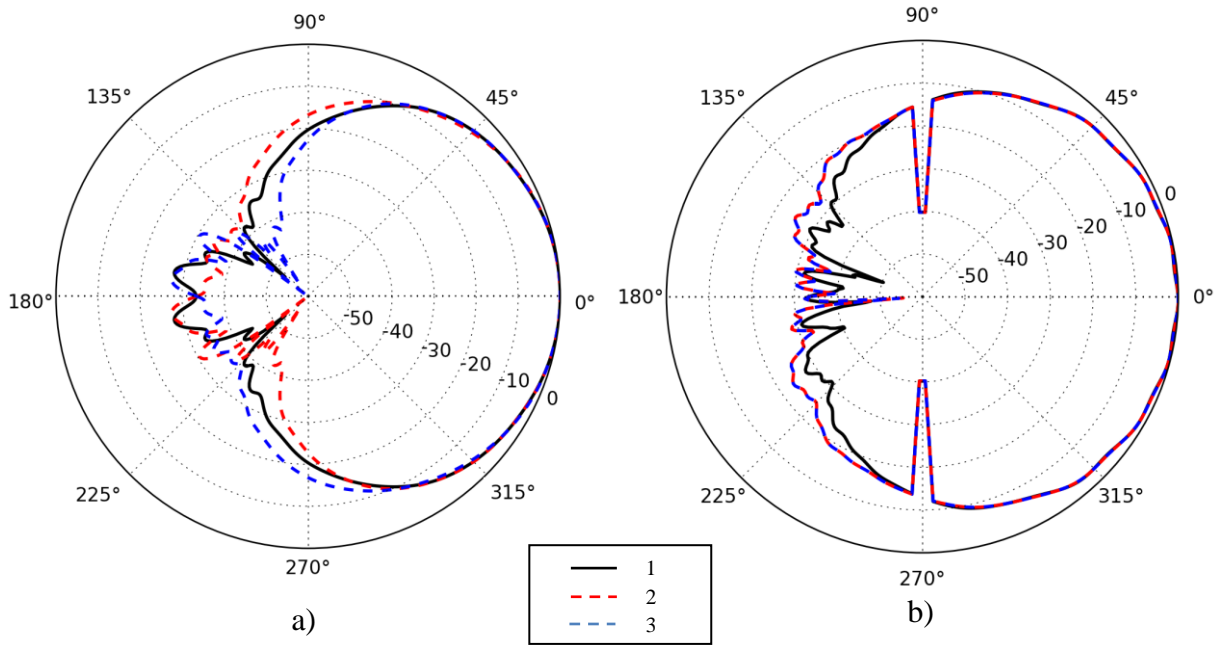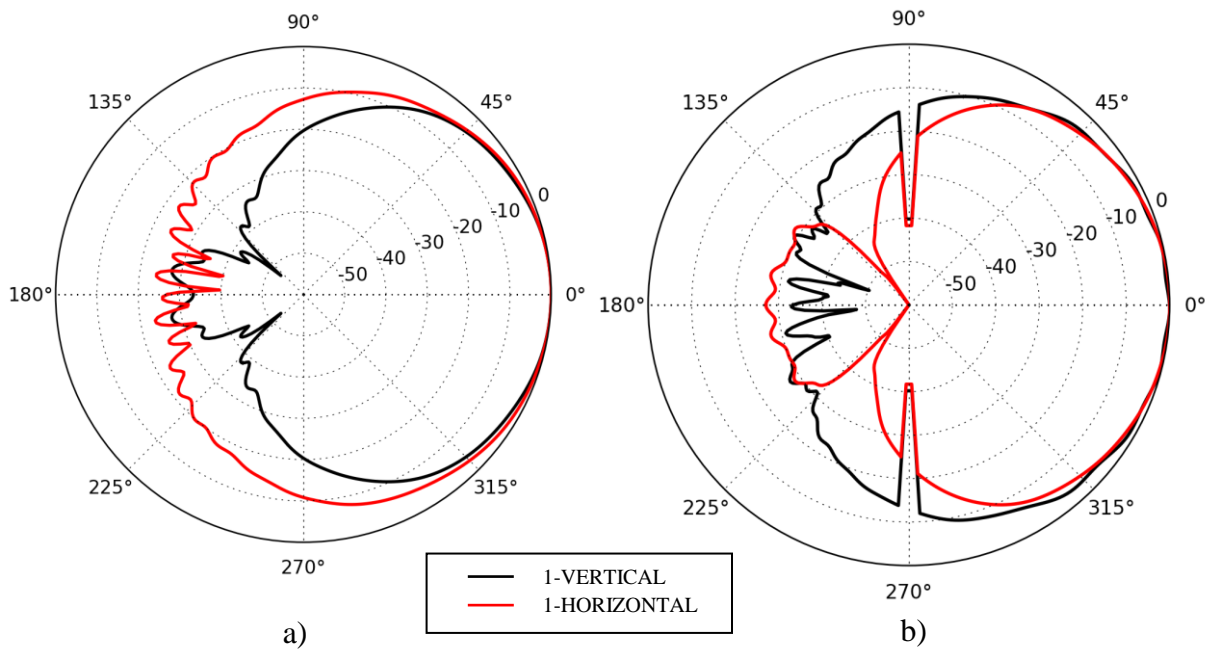**Fig. 3- 32 Measured (transformed) normalized radiation patterns (co-polar components) of 5GHz (f_0=4.965GHz) AUT at wearable patch antenna position 1 on HOCS phantom for Vertical and Horizontal polarizations at: a) Azimuth, b) Elevation planes**

3.4.2.2 Far field parameters

The derived far field parameters (gain, directivity and efficiency) from the CNF measurements, shown in previous subsection (3.4.1), for the 2; 2.5 and 5GHz cases for all HOCS phantom positions and for both polarizations, at their respective resonance frequencies (1.987GHz, 2.485GHz and 4.965GHz) are shown in Tables 3-13, 3-14 and 3-15.

From all the frequencies examined (2; 2.5 and 5GHz) it is clear that the variation of the wearable patch antenna position on HOCS phantom did not significantly changed the far field parameters. The far field radiation characteristic which changed was the direction of the maximum directivity and gain (power radiated) depending on the position, as shown in previous sub subsection (3.4.2.1). This means that the Off-body link budget for each frequency examined will differ only in the direction of maximum power radiated. Additionally, it must be noticed that the horizontal polarization scenarios yielded a lower directivity (as assumed from near field results, "less directive", sub subsection 3.4.1.2, p. 3-56) and a lower gain, for most positions, AUT compared with the vertical scenarios. In terms of practical off-body wearable antenna use, depending on the off-body receiver polarization the respective wearable antenna polarization must be selected, so as to avoid polarization losses [46].

Table 3- 13 Far field parameters derived (produced) from CNF measurements, for AUT = HOCS + 2GHZ patch antenna, for positions 1 up to 7 at f_0 = 1.987GHz

Position	Gain (dBi)		Directivity (dBi)		Efficiency (%)	
	Vertical	*Horizontal*	*Vertical*	*Horizontal*	*Vertical*	*Horizontal*
1	6.38	6.13	8.28	7.75	64.56	68.86
2	6.01	6.00	7.92	7.64	64.41	68.54
3	6.05	5.95	7.97	7.61	64.26	68.23
4	6.18	5.75	7.98	7.33	66.06	69.50
5	6.27	5.85	8.01	7.52	66.98	68.07
6	6.16	5.91	7.99	7.60	65.61	67.76
7	6.35	5.91	8.18	7.59	65.61	67.92

Table 3- 14 Far field parameters derived (produced) from CNF measurements, for AUT = HOCS + 2.5GHZ patch antenna, for positions 1 up to 7 at f_0 = 2.485GHz

Position	Gain (dBi)		Directivity (dBi)		Efficiency (%)	
	Vertical	*Horizontal*	*Vertical*	*Horizontal*	*Vertical*	*Horizontal*
1	6.78	6.51	8.45	7.82	68.07	73.96
2	6.96	6.34	8.61	7.62	68.39	74.47
3	6.94	6.25	8.59	7.59	68.39	73.45
4	6.82	6.40	8.39	7.70	69.66	74.13
5	6.92	6.60	8.47	7.89	69.98	74.30
6	7.60	6.55	9.19	7.82	69.34	74.64
7	7.09	6.46	8.66	7.80	69.66	73.45

Table 3- 15 Far field parameters derived (produced) from CNF measurements, for AUT = HOCS + 5GHZ patch antenna, for positions 1 up to 7 at f_0 = 4.965GHz

Position	Gain (dBi)		Directivity (dBi)		Efficiency (%)	
	Vertical	*Horizontal*	*Vertical*	*Horizontal*	*Vertical*	*Horizontal*
1	7.26	7.12	8.59	8.36	73.62	75.16
2	7.57	6.56	9.06	8.04	70.95	71.12
3	7.14	6.50	8.77	8.03	68.70	70.30
4	7.32	6.60	8.78	8.03	71.44	71.94
5	7.51	6.62	8.87	8.19	73.11	69.66
6	7.68	6.78	9.04	8.18	73.11	72.44
7	7.37	6.77	8.83	8.22	71.44	71.61

In conclusion from this section, the new methodology for evaluating wearable patch antennas performance for Off-body communication link, by using the CNF measurement technique, has been extensively described. The near field amplitude contour plots derived from the CNF measurement results, for all antennas and polarization scenarios examined, provide information and lead to assumptions about how the AUT = HOCS + wearable patch antenna radiates, including maximum direction of radiation, which geometrical plane yielded wider beam, which scenario yielded more or less directive beam. The radiation information was derived by the radiation patterns produced from NFtoFF transformation, verifying the assumptions about the radiation of the AUT. Additionally, the far field parameters (gain, directivity and efficiency) were derived from the near field results, verifying the assumptions

about the directivity of the AUT and characterizing by this way the off-body operation of the examined AUTs.

Finally, for the specific patch antennas polarization scenarios examined it can be concluded that: *the horizontal polarization scenarios could cover more angles around HOCS phantom in terms of off-body communications with the decreased AUT gain trade-off at most positions. The vertical scenarios could cover off-body links in front of HOCS phantom compared with the horizontal ones.*

3.5 Conclusions

This chapter presented a new methodology, which exploits the cylindrical near field measurement technique in order to evaluate wearable antennas performance parameters. Three patch antennas operating at 2; 2.5 and 5GHz were used. Main advantage of this methodology was that less physical space is required, compared to a far field test site and the use of a heavy duty roll axis, so as to rotate the phantom for 3D pattern coverage is excluded (this is a lab requirement) compared to a conventional spherical near field test site. These advantages could significantly reduce the cost and the complexity of the measurement.

The geometry of HOCS torso phantom in a cylindrical near field (CNF) test site has been introduced. Limitations and risks of finding an optimum cylindrical volume (*measurement CNF volume which would result into transformed far field parameters as accurately as possible (closest) to the simulation far field parameters*) for the near field measurements were notified, alarming the need for evaluating the CNF test site, so as to define an optimum volume. Subsequently an evaluation technique, which was targeted for the CNF test site, appropriate for wearable antenna measurements mounted on HOCS phantom, was proposed. The goal of the evaluation technique was to find the optimum CNF measurement volume which would result into transformed far field parameters which will be closest to the simulation far field results. Additionally, the evaluation technique could be described as being an attempt to get the measurement system (CNF) measuring as accurately as possible. The evaluation technique used a 2mm thick ConDucting Plate (CDP) whose dimensions (height and width) were equal to the cross sectional dimensions of the HOCS phantom. It was proved that this technique is effective and useful as an evaluation of cylindrical near field wearable antenna measurements and removed the necessity of using the

phantom, during the measurement preparation procedure (to define optimum CNF volume). The evaluation technique was assessed by comparing the far field performance parameters (gain, directivity and efficiency), derived from the cylindrical near field measurements, with simulations and with direct far field measurements. Validation of the evaluation technique was carried out by applying the evaluated cylindrical near field volumes (EGSP-derived from the evaluation technique procedure) on HOCS phantom, for all three antennas, by measuring and comparing them with simulations. The CDP, for all the patch antennas examined, for the evaluation technique, yielded deviation between near field to far field measurements and simulations less than 0.68dB, 1.28dB and 22.6% in terms of Gain, Directivity and Efficiency, respectively. The validation of the evaluation technique, by using the HOCS phantom instead of the CDP yielded deviation between measurements and simulations less than 0.95dB, 0.74dB and 22% in terms of Gain, Directivity and Efficiency, respectively.

The new methodology for wearable antennas performance evaluation was analytically presented. The wearable patch antennas were positioned in different locations on HOCS phantom. The new methodology can be summarized as follows: *The near field amplitude (E-field) distribution for each antenna and each location was recorded. From the near field results, assumptions for the maximum direction of radiation, for the radiation and for the directivity were derived. The far field radiation patterns and parameters (gain, directivity and efficiency) were produced from the near field results, validating the assumptions made from the near field amplitude contour plots.*
Finally, it is suggested that the CNF measurement technique should not be applied when a wearable antenna is mounted on top (above) (e.g. helmet antenna or on top of shoulders antenna) or bottom (below) the phantom (generally antennas that their main radiation is on the elevation plane parallel to the phantoms height) because the lack of sampling and the non-definition of Hankel functions (used for NFtoFF) in these points will lead in missing important data for the radiation of these wearable antennas.

The evaluation technique and the methodology (using the CNF measurement technique) for wearable antennas performance evaluation could be applied for other types of antennas (e.g. dipole, loop, spiral) than patch antennas as well and for other frequencies as well.

References

[1]   P. Hall and Y. Hao, *Antennas and Propagation for Body-Centric Wireless Communications*, 2nd ed. London / Boston: Artech House, 2012.

[2]   B. Gupta, S. Sankaralingam, and S. Dhar, "Development of Wearable and Implantable Antennas in the Last Decade: A review," in *Microwave Symposium (MMS), Mediterranean*, 2010, pp. 251–267.

[3]   C. Psychoudakis, D , Volakis,J.L., Chen, C, "Optimizing Wearable UHF Antennas for On-Body Operation," *International Symposium on Antennas and Propagation*, pp. 4184–4187, 2007.

[4]   R. Chandra and A. J. Johansson, "An Analytical Link Loss Model for On-Body Propagation Around the Body Based on Elliptical Approximation of the Torso with Arms ' Influence Included," *Antennas and Wireless Propagation Letters, IEEE*, vol. 12, pp. 528–531, 2013.

[5]   H. M. R. Nurul, F. Malek, P. J. Soh, G. A. E. Vandenbosch, V. Volski, S. L. Ooi, and I. Adam, "Evaluation of a Wearable Hybrid Textile Antenna," in *Loughborough Antennas & Propagation Conference, 8-9 November*, 2010, November, pp. 337–340.

[6]   R. Chandra and A. J. Johansson, "An Elliptical Analytic Link Loss Model for Wireless Propagation Around the Human Torso," in *6th European Conference on Antennas and Propagation (EUCAP), 26-30 March*, 2012, pp. 3121–3124.

[7]   C.-H. Lin and K. Ito, "A Compact Dual-Mode Wearable Antenna for Body-Centric Wireless Communications," *Electronics*, vol. 3, no. 3, pp. 398–408, Jul. 2014.

[8]   C.-H. Lin, Z. Li, K. Ito, M. Takahashi, and K. Saito, "Dual-mode antenna for on-/off-body communications (10 MHz/2.45 GHz)," *Electronics Letters*, vol. 48, no. 22, pp. 1383 – 1384, 2012.

[9]   H. R. Raad, A. I. Abbosh, H. M. Al-Rizzo, and D. G. Rucker, "Flexible and Compact AMC Based Antenna for Telemedicine Applications," *IEEE Transactions on Antennas and Propagation*, vol. 61, no. 2, pp. 524–531, 2013.

[10]   T. F. Kennedy, P. W. Fink, A. W. Chu, N. J. Champagne, G. Y. Lin, and M. A. Khayat, "Body-Worn E-Textile Antennas : The Good , the Low-Mass , and the Conformal," *IEEE Transactions on Antennas and Propagation*, vol. 57, no. 4, pp. 910–918, 2009.

[11]   A. Tsolis, W. Whittow, A. Alexandridis, and J. Vardaxoglou, "Embroidery and Related Manufacturing Techniques for Wearable Antennas: Challenges and Opportunities," *Electronics*, vol. 3, no. 2, pp. 314–338, May 2014.

[12]   J. Park and J. Woo, "Miniaturization of microstrip line monopole antenna for the wearable applications," *2008 Asia-Pacific Microwave Conference*, pp. 1–4, Dec. 2008.

[13]   P. J. Soh, G. A. E. Vandenbosch, and J. Higuera-Oro, "Design and Evaluation of Flexible CPW-fed UltraWide Band (UWB) Textile Antennas," in *IEEE Int. RF Microw. Conf. (RFM 2011), Seremban, Malaysia*, 2011, pp. 133–136.

[14]   T. Kellomaki, J. Heikkinen, and M. Kivikoski, "Wearable antennas for FM reception," in *1st European Conference on Antennas and Propagation (EuCAP), 6-10 Novmber*, 2006, pp. 1–6.

[15]   A. Kuramoto and Y. Furuya, "Wideband Wearable Antenna," in *Proceedings of ISAP, Niigata, Japan*, 2007, pp. 1086–1089.

[16]   J.-S. Roh, Y.-S. Chi, J.-H. Lee, Y. Tak, S. Nam, and T. J. Kang, "Embroidered Wearable Multiresonant Folded Dipole Antenna for FM Reception," *IEEE Antennas and Wireless Propagation Letters*, vol. 9, pp. 803–806, 2010.

[17]   M. E. Jalil, M. K. a. Rahim, N. a. Samsuri, O. Ayop, M. a. Abdullah, and M. F. Ismail, "Investigation the performance of Koch fractal multiband textile antenna for on-body measurement," in *2012 Asia Pacific Microwave Conference Proceedings*, 2012, pp. 1373–1375.

[18]   C. A. Balanis, *Antenna Theory Analysis and Design*, 3rd ed. New Jersey: John Wiley & Sons, 2005.

[19]   D. L. Paul, H. Giddens, M. G. Paterson, G. S. Hilton, and J. P. Mcgeehan, "Impact of Body and Clothing on a Wearable Textile Dual Band Antenna at Digital Television

andWireless Communications Bands," *IEEE Transactions on antennas and propagation*, vol. 61, no. 4, pp. 2188–2194, 2013.

[20]   T. H. Loh, D. Cheadle, and L. Rosenfeld, "Radiation Pattern Measurement of a Low-Profile Wearable Antenna Using an Optical Fibre and a Solid Anthropomorphic Phantom," *Electronics*, vol. 3, no. 3, pp. 462–473, 2014.

[21]   Z. Wang, L. Zhang, D. Psychoudakis, and J. L. Volakis, "Flexible textile antennas for body-worn communication," *IEEE International Workshop on Antenna Technology (iWAT)*, pp. 205–208, Mar. 2012.

[22]   D. Psychoudakis, G. Lee, C. Chen, and J. L. Volakis, "Military UHF Body-Worn Antennas for Armored Vests," in *European Conference on Antennas and Propagation (EuCAP)*, 2010, pp. 1–4.

[23]   J. C. G. Matthews and G. Pettitt, "Development of Flexible , Wearable Antennas," in *3rd European Conference on Antennas and Propagation (EuCAP)*, 2009, pp. 273–277.

[24]   B. Loader, D. Bownds, and A. Gregory, "Assessing The Isotropy of Personal Electromagnetic Field Monitors." pp. 1–4.

[25]   L. Zhang, Z. Wang, D. Psychoudakis, and J. L. Volakis, "E-fiber electronics for body-worn devices," in *6th European Conference on Antennas and Propagation (EUCAP)*, 2012, pp. 760–761.

[26]   Q. Bai, S. Swaisaenyakorn, H.-J. Lee, K. L. Ford, J. C. Batchelor, and R. J. Langley, "Investigation of a Switchable Textile Communication System on the Human Body," *Electronics*, vol. 3, no. 3, pp. 491–503, 2014.

[27]   S. J. Boyes, Y. Huang, N. Khiabani, P. J. Soh, and G. A. E. Vandenbosch, "Repeatability and Uncertainty Evaluations of On-body Textile Antenna Efficiency Measurements in a Reverberation Chamber," in *Loughborough Antennas & Propagation Conference (LAPC)*, 2012, pp. 1–5.

[28]   P. J. Soh, G. A. E. Vandenbosch, X. Chen, P. S. Kildal, S. L. Ooi, and H. Aliakbarian, "Wearable Textile Antennas' Efficiency Characterization using a Reverberation

Chamber," in *IEEE International Symposium on Antennas and Propagation (APSURSI)*, 2011, pp. 810–813.

[29] S. J. Boyes, P. J. Soh, Y. Huang, G. A. E. Vandenbosch, and N. Khiabani, "Measurement and Performance of Textile Antenna Efficiency on a Human Body in a Reverberation Chamber," *IEEE Transactions on Antennas and Propagation*, vol. 61, no. 2, pp. 871–881, 2013.

[30] G. A. Conway, W. G. Scanlon, C. Orlenius, and C. Walker, "In Situ Measurement of UHF Wearable Antenna Radiation Efficiency Using a Reverberation Chamber," *Antennas and Wireless Propagation Letters*, vol. 7, pp. 271–274, 2008.

[31] G. A. Conway, W. G. Scanlon, C. Nunn, and A. Burdett, "Layered RF Phantom Characterization for Wireless Medical Vital Sign Monitors," in *Antennas and Propagation Society International Symposium (APS-URSI), IEEE*, 2013, pp. 2201–2202.

[32] A. Alomainy and T. H. Loh, "Experimental Evaluation of Wearable Antenna Efficiency for Applications in Body-Centric Wireless Networks," in *RF ana Wireless Technologies for Biomedical and Healthcare Applications (IMWS-Bio)*, 2014, pp. 1–2.

[33] T. Salim and P. S. Hall, "Efficiency measurement of antennas for on-body communications," *Microwave and Optical Technology Letters*, vol. 48, no. 11, pp. 2256–2259, 2006.

[34] P. O. Iversen, P. Garreau, and D. Burrell, "Real-Time Spherical Near-Field Handset Antenna Measurements," *Antennas and Propagation Magazine*, vol. 43, no. June, pp. 90–94, 2001.

[35] J. Krogerus, J. Toivanen, C. Icheln, and P. Vainikainen, "Effect of the Human Body on Total Radiated Power and the 3-D Radiation Pattern of Mobile Handsets," *Transactions on instrumentation and measurement*, vol. 56, no. 6, pp. 2375–2385, 2007.

[36]   G. A. Conway and W. G. Scanlon, "Antennas for Over-Body-Surface Communication at 2.45GHz," *IEEE Transactions on Antennas and Propagation*, vol. 57, no. 4, pp. 844–855, 2009.

[37]   A. Guraliuc, N. Chahat, C. Leduc, M. Zhadobov, and R. Sauleau, "End-Fire Antenna for BAN at 60 GHz: Impact of Bending, On-Body Performances, and Study of an On to Off-Body Scenario," *Electronics*, vol. 3, no. 2, pp. 221–233, Apr. 2014.

[38]   J. C. G. Matthews, B. Pirollo, A. Tyler, and G. Pettitt, "BODY WEARABLE ANTENNAS FOR UHF / VHF," in *Loughborough Antennas & Propagation Conference (LAPC)*, 2008, pp. 357–360.

[39]   C. Parini, S. Gregson, J. Mccormick, and D. Janse van Rensburg, *Theory and Practice of Modern Antenna Range Measurements*. IET, London, UK, 2015.

[40]   IEEE, *IEEE Recommended Practice for Near-Field Antenna Measurements*, December. 2012.

[41]   F. Harrysson, S. Member, J. Medbo, A. F. Molisch, A. J. Johansson, F. Tufvesson, and S. Member, "Efficient Experimental Evaluation of a MIMO Handset with User Influence," *Transactions on wireless communications*, vol. 9, no. 2, pp. 853–863, 2010.

[42]   S. V Bagad, *Microwave Engineering*, 1st ed. 2009.

[43]   D. M. Pozar, *Microwave Engineering*, 4th ed. 2012.

[44]   "http://www.orbitfr.com/", accessed September 2016.

[45]   "http://www.indexsar.com/", accessed September 2016.

[46]   C. A. Balanis, *Modern Antenna Handbook*. John Wiley & Sons, 2008.

[47]   A. Tsolis, W. G. Whittow, A. Chauraya, A. A. Alexandridis, and J. Y. C. Vardaxoglou, "Evaluation of a Realized Hollow Torso Phantom for Wearable Antenna Measurements," in *Loughborough Antennas & Propagation Conference (LAPC)*, 2014, no. November, pp. 560–561.

[48]   A. Tsolis, W. G. Whittow, A. A. Alexandridis, and J. C. Vardaxoglou, "Evaluation of a Human Body Phantom for Wearable Antenna Measurements at the 5.8GHz Band," in *Loughborough Antennas & Propagation Conference (LAPC), 11-12 November, Loughborough, UK*, 2013, pp. 414–419.

CHAPTER 4

TEXTILE TRANSMISSION LINES INTERCONNECTION METHODS

Abstract

In this chapter two new methods for interconnecting textile transmission lines (TLs) are presented in terms of design and fabrication. The proposed TLs interconnection models follow the basic structure of the stripline. The straight stripline (*ST*), with no interconnections involved, is used as a reference and is compared with the proposed interconnection methods. The proposed methods, slotted (*SO*) and complementary (*CO*) overlap, stripline exclude the use of rigid coaxial connectors in order to achieve the interconnection. The most efficient method (*CO*) has been fabricated with purely textile materials (all-textile) so as to meet the "wearable textile" criteria. Additionally, the complementary overlap interconnection is implemented by using Velcro, providing a practical and a flexible interconnection way.

Chapter 4 introduces the stripline theory which is implemented for the design of the *ST*, *SO* and *CO* models. The geometry of the models and the wearable criteria are described. The textile materials properties characterization and selection, which are used to design and fabricate the models, are presented. These materials are the dielectric substrate and the conductive parts (ground planes and stripline). Various adhesive techniques, so as to attach the dielectric with the conductive textile, are examined in terms of inesrtion losses (S_{21}) and reflection coefficient (S_{11}) using the *ST* model.

The design and the results of the SO and CO are presented and compared with the reference *ST* model. Regarding the *SO* a parametric analysis of a metallic via and the side shielding effect are examined via simulations, yielding that the metallic via with 3mm diameter is the most effective in terms of S_{21} performance of the model and the side shielding improves the S_{21} performance of the *SO*. Additionally, the *SO* was prototyped and measured showing a reasonable agreement with simulations. Regarding the *CO*, the geometrical discontinuities effect in S_{21} performance is modelled and a solution, of extending the upper

ground planes so as to improve its performance when these occur, is proposed. The *CO* is prototyped and measured showing good agreement with simulations. The *CO* model was fabricated as an all-textile one and a practical and flexible interconnection of the *CO* is achieved by using Velcro.

4.1 Introduction

4.1.1 Textile transmission lines and methods of interconnection

Wearable antennas and electronics have been widely studied over the last decade [1], [2] following the demand for more flexible and smart wearable electronics. This means that wearable electronics should be user friendly but perform well. One of the most important parts of wearable communication systems is the antenna. Hence the connection between wearable antennas with the wearable electronics / sensors is critical for the development of a wearable communication system. Several papers have successfully proposed wearable antenna designs but they rarely consider the connection between antenna and wearable electronics and they use bulky connectors (e.g. SMA) and coaxial cables for measurement purposes [2]. Recent works have successfully presented the idea of using wearable textile transmission lines for feeding and interconnecting wearable devices and antennas providing by this way a textile and flexible interconnecting solution [3],[4].

In [5], [6] a broadband (1-8GHz) shielded wearable textile stripline was presented and yields maximum losses equal to 1dB over 100mm (Fig. 4-1a). The flexibility of the stripline was examined by bending it and yielded maximum insertion losses equal to 1.5dB. In [7],[8],[9],[10] a 600mm long shielded stripline (Fig. 4-1b), part of a switchable on/off body system, was described. This long stripline yielded transmission losses, at 1-4GHz, of approximately 5dB. Bending, twisting and crumpling effects were examined yielding +3dB losses as a worst case scenario. Both referred striplines suffer increase of losses only when shape distortion effects occur (which are expected on-body). They do not suffer any effects from the lossy human body because they are shielded. This in addition with the broadband operation makes the stirpline model a very good candidate for wearable operation. In [11],[12] wearable microstrip textile TL were presented (Fig. 4-1c). The realized microstrip textile lines yielded maximum attenuation 0.37dB/cm at the range of 30MHz up to 6GHz. The textile microstrip lines are easier in terms of fabrication, compared to striplines. But microstrip lines could suffer great performance degradation compared to striplines due to human body

interaction, because they lack of a ground plane shielding over the main line. In [13] an elliptical cross-section textile knitted waveguide for X-band operation was presented (Fig. 4-1d). That waveguide yielded losses below 10dB, over a 320mm length, between 8-10GHz. Bending added 1dB in terms of losses. In [14] a substrate integrated textile waveguide was presented (Fig. 4-1e). A 135mm long prototype yielded 2.3dB losses at 5.5GHz. Bending and twisting added 0.5 and 0.6dB into losses respectively. Textile waveguides are good candidates for wearable operation (shielded and not affected by human body) with the weakness of operating under a cut-off frequency condition deteriorating the operation in a more narrowband than striplines and microstrip lines. Another weakness is their increased dimensions compared to striplines and microstrips.

All the above transmission lines and waveguides were continuous lines. An issue which few papers examined is methods of textile and flexible interconnection between transmission lines. In [12] an interconnection method between textile microstrip lines using a metallic pin (via) was demonstrated (Fig. 4-2a). The attenuation, including the microstrip lines with the interconnection method was equal to 0.34dB/cm up to 4GHz. Recently, RF measurements have demonstrated the feasibility of using conductive Velcro as an RF connection mechanism at the low GHz frequency range [15] between rigid microstrip lines (Fig.4-2b). Measurements yielded that the RF connector losses are <1dB up to 4GHz. The proposed flexible RF connector [15] has the advantage that the transmission lines can be easily connected and disconnected. In [16] a promising microwave transition (connector) between microstrip lines, using magnets, was presented (Fig. 4-2c). The losses are less than 1dB up to 2.7GHz which means that at least 79% of the power is transmitted up to this frequency. Finally a coaxial to microstrip transition using a Snap-on button, as an RF connector, is achieved and presented in [17] (Fig. 4-2d). This is a promising transition for the wearables and yielded reflection coefficient magnitude below -10dB from 50MHz up to 3GHz.

In this thesis chapter two new textile stripline interconnection methods are presented (*SO* and *CO*). Both methods are compared with a reference straight continuous stripline (*ST*) with no interconnections involved. Goals of the proposed methods are: a) flexibility in interconnecting the transmission lines on-body at different positions and b) no coaxial cables and rigid connectors (e.g. SMA) will be needed for the interconnection between the TLs. Both methods can be used for interconnecting/feeding wearable textile patch antennas (see Chapter 5). The *CO* method (as having a better performance) is fabricated as an all-

textile (using conductive Nora-dell [18] instead of copper tape), more practical and flexible interconnection structure, by using Velcro. The frequency range of 1 up to 6GHz where lots of modern commercial bands such as L (GPS), ISM (WLAN, Bluetooth, Zigbee, etc.) exist, was selected for the analysis in this chapter.

a)
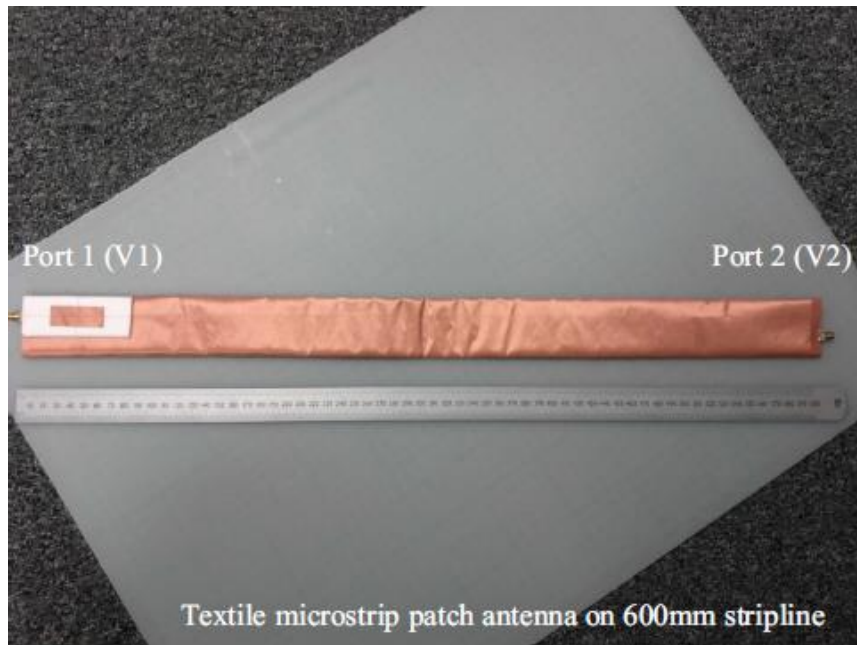
b)
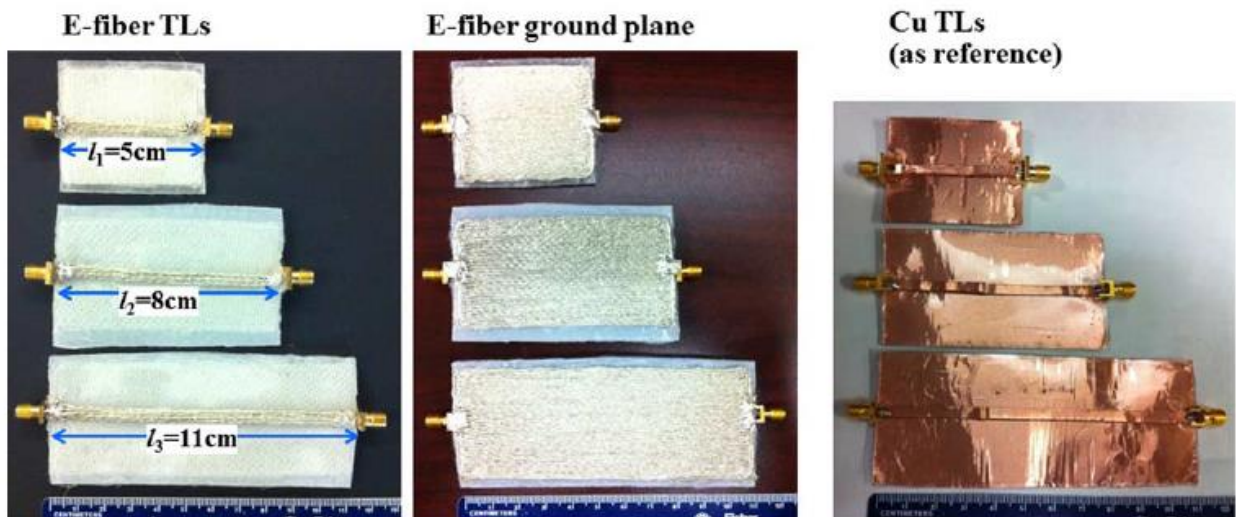
c)

d)
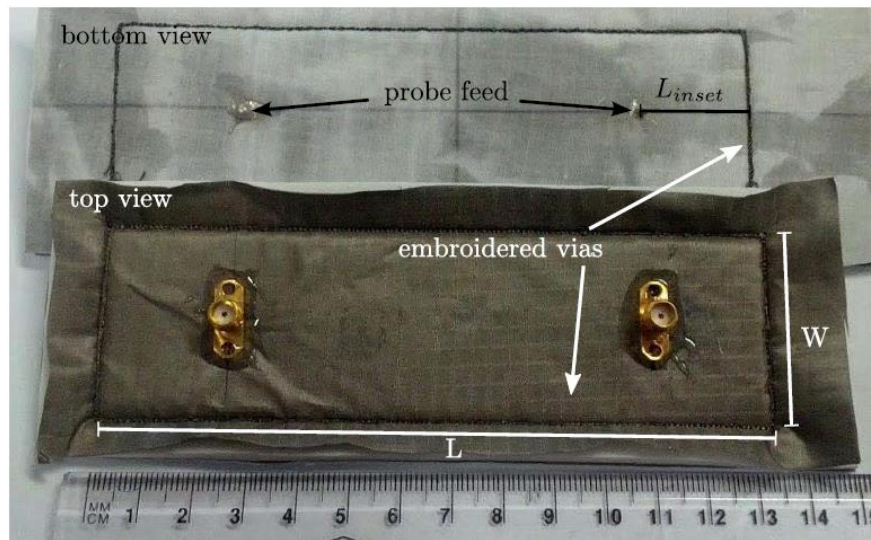
e)

Fig. 4- 1 a) Textile stripline [5], b) Fabricated switchable on/off-body textile microstrip antenna on stripline (600mm) [8],
c) Fabricated e-fiber TLs and Cu reference TLs [11], d) configuration of a straight knitted waveguide [13],
e) SIW structure from top and bottom view [14]
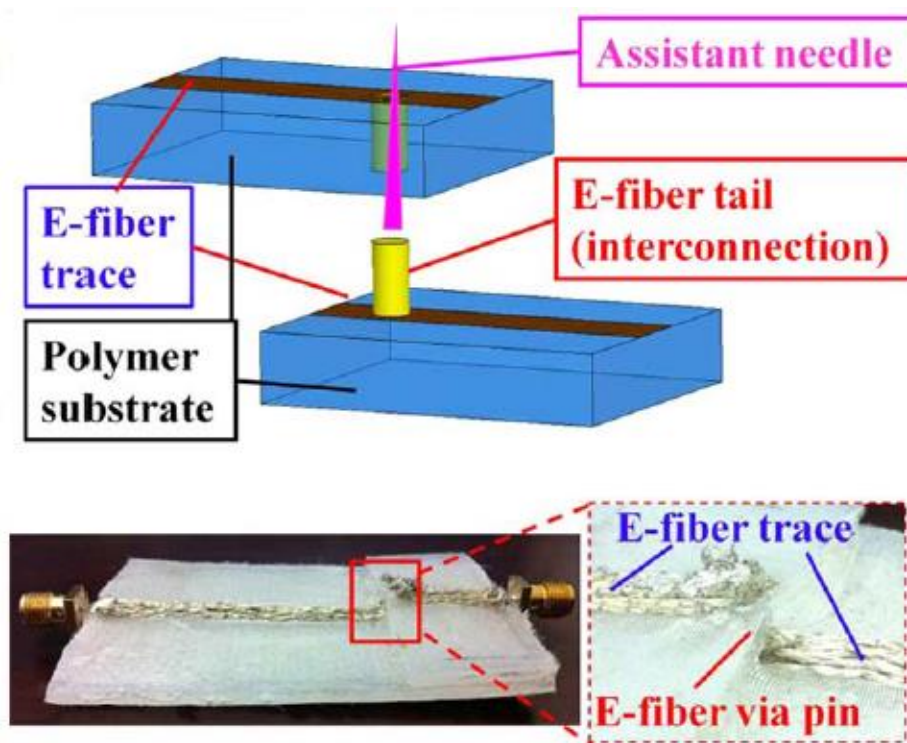
a)
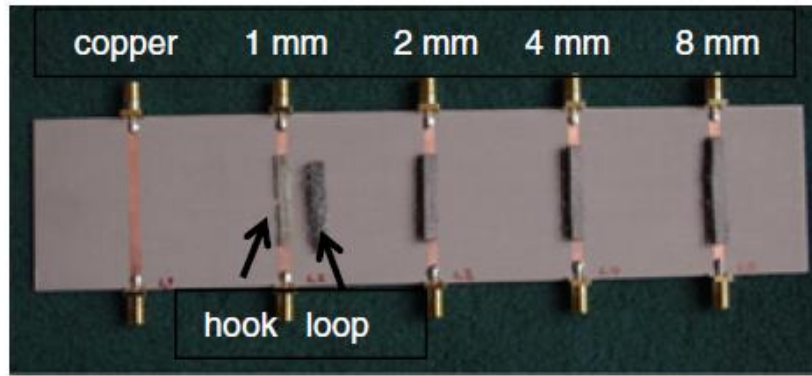
b)
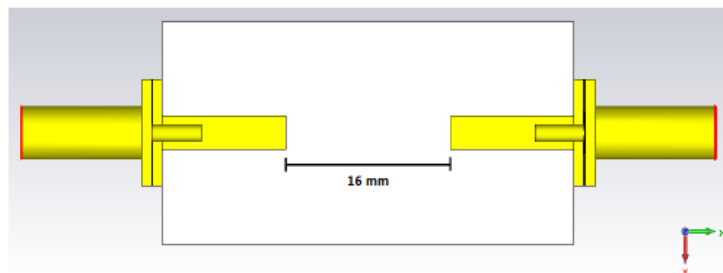
Top view of the microstrip transition without the textile or magnets
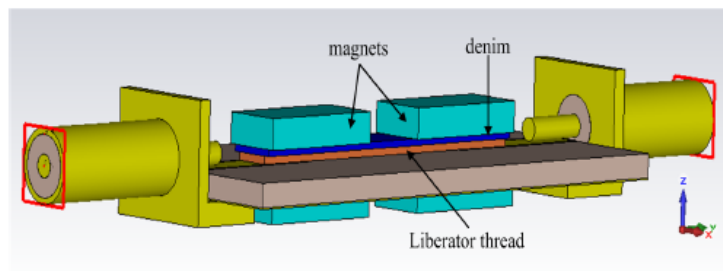
Perspective view of the microstrip transition with textile line

c)

d)

Fig. 4- 2 a) Microstrip lines via interconnection [12], b) Hook and loop setup [15], c) Interconnection between textile and rigid substrates with magnets [16], d) Snap-on buttons for coaxial to microstrip transition [17]

4.1.2 Outline of this chapter

In Section 4.2 the stripline theory and geometry are presented. The wearable criteria for choosing the stripline structure, so as to design the interconnection methods are described. Additionally the reference stripline (ST) model design, geometry and dimensions are presented. In Section 4.3 the textile materials properties characterization and selection which are used to design and fabricate the models, are presented. These are the materials of the dielectric substrate and the conductive parts (ground planes and stripline). Various adhesive ways are examined, through measurements, in terms of insertion losses (S_{21}), using the *ST* model, so as to attach the dielectric with the conductive textile. In Section 4.4 the design and the results of the SO and CO are presented and compared with the reference *ST* model via simulations and measurements. Regarding the *SO* a parametric analysis of a metallic via and the side shielding effect are examined, in terms of transmitted power (S_{21}), via simulations and measurements. Additionally, regarding the *CO*, the geometrical discontinuities effect in S_{21} performance is modelled and a solution to improve its performance when these occur is proposed. The *CO* model fabrication as an all-textile one and as a practical and flexible interconnection by using Velcro is presented and evaluated and compared with the *ST* all-textile realized model, via measurements. In Section 4.5 conclusions from this chapter are drawn.

4.2 Stripline theory and geometry

4.2.1 Wearable stripline criteria

A comparison of common transmission lines and waveguides is presented in Table 4-1 [19]. A wearable TL is required to operate in an environment where the existence of the lossy human body introduces interference which can cause performance degradation. Therefore a shielded TL should be used. Therefore, the microstrip TL is not a good candidate for wearable operation, due to its lack of upper ground plane, shielding the main line. Additionally, the waveguide model is shielded from human body interference but it does not support a TEM mode having a lower cut-off frequency and it has a low bandwidth and loss with a large physical size. This means that a waveguide could be a suitable candidate for wearable narrowband operation at high GHz (e.g. X-band) frequencies where the dimensions are smaller than low GHz frequencies (e.g. L-band) [19]. The coaxial TL could be a good

candidate for broadband wearable operation. Though compared with the stripline model its physical size is larger and its fabrication is harder. These are the reasons and the wearable criteria for choosing the stripline model for the interconnection methods design and use.

Table 4- 1 Comparison of common transmission lines and waveguides [19]

Characteristic	Coax	Waveguide	Stripline	Microstrip
Modes: Preferred	TEM	TE_{10}	TEM	Quasi-TEM
Other	TM, TE	TM, TE	TM, TE	Hybrid TM, TE
Dispersion	None	Medium	None	Low
Bandwidth	High	Low	High	High
Loss	Medium	Low	High	High
Power capacity	Medium	High	Low	Low
Physical size	Large	Large	Medium	Small
Ease of fabrication	Medium	Medium	Easy	Easy
Integration with	Hard	Hard	Fair	Easy

4.2.2 Stripline design

The geometry and dimensions on the YZ-plane (height and width) of the proposed stripline *ST* model which was used for the design of the *SO* and the *CO* models are shown in Fig. 4-3. The conductive parts are copper (copper tape / thickness = 120μm) and the textile dielectric (black color) is Felt (ε_r=1.17) (see Section 4.3). Each felt part, out of the two used to structure the stripline, which had been implemented for the design and fabrication, is 4mm thick. So the total height, geometrical parameter *b*, is equal to 8.12mm (two pieces of felt plus the 120μm of the stripline piece). The design equation which connects the stripline width (*W*) with the height (*b*) and the line impedance (Z_o) is the (4.1) [19]. For Z_o = 50 Ohms, which is the most usual impedance matching with most commercial electronics, and for b = 8.12mm the stripline width should be W = 10.56mm. For the ease of fabrication the width of stripline is selected to be W = 10mm. This results in a line impedance Z_o = 51.71Ohms, which is close to the desired 50 Ohms. This means that the stripline will yield a small reflection [19] with a value equal to 0.0171 when connected to an electronic circuit with input/output impedance of 50 Ohms. The simulations, using Empire-XPU software, of the ST stripline model yielded that the magnitude of the impedance seen by ports 1 and 2 (Fig. 4-4) for 1 up to 6GHz is between 42-53Ohms close to the desired 50Ohm.

The Stripline structure supports a TEM mode (Table 4-1) and a higher TE mode, with a cut-off frequency determined by equation (4.2) [20]. This TE mode is undesirable due to possible signal distortion it can cause [20]. The TE mode cut-off frequency needs to be taken into account in order to ensure a single TEM mode propagation for the desirable frequency range (1-6GHz). The chosen dimensions excite a TE higher mode with a cut-off frequency equal to 8.46GHz. Different combinations of *W*, *b* geometrical parameters and the resulted TE cut-off frequencies are shown in Table 4-2. The pair values of *W* and *b* result into line impedance approximately to 50 Ohm [19]. It can be seen from Table 4-2 that cases No. 1,2 and 3 can be used in order to ensure single TEM mode propagation for the frequency range 1GHz to 6GHz. For the work in this thesis and chapter case No.1 was selected for simulation and experimental studies, due to ease of fabrication compared with cases No. 2 and 3. Additionally, in terms of single TEM mode propagation avoiding higher TE modes excitation the conditions described in equation (4.3) must be satisfied for the examined frequency range. According to Table 4-3 the condition (4.3) is satisfied for all frequencies for parameter *b*. As for the width of the ground planes of the Stripline, parameter W_{GD} should be less than 23.11mm. For the ease of fabrication it was selected to be equal to 25mm. This value satisfies condition (4.3) for frequencies 1-5GHz and it is quite close with the condition value at 6GHz. Due to this, there is a possibility that at 6GHz higher modes could occur and cause signal distortion resulting into performance degradation. As it will be seen from reflection and transmission coefficient simulations and measurements this possibility has not been observed.
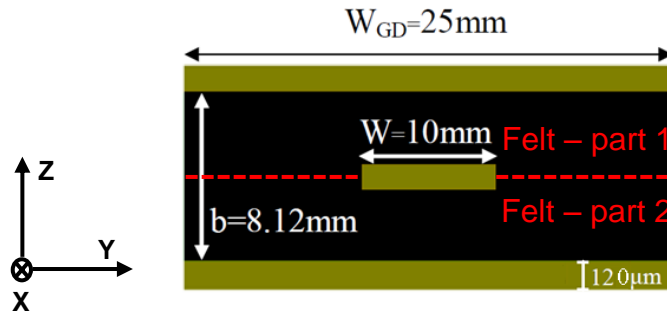
Fig. 4- 3 Stripline geometry on the YZ-plane

$$\frac{W}{b} = \begin{cases} x & \text{for } \sqrt{\epsilon_r}Z_0 < 120\ \Omega \\ 0.85 - \sqrt{0.6 - x} & \text{for } \sqrt{\epsilon_r}Z_0 > 120\ \Omega \end{cases}$$

(4.1)

$$x = \frac{30\pi}{\sqrt{\epsilon_r}Z_0} - 0.441$$

$$fc = \frac{15}{b\sqrt{\varepsilon_r}} * \frac{1}{\frac{W}{b} + \frac{\pi}{4}} \text{ (GHz)},$$

(4.2)

where W, b in cm
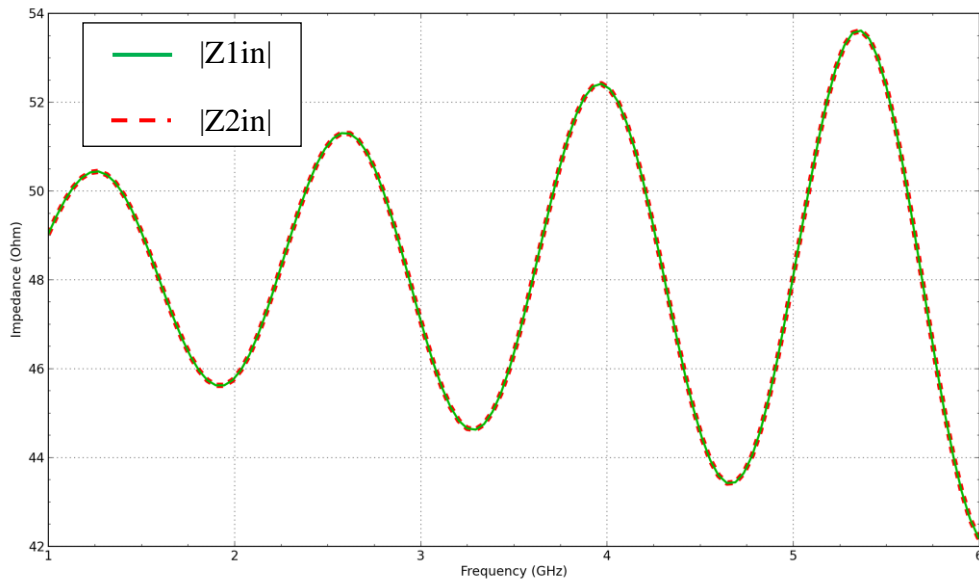
Fig. 4- 4 Simulated magnitude of the impedance seen by port 1 and 2 of the *ST* Stripline model

Table 4- 2 Stripline TE modes cut-off frequencies vs geometrical dimensions

No.	Stripline geometric parameters vs TE mode fc		
	W (mm)	*b (mm)*	*f_c (GHz)*
1	10.0	8.12	8.46
2	5.3	4.12	16.24
3	2.7	2.12	31.76
4	20.8	16.12	4.14

$$W_{GD} \text{ \& } b < \frac{\lambda_d}{2}$$

(4.3)

$$\lambda_d = \frac{c}{\sqrt{\varepsilon_r} f}$$

Table 4- 3 Frequency vs medium half wavelength

Frequency (GHz)	$\lambda_d/2$ (mm)
1	138.67
2	69.33
3	46.22
4	34.66
5	27.73
6	23.11

The total length of the reference *ST* model stripline and subsequently *SO* and *CO* models, selected for this chapter analysis is equal to 10cm. Though, ST model simulated (S_{21} & S_{11}) for 10, 20 and 30cm (Fig. 4-5). According to simulated S_{21} results the insertion losses increase by frequency. The losses will increase approximately 0.3dB every 10cm. The losses increase due to extra length of straight line. So, if the total length of the ST or the SO and CO (when increase will occur only in the part of the straight Stripline not in the part of the overlap interconnection of the 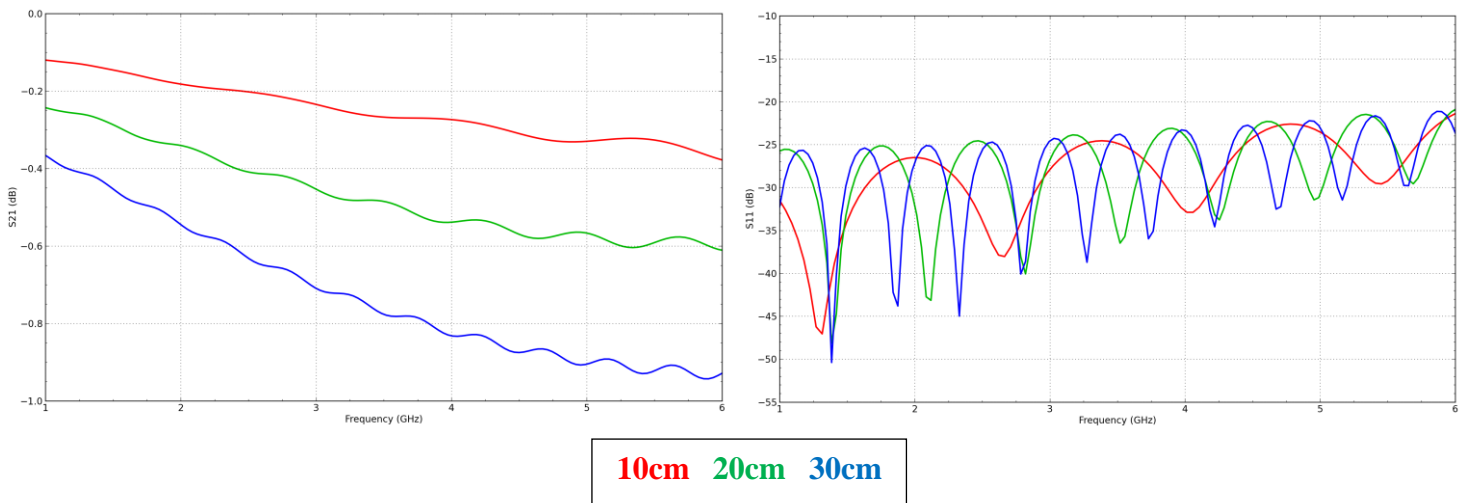SO and the CO models – Fig. 4-10) models increase in terms of length the losses will be increased. According, to S_{11} simulated results for all lengths examined the reflection coefficient is well kept below the desired -10dB [21].

10cm   20cm   30cm

Fig. 4- 5 Simulated Transmission (S_{21}) and Reflection (S_{11}) coefficient for the ST Stripline model

The total attenuation in the stripline is a sum of conductor and dielectric attenuation [19]. The attenuation of the stripline increases by frequency. This is expected and verified by simulations and measurements.

4.3 Textile material characterization

4.3.1 Textile dielectric substrate

The substrate material selection for a wearable transmission line or antenna is of crucial importance. The substrate selection requires a low loss material so as to have better chances of increased TL or antenna performance [2]. For the purposes of the new methods design and fabrication (*ST*, *SO* and *CO*) textile dielectric substrates were chosen. The textile substrate choice fits well with the idea of wearable TLs and provides the ability of being flexible and more easily integrated into clothes than rigid substrates (e.g. FR4).

For the analysis in this chapter, felt was used as the textile substrate. Felt was chosen due to its low loss dielectric properties [22]. For the design and the fabrication of the prototypes (*SO* and *CO*) a 4mm thick black felt with *$\varepsilon_r = 1.17$* and *$tan\delta = 0.004$* at 1.9GHz and *$\varepsilon_r = 1.17$* and *$tan\delta = 0.03$* at 10GHz For the fabrication of the practical and flexible (with Velcro interconnection) all-textile CO model, a 4mm thick crimson felt with *$\varepsilon_r = 1.1$* and *$tan\delta = 0.0012$* at 1.9GHz and *$\varepsilon_r = 1.18$* and *$tan\delta = 0.012$* at 10GHz, was used.

4.3.2 Conductive materials

For the initial design, fabrication and evaluation of the *ST*, *SO* and *CO* models copper tape (thickness = 120μm) was used for the conductive parts. It is very easy to attach copper tape on a textile substrate but it is also possible that the copper tape might be detached or wrinkled (increasing the losses) while bending, due to use and even due to environmental conditions (i.e. humidity, heat) [2], see Fig. 4-6. In terms of final all-textile and flexible implementation of the *CO* model the conductive cloth Nora-dell (thickness=130μm) [18] is used instead of copper tape. The use of Nora-dell results in a more tolerant, with no wrinkles Stripline structure compared to using copper tape.

Copper tape has conductivity equal to 5.7×10^7 S/m. Nora-dell characteristic sheet resistance is 0.009Ohms/sq resulting into a 0.17×10^7 S/m conductivity [23]. For such thin conductive materials it is necessary to consider the skin effect which is expressed by the parameter known as skin depth (δ) (equation 4.4). The skin depth at 1GHz of copper tape is 2.06μm and of Nora-dell is 12.2μm. The thicknesses of copper tape and Nora-dell are at least five times

larger than the skin depth at the lower limit (1GHz) of the examined frequency range. According to equation (4.4) this would be valid for the higher examined frequencies, up to 6GHz. So, the skin effect will not affect the Ohmic losses, the efficiency of the TLs and Antennas using these specific conductive materials, at the frequency range of 1 up to 6GHz. In order to experimentally compare copper tape and Nora-dell, two 10cm long *ST* prototypes were fabricated and measured. Prototype 1 used copper tape for the conductive parts and prototype 2 used Nora-dell for the conductive parts. The Nora-dell prototype used Hemming-web to attach Nora-dell on the felt (see subsection 4.3.3). The S_{21} and S_{11} measurement results for both prototypes are shown in Fig. 4-7. The minimum measured S_{21} value of the ST copper tape Stripline was equal to -0.5dB and the respective Nora-dell was equal to -0.6dB. The Nora-dell use increased the insertion losses by 0.1dB compared with the copper tape. This increase in losses is not significant (transmitted power is reduced by ~2%). Additionally, both prototypes yielded very good S_{11} results lower than -10dB for the examined frequency range (1-6GHz). However, the Nora-dell prototype is more appropriate than the copper tape for all-textile applications.

a)
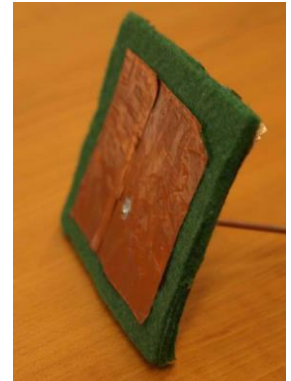
b)

Fig. 4- 6 a) ST prototype with wrinkles in copper after lots of measurements, b) textile patch (2.5GHz) with partially detached copper tape due to environmental conditions (humidity variation)

$$\delta = \sqrt{\frac{1}{\sigma \pi f \mu_r \mu_0}}$$ (4.4)

Where σ is the conductivity (S/m), f is the frequency in Hz, μ_r is relative permeability of material, and the μ_0 is the permeability of free space which equal to $4\pi \times 10^{-7}$ H/m.
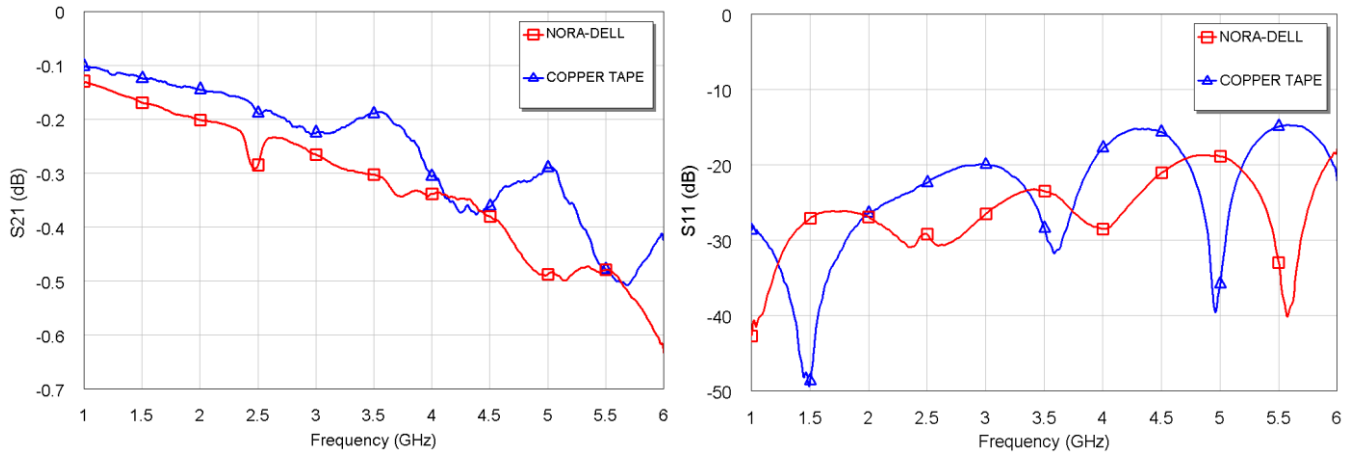
Fig. 4- 7 Measured S21 and S11 of the Nora-dell and Copper tape ST prototypes

4.3.3 Adhesive ways

For the implementation of the all-textile *CO* model the Nora-dell conductive fabric was required to be attached to the textile substrate felt. Three different ways were examined: (i) a universal adhesive (UHU −glue); (ii) a fusible adhesive that is designed to be used to hem garments (Hemming Web) and (iii) sewing (by using non-conductive thread). To assess which way yields the best performance, three 10cm long ST prototypes using these three methods of attaching Nora-dell to felt were fabricated. The two parts arising after attaching Nora-dell to felt are part 1: ground plane felt and part 2: ground plane, felt and stripline (Fig. 4-8). These two parts are used to assemble the "sandwich" structure of the stripline. For all three examined prototypes hemming-web was used to attach part 1 and 2 (Fig. 4-8) together to form the "sandwich".
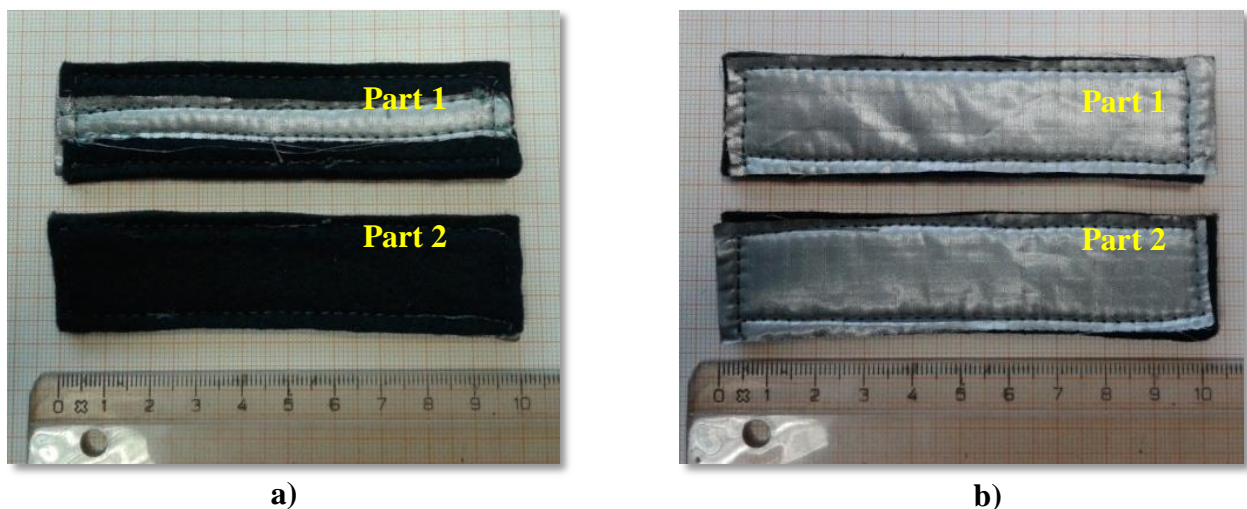

a)   b)

Fig. 4- 8 Parts of Stripline for which Nora-dell attached to felt by sewing at:
a) front side and b) back side

The measured S_{21} and S_{11} of the *ST* prototypes are shown in Fig. 4-9. The case of Hemming-web yielded the best S_{21} performance. It has lower insertion losses than the UHU glue and the sewed cases. Hemming-web has the lowest S_{11} for the examined frequency range (1-6GHz). Based on the above, it can be stated that the use of Hemming-web, to attach Nora-dell to felt, is the most promising in terms of losses compared with the other two examined cases.
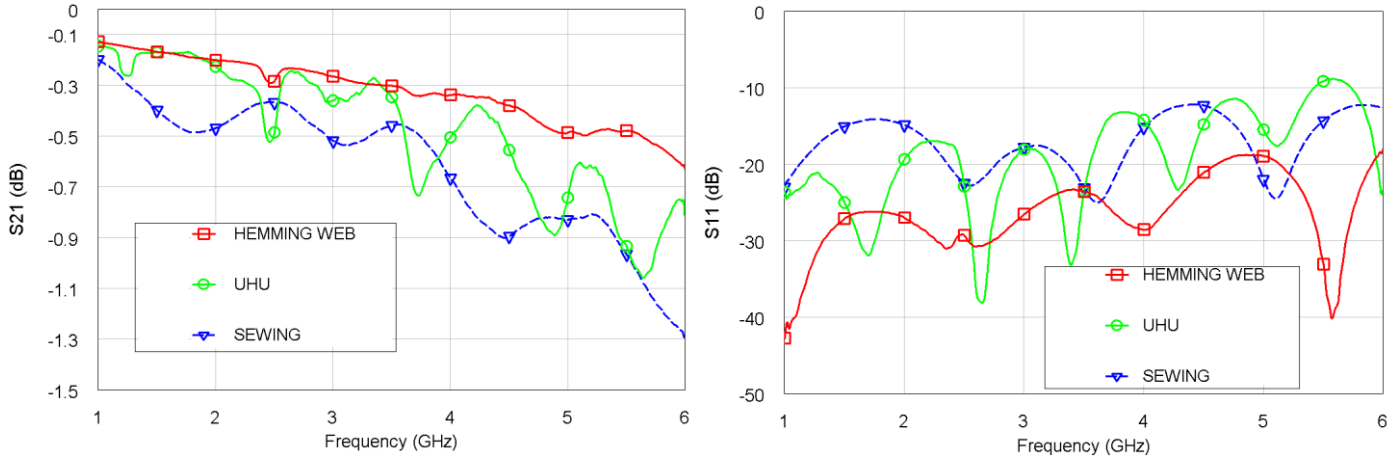
Fig. 4- 9 Measured S21 and S11 of the ST prototypes with Nora-dell using different adhesives

4.4. Textile connectivity methods using stripline model

4.4.1 Connectivity methods

In this section the Slotted Overlap (*SO*) and Complementary Overlap (*CO*) interconnection models are presented and compared with the reference *ST* Stripline model, for which no interconnections are involved. The simulation setup geometry (dimensions on YZ-plane described in subsection 4.2.2) of the ST, SO and CO models is shown in Fig. 4-10. The total length of all models is equal to 10cm. The ST is a straight continuous stipline 10cm long. The SO and CO models are composed by two individual 6cm long pieces which overlap each other by 2cm. The SO was investigated in three versions: (a) Slot in top GND-1 (Ground of Stripline 1) and in bottom GND-2 (Ground of Stripline 2); (b) Slot in top GND-1, in substrate-1 (Substrate of Stripline 1), in bottom GND-2 and in substrate-2 (Substrate of Stripline 2) and (c) Version (b) plus a cylindrical copper via (diameter = 1mm) which connects Stripline 1 with Stripline 2 (Fig. 4-10). After parametric analysis the optimized

dimensions for the rectangular slot are: 20mm along Y-axis and 13mm along X-axis. The optimization criterion which was followed is the best S_{11} and S_{21} performance.
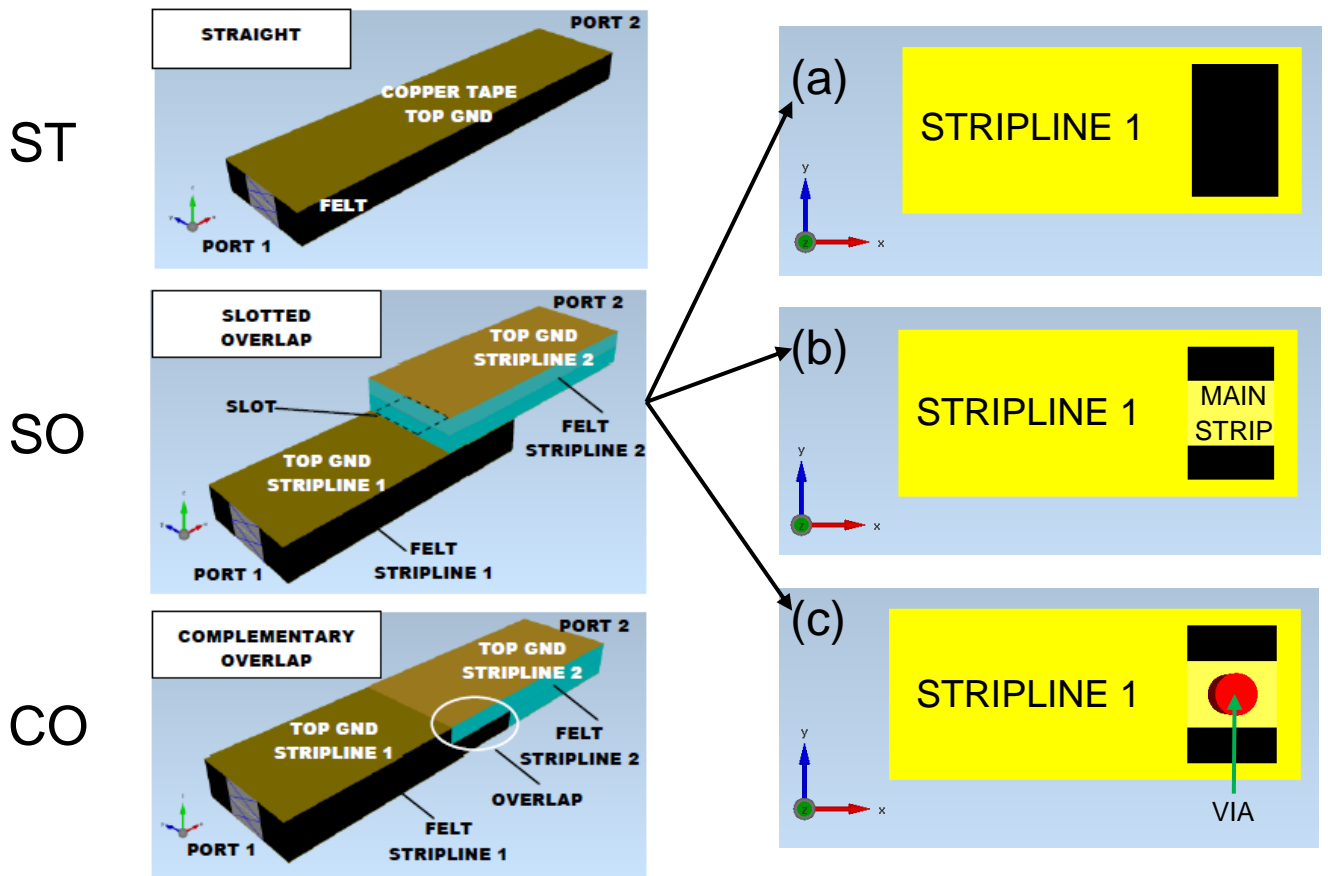

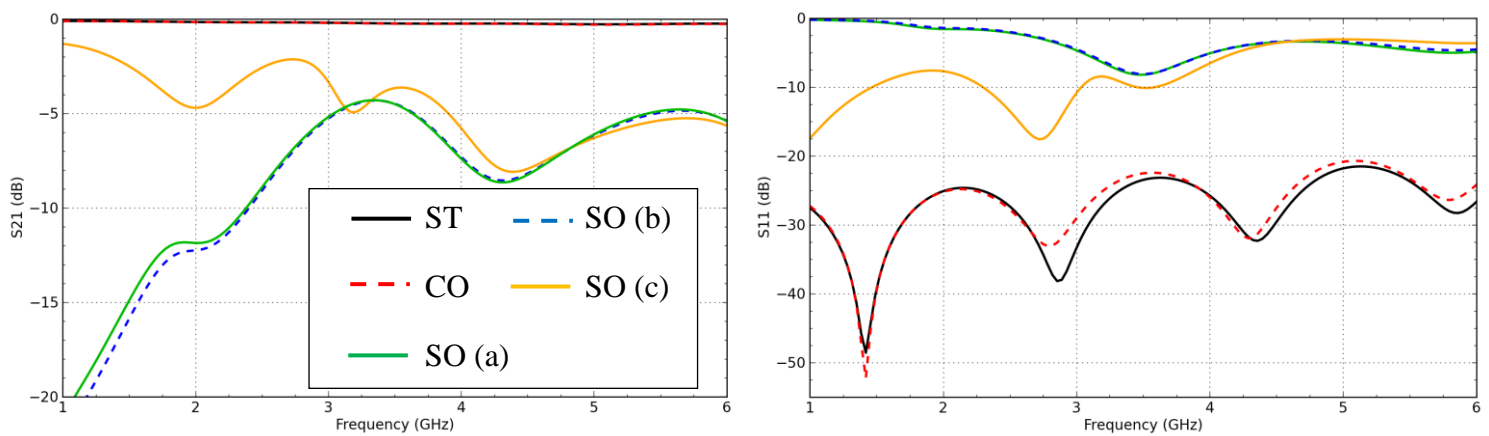**Fig. 4- 10 Textile stripline interconnection models**

Fig. 4- 11 Simulated transmission coefficient (S_{21}) and reflection coefficient (S_{11}) of the textile stripline interconnection models

The S_{21} and S_{11} simulation results for all the models are shown in Fig. 4-11. The S_{12} and S_{22} are not shown, but due to *two port network symmetry and reciprocity* [19] they are identical to the S_{21} and S_{11} respectively. It is clear that the CO interconnection stripline method was closer to the reference ST stripline performance compared with the SO method. Insertion losses (S_{21}) were worse in the case of SO compared to the CO. Though, the SO versions (a) and (b), which yielded similar performance, were improved by using a cylindrical copper via, version (c). The addition of the cylindrical copper via improved the S_{21}, compared to the SO versions with no via, yielding values higher than -6dB (25% of the power is transmitted) at most frequencies regarding the examined frequency range (1-6GHz). Regarding the reflection coefficient (S_{11}) the *CO* is below -10dB (less than 10% of the power is reflected) and well matched with the *ST*. Regarding *SO*, versions (a) and (b) the reflection coefficient is above -10dB for the examined frequency range. Finally, the SO (c) version yields S_{11} below -10dB for specific frequency ranges (1-1.5GHz and 2.25-3GHz). The addition of the cylindrical copper via decreases the reflection of the transmitted signal for both ports (Fig. 4-11).

From above simulations and regarding the frequency range of 1 up to 6GHz it has been shown that the most promising technique is the *CO* interconnection method. The interconnection method, *SO* with the cylindrical via is promising for a 6dB insertion losses for most of the frequencies between 1 and 6GHz.

4.4.2 Slotted overlap method

In this subsection details of the version of slotted overlap with the best performance, SO (c), are presented. Details and parametric analysis in terms of cylindrical copper via diameter and the effect of side shielding in terms of insertion losses (S_{21}) are given.

4.4.2.1 Via diameter effect

A parametric analysis, using simulations, in terms of the cylindrical copper via diameter was performed, in order to examine the effect of this parameter on the transmission coefficient (S_{21}) of Stripline interconnection method, SO (c). The S_{21} simulation results, for via diameter 1 up to 10mm is shown in Fig. 4-12. It is clear that the via diameter affects the S_{21} performance. For each via diameter the S_{21} was similar at the frequency range of

1-2GHz. Each via diameter, from 1-5mm, yielded peak power transfer (S_{21}) at different frequency between the range of 2 and 6GHz. The case where the via diameter is equal to 3mm, transmits more than half of the power (S21>-3dB) for most frequencies at the examined frequency range. If the insertion loss criterion is settled to 3dB then the 3mm via case is appropriate for specific frequency ranges (1-1.65GHz and 2.5-3.7GHz). If the criterion is settled to 3dB between 2-3GHz then the most suitable case would be the 1mm via diameter. The via diameter cases 6-10mm yielded similar S_{21} performance with the same peak power transfer frequency (3.41GHz). Regarding the reflection coefficient (S_{11}) it is below -10dB for via diameters 1-5mm, resonating at different frequencies which matches with the peak power transfer one (Fig. 4-12). The via diameter cases 6-10mm yield S_{11} below -10dB and equal to -10.2dB at the resonance frequency (3.41GHz).

Fig. 4- 12 Simulated transmission coefficient (S21) results for various values of the diameter of the via in SO (c) stripline interconnection scenario

4.4.2.2 Side shielding effect

In this sub subsection the effect of side shielding (copper on the sides of the striplines) by using simulations on the S_{21} performance of the SO (b) and (c) Stripline interconnection scenarios is investigated. The side shielding is examined because it will be important for a wearable textile Stripline so as to minimize possible dielectric effect from the body [7] and to be shielded from other possible wearable electronics interference. The S_{21} simulation results

of cases SO (b) and (c) (3mm via diameter) with (**S**) and without side shielding (**NS**) are shown in Fig. 4-13. Side shielding highly affects the S_{21} performance of the SO (b) and (c). It is clear that the case of the SO (c) (via) performs better than SO (b). Regarding, the case SO (b) the S_{21} performance was improved by the addition of side shielding at 3.2-6GHz. As for the case of SO (c-3mm via diameter) the S_{21} was improved for most of the examined frequencies, by the addition of side shielding. The SO (c) side shielding case yielded a cut-off power transmission frequency range (3.4-3.97GHz) for which its S21 performance was worse than the case of SO (c) without side shielding. Regarding the reflection coefficient (S_{11}) SO (b) case with side shielding was slightly improved compared without the side shielding one. The main resonance was shifted to the peak S_{21} frequency (Fig. 4-13). Regarding the S_{11} of the SO (c-3mm via diameter) the addition of side shielding improved the S_{11} yielding it lower (except 3.17-4.29GHz) than the one derived from the case without the side shielding.
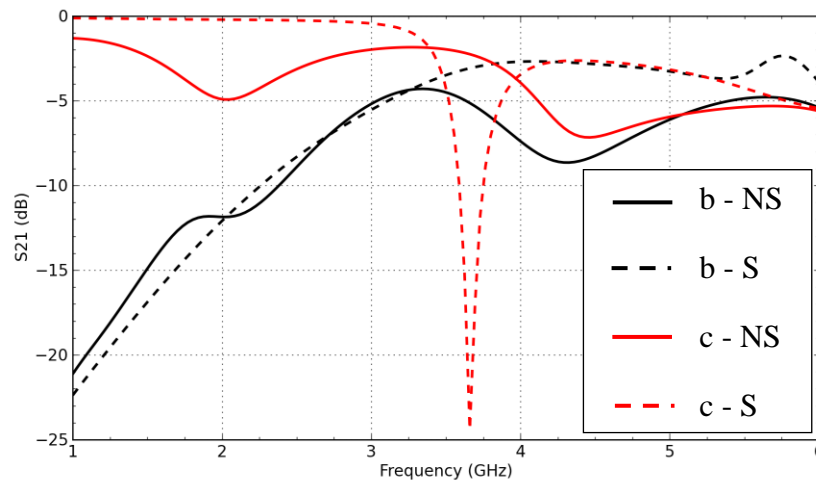
Fig. 4- 13 Simulated transmission coefficient (S21) results with (S) and without (NS) side shielding for the cases of SO (b) and (c-3mm via diameter)

As previously shown the cylindrical via diameter affects the S_{21} performance. In Fig. 4-14 a via diameter parametric analysis, in terms of S_{21}, for the case of SO (c) with side shielding is presented. It can be seen that the cut-off power transmission frequency shifted up by 0.1GHz every 1mm of diameter increase. The best S_{21} performance case is the 10mm via diameter. The S_{11} yielded more values lower than -10dB by the increase of the via diameter. The best S_{11} case was the 10mm.
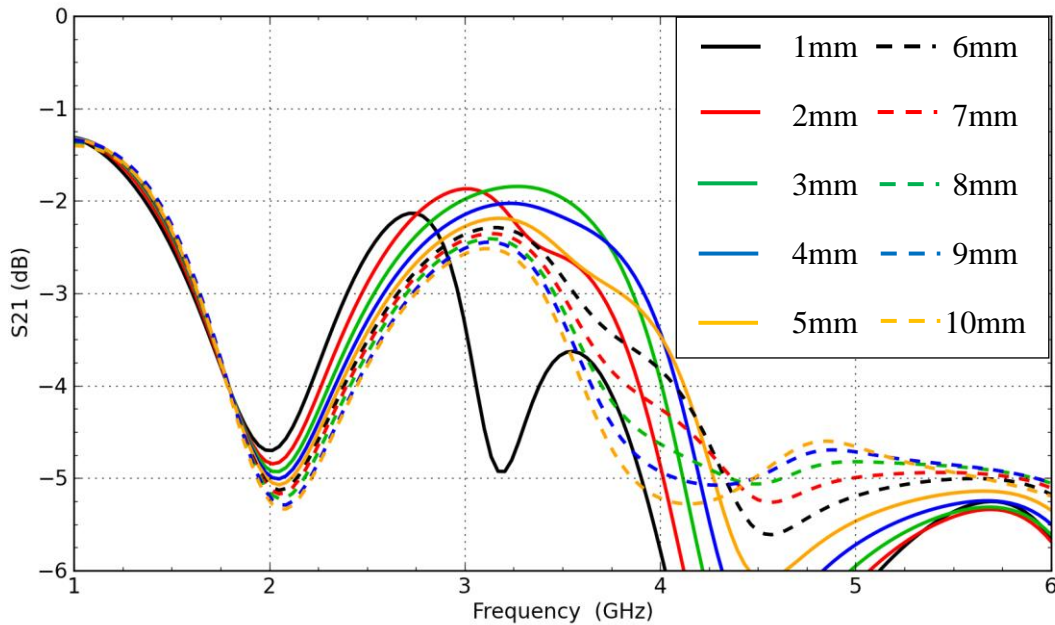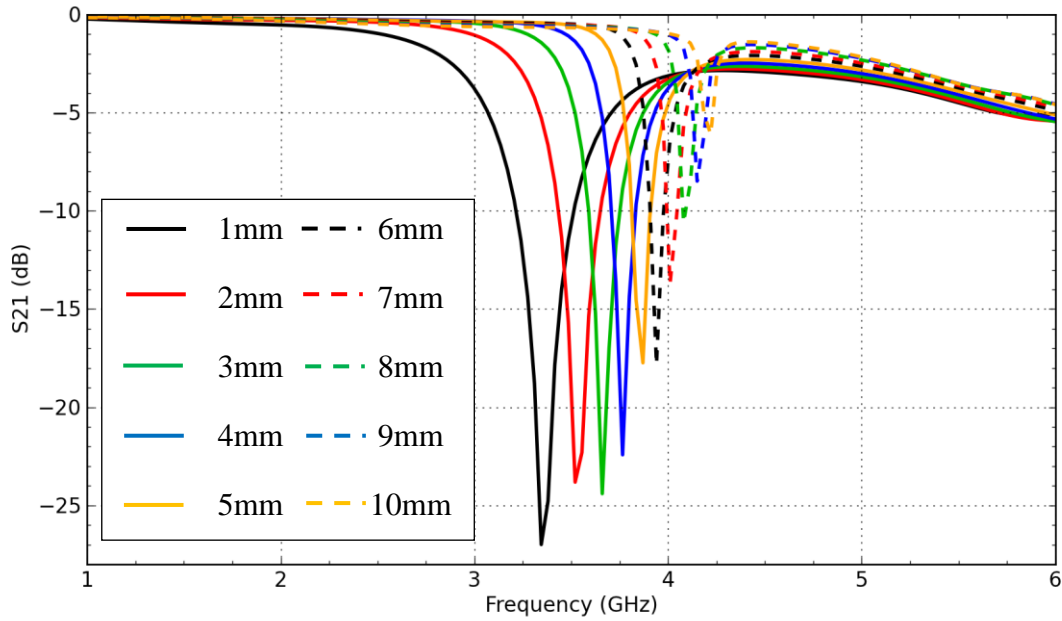
**Fig. 4- 14 Simulated transmission coefficient (S21) results for various values of the diameter of the
via in SO (c) stripline interconnection scenario with side shielding**

4.4.2.3 Prototyping and measurements

In order to evaluate the simulation results of the *SO* (c) model, which turned out to be
the most promising out of all the designed versions of the SO, prototypes of the ST and SO (c)
models were fabricated. The prototypes include the black felt and copper tape (Section
4.3).The prototypes are shown in Fig. 4-15. The SO (c) prototype's via diameter is equal to
6mm.
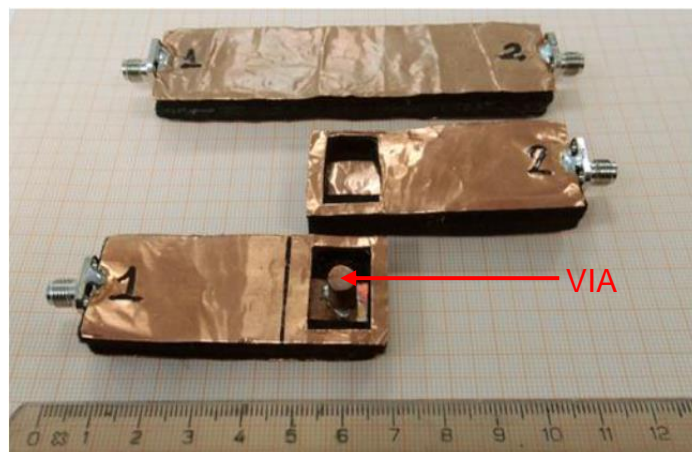
**Fig. 4- 15 Fabricated ST and SO (c) (via diameter = 6mm)
Stripline models**

The S_{21} and the reflection coefficient (S_{11}, S_{22}) measurement results of the SO (c) with and
without side shielding and compared with the ST model are shown in Fig. 4-16 and 4-17

respectively. The ST Stripline model performed the same, in terms of S_{21}, S_{12} and S_{11}, S_{22} with and without side shielding.
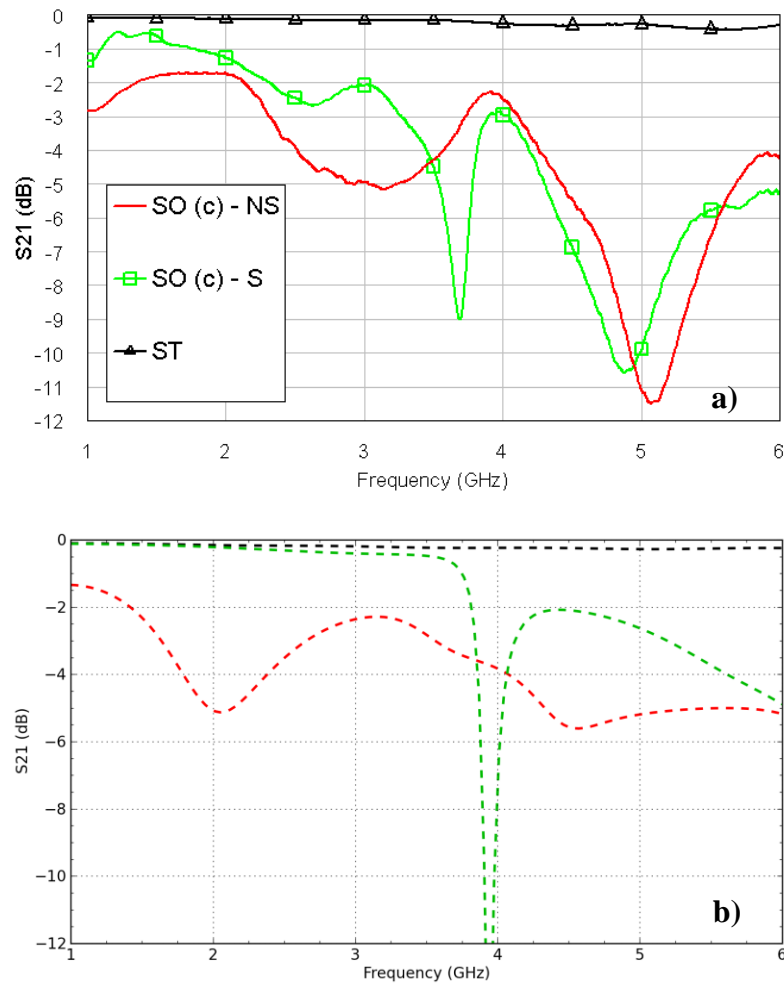
Fig. 4- 16 S21 results of SO (c) (6mm via diameter) with (S) and without (NS) side shielding and of ST stripline models for: a) measurements and b) simulations
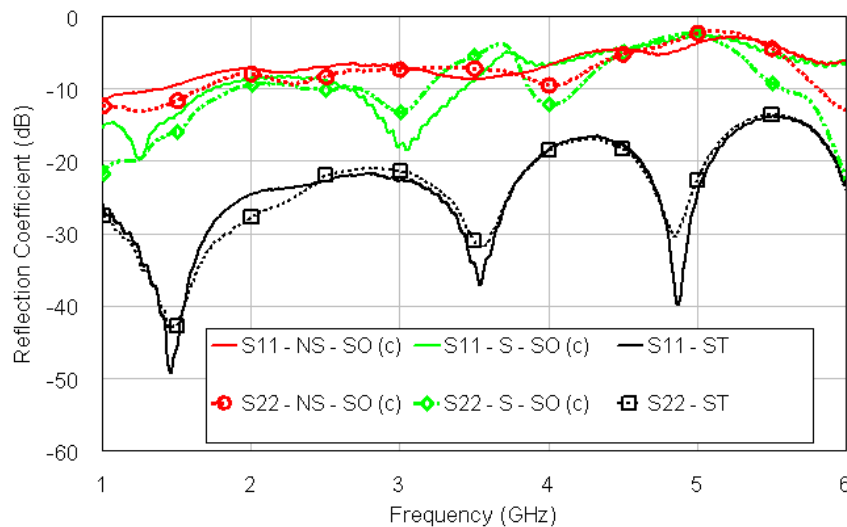
Fig. 4- 17 Measurement results of reflection coefficient of SO (c) with (S) and without (NS) and of ST Stripline models

It is clear from Fig. 4-16 that simulations and measurements are in a reasonable agreement. The differences between simulations and measurements are mainly due to fabrication imperfections such as slot dimensions, via position and felt thickness decrease due to soldering process followed in order to attach copper via to Stripline 1. The fabrication was manually done. The use of side shielding (Fg. 4-16a) improved the S_{21} performance of the SO (c) up to 3.5GHz compared with the case without side shielding ($S_{21S}>S_{21NS}$). Around 3.5GHz an abrupt decrease of the propagation is noticed, probably due to a strong standing wave [19]. The frequency of the standing wave depends on via's diameter (sub subsection 4.4.2.2.). For frequencies higher than 4GHz the measured S_{21} with and without side shielding were quite close deviating from the simulated results (Fig. 4-16b). Regarding the measured reflection coefficient the addition of the side shielding improved the S_{11} and S_{22} bringing them lower than -10dB at some frequency areas of the examined range verifying the reasonable agreement with simulations. The measured S_{11} deviated from S_{22} for the cases of SO (c) with and without side shielding revealing the lack of absolute *two port network symmetry* due to fabrication imperfection issues.

It has been shown via measurements that SO (c) with the side shielding is a promising interconnection scenario. It is appropriate for specific frequency ranges where an insertion loss criterion is settled to 3dB.

4.4.2.4 Conclusions for SO interconnection Stripline scenario

The idea of interconnecting two striplines through slotted overlaping by adding a cylindrical copper via (in order to connect the two strips) is quite promising. The addition of the via significantly improved the power transmission performance by decreasing the insertion loss. The via diameter affected and changed the peak S_{21} frequency. Additionally, the power transmission performance was improved by the addition of side shielding, which is a requirement for isolation from the lossy human body and for shielding from other possible transmissions of other wearable electronics. An issue with the SO (c) interconnection scenario is that the implementation of a via in terms of fabrication and wearable application cannot be a soldered copper cylinder as it is not practical and could increase fabrication difficulty. A possible practical solution, which would lead to an all-textile SO interconnection scenario implementation, could be a snap-on button [17] or a screw where the two parts of the individual striplines could easily be connected and disconnected.

4.4.3 Complementary overlap method

In this subsection details of the complementary overlap (CO) Stripline interconnection method are presented. Details of the effect of the physical (geometrical) discontinuities on the S_{21} performance are presented. Additionally, a solution for improving the performance of the CO method when discontinuities occur is described. More specifically, the ground planes of the longest side (GND) of both individual Stripline parts, of the CO structure, are extended by 10mm. The performance of the fabricated prototypes is presented. An all-textile, practical and flexible fabrication of the CO model is demonstrated.

4.4.3.1 Discontinuities modelling and solution

As presented in subsection 4.4.1 the power transmission performance of the *CO* method is almost the same with the *ST* model. This is an ideal model assuming that there are no discontinuities (physical gaps) between the two individual modified Stripline parts that are connected together so as to structure the *CO* interconnection method. In this sub subsection the modelling of the discontinuities via simulations and their effect on the insertion loss (S_{21}) is presented. The simulation models of the parameters (D_x, D_y, D_z) that describe the discontinuities are shown in Fig. 4-18.
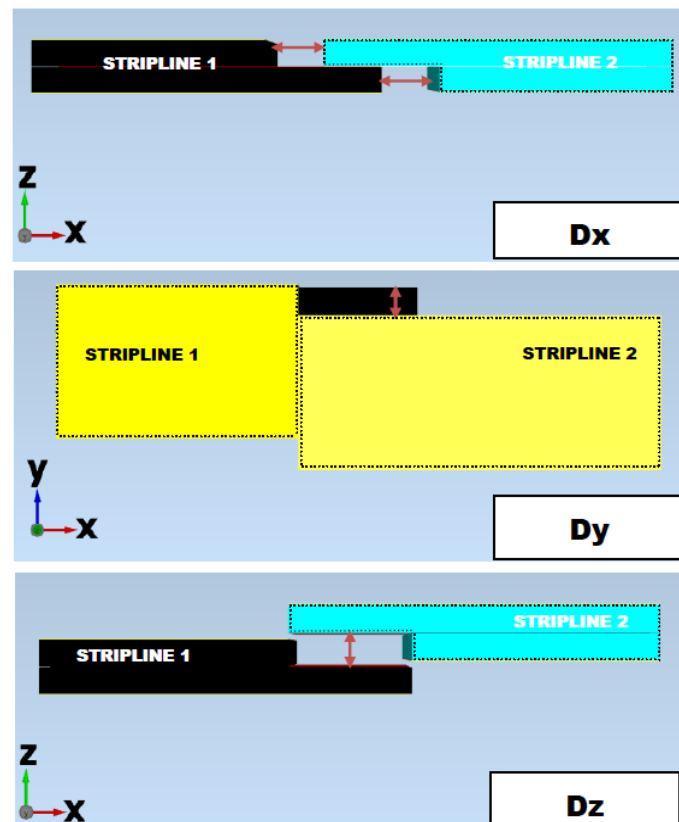
Fig. 4- 18 Complementary Overlap discontinuities simulation modelling

The S_{21} simulation results for various values of the parameters D_x, D_y and D_z are shown in Fig. 4-19. It can be seen that all the discontinuity parameters degraded the power transmission performance, in the case of the *CO* method. The most sensitive out of all the three discontinuity parameters is the D_z. The CO method is affected by the discontinuities between the two ends of the individual parts of the connected striplines.
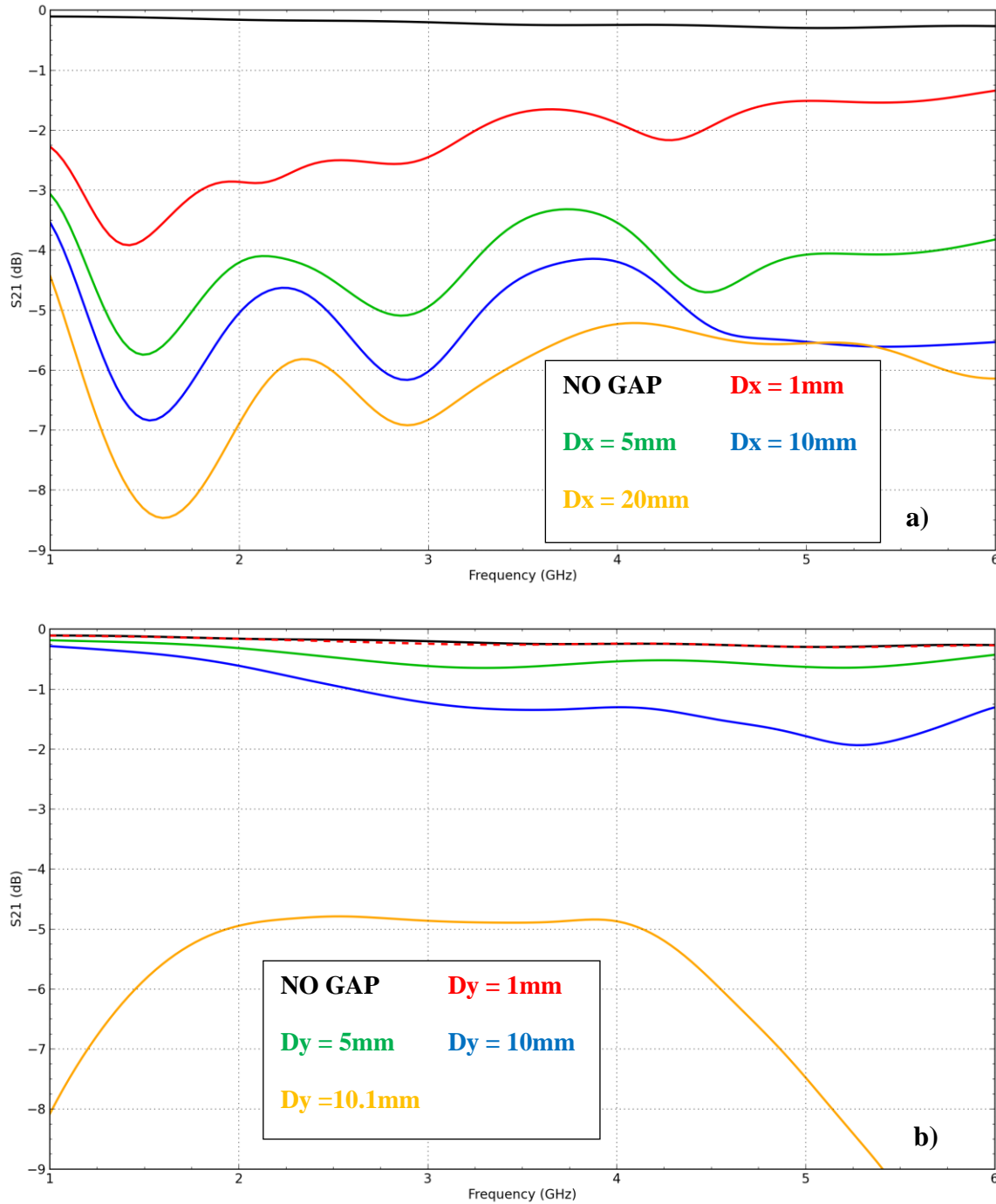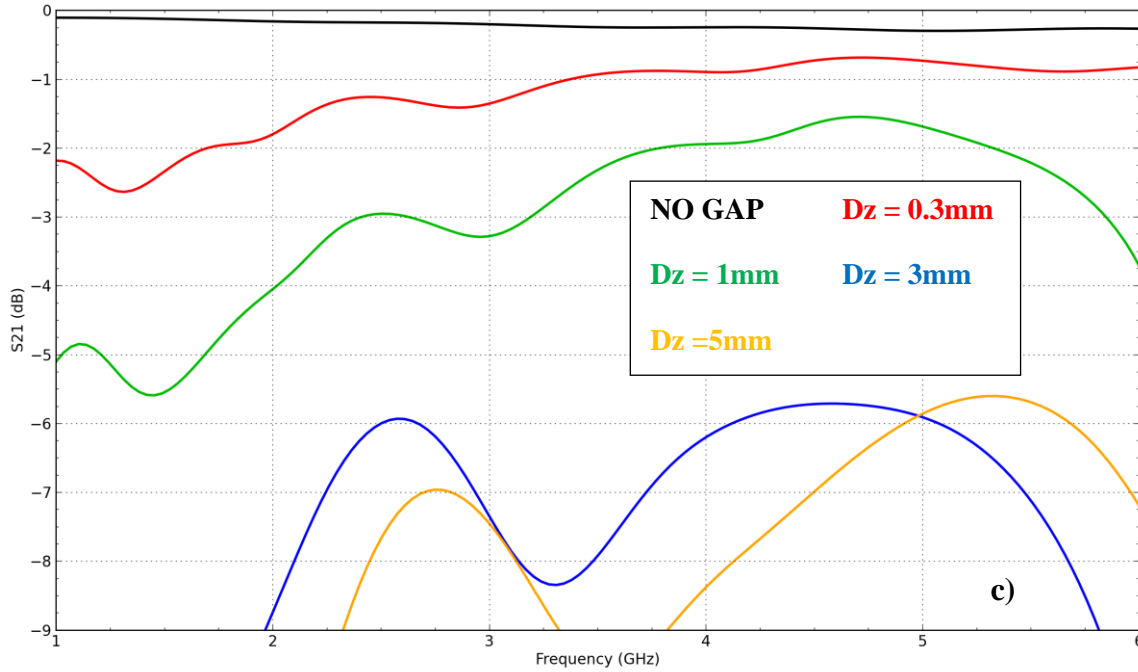
Fig. 4- 19 Transmission coefficient (S21) simulation results for various values of: a) D_x, b) D_y and c) D_z

To ensure better power transmission (less insertion loss) when geometrical discontinuities occur while interconnecting both Stripline parts of the *CO* structure the ground planes of the longest side (GND) of both individual Stripline parts were extended by 10mm (Fig. 4-20). The simulated S_{21} results for the D_x, D_y and D_z values with the extended ground plane (**EG**), for which the non-extended ground plane (**NG**) yielded S_{21} lower than -3dB (Fig. 4-19), are shown in Fig. 4-21.

It can be said that the S_{21} was improved by the extension of the GNDs in the case of D_x and D_z. The D_y=10.1mm was not improved by the extension of the GNDs. But this value means that the two strips make no contact at all. Regarding the concept of CO in terms of practical application the scenario D_y=10.1mm would be a very rare one. From Fig. 4-19b it can be seen that in a scenario of D_y=10mm, where the two strips have a tangential contact the S_{21} was kept higher than -3dB. In terms of practical application of CO the $D_x$ and D_z discontinuities are more likely to occur. The choice of enhancing the *CO* design by extending the GND planes by 10mm, improves the Stripline interconnection method by minimizing the effect of possible connection discontinuities. Regarding the reflection coefficient, when D_x, D_y and D_z occur, it was degraded above -10dB at most frequencies while the discontinuity parameters increased. The extension of the ground planes improved the reflection coefficient at D_x case at all the examined frequency range. Regarding the D_z and D_y the extension of the ground planes didn't significantly affect the reflection coefficient.
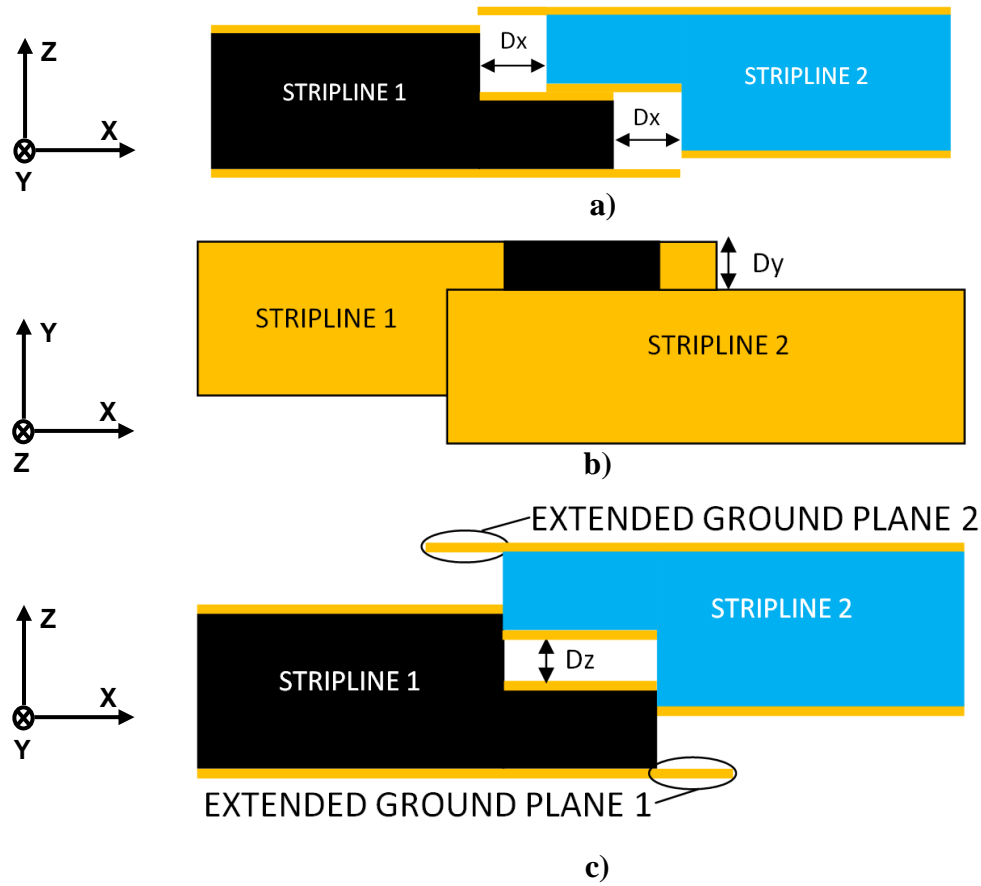
Fig. 4- 20 Schematic of CO geometrical discontinuities: a) Dx, b) Dy and c) Dz with extended ground planes
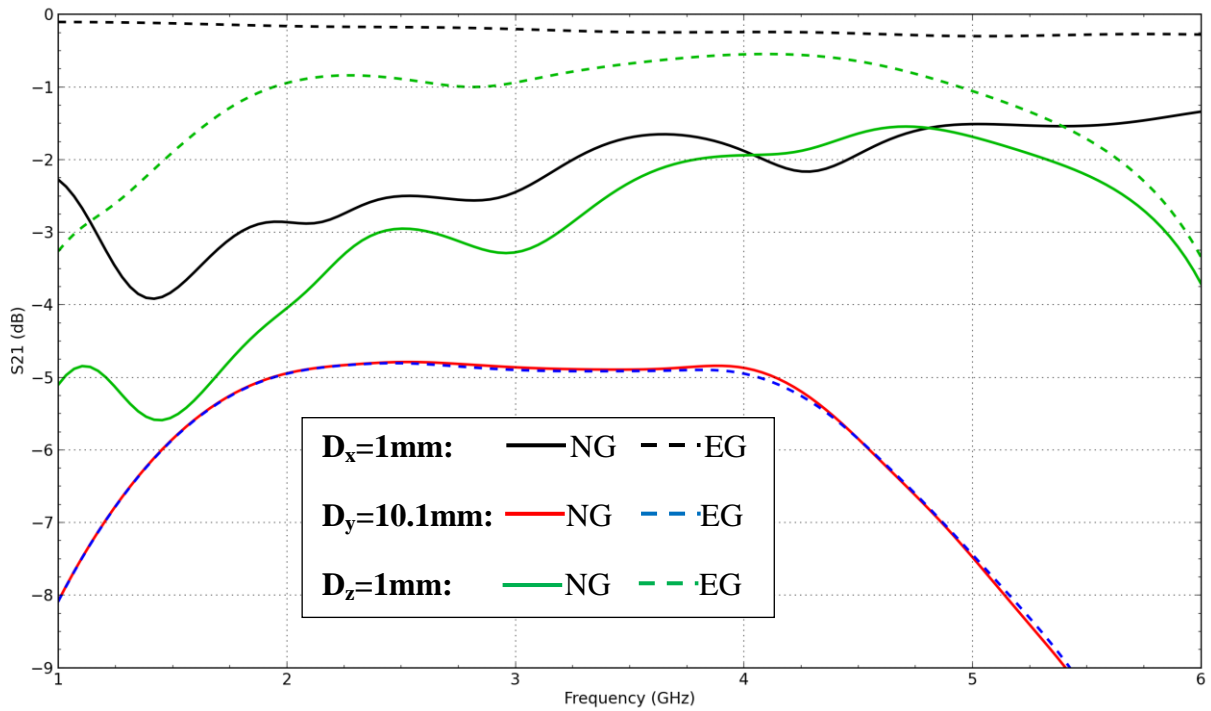
Fig. 4- 21 S_{21} simulation results of CO discontinuity parameters with (EG) and without (NG) extended ground plane

In terms of practical implementation of the CO the physical discontinuities should be avoided. This is an ideal scenario. The extension of the ground planes is proposed as a solution to minimize the effect of possible occurrence of discontinuities in practical applications (real life scenarios).

Finally, regarding the side shielding, which fulfills the wearable criteria [10] and shielding from other electronics requirement, it was found via simulations that the cases of CO with and without side shielding yielded similar performance.

4.4.3.2 Prototyping and measurements

In terms of evaluating the simulated results (Fig. 4-11) a prototype of the *CO* model was fabricated using the black felt as dielectric and copper tape for the conductive parts. This prototype was compared with the respective *ST* (reference) one (Fig. 4-22).

Fig. 4- 22 Fabricated ST and CO prototypes of striplines

The measured transmission coefficient (S_{21}) and reflection coefficient (S_{11}, S_{22}), of the realized striplines, are shown in Fig. 4-23 and 4-24 respectively. The initial prototype of the CO was fabricated without the extended ground planes. For the case of the CO, appropriate measurement setup by using clamps was followed, so as to minimize the gaps (discontinuities) between two strip lines and achieve almost perfect contact of the two parts of the TLs (as in Fig. 4-26). Additionally, the case without using clamps for the S_{21} measurement of the *CO* was examined so as to notice the effect of possible discontinuities occurrence.

The clamps minimized the effect of the possible discontinuities, see Fig. 4-23. The case where discontinuities occur, without the use of clamps, seemed to significantly degrade in S_{21} performance compared with the case where clamps were used. The cases of ST and of the firmly connected CO (with clamps) are in good agreement with simulations (Fig. 4-11). By using the CO method the total stripline model yielded insertion losses less than 0.7dB which is a very promising result in comparison with the 0.5dB insertion losses derived from the ST Stripline model. The reflection coefficient the *CO* with the clamps case is presented in Fig. 4-24. Both prototypes (*ST* and *CO*) yielded S_{11} and S_{22} lower than -10dB. Additionally, good *two port network symmetry* of the realized striplines was noticed as can be seen that S_{11} and S_{22} are quite close. It can be said that the *CO* is a good solution to avoid a coaxial connector, as long as discontinuities are minimized, between striplines in order to transmit power from one stripline to another.
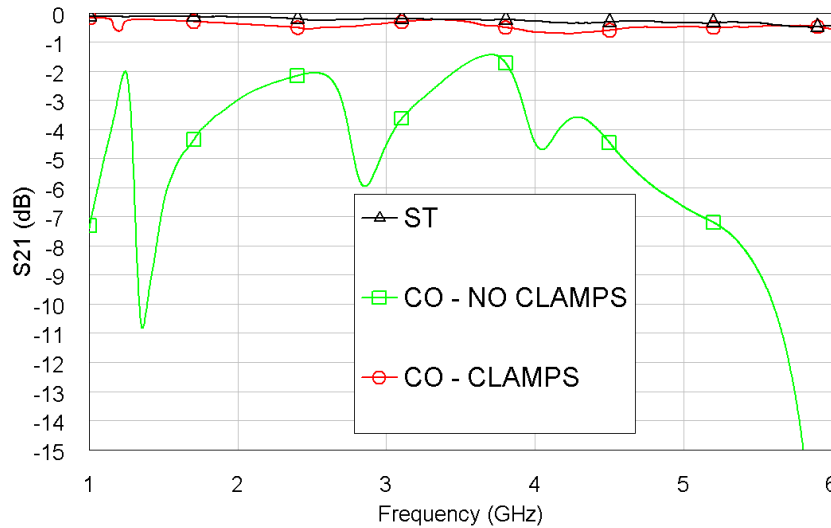
Fig. 4- 23 Measured S21 results of ST and CO prototypes stripline models
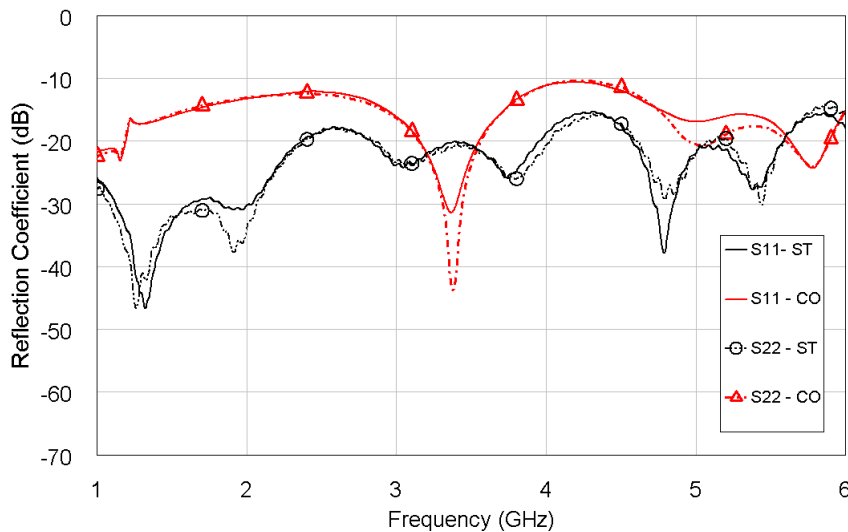
Fig. 4- 24 Measured reflection coefficient (S11 & S22) results of ST and CO (with clamps) prototypes stripline models

4.4.3.3 All-textile fabricaton

The all-textile realization of the *CO* and the *ST* Stripline models were fabricated using the black felt as the dielectric substrate and Nora-dell for the conductive parts. The all-textile version of the *CO* was fabricated by adding the extension (10mm – Fig. 4-20) to the ground planes. The fabricated prototypes of the *ST* and the *CO* TLs are shown in Fig. 4-25.
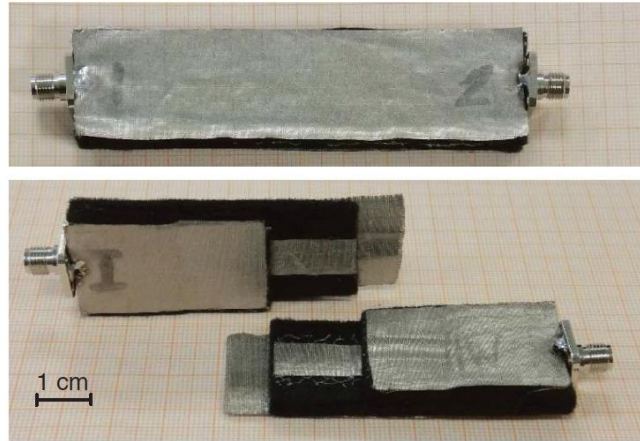
Fig. 4- 25 Fabricated all-textile: ST and CO stripline models

In order to facilitate the measurement of the CO prototype and minimize possible discontinuities, clamps were used to keep the two stripline individual parts of the CO firmly connected (Fig. 4-26). The steps of the CO connection are shown in Fig. 4-26.

Fig. 4- 26 Steps of CO connection for measurement using clamps

The CO was measured with and without using clamps so as to notice differences, in terms of S_{21}, when discontinuities occur. The S_{21} and the reflection coefficient results of the ST and the CO are shown in Fig. 4-27 and 4-28. The S_{21} performance of the *CO* was significantly improved when clamps applied and the discontinuities were minimized. Additionally, a notice that can be said is that the case of *CO* when measured without clamps (discontinuities occur) yielded better S_{21} performance when the extension of ground plane was added (Fig. 4-27) compared with the case without the extension of the ground plane (Fig. 4-23), showing that the use of the extended ground planes is efficient in improving the *CO* power transmission performance when discontinuities occur. The firmly connected CO yielded S_{21} better than -2dB. The nulls in the S_{21} could be due to the pressure applied from the connecting clamps. The height of the dielectric is changing and this affects the line impedance which increases the losses and initiates standing waves [19]. Regarding the reflection coefficient for both all-textile prototypes the S_{11} and S_{22} were lower than -10dB in the examined frequency range. Perfect *two port network symmetry* of both prototypes is not achieved and this is revealed by the S_{11} and S_{22} are not identical.

The maximum insertion loss in the examined frequency range for the 10cm long ST stripline model was 0.6dB (at least 87% of the power is transmitted) and for the same total length CO stripline model it was 1.8dB (at least 66.1% of the power is transmitted).

The losses that the CO interconnection inserts are obviously larger than those of an SMA connector. However, the all-textile CO can be easily incorporated into garments, becoming a flexible solution for interconnecting textile, wearable antennas and electronics. For example, it is proven that a stripline transmission yields significantly less losses than a wireless non-line-of-sight on-body communication link [7] (e.g. chest to back on-body path). Therefore, the CO instead of an SMA connector, can be used efficiently in such a communication link. However, in terms of final wearable, practical and flexible realization, instead of clamps, another solution such as Velcro is proposed in the next sub subsection.
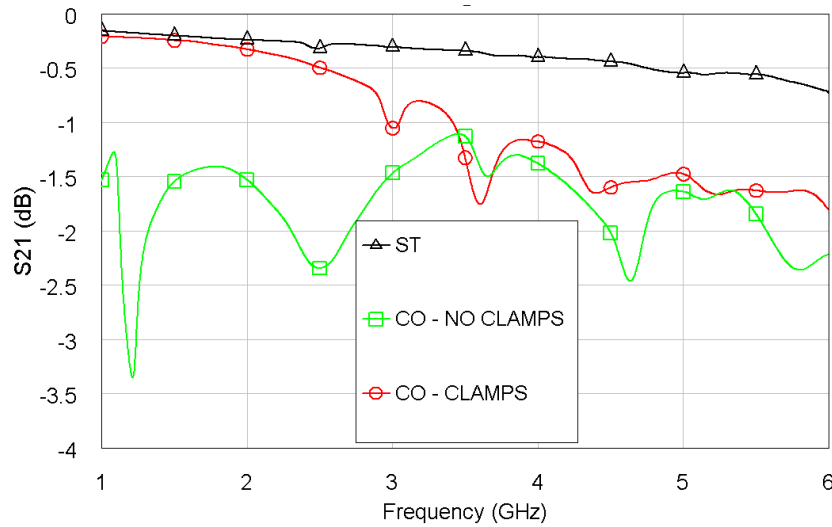
Fig. 4- 27 Measured S21 of all-textile ST and CO stripline models

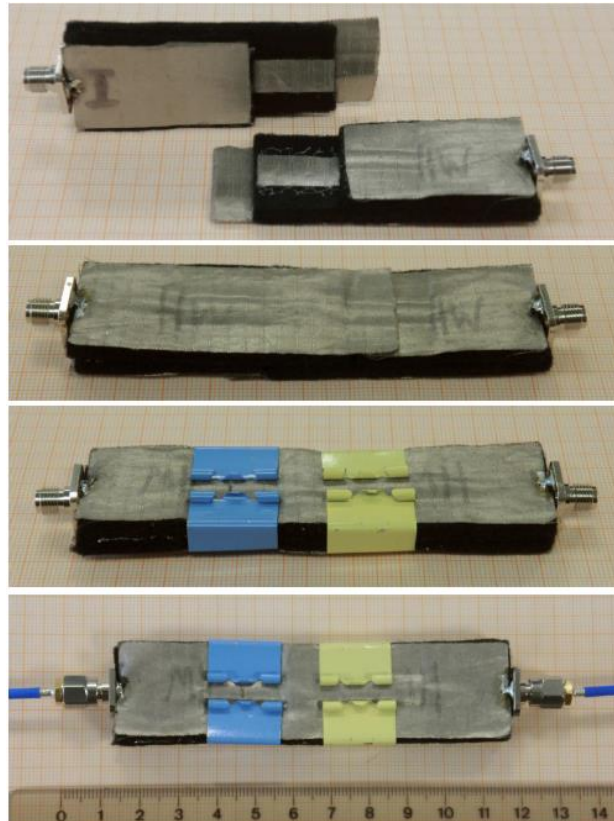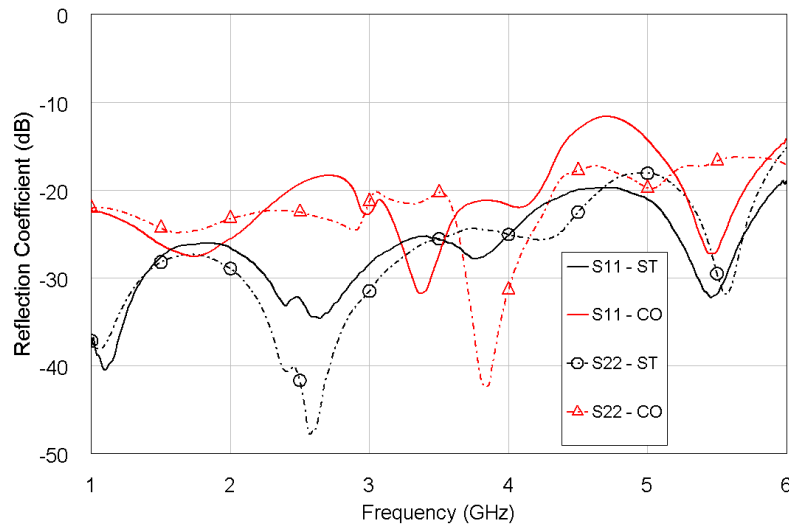**Fig. 4- 28 Measured reflection coefficient of all-textile ST and CO (with clamps) stripline models**

4.4.3.4 Realistic, practical and flexible interconnection implementation

In this subsection the realistic, practical and flexible implementation of the interconnection of the *CO* model, with extended ground planes, is presented. The flexible interconnection is achieved by using non-conductive Velcro. Two prototypes (*ST* and *CO*) are fabricated using the crimson felt as substrate and Nora-dell for the conductive parts. Hooks of the Velcro the were permanently attached to the upper ground planes of the two individual striplines of the *CO* model so as the loops of the Velcro to be used for the interconnection. The *CO* using the Velcro is compared with the CO using the clamps and with the ST-reference model. The *CO* Velcro interconnection is examined for various modifications (Fig. 4-29) which could be real life scenarios ("users way"). Regarding, modifications 1 and 2 the

concept was the same, the hook attached with the loops along the *CO* Stripline length. The loop parts in the case of mod. 1 was 10cm covering the whole length of the *CO*. The loop parts in the case of mod. 2 were 4cm long so as to achieve connection on the 2cm overlapping parts with an extension of 1cm on each side to cover the extended ground planes.

Clamps
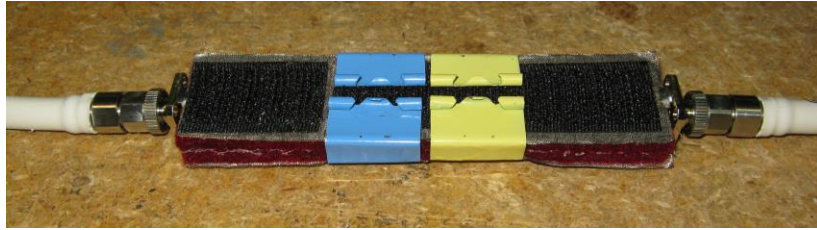
Mod. 1&2

Mod. 3

Mod. 4

Mod. 5

Fig. 4- 29 Measurement setup of CO stripline interconnection model using clamps and various modifications with Velcro

The measured S_{21} and reflection coefficient results (S_{11} and S_{22}) are shown in Fig. 4-30, 4-31 and 4-32 respectively. From Fig. 4-30 it can be said that the modification 1 of Velcro interconnection is the best scenario and yielded S_{21} results (minimum, -2.2dB- more than 60% of power is transmitted) similar to the clamps (-2.2dB) interconnection case. Obviously, modification 1 interconnection scenario resulted into minimization of discontinuities compared with the other examined scenarios (modifications in Fig.4-29). Modification 2 and 5 are the worst cases yielding minimum S_{21} values equal to -4.9dB and -6.5dB respectively. Velcro modifications 3 and 4 are promising and acceptable yielding minimum S_{21} values -3.2dB and -3.1dB at 6GHz and being higher than -3dB (50% power transmitted) at almost all over the examined frequency range. Regarding the $S_{11,}$ all the cases yielded values lower than -10dB except modification 5 which yielded values higher than -10dB at 4.7-5.2GHz. The S_{22} measured values were lower than -10dB for all examined cases. The differences between S_{11} and S_{22} reveal the non-perfect symmetry due to fabrication imperfections and change of height due to pressure applied (by the clamps or the Velcro used, for all the different modifications, Fig. 4-29).

This sub subsection demonstrated an all-textile, practical and flexible connection of the *CO*, using Velcro (modification 1) with very good results yielding insertion losses less than 1dB (79.4% of the power is transmitted) at 1-4GHz, 1.3dB (74.1% power transmitted) at 5GHz and 2.2dB (60% of the power is transmitted) at 6GHz. Finally, this interconnection yielded very good reflection coefficient results lying below -10dB.
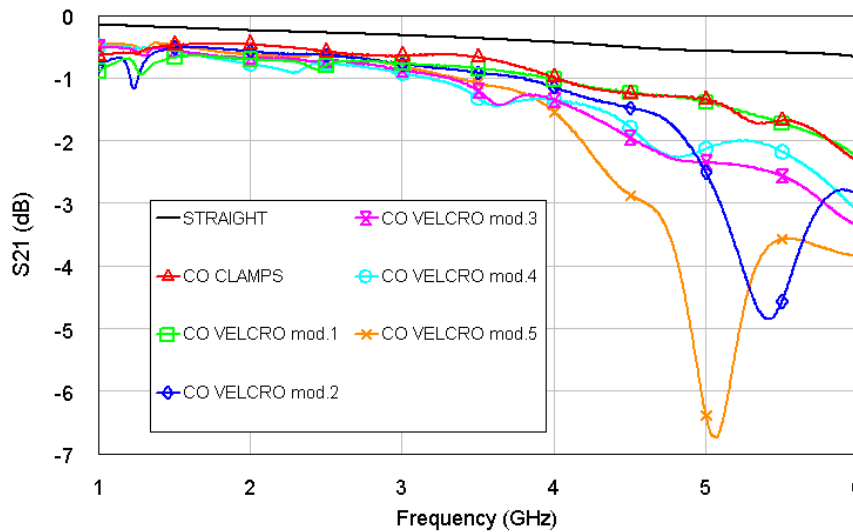
Fig. 4- 30 Measured transmission coefficient (S21) of ST and CO using clamps and Velcro
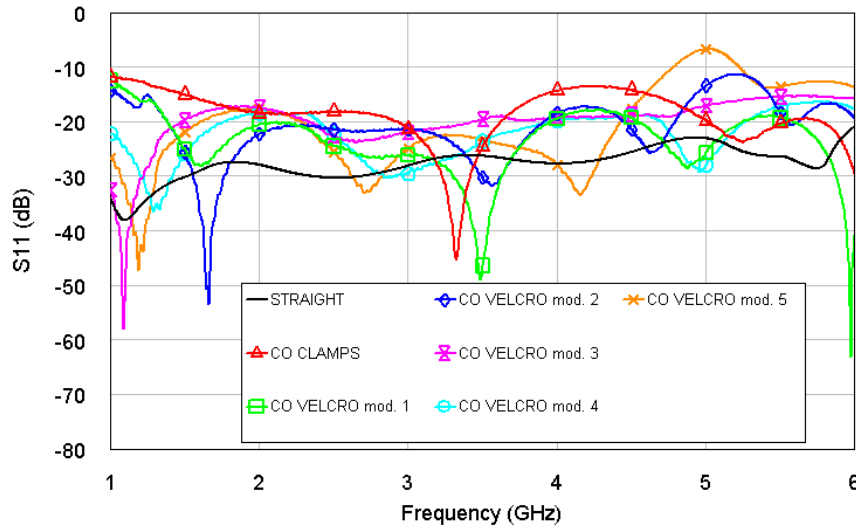
Fig. 4- 31 Measured reflection coefficient (S11) of ST and CO using clamps and Velcro
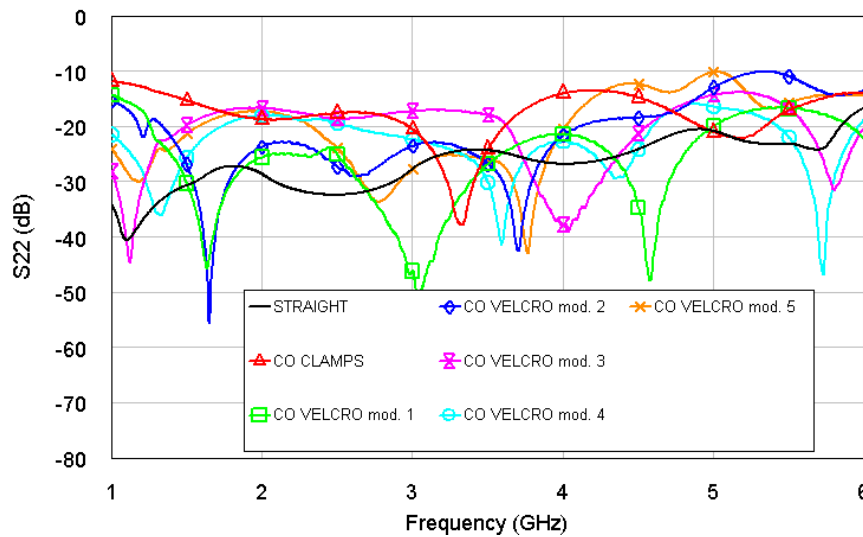
Fig. 4- 32 Measured reflection coefficient (S22) of ST and CO using clamps and Velcro

4.4.3.5 Conclusions for CO interconnection Stripline scenario

The idea of interconnecting two striplines through complementary overlapping (*CO*) each other has been shown to be effective so as to avoid the use of rigid coaxial connectors. It was proved that the physical discontinuities, which could occur, degraded the power transmission performance. The addition of extended ground planes, to the longest sides of both individual striplines forming the *CO* model, improved significantly the S_{21} performance. The *CO* prototype made of felt and copper tape, was very close to the performance of the *ST*

reference stripline model. Finally, the all-textile (felt and Nora-dell) practical and flexible, by using Velcro, realization of the *CO* was proved to be an effective and appropriate wearable solution, yielding insertion losses 1dB up to 4GHz, 1.3dB at 5GHz and 2.2dB at 6GHz. Finally regarding the side shielding wearable requirement, as discussed in sub section 4.4.2, it was found that the CO with and without side shielding yield similar performance. In terms of wearable implementation of the CO scenario it is suggested to add side shielding so as to isolate the stripline from interference coming from the lossy human body and from other possible wearable devices.

4.5 Conclusions

This chapter has presented two novel methods (*SO* and *CO*) for interconnecting stripline transmission lines by excluding the use of rigid coaxial connectors, in terms of design and fabrication. The two methods were compared with a reference conventional straight (*ST*) stripline for which no interconnections are involved. The most efficient and closer to the ST method proved to be the CO one. However, the SO gave promising performance (for a 3dB insertion losses criterion) when a cylindrical copper via was added so as to connect the two strips at the interconnection point.

The stripline theory was introduced, which was used for the design of the *ST*, *SO* and *CO* models. The geometry of the models and the wearable criteria were described, such as the ability of the stripline model shielding the main signal transmission strip from the body. The textile materials properties characterization and selection which were used to design and fabricate the models were presented. These materials are, low loss felt for the dielectric substrate and copper tape and Nora-dell for the conductive parts. It was proved via measurements that the use of conductive cloth Nora-dell increases the insertion losses just by 0.1dB compared to copper tape. Various adhesive techniques were examined in terms of insertion losses (S_{21}), using the *ST* model, so as to attach the dielectric with the conductive textile. Hemming-web adhesive proved to yield less losses than the other examined adhesive ways examined such as the use of UHU glue and non-conductive yarn sewing.

Regarding the *SO* method it was proved through simulations that each via diameter, from 1-5mm, yields a different peak power transfer frequency at 2-6GHz. Additionally, the

case of via diameter equal to 3mm transmits more than half of the power for most of the frequencies at 2-6GHz compared to the other via diameter cases. Additionally, through simulations the side shielding addition effect was studied. Side shielding improves power transfer (for most frequencies at the frequency range of 1-6GHz) of the SO with a trade-off of a cut-off frequency bandwidth occurrence, which depends on via diameter. The best case of the SO with side shielding proved to the one with via diameter equal to 10mm yielding 1dB insertion losses up to 4.1GHz, 6dB at 4.15GHz (cut-off frequency) and 2dB up to 5dB losses at 4.2-6GHz. The SO method was fabricated using felt as dielectric and copper tape as for the conductive parts and compared with an ST model prototype. It was proved that simulations and measurements are in reasonable agreement. They differ due to fabrication imperfections such as slot dimensions, via position and felt thickness decrease due to soldering process in order to attach copper via to Stripline 1. Finally, in terms of real life all-textile, flexible and wearable implementation of the SO a more practical and flexible solution than the copper via should be found. Such a solution could be a snap-on button or a screw.

Regarding the CO it was proved that the physical discontinuities which could occur degrade the power transmission performance. The addition of extended ground planes, of the longest sides of both individual striplines forming the *CO* model, improves significantly the S_{21} performance. The *CO* prototype which was made of felt and copper tape, is very close to the performance of the *ST* reference stripline model. Finally, the all-textile (felt and Nora-dell) practical and flexible, by using Velcro prototype of the CO was fabricated and proved through measurements to be an effective and appropriate "wearable textile targeted solution", yielding insertion losses 1dB up to 4GHz, 1.3dB at 5GHz and 2.2dB at 6GHz. Finally, regarding the side shielding, it was found that the CO with and without side shielding yield similar performance. In terms of wearable implementation of the CO scenario it is suggested to add side shielding. The side shielding is used in Chapter 5 where side CO is applied to interconnect and feed a wearable textile patch antenna with a stripline.

References

[1] P. Hall and Y. Hao, *Antennas and Propagation for Body-Centric Wireless Communications*, 2nd ed. London / Boston: Artech House, 2012.

[2]   A. Tsolis, W. Whittow, A. Alexandridis, and J. Vardaxoglou, "Embroidery and Related Manufacturing Techniques for Wearable Antennas: Challenges and Opportunities," *Electronics*, vol. 3, no. 2, pp. 314–338, May 2014.

[3]   C. Liou, H. Lu, Y. Lin, S. Chuang, W. Ko, and J. Hu, "Low Loss Transmission Lines on Flexible COP Substrate by Standard Lamination Process," in *Electronic Components and Technology Conference (ECTC), IEEE, 64th*, 2014, pp. 1944–1948.

[4]   F. Declercq and H. Rogier, "Characterization of electromagnetic properties of textile materials for the use in wearable antennas," in *Antennas and Propagation Society International Symposium (APS-URSI)*, 2009, pp. 1–4.

[5]   Z. Xu, T. Kaufmann, and C. Fumeaux, "Wearable Textile Shielded Stripline for Broadband Operation," *IEEE Microwave and Wireless Components Letters*, vol. 24, no. 8, pp. 566–568, 2014.

[6]   T. Kaufmann and C. Fumeaux, "Quantifying the Impact of Seam Compression on Embroidered Textile Substrate-Integrated Structures," in *9th European Conference on Antennas and Popagation (EuCAP)*, pp. 1–4.

[7]   Q. Bai, S. Swaisaenyakorn, H.-J. Lee, K. L. Ford, J. C. Batchelor, and R. J. Langley, "Investigation of a Switchable Textile Communication System on the Human Body," *Electronics*, vol. 3, no. 3, pp. 491–503, 2014.

[8]   R. J. Langley, K. L. Ford, and H. Lee, "Switchable on / off-body Communication At 2 .45GHz Using Textile Microstrip Patch Antenna on Stripline," in *6th European Conference on Antennas and Propagation (EUCAP)*, 2011, pp. 728–731.

[9]   H. J. Lee, K. L. Ford, and R. J. Langley, "Switchable on/off-body communication at 2.45 GHz using textile microstrip patch antenna on stripline," *Electronics Letters*, vol. 48, no. 5, p. 254, 2012.

[10]   Q. Bai, H. Lee, K. L. Ford, and R. J. Langley, "Switchable Textile Microstrip Antenna for on / off- body Communications and Shape Distortion Study," in *Asia-Pacific Conference on Antennas and Propagation, IEEE*, pp. 19–20.

[11] L. Zhang, Z. Wang, and J. L. Volakis, "Textile Antennas and Sensors for Body-Worn Applications," *IEEE Antennas and Wireless Propagation Letters*, vol. 11, pp. 1690–1693, 2012.

[12] W. Zheyu, L. Zhang, Y. Bayram, and J. L. Volakis, "Embroidered Conductive Fibers on Polymer Composite for Conformal Antennas," *IEEE Trans. Antennas and Propagation*, vol. 60, no. 9, pp. 4141–4147, 2012.

[13] X. Jia, A. Tennant, R. J. Langley, W. Hurley, and T. Dias, "Knitted Textile Waveguide Bending," in *9th European Conference on Antennas and Popagation (EuCAP)*, pp. 1–4.

[14] T. Kaufmann, Z. Xu, and C. Fumeaux, "Wearable Substrate-Integrated Waveguide with Embroidered Vias," in *8th European Conference on Antennas and Propagation (EuCAP)*, 2014, pp. 1746–1750.

[15] R. D. Seager, W. Whittow, Y. Vardaxoglou, A. Chauraya, and S. Zhang, "Flexible radio frequency connectors for textile electronics," *Electronics Letters*, vol. 49, no. 22, pp. 1371–1373, Oct. 2013.

[16] S. Duarte, R. D. Seager, and A. James, "Microwave Interconnects Between Textile and Rigid Substrates Using Permanent Magnets," in *9th European Conference on Antennas and Popagation (EuCAP)*, 2015, pp. 1–2.

[17] T. Kellomäki, "Snap-On Buttons in a Coaxial-to-Microstrip Transition," in *Loughborough Antennas & Propagation Conference (LAPC)*, 2009, no. November, pp. 437–440.

[18] "http://www.statex.biz/index.php/en/2012-04-06-13-28-47/item/159-shieldex%C2%AE-gewebe", accessed September 2016.

[19] D. M. Pozar, *Microwave Engineering*, 4th ed. John Wiley & Sons, 2012.

[20] S. V Bagad, *Microwave Engineering*, 1st ed. Technical Publications Pune, 2009.

[21] C. A. Balanis, *Modern Antenna Handbook*. John Wiley & Sons, 2008.

[22]   S. Zhang, "Design Advances of Embroidered Fabric Antennas", PhD Thesis, Loughborough, 2014.

[23]   C. A. Balanis, *Advanced Engineering Electromagnetics*, 2nd ed. John Wiley & Sons, 2012.

CHAPTER 5

FEEDING METHODS FOR WEARABLE TEXTILE PATCH ANTENNAS

Abstract

In this chapter the two stripline TLs interconnection methods (*SO(c)* and *CO*) described in Chapter 4 are used for feeding textile patch antennas with striplines. The patch antennas are designed to operate at the 2.5GHz band. Probe-feeds and microstrip-feeds for the SO(c) and CO interconnecting methods are used respectively. The antennas geometry and design is derived from the reference probe and microstrip fed patch antennas with no striplines involved. The proposed antenna structures, with the feeding striplines, are called as PFPA-SO(c) (probe fed patch antenna − slotted overlap (c)) and MFPA-CO (microstrip fed patch antenna − complementary overlap) respectively

The design and the modelling of the reference probe fed patch and of the PFPA-SOc antennas are presented. A cylindrical copper via parametric analysis is carried out, through simulations, yielding the 3mm via diameter one as the best in terms of S_{11} performance matching closer to the reference probe fed antenna. Additionally, the PFPA-SO(c) is compared with the reference antenna in terms of radiation characteristics via simulations. Differences are noticed. The radiation patterns in the case of the PFPA-SO(c) antenna are slightly changed due to stripline existence. However, the PFPA-SO(c) antenna satisfies the broadside patch antenna radiation. Finally, the effect of the feeding stripline length into antenna performance (fc, S_{11}, BW, Gain, Directivity and radiation efficiency) is examined via simulations. Noticeable are the bandwidth increase and the efficiency decrease by stripline length increase.

The design and the modelling of the reference microstrip and of the MFPA-CO antennas are presented. The simulated S_{11} results of the MFPA-CO yields a 0.9GHz downshift in the resonance frequency compared with the reference antenna. Additionally, the MFPA-CO antenna is compared with the reference one in terms of radiation characteristics.

Differences are noticed, such as more power radiated at the side of stripline (MFPA-CO antenna) due to stripline existence. However, the MFPA-CO satisfies the broadside patch antenna radiation. The effect of the feeding stripline length into antenna performance (fc, S_{11}, BW, Gain, Directivity and radiation efficiency) is examined via simulations. The efficiency decreases by stripline length increase. Additionally, the all-textile, practical and flexible (by using Velcro) fabrication of the MFPA-CO, using a 6cm long feeding stripline is presented. The measured S_{11} results show good agreement with the simulations and they are repeatable. The measured radiation patterns are in acceptable agreement with simulations. The fabricated MFPA-CO antenna yields a truly all-textile flexible feeding/interconnecting of a patch antenna enabling a realized wearable antenna.

Finally a real life wearable scenario of the MFPA-CO antenna is implemented. This scenario includes the all-textile feeding stripline of the MFPA-CO which is fed in front of the trunk of a volunteer and it is bended around the trunk like a belt, feeding the patch antenna of the MFPA-CO on the back of the trunk. This real life scenario of the MFPA-CO antenna includes a 54cm long feeding stripline.

5.1 Introduction

5.1.1 Feeding methods of wearable textile antennas

As noticed in Chapter 4 one of the most important parts of wearable communication systems is the antenna and its connection with the wearable electronics is critical for the development of such a system. So far lots of papers have already successfully proposed wearable textile antennas (see Chapter 1) and more specifically patch antennas[1] serving the wearable criteria [2],[3],[4]. The published patch antenna designs rarely consider the connection between the wearable antenna and wearable electronics (e.g. transceiver and/or RF amplifiers). They use rigid connectors and coaxial cables for measurement purposes.

A U.FL low profile connector in combination with a flexible cable could be a possible solution for wearable textile patch antennas feeding [5] (see Fig. 5-1). Also, the use of metallic Snap-on buttons, as an easily detachable wearable solution, has been successfully proposed for RF connectors to feed/connect a wearable textile antenna [6], [7] (see Fig. 5-2). The antenna in Fig. 5-2a is fed with the Snap-on buttons coaxial cable presented in Fig. 4-2d.
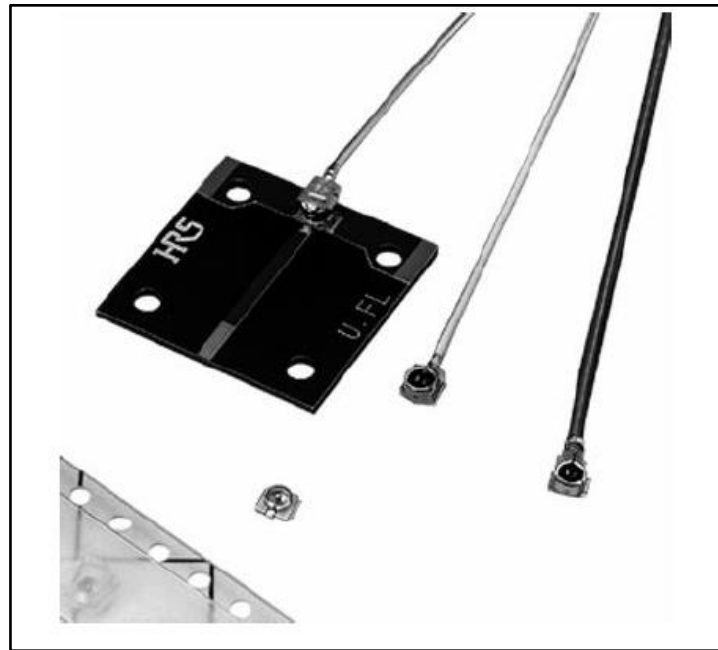
a)

b)

Fig. 5- 1 a) U. FL low profile connectors [5], b) Covered low profile U. FL connector with flexible cable

a)

b)
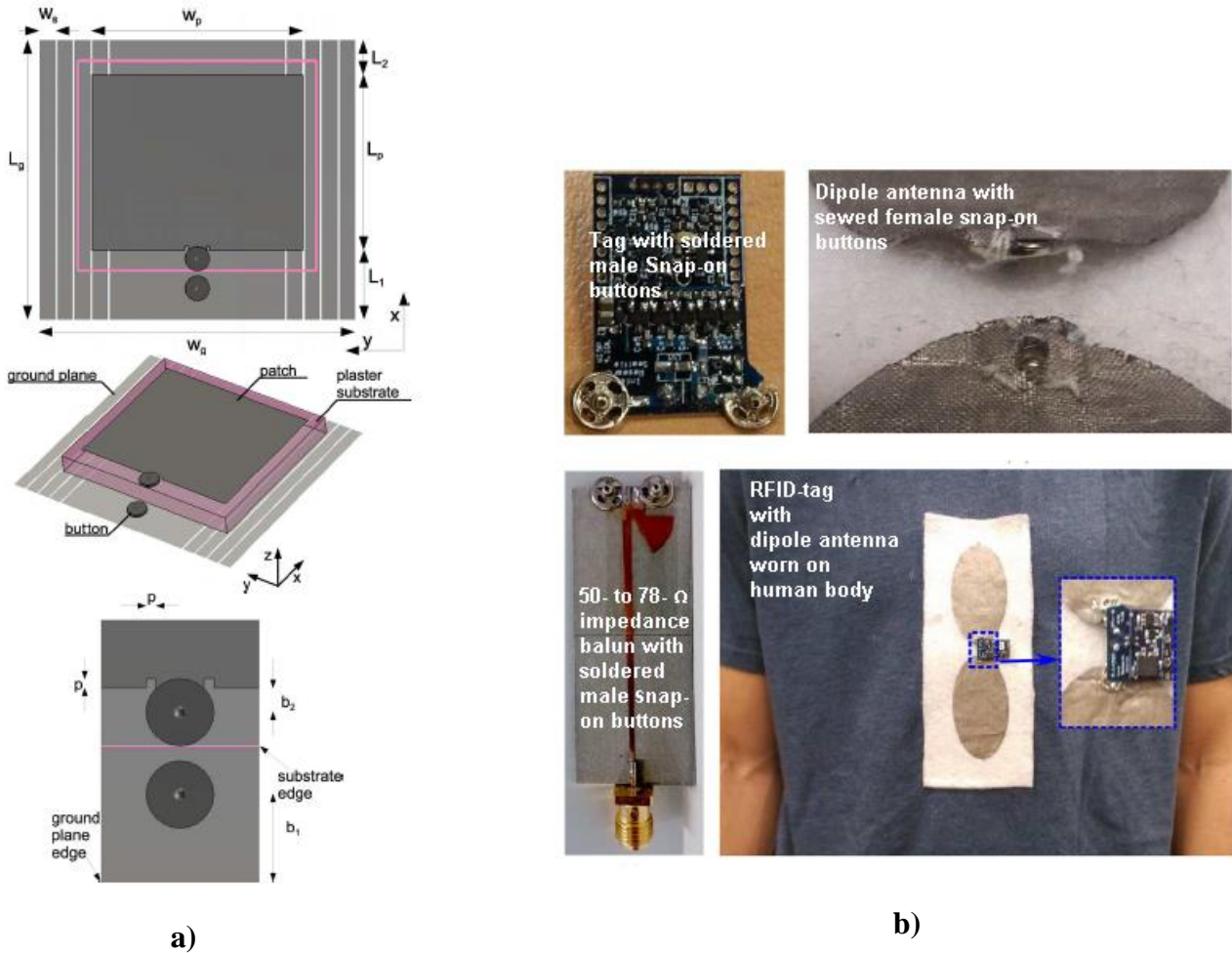
Fig. 5- 2 a) Plaster patch antenna (2.45GHz) structure [6], b) Snap-on button feeding arrangement (RFID-tag with dipole antenna operating at 923MHz) [7]

In this Chapter two new textile patch antennas feeding models (PFPA-SO(c) and MFPA-CO) are presented. The models use the SO(c) and CO methods [8] described in Chapter 4. Both antenna models are compared with the reference probe-fed and microstrip-fed patch antennas respectively. Goals of the proposed feeding patch antenna structures are: a) flexibility in feeding the patch antennas on-body at different positions and b) no rigid (e.g. SMA) connectors will be needed for the feeding/interconnection of the patch antennas by using textile striplines. The PFPA-SO(c) antenna is examined in terms of simulations and a more practical solution than the cylindrical copper via need to be found. The MFPA-CO antenna is examined via simulations and fabricated as an all-textile wearable antenna [9],[10]. The fabricated MFPA-CO antenna provides a practical and flexible antenna which could be attached and detached from feeding stripline without using rigid connectors. This is demonstrated by the implementation of a real life wearable MFPA-CO antenna scenario. The

frequency band of 2.5GHz (ISM, WLAN), was selected for the analysis and design followed in this chapter.

5.1.2 Outline of this chapter

In Section 5.2 the design and modelling of the reference probe-fed patch antenna and of the PFPA-SO(c) antenna is presented. Additionally a metallic via parametric analysis of the PFPA-SO(c) antenna, in terms of S_{11}, is presented and compared with the reference probe fed patch antenna through simulations. Additionally the radiation characteristics of the PFPA-SO(c) antenna and the effect of the feeding stripline length are examined via simulations. In Section 5.3 the design and the modelling of the reference microstrip-fed and of the MFPA-CO antennas is presented. The S_{11}, the radiation characteristics and the effect of the feeding stripline length are examined via simulations. The all-textile flexible prototyping and fabrication of the MFPA-CO antenna is described and presented. The fabricated MFPA-CO antenna is measured in terms of S_{11} and radiation characteristics. In Section 5.4 the implementation of a real life wearable scenario of the MFPA-CO antenna is presented and evaluated using S_{21} power transmission measurements. In Section 5.5 conclusions from this chapter are drawn.

5.2 Probe fed textile patch antenna using slotted overlap-via method

In this section the feeding of a patch antenna with a stripline using the slotted overlap via (*SO(c)*) with side shielding method, described in Chapter 4, Section 4.4, is presented. This antenna has been defined as PFPA-SO(c) (probe fed patch antenna-slotted overlap (c)). For the design of this structure a conventional reference probe fed patch antenna [11] was designed to operate at 2.5GHz. The PFPA-SO(c) design was consisted of the reference patch antenna fed through a stripline using SO(c) method with side shielding. Additionally, a cylindrical copper via diameter parametric analysis was carried out to found the optimum value of diameter, resulting into S_{11} closer to the reference patch antenna. The simulated far field and radiation characteristics of the PFPA-SO(c) were compared with those derived from the reference antenna. The effect of the stripline length of the PFPA-SO(c) into antenna performance is presented.

5.2.1 Patch antennas design and modelling

The materials used for the design and simulation of the reference and PFPA-SO(c) antennas are: the 4mm thick black felt (Chapter 4, Section 4.3) for the dielectric parts and 120μm thick copper for the conductive parts. The geometry of the reference probe fed patch antenna is shown in Fig. 5-3 [12]. The PFPA-SO(c) antenna is: a) the individual part of SO(c) model (Chapter 4, Section 4.4), 6cm long Stripline 1 with the cylindrical copper via with side shielding and b) the reference probe fed patch antenna with a rectangular slot on its ground plane and substrate so as to match the slot of part a). The concept of the PFPA-SO(c) model feeding and interconnecting is shown in Fig. 5-4. In real life implementation the copper via could be a Snap-On button [13] or a screw.
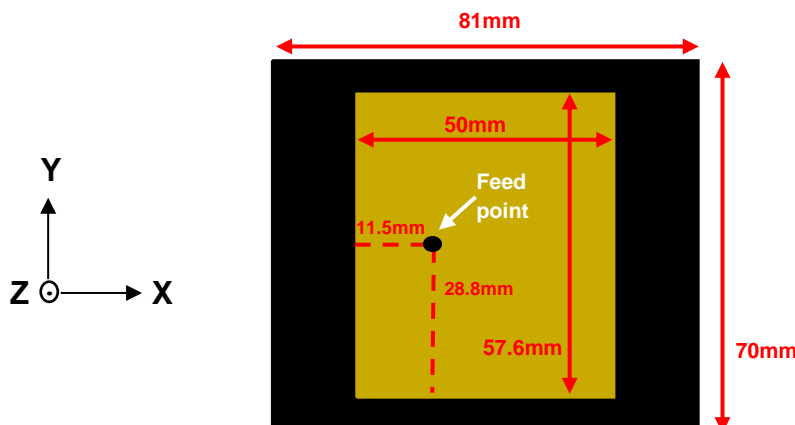
Fig. 5- 3 Geometry of reference probe fed 2.5GHz patch antenna
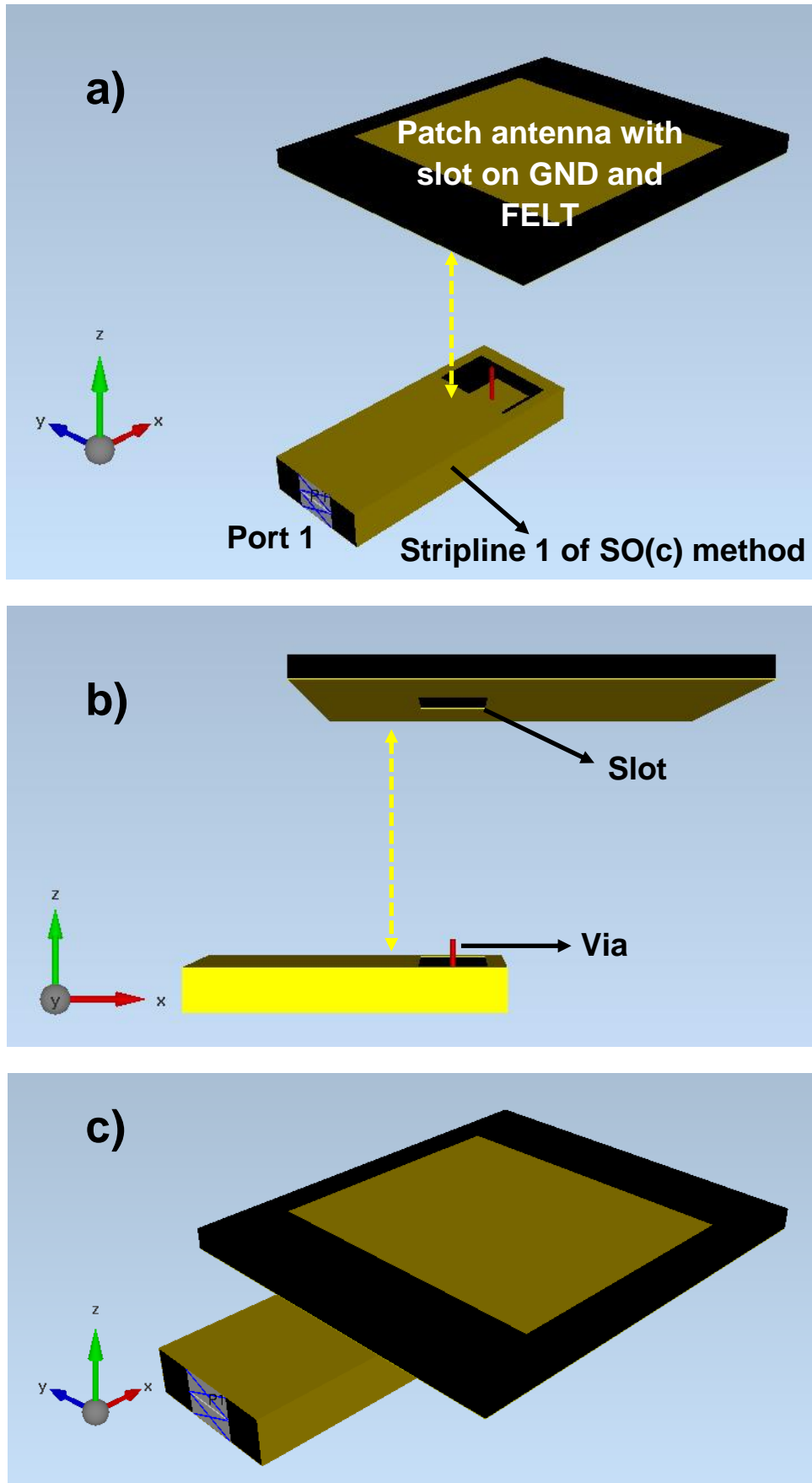
Fig. 5- 4 Concept of PFPA-SO(c) structure (Empire-XPU simulation environment display): a) 3D view disconnected, b) XZ-plane disconnected and c) 3D view connected

5.2.2 Via diameter parametric analysis

A parametric analysis, using simulations, in terms of the cylindrical copper via diameter was performed, in order to examine the effect of this parameter into the reflection coefficient (S_{11}) of the PFPA-SO(c). The parametric analysis was aimed to find the value of the via diameter which results to S_{11} matching better with the corresponding reference probe fed patch antenna. The S_{11} simulation results, for via diameter values, from 1 to 10mm and for the reference probe fed patch antenna are shown in Fig. 5-5.
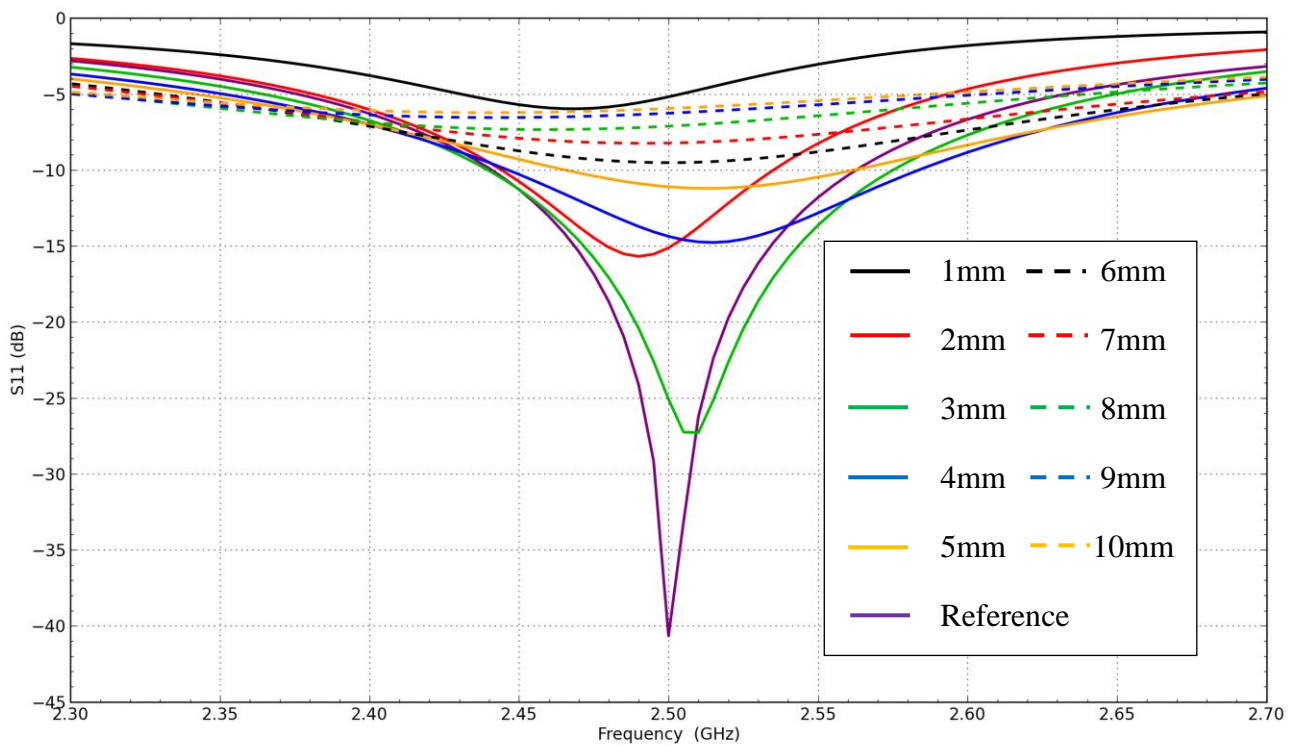
Fig. 5- 5 Simulated reflection coefficient (S_{11}) of the reference patch antenna and of the PFPA-SO(c) for various values of the cylindrical copper via

According to Fig. 5-5 the cases of via diameter equal to 2, 3, 4 and 5mm yielded S_{11} lower than -10dB. The best case was the 3mm via diameter which matches better to the S_{11} yielded from the reference patch antenna and resulted into S_{11} with the lowest values. So, the optimum via diameter is the 3mm one. The following analysis in the next subsections of this section (5.2) use the 3mm value for via diameter.

5.2.3 Simulated radiation characteristics

In this subsection the simulated radiation patterns of the PFPA-SO(c) antenna were compared with the reference probe fed patch antenna so as to examine possible effect of the existence of the stripline feeding structure to the radiation. The radiation patterns which were normalized to maximum value for the azimuth (YZ-plane) and elevation (XZ-plane) for both antenna structures are shown in Fig. 5-6.
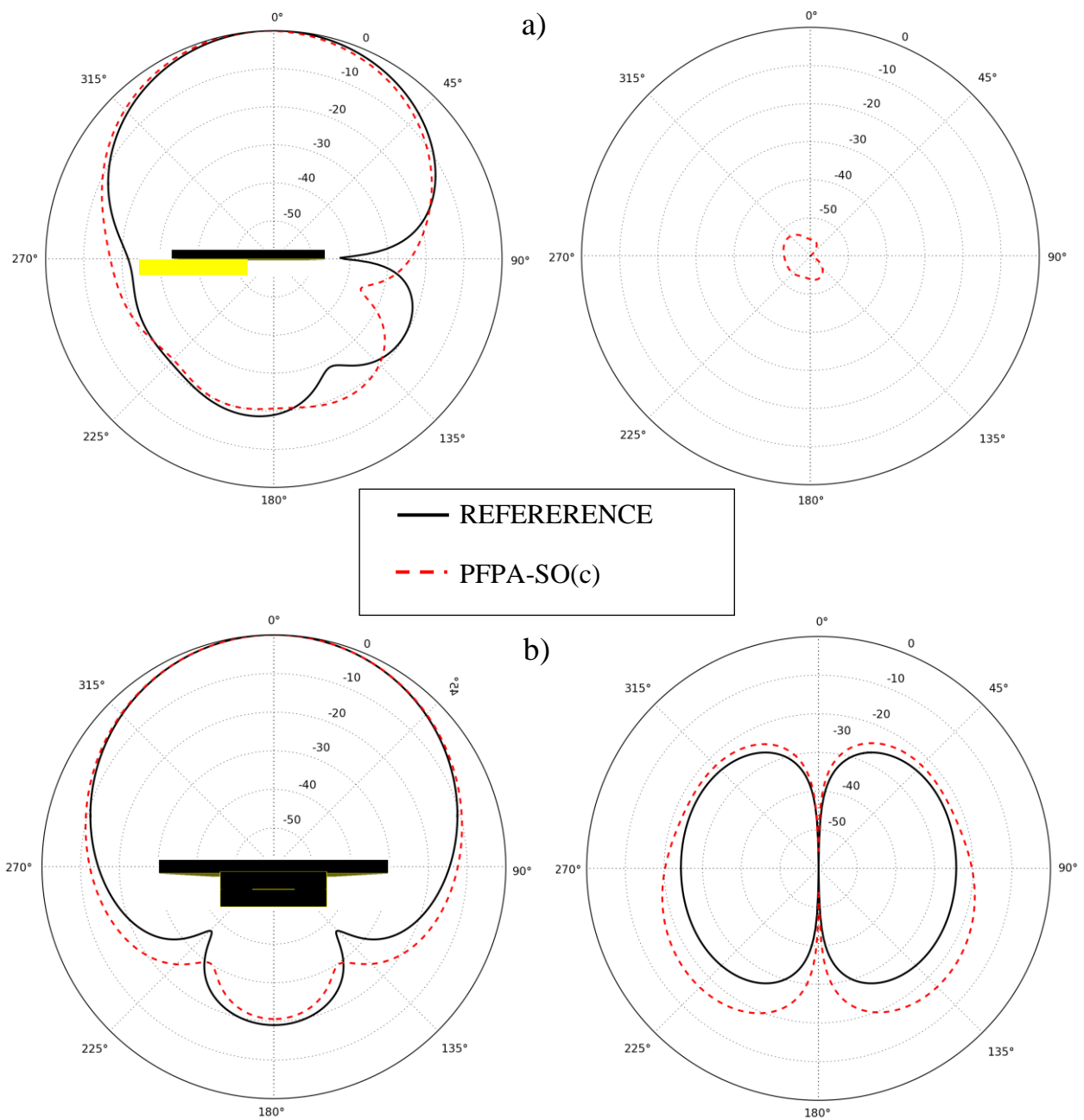
Fig. 5- 6 Simulated normalized to maximum value radiation patterns for PFPA-SOc (2.51GHz) and reference probe fed patch antenna (2.50GHz) at: a) Elevation (XZ) plane and b) Azimuth (YZ) plane where left column are the co-polar and the right column are the cross-polar patterns

It can be seen from Fig. 5-6 that differences are noticed between the radiation patterns derived from the PFPA-SO(c) compared with the reference probe fed patch antenna. A noticeable difference was the increased cross-polar in the case of the PFPA-SO(c) antenna (notice that in Fig.5-6a the cross polar of the reference patch is negligible, around -150dB and not shown). Additionally it is noticed that on the elevation plane the co-polar main lobe (Fig. 5-6a) of the PFPA-SO(c) was a little shifted towards the stripline (270°). At 270° (the stripline side) more power is radiated compared with the reference patch antenna. Additionally and regarding the co-polar elevation plane (Fig. 5-6a) differences are noticed at the angles between 90°-270° (back side of the structures). Regarding the azimuth plane (Fig. 5-6b) and the co-polar components the PFPA-SO(c) yielded wider main lobe, more power radiated at 90° and 270°. Finally, it could be said that the PFPA-SO(c) satisfies the broadside patch antenna radiation.

5.2.4 Feeding stripline length effect on antenna performance

In this subsection the effect of the length of the feeding stripline part of the PFPA-SO(c) antenna, on antenna performance is presented. This effect was examined through simulations. The initial design (subsection 5.2.1) of the PFPA-SO(c) antenna used a 6cm long feeding stripline. A PFPA-SO(c) antenna with a 10cm, 20cm, 30cm and 60cm long feeding stripline was simulated. The simulated results for these versions of the PFPA-SO(c) and of the reference probe fed patch antenna are shown in Table 5-1.

Table 5- 1 Simulated results of reference probe fed patch antenna and of the PFPA-SOc for 6cm, 10cm, 20cm, 30cm and 60cm long feeding stripline

	Reference	6cm	10cm	20cm	30cm	60cm
f_0 **(GHz)**	2.5	2.51	2.51	2.51	2.51	2.51
S_{11} **(dB)**	-40.66	-27.28	-36.10	-29.19	-26.16	-30.08
BW (MHz)	125	135	145	150	160	180
Gain (dBi)	8.22	7.93	7.10	7.59	7.49	7.05
Directivity (dBi)	8.72	8.50	7.70	8.37	8.52	8.61
e_{rad} **(%)**	88.96	87.70	87.00	83.50	78.83	69.78

As can be seen from Table 5-1 the resonant frequency was shifted by 10MHz in the case of PFPA-SO(c) (for all versions examined) compared with the reference probe fed patch antenna.

The S_{11} was well kept lower than -10dB revealing that the feeding of the PFPA-SO(c) is well matched. Regarding the bandwidth (BW) all the versions of the PFPA-SO(c) yielded BW larger than the reference probe fed patch antenna. In the case of the PFPA-SO(c) the BW increased by length. All the versions of the PFPA-SO(c) yielded lower gain and directivity than the reference antenna. But still, the gain and the directivity for all the versions of the PFPA-SO(c) was kept at the expected levels of a patch antenna [12]. As expected and due to stripline existence the radiation efficiency decreased in the case of the PFPA-SO(c) compared with the reference antenna and decreasing by stripline length increasing. At the case of 60cm PFPA-SOc, the radiation efficiency was decreased by 19.18% compared with the reference one, which decrease includes the stripline and patch antenna losses. The efficiency value of 69.78% is a good efficiency, considering the use of a long (60cm) stripline, making this structure an acceptable candidate for wearable application.

5.3 Microstrip fed textile patch antenna using complementary overlap method

In this section the feeding and interconnection of a patch antenna with a stripline using the complementary overlap (*CO*) with side shielding method, as described in Chapter 4, is presented. This antenna has been called as MFPA-CO (microstrip fed patch antenna-complementary overlap). For the design of this structure a conventional reference microstrip fed patch antenna [11] was designed to operate at the 2.5GHz band. The MFPA-CO design is consisted of the reference patch antenna fed through a stripline using CO with side shielding method. The stripline is connected with a microstrip fed patch antenna, so an appropriate transition is required [14]. Simulation results derived from the MFPA-CO were compared with the reference microstrip fed patch antenna. These results are presented in terms of reflection coefficient, radiation characteristics and effect of the feeding stripline length on the antenna performance. Finally, the all-textile, practical and flexible (using Velcro) realization of the MFPA-CO antenna is described and measurement results are presented as well.

5.3.1 Design and modelling of microstrip fed patch antennas

The materials used for the simulation and design of the reference and the MFPA-CO antennas are: the 4mm thick crimson felt (Chapter 4. Section 4.3) for the dielectric parts and the 130μm thick cloth Nora-dell [15] for the conducting parts. The geometry of the reference microstrip fed patch antenna is shown in Fig. 5-7 [12]. The feeding width [16] was followed up to the patch by a quarter-wave impedance transformer [17] so as to match the patch antenna impedance to the approximate 50 Ohms impedance of the feeding width. Simulation parametric analysis was followed (criterion best S_{11} performance) so as to conclude to the 5mm width of the transformer. This model was selected as it is simpler to fabricate than a microstrip inset feed patch antenna (see Appendix B) in terms of an all-textile implementation. The MFPA-CO antenna consists of (Fig. 5-8): a) the individual part of CO model (Chapter 4), 6cm long Stripline 1 with side shielding (with 1.5cm long, the CO part) and b) the reference microstrip fed patch antenna starting with the 1.5cm upper part of the CO and a 5mm long stripline to microstrip transition. The stripline to microstrip transition was required to provide smooth electromagnetic field matching (from TEM to quasi-TEM) and almost unchanged characteristic impedance along the transition section [14]. This means that losses due to transition from reflections will be minimized. The stripline to microstrip transition was achieved by a tapered slot in the upper ground plane (progressively widening the slot width) and by widening the main transmission line width (from 10mm to 17mm). The substrates and the bottom ground plane of the transition were not changed. The geometry of the transition is shown in Fig. 5-8. The losses inserted by the transition part were 0.41dB at 2.5GHz (Fig. 5-9). The reflection coefficient (S_{11}) of the transition is well kept below -10dB. These losses were less than 0.5dB which is assumed acceptable as described in [14]. The concept of the MFPA-CO model feeding and interconnecting concept is shown in Fig. 5-8. In terms of implementation, the MFPA-CO is proposed (subsection 5.3.3) to be achieved by using a non-conductive Velcro, yielding a flexible and a user friendly solution.
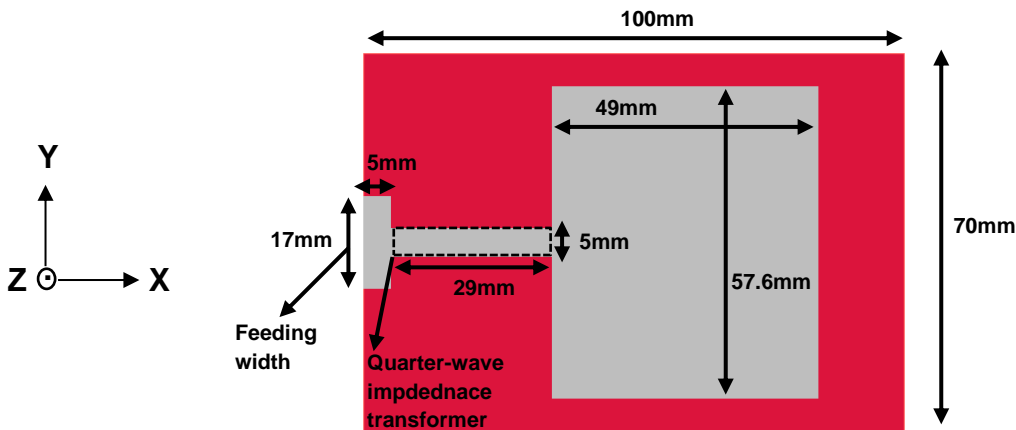
Fig. 5- 7 Geometry of the reference microstrip-fed 2.5GHz band patch antenna

a)

Patch antenna with stripline to microstrip transition

Port 1

Stripline 1 of CO method

b)

Reference patch antenna100mm

Stripline 60mm

Stripline to microstrip transition 5mm

10mm → **17mm**

Main TL transition 5mm long

Upper ground plane transition 5mm long
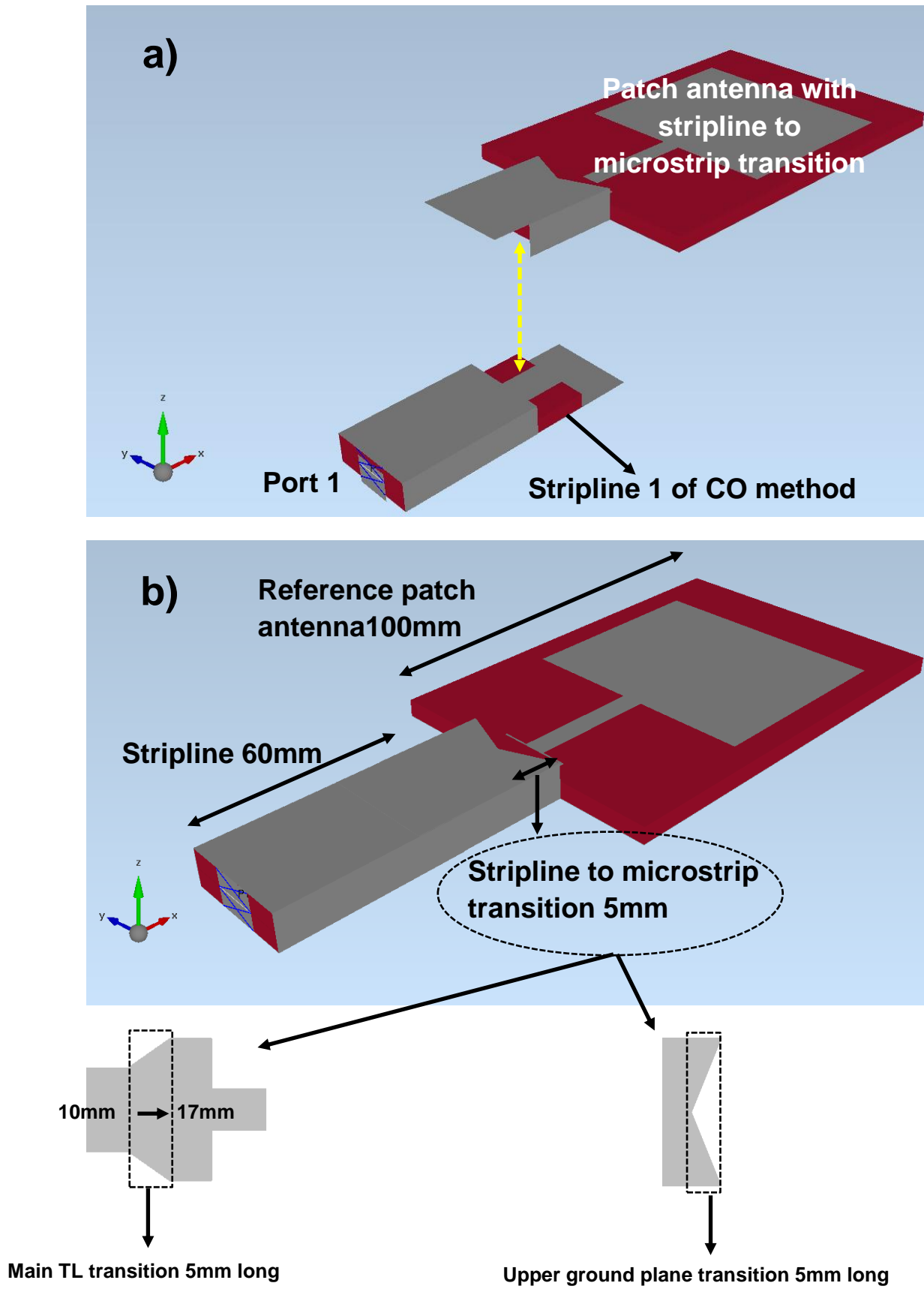
Fig. 5- 8 Concept of MFPA-CO structure (Empire-XPU simulation environment display): a) disconnected and b) connected
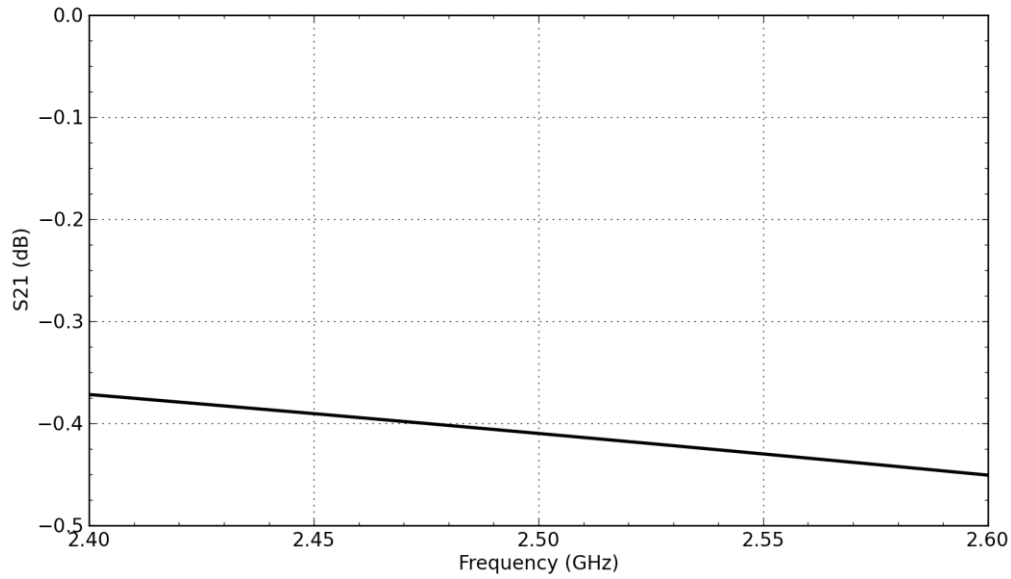
Fig. 5- 9 Simulated transmission coefficient (S21) of the 5mm long Stripline to microstrip transition line with total length equal to 25mm

5.3.2 Simulation results

5.3.2.1 Reflection coefficient

The simulated reflection coefficient (S_{11}) results of the MFPA-CO (6cm stripline) antenna compared with the reference microstrip fed patch antenna are shown in Fig. 5-10. The reference patch antenna yielded resonance at 2.56GHz and the MFPA-CO downshifted at 2.47GHz. So, if an MFPA-CO antenna is required to resonate at 2.5GHz then the reference should be designed for resonating at approximately 2.6GHz.
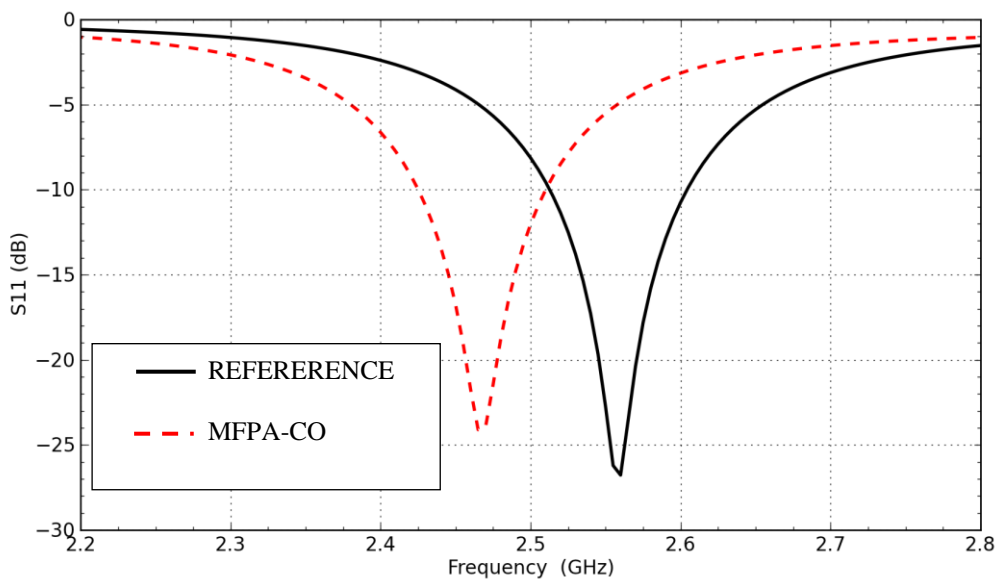
Fig. 5- 10 Simulated reflection coefficient (S11) for the reference microstrip fed patch antenna and for the MFPA-CO antenna

5.3.2.2 Radiation characteristics

In this subsection the radiation patterns derived from the simulation of the MFPA-CO were compared with the reference microstrip fed patch antenna so as to examine possible effect of the existence of the stripline feeding structure to the radiation. The radiation patterns normalized to maximum value for the azimuth (YZ-plane) and elevation (XZ-plane) for both antenna structures are shown in Fig. 5-11.
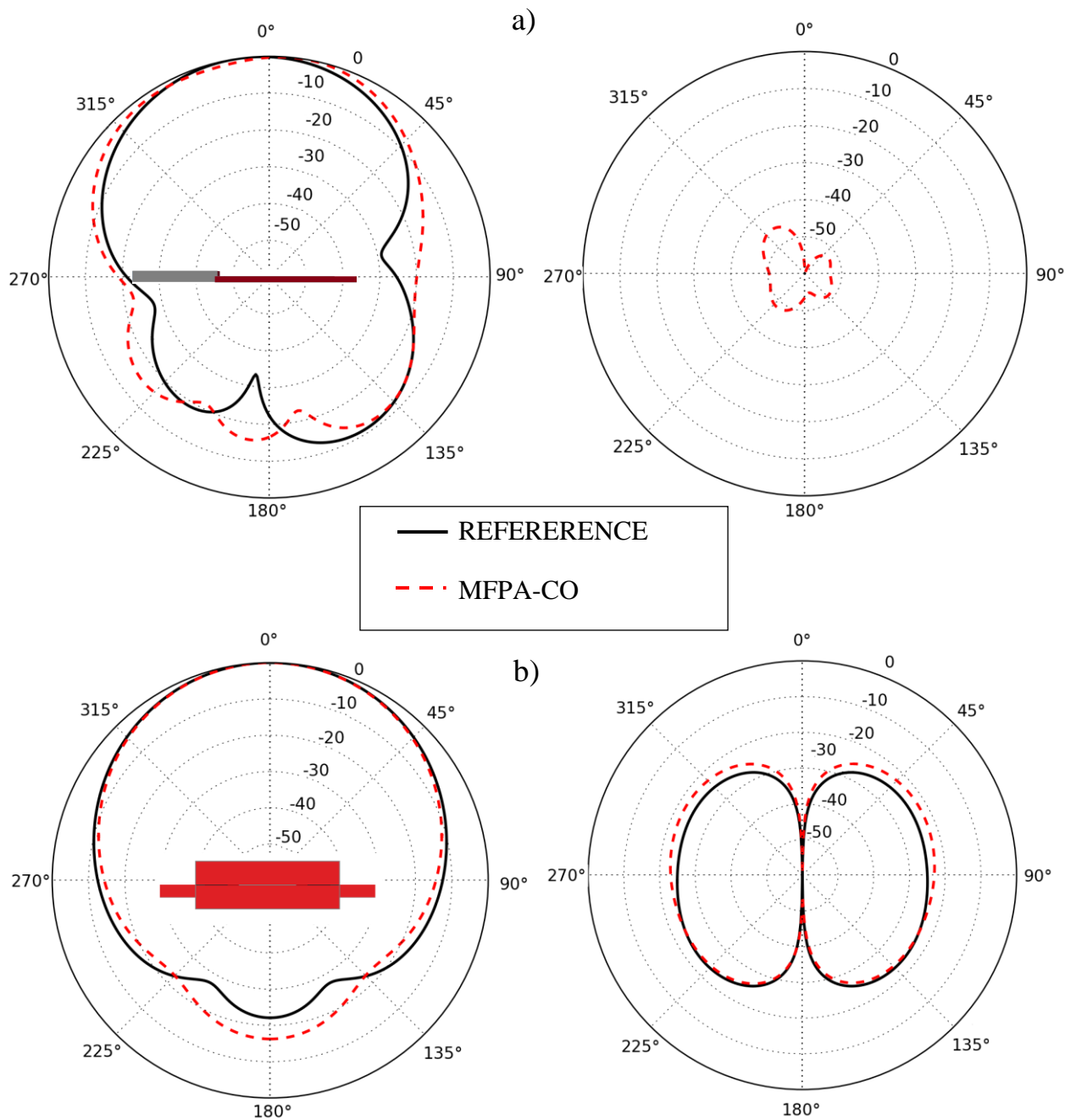
Fig. 5- 11 Simulated normalized to maximum value radiation patterns for MFPA-CO (2.47GHz) and reference microstrip fed patch antenna (2.56GHz) at: a) Elevation (XZ) plane and b) Azimuth (YZ) plane where left column are the co-polar and the right column are the cross-polar patterns

It can be seen from Fig. 5-11 that differences were noticed between the radiation patterns derived from the MFPA-CO compared with the reference microstrip fed patch antenna. A noticeable difference is the increased cross-polar in the case of the MFPA-CO antenna (notice that in Fig.5-11a the cross polar of the reference patch is negligible, around -150dB and is not shown). Additionally it is noticed that on the elevation plane the co-polar main lobe (Fig. 5-11a) of the MFPA-CO was wider and more power is radiated (possible reflected) on the side of the stripline (270°). Regarding the co-polar elevation plane (Fig. 5-11a) differences are noticed at the angles between 90°-270° (back side of the structures). Regarding the azimuth plane (Fig. 5-11b) and the co-polar components the MFPA-CO yielded narrower main lobe and also more power is radiated at the back lobe. Finally, it could be said that the MFPA-CO satisfies the broadside patch antenna radiation.

5.3.2.3 Effect of stripline length on antenna performance

The effect of the length of the feeding stripline part of the MFPA-CO, on antenna performance is presented. This effect was examined through simulations. The initial design (subsection 5.3.1) of the MFPA-CO antenna used a 6cm long feeding stripline. An MFPA-CO antenna with a 10cm, 20cm, 30cm and 60cm long feeding stripline was simulated. The simulated results for these versions of the MFPA-CO and of the reference microstrip fed patch antenna are shown in Table 5-2.

Table 5- 2 Simulated results of reference microstrip fed patch antenna and of the MFPA-CO for 6cm, 10cm, 20cm, 30cm and 60cm long feeding striplines

	Reference	6cm	10cm	20cm	30cm	60cm
f_0 (GHz)	2.56	2.47	2.47	2.47	2.47	2.47
S_{11} (dB)	-26.77	-23.92	-23.97	-21.86	-24.75	-25.23
BW (MHz)	90	90	90	90	97	110
Gain (dBi)	+8.60	+7.47	+7.80	+7.52	+7.18	+6.56
Directivity (dBi)	+8.79	+8.15	+8.51	+8.49	+8.35	+8.32
e_{rad} (%)	95.76	85.51	84.97	80.00	76.40	66.65

As can be seen from Table 5-2 the resonant frequency was shifted by 900MHz in the case of MFPA-CO, for all versions examined, compared with the reference microstrip fed patch antenna. The S_{11} was well kept lower than -10dB revealing that the feeding of the MFPA-CO was well matched. Regarding the bandwidth (BW), the 6cm, 10cm and 20cm versions of the MFPA-CO, yielded BW equal to that of the reference antenna. The other versions (30cm and 60cm) of the MFPA-CO yielded higher BW than the reference antenna equal to 97MHz and 110MHz respectively. All the versions of the MFPA-CO yielded lower gain and directivity than the reference antenna. But still, the gain and the directivity for all the versions of the MFPA-CO was kept at the expected levels of patch antennas [12]. As expected and due to stripline existence the radiation efficiency decreased in the case of the MFPA-CO compared with the reference and decreasing by stripline length increasing. At the case of 60cm MFPA-CO, the radiation efficiency was decreased by 29.11% compared with the reference one which decrease includes the increased stripline length and patch antenna losses. The efficiency value of 66.65% is a good efficiency considering the use of a long (60cm) stripline, making the MFPA-CO structure an acceptable candidate for a wearable application.

5.3.3 Prototyping and measurements

In this subsection the implementation of an all-textile, practical and flexible (by using Velcro) (Chapter 4 – Section 4.4.3), of the MPFA-CO antenna, using a 6cm long stripline (subsection 5.3.1, Fig. 5-8), is presented. The measurement results in terms of reflection coefficient and radiation patterns are presented as well.

5.3.3.1 Fabrication

The MFPA-CO was fabricated using the crimson felt and Nora-dell for the dielectric and the conductive parts respectively (Chapter 4, Section 4.3). The adhesive way used for attaching Nora-dell to felt was the Hemming-web due to reasons described in Chapter 4, subsection 4.3.3. The parts structuring the microstrip patch antenna with the stripline to microstrip transition and the upper structure of the CO (1.5cm long) (Fig. 5-8), before assemble are shown in Fig. 5-12. The parts were manually cut with a scissor. The radiator part was quite tricky and difficult. In terms of mass production a more effective and digitize way

should be found [5]. The fabricated parts of the MFPA-CO: a) feeding stripline and b) microstrip patch antenna with stripline to microstrip transition and the upper structure of the CO (1.5cm long) with the hooks (of Velcro) attached on them are shown in Fig. 5-13.
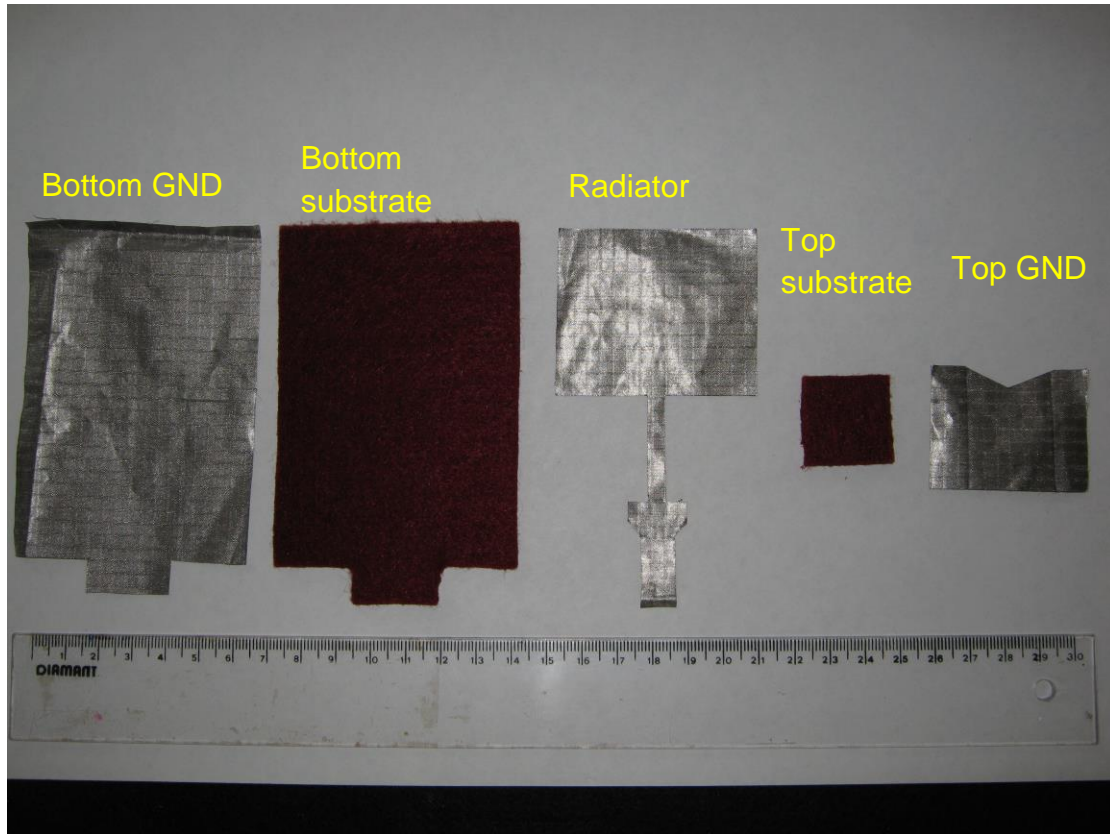
Fig. 5- 12 Parts of the microstrip patch antenna with the stripline to microstrip transition of the MFPA-CO antenna
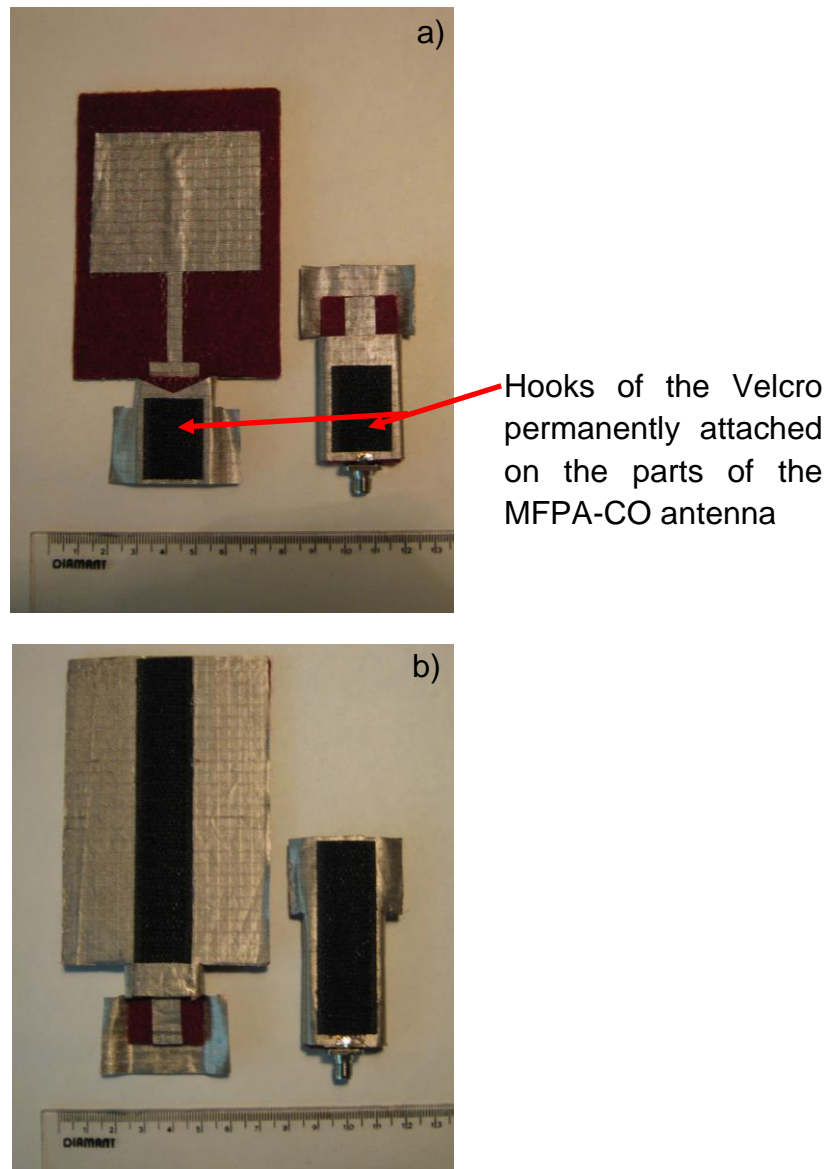
Fig. 5- 13 Fabricated parts of the all-textile flexible MFPA-CO antenna: a) front side and b) back side

5.3.3.2 Measurement results

The reflection coefficient (S_{11}) of the all-textile flexible MFPA-CO antenna prototype was measured so as to assess the simulation results. For the measurement, modification 1 (Chapter 4, sub subsection 4.4.3.4) of Velcro connection was used. Additionally, a Velcro part was wrapped around the CO interconnection point (Fig. 5-14), so as to minimize any possible discontinuities on CO. The S_{11} measurement results are shown in Fig. 5-15. Three 10, 20 and 30 minutes averaging measurements, of the same antenna, were carried out so as to examine the repeatability of the results due to possible loosening of the Velcro by time. As can be seen the three measurements yielded similar S_{11} verifying the repeatability.

Additionally, the resonance was found at 2.48GHz with an 80MHz BW showing good agreement with simulations.

a)

b)
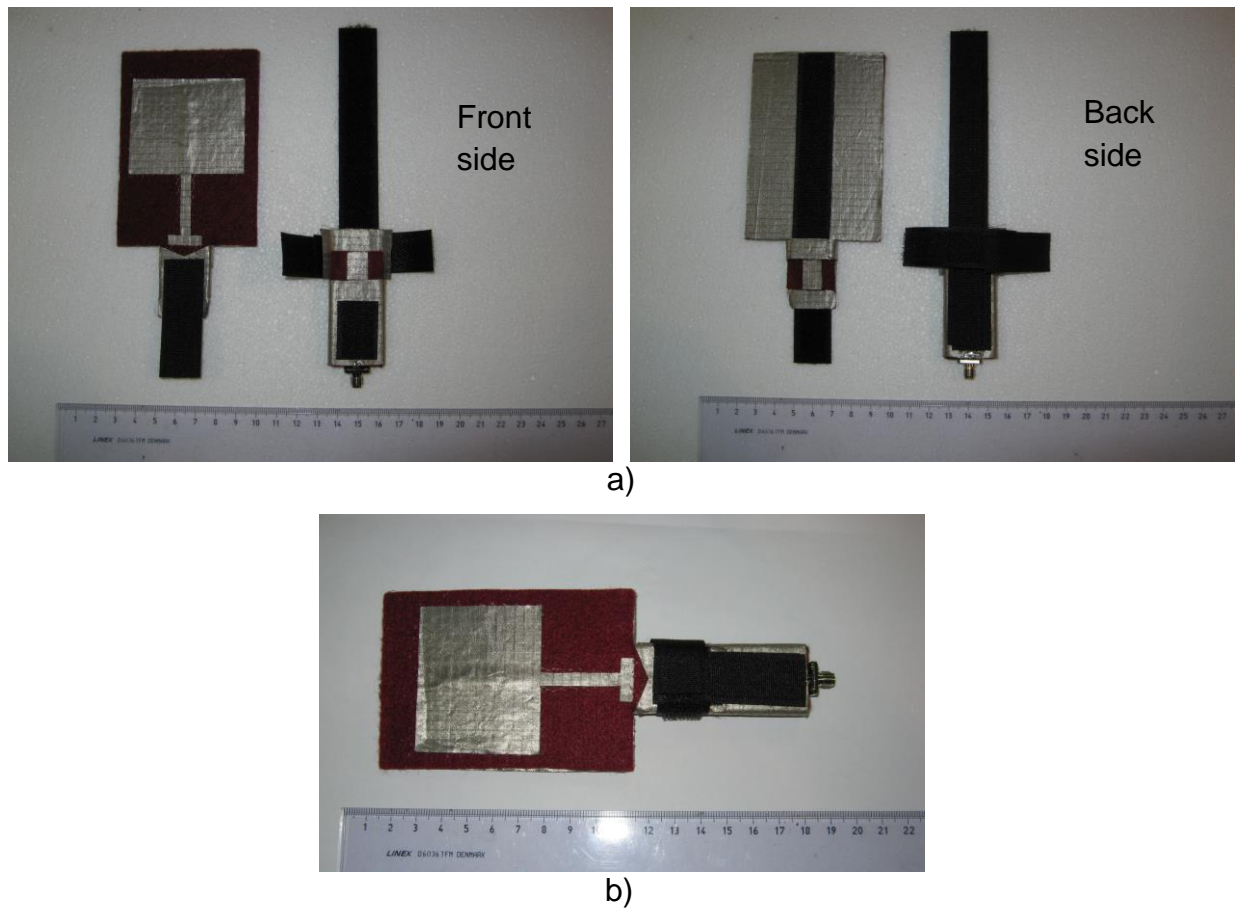
Fig. 5- 14 MFPA-CO antenna prototype with Velcro: a) disconnected and b) connected
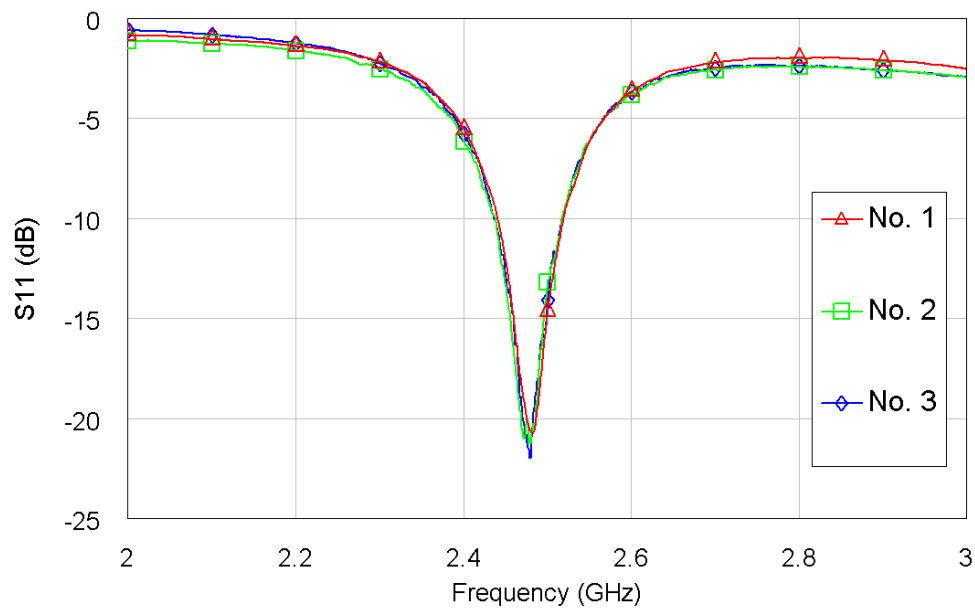
Fig. 5- 15 Measured reflection coefficient (S_{11}) of the MFPA-CO antenna

Additionally, the MFPA-CO antenna was measured inside a full wave anechoic chamber (Fig. 5-16) so as to determine the radiation at azimuth and elevation planes. The radiation patterns which were normalized to maximum value for azimuth and elevation planes of the MFPA-CO antenna are shown in Fig. 5-17. The orientation of the antenna in the radiation patterns is the same as in Fig. 5-11.
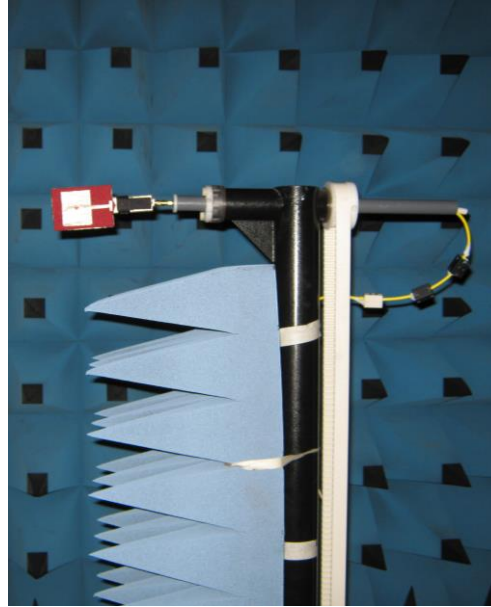
Fig. 5- 16 MFPA-CO antenna far field measurement setup inside an anechoic chamber

a)   —— Co-polar   b)

– – · Cross-polar
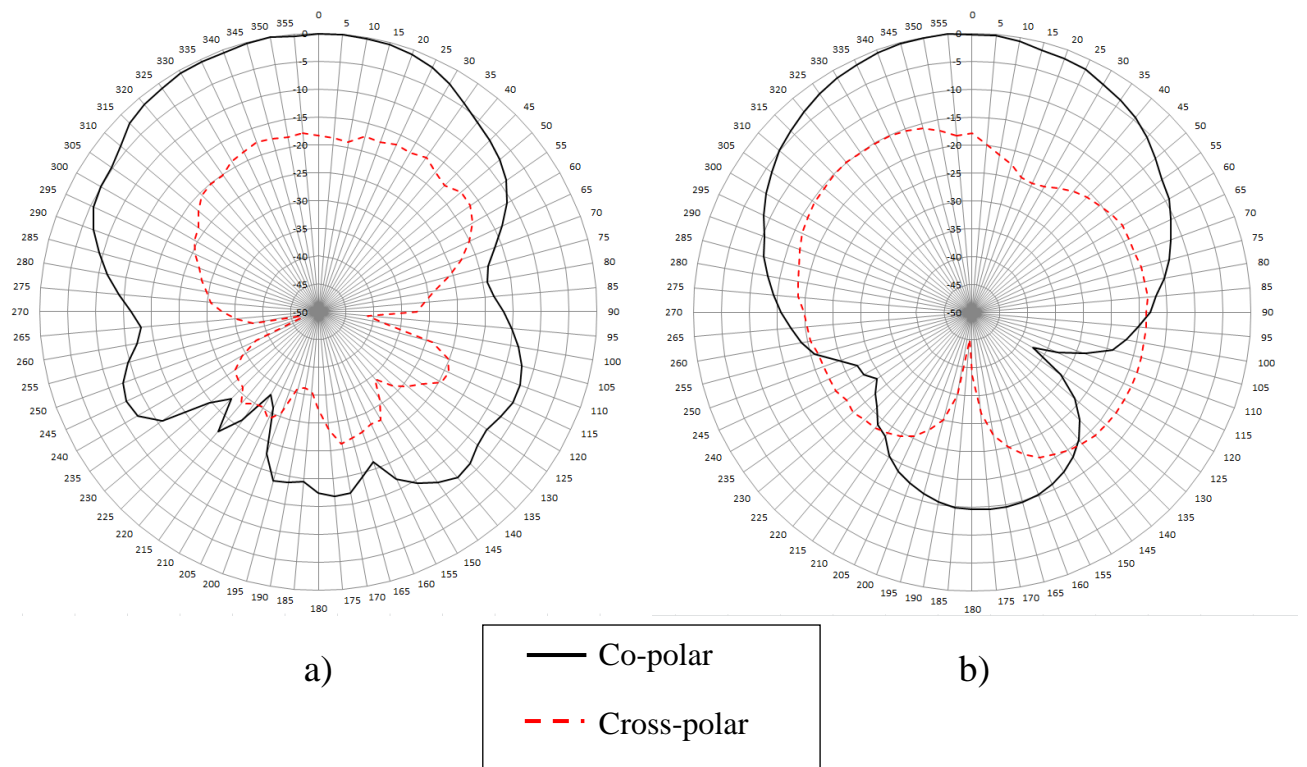
Fig. 5- 17 Measured normalized to maximum value radiation patterns of the MFPA-CO antenna at 2.48GHz: a) elevation and b) azimuth plane

From Fig. 5-17 the broadside patch antenna radiation characteristic of the MFPA-CO antenna has been verified with measurements. The measured radiation patterns are in acceptable agreement with simulations. Though, differences such as the increased cross-polar in the elevation plane in the measurement case compared with simulations have been occurred.

5.4 Wearable textile patch antenna, a real life scenario

To demonstrate the use of the MFPA-CO antenna feeding/interconnection method a possible real life scenario where no rigid connectors are used, for the interconnecting of a wearable textile patch antenna with a stripline, was created. The proposed real life scenario includes a long (54cm) stripline, feeding the 2.5GHz band microstrip fed textile patch antenna (Section 5.3). The scenario is shown in Fig. 5-18. The long stripline is fed in front of the trunk of the volunteer; it is bended around the trunk like a belt feeding the patch antenna, which is mounted at the back of the trunk of the volunteer. In terms of real life scenario the long stripline could be connected with a sensor, mounted in front of the trunk. The long stripline transmits signal to the patch antenna which by itself transmits the signal to an Off-body base station or monitor. Main advantage is that the patch antenna can be flexibly connected and disconnected from the feeding stripline without using a rigid connector (e.g. SMA).

a)   **b)**
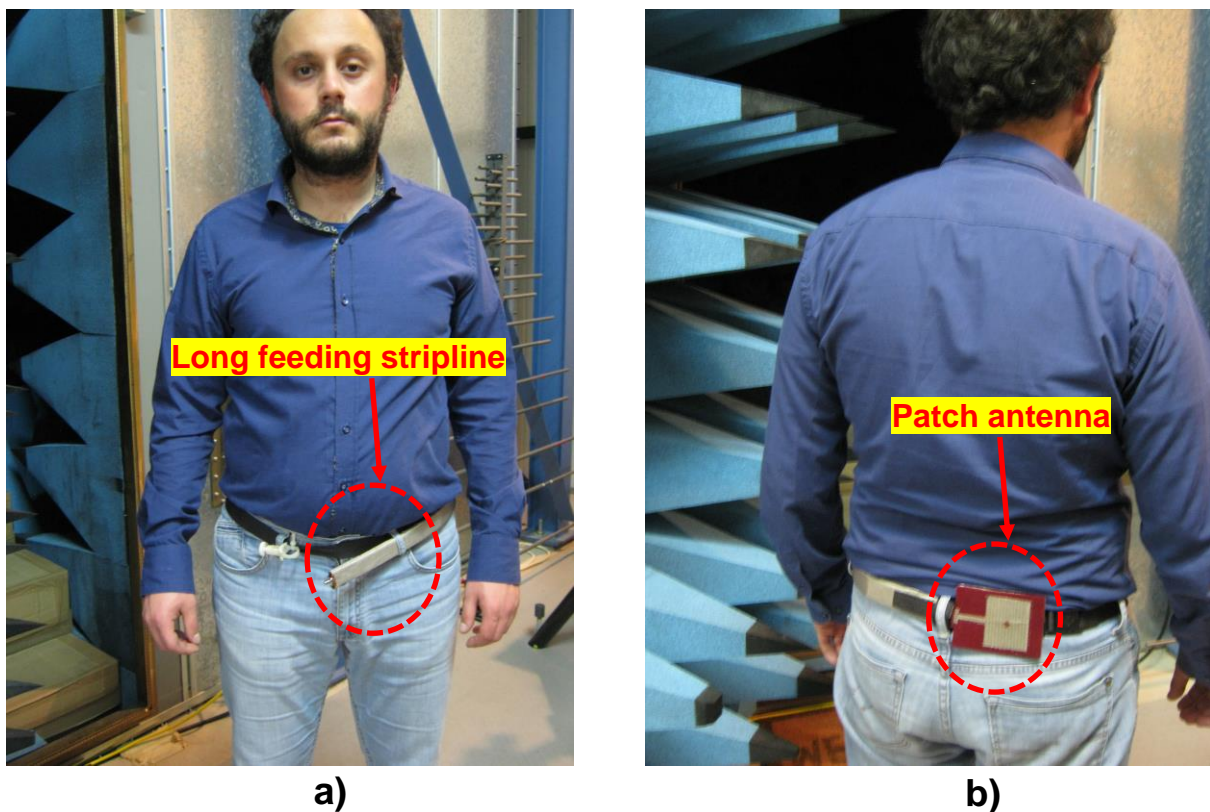
**Fig. 5- 18 Real life scenario of a wearable patch antenna:
a) front side and b) back side of the user**

For the evaluation of the MFPA-CO antenna with the long (54cm) feeding stripline a comparison was done with the respective MFPA-CO antenna with the 6cm (subsection 5.3.3) long feeding stripline (see Fig. 5-19). This included measuring the two MFPA-CO antennas inside an anechoic chamber in terms of transmission (S_{21}), in the line of sight (LOS), using a reference Horn antenna (Fig. 5-20).

Fig. 5- 19 Long and short feeding textile striplines

Fig. 5- 20 Measurement setup for wearable textile patch antenna transmission

The S_{21} measurement results are shown in Fig. 5-21. The measurement results yielded about 1dB increased losses for the long stripline compared with the short stripline. This was expected due to increased length of the feeding stripline.
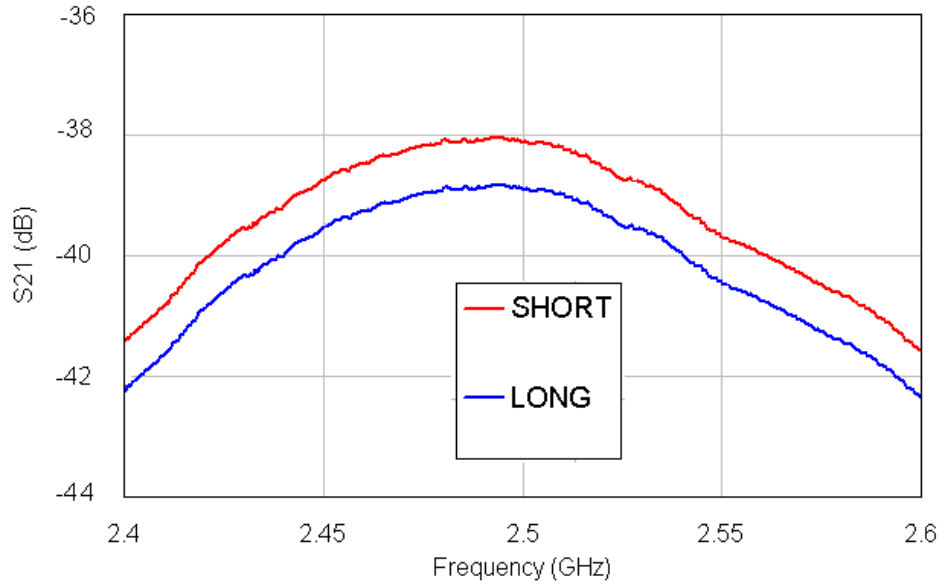
Fig. 5- 21 S21 measurement results for the MFPA-CO antenna with short and long feeding stripline

The proposed MFPA-CO antenna with the long stripline bended around the trunk of a human like a belt, yields a truly wearable textile structure which could be applied in a real life scenario.

5.5 Conclusions

This chapter has presented two novel methods (SO(c) and CO), which were analytically described in Chapter 4, for feeding wearable textile patch antennas (2.5GHz) with striplines. The SO(c) method resulted in a structure which includes the feeding stripline and probe fed patch antenna. This antenna structure was called PFPA-SO(c). The CO method resulted into a structure which includes the feeding stripline and a microstrip fed patch antenna. This antenna structure was called MFPA-CO. Each of the novel antenna structures (PFPA-SO(c) and MFPA-CO) was compared with the reference probe and microstrip fed antennas respectively.

Regarding the PFPA-SO(c) antenna a via parametric simulation analysis was carried out and yielded the 3mm diameter value as the best matching to the S_{11} of the reference antenna. The simulated radiation patterns of the PFPA-SO(c) antenna yielded differences compared with the reference antenna due to the stripline existence. Though, the broadside patch antenna radiation characteristic was maintained. Finally a simulation investigation regarding the stripline length was carried out and yielded that the BW increases and efficiency decreases by stripline length increase. The longest stripline case examined which was equal to 60cm, yielded radiation efficiency 69.78% which is a good efficiency making this structure an acceptable candidate for wearable operation. The simulations of the PFPA-SO(c) antenna yielded a promising textile patch antenna model feeding / interconnecting using the SO(c) method. In terms of fabrication and implementation of a more practical and realistic solution, a Snap-On button or a screw should replace the cylindrical copper via.

Regarding the MFPA-CO antenna the S_{11} simulations yielded a 0.9GHz (from 2.56GHz to 2.47GHz) resonance frequency downshift compared with the reference. The simulated radiation patterns of the MFPA-CO yielded differences (increased radiation power at the side of the stripline) compared with the reference antenna. Though, the broadside patch antenna radiation characteristic was maintained. Finally, in terms of simulation the effect of the feeding stripline length was examined and yielded efficiency decrease with length increase. The longest case examined is equal to 60cm and yielded efficiency equal to 66.65% which is a good efficiency making this structure an acceptable candidate for wearable operation. An all-textile MFPA-CO antenna prototype using Velcro to fix the connections and to provide a practical and flexible solution was fabricated. The measured S_{11} results show good agreement with simulations and yielded resonance frequency at 2.48GHz. The measured radiation patterns yielded acceptable agreement with simulations and the broadside patch antenna radiation characteristic was verified. The all-textile flexible MFPA-CO antenna structure could provide a user friendly feeding/interconnection of a wearable patch antenna, excluding the use of rigid connectors (e.g. SMA) for the interconnection of the stripline with the textile patch antenna.

A real life scenario was demonstrated so as to show the use of the MFPA-CO antenna feeding/interconnecting method. The proposed MFPA-CO antenna with a 54cm long feeding stripline was bended around the trunk of a human like a belt and yielded 1dB increased transmission losses (communicating with an Off-body antenna) compared with the short (6cm long) feeding stripline MFPA-CO antenna. A truly wearable textile MFPA-CO antenna

structure could be applied in a real life scenario with main advantage, the flexible and user friendly interconnection of the stripline with the textile patch antenna, excluding the use of rigid connectors.

References

[1] A. Tsolis, W. Whittow, A. Alexandridis, and J. Vardaxoglou, "Embroidery and Related Manufacturing Techniques for Wearable Antennas: Challenges and Opportunities," *Electronics*, vol. 3, no. 2, pp. 314–338, May 2014.

[2] P. Hall and Y. Hao, *Antennas and Propagation for Body-Centric Wireless Communications*, 2nd ed. London / Boston: Artech House, 2012.

[3] B. Gupta, S. Sankaralingam, and S. Dhar, "Development of Wearable and Implantable Antennas in the Last Decade: A review," in *Microwave Symposium (MMS), Mediterranean*, 2010, pp. 251–267.

[4] G. A. Conway and W. G. Scanlon, "Low-Profile Patch Antennas for Over-Body-Surface Communication at 2 . 45 GHz," in *International Workshop on Antenna Technology: Small and Smart Antennas Metamaterials and Applications, IWAT*, 2007, pp. 416–419.

[5] S. Zhang, "Design Advances of Embroidered Fabric Antennas", PhD Thesis, Loughborough, 2014.

[6] T. Kellomaki and W. G. Whittow, "Bendable plaster antenna for 2.45 GHz applications," in *Loughborough Antennas & Propagation Conference (LAPC)*, 2009, no. March, pp. 453–456.

[7] S. J. Chen, C. Fumeaux, D. C. Ranasinghe, and T. Kaufmann, "Paired Snap-On Buttons Connections for Balanced Antennas in Wearable Systems," *IEEE Antennas and Propagation Letters*, vol. 14, pp. 1498–1501, 2015.

[8]   A. Tsolis, A. A. Alexandridis, W. G. Whittow, and J. C. Vardaxoglou, "Investigation of Textile Striplines Connectivity for Feeding and Connecting Wearable Antennas," in *European Conference on Antennas and Propagation (EuCAP)*, 2015, pp. 1–5.

[9]   A. Tsolis, A. A. Alexandridis, W. G. Whittow, and J. C. Vardaxoglou, "Connecting wearable textile transmission lines: all-textile fabrication solutions and design techniques," *Electronics Letters*, vol. 51, no. 15, pp. 1136–1138, Jul. 2015.

[10]   I. Locher, M. Klemm, T. Kirstein, and G. Tröster, "Design and Characterization of Purely Textile Patch Antennas," *IEEE Transactions on Advanced Packaging*, vol. 29, no. 4, pp. 777–788, 2006.

[11]   C. A. Balanis, *Antenna Theory Analysis and Design*, 3rd ed. New Jersey: John Wiley & Sons, 2005.

[12]   C. A. Balanis, *Modern Antenna Handbook*, 1st ed. John Wiley & Sons, 2008.

[13]   T. Kellomäki, "Snap-On Buttons in a Coaxial-to-Microstrip Transition," in *Loughborough Antennas & Propagation Conference (LAPC)*, 2009, November, pp. 437–440.

[14]   T. Maleszka and G. Jaworski, "Broadband Stripline to Microstrip Transition with Constant Impedance Field Matching Section for Applications in Multilayer Planar Technologies," in *18th International Conference on Microwave Radar and Wireless Communications (MIKON)*, 2010, pp. 1–4.

[15]   "http://www.statex.biz/index.php/en/2012-04-06-13-28-47/item/159-shieldex%C2%AE-gewebe", accessed September 2016.

[16]   D. M. Pozar, *Microwave Engineering*, 4th ed., John Wiley & Sons, 2012.

[17]   C. A. Balanis, *Advanced Engineering Electromagnetics*, 2nd ed. John Wiley & Sons, 2012.

CHAPTER 6

CONCLUSIONS AND FUTURE WORK

6.1 Use of research novelties achievements

The research novelty achievements of this thesis are related with: a) wearable antenna measurements, b) textile transmission lines interconnecting and c) wearable textile patch antennas feeding.

6.1.1 Wearable antenna measurements

Regarding the wearable antennas performance assessment measurements, three research novelties have been achieved, as referred in Chapter 1 and illustrated in Chapters 2 and 3 of this thesis. These novelties are: (1) the HOCS phantom for wearable antenna performance assessment; (2) the evaluation technique for a CNF test site for wearable antennas measurement and (3) the methodology for wearable antennas (mounted on HOCS phantom) performance assessment by using the CNF measurement technique.

Regarding the HOCS liquid torso phantom, its practical use would be the wearable antenna measurement facilitation due to its light weight and low cost. These characteristics make this phantom also attractive for academic/educational purposes. The procedure followed for the design and evaluation of the HOCS torso phantom could be applied for any type; shape of phantom and for other frequency range.

As for the measurement evaluation technique, its practical use would be the evaluation of a CNF test site appropriate for wearable antenna on-torso phantom measurements and use for better understanding of a CNF measurement test site performance in terms of antenna engineering near field measurements and academic purposes. The evaluation technique could be extended and used for any type and shape of phantom and adjusted for any other type of wearable antennas than the patch antennas.

Regarding the measurement methodology, its practical use would be the wearable antenna on-phantom/body performance assessment by using the CNF measurement technique. This methodology could be applied for any other type of phantom, for a whole human body phantom. In terms of real life scenarios and applications this methodology could be applied for e.g. on evaluating the wearable antennas mounted on a firefighter, extravehicular suit where more complicated wearable systems could exist which will require the near field measurement to spot details in terms of electric field distribution and electronic interference. Though, it is suggested that the CNF measurement technique should not be applied when a wearable antenna is mounted on top (above) (e.g. helmet antenna or on top of shoulders antenna) or bottom (below) the phantom (generally antennas that their main radiation is on the elevation plane parallel to the phantoms height) because the lack of sampling in these points will lead in missing important data for the radiation of these wearable antennas.

6.1.2 Textile transmission lines interconnecting

Regarding the textile transmission lines interconnecting, research novelty (4) has been achieved, as referred in Chapter 1 and illustrated in Chapter 4 of this thesis. Two new methods (*SO* and *CO*) for interconnecting textile striplines have been designed, studied and fabricated. The most efficient method (*CO*) has been used to implement a laboratory prototype to demonstrate its utilization in an all-textile, practical and flexible (by using Velcro) wearable application. This method could be used to provide a flexible solution for interconnecting wearable textile striplines integrated on the clothes of a user, providing flexibility and comfort ability (e.g. for a wearable patient monitoring system, sensors mounted on different locations on-body where short or long striplines will be used to connect them with an antenna or electronic system. The feeding stripline of the antenna or electronic will be stable and by the CO technique the short or long striplines will be connected and disconnected).

6.1.3 Wearable textile patch antennas feeding

Regarding the wearable antennas feeding, research novelty (5) has been achieved, as referred in Chapter 1 and had been illustrated in Chapter 5 of this thesis. The all-textile

flexible *CO* interconnection method was used to feed and interconnect a microstrip fed patch antenna with a respective stripline and resulted into an all-textile flexible antenna structure called as MFPA-CO. This antenna structure (novel feeding) could be used to satisfy an all-textile flexible body wearable coms system. The wearable coms system could include an on body sensor connected with a stripline sending signal (information) to the patch antenna. Then the patch antenna as a very good-off body antenna will transmit the information to an off-body monitor. The use of the MFPA-CO structure will provide flexibility in terms of connecting and disconnecting the patch antenna with the stripline. This has been demonstrated by implementing a real life wearable MFPA-CO antenna scenario. This scenario included a stripline, which is fed in front of the trunk of a user, bended (like a belt) around the trunk and feeding a textile patch antenna mounted at the back of the trunk of the user. Such scenarios could be applied on patents smart robes, on firefighter's clothes or at astronaut suits.

6.2 Summary of results

In Chapter 2 the design, realization and evaluation of a low cost and lightweight hollow torso phantom appropriate for wearable antenna performance assessment has been presented. The cost and the volume of the proposed hollow torso phantom are reduced by 2/3 and 60% respectively, compared with the respective full liquid phantom. The main advantage of the proposed HOCS phantom is that its performance in terms of wearable antenna evaluation is comparable with full liquid, anthropomorphic phantoms and real human bodies. In terms of S_{11} wearable antenna performance HOCS phantom is in better agreement with real human bodies for frequencies higher than 2GHz. In terms of electric field distribution or penetration, the HOCS phantom deviates from the full liquid phantom, at lower frequencies close to 2GHz and it is close with the full liquid at frequencies close to 6GHz (e.g. 5.5GHz). The electric field penetration and distribution are improved with the addition of a simulated RF absorbing material. Additionally, the path loss performance, when considering two antennas either side of the HOCS phantom, differs from the full liquid phantom. The path loss performance of the HOCS phantom was brought closer with the full liquid one by the addition of a simulated RF absorbing material as well. In terms of far field wearable antenna performance the HOCS phantom yielded almost same performance with the full liquid

phantom. Additionally the HOCS phantom yielded deviation less than 2.5dB, 1.3dB and 6.6% in gain, directivity and efficiency respectively compared with an anthropomorphic simulated phantom. Also, the deviation compared with a measured anthropomorphic phantom is less than 1.2dB, 0.5dB and 4% in terms of gain, directivity and efficiency respectively.

In Chapter 3 a new methodology, which had implemented the cylindrical near field measurement technique in order to evaluate wearable antennas performance parameters had been demonstrated. Three patch antennas operating at 2; 2.5 and 5GHz were used. Main advantage of this methodology was that less physical space, for the measurement site, is required compared to a far field test site and the use of a heavy duty roll axis, so as to rotate the phantom for 3D pattern coverage is excluded compared to a conventional spherical near field test site. These advantages could significantly reduce the cost and the complexity of the measurement.The geometry of HOCS torso phantom in a cylindrical near field (CNF) test site has been introduced. An evaluation technique, which was targeted for the CNF test site, appropriate for wearable antenna measurements mounted on HOCS phantom, in order to define optimum CNF scanning volume which will result into the closest produced far field parameters compared with simulations, was proposed. The evaluation technique used a 2mm thick ConDucting Plate (CDP) whose cross sectional dimensions were equal to that of the HOCS phantom. It was proved that this technique is effective and useful as an evaluation of cylindrical near field wearable antenna measurements and removed the necessity of using the phantom, during the measurement preparation procedure (define optimum CNF volume). The evaluation technique was assessed by comparing the far field performance parameters, derived from the cylindrical near field measurements, with simulations and with direct far field measurements. Validation of the evaluation technique was carried out by applying the optimum (evaluated) cylindrical near field volumes on HOCS phantom, for all three antennas, by measuring and comparing them with simulations. The CDP for all the patch antennas examined, for the evaluation yielded deviation between near field to far field measurements and simulations less than 0.7dB, 1.3dB and 22% in terms of Gain, Directivity and Efficiency, respectively. The validation of the evaluation technique, by using the HOCS phantom instead of the CDP yielded deviation between measurements and simulations less than 0.9dB, 0.7dB and 22% in terms of Gain, Directivity and Efficiency, respectively.

The new methodology was described and demonstrated. The wearable patch antennas were positioned in different locations on HOCS phantom. The steps of the new methodology can

be listed as follows: *1) The image of the E-field on the near field area for each antenna and each location was recorded. 2) From the near field (E-field) results conclusions for the maximum direction of radiation, for the radiation at the main geometrical planes and for the directivity were derived. 3) Finally, the far field radiation patterns and parameters (gain, directivity and efficiency) were produced from the near field results, validating the assumptions made from the near field contour plots.*

Chapter 4 has presented the design and fabrication of two novel methods (*SO* and *CO*) for interconnecting stripline transmission lines aiming to avoid the use of rigid connectors. The two methods were compared with a reference conventional straight (*ST*) stripline for which no interconnections are involved. The most efficient and closer to the ST method proved to be the CO one. But, the SO gave promising performance (for a 3dB insertion losses criterion), for one out of three examined versions, when a cylindrical copper via was added so as to connect the two strips at the interconnection point.

Regarding the *SO* method the case of via diameter equal to 3mm transmits more than half of the power for most frequencies at 2-6GHz. Additionally, through simulations the use of side shielding (as a wearable requirement) improved power transfer of the SO with a trade-off of a cut-off frequency bandwidth occurrence, which depends on via diameter. The best case of the SO with side shielding proved to be the one with via diameter equal to 10mm yielding 1dB insertion losses up to 4.1GHz, 6dB at 4.15GHz (cut-off frequency) and 2dB up to 5dB insertion losses at 4.2-6GHz. The SO method was fabricated using felt as dielectric and copper tape as for the conductive parts. Simulations and measurements are in reasonable agreement. Differences occurred due to fabrication imperfections such as slot dimensions, via position and felt thickness decrease due to soldering process in order to attach copper via to Stripline 1.

Regarding the CO it was proved that the physical discontinuities which could occur at the interconnection points degrade the power transmission performance. The use of extended ground planes, at the longest sides of both individual striplines forming the *CO* model, improves significantly the S_{21} performance. The *CO* prototype which was made of felt and copper tape, is very close to the performance of the *ST* reference stripline model. Finally, the all-textile (felt and Nora-dell) practical and flexible, by using Velcro prototype of the CO was fabricated and proved through measurements to be an effective and appropriate flexible wearable solution, yielding insertion losses 1dB up to 4GHz, 1.3dB at 5GHz and 2.2dB at

6GHz. It was found that the CO with and without side shielding yield similar performance. In terms of wearable implementation of the CO scenario it is suggested to add side shielding. The side shielding was used in Chapter 5 where side CO is applied to interconnect and feed a wearable all-textile patch antenna with a stripline.

Chapter 5 has presented two novel methods (SO(c) and CO), which were analytically described in Chapter 4, for feeding wearable textile patch antennas (2.5GHz frequency band) with textile striplines. The SO(c) method used with a structure which includes the feeding stripline and probe fed patch antenna. This antenna structure was called PFPA-SO(c). The CO method used with a structure which includes the feeding stripline and a microstrip fed patch antenna. This antenna structure was called MFPA-CO. Each of the novel antenna structures (PFPA-SOc and MFPA-CO) was compared with the reference probe and microstrip fed patch antennas respectively.

Regarding the PFPA-SO(c) antenna parametric simulation analysis yielded the 3mm via diameter as the best matching to the S_{11} of the reference antenna. The simulated radiation patterns of the PFPA-SOc antenna yielded differences compared with the reference antenna due to the stripline existence. Though, the broadside raditiation is maintained. Finally a simulation investigation regarding the stripline length yielded that the BW increases and efficiency decreases as stripline length increases. The longest case examined equal to is 60cm long stripline and yielded radiation efficiency 69.8% which is a good efficiency making the use of this structure feasible for a wearable application. The simulations of the PFPA-SO(c) antenna yielded a promising textile patch antenna feeding model, by using the SO(c) method.

Regarding the MFPA-CO antenna the S_{11} simulations yielded a 0.9GHz (from 2.56GHz to 2.47GHz) resonance frequency downshift compared with the reference antenna. The simulated radiation pattern of the MFPA-CO yielded differences (increased radiation power at the side of the stripline) compared with the reference antenna. Though, broadside patch antenna radiation is maintained. Finally, in terms of simulation the effect of the feeding stripline length yielded efficiency decrease with length increase. The longest case examined is equal to 60cm and yielded efficiency equal to 66.6% which is a good efficiency making this structure an acceptable candidate for a wearable application. The MFPA-CO antenna was fabricated as an all-textile, practical and flexible (by using Velcro). The measured S_{11} results showed good agreement with simulations and yielded resonance frequency at 2.48GHz. The measured radiation patterns yielded acceptable agreement with simulations, showing

increased cross polar components. The all-textile flexible MFPA-CO antenna structure could provide a user friendly feeding/interconnection of a patch antenna, excluding the use of rigid connectors (e.g. SMA) for the interconnection of the stripline with the textile patch antenna.

A real life scenario was demonstrated so as to show the use of the MFPA-CO antenna feeding/interconnecting method. The proposed MFPA-CO antenna with a 54cm long feeding stripline was bended around the trunk of a human like a belt and yielded 1dB increased transmission losses (communicating with an Off-body antenna) compared with the short (6cm long) feeding stripline MFPA-CO antenna. A truly wearable textile MFPA-CO antenna structure could be applied in a real life scenario with main advantage, the flexible and user friendly interconnection of the stripline with the textile patch antenna, excluding the use of rigid connectors. This means that the patch antenna can be flexibly connected and disconnected from the feeding stripline without using a rigid connector (e.g. SMA).

6.3 Future work

6.3.1 HOCS Phantom

As for the phantom shell a material with a lower dielectric constant should be found or produced for example using the 3D printing new tech. The absorber proposed solution should be tested with real prototypes and measured in terms of path loss and near field comparing the performance of HOCS phantom with the HOCS using the various absorbers and with the full liquid phantom. This means that the full liquid phantom fabrication is a task. Additionally, by using the HOCS as for the torso a whole body phantom should be designed and constructed, with legs, arms and a head. The hollow volume reduction concept should be applied for the other parts (legs, arms and head) of the phantom.

6.3.2 Cylindrical near field measurement technique for wearable antenna performance assessment

The proposed methodology, for the wearable antenna performance assessment should be extended to other types and shapes of phantoms (whole body, anthropomorphic etc.) and to

more complex wearable electronics and antennas systems. Additionally, the CNF measurement technique, using HOCS phantom, should be compared with direct far field measurements and with linear and spherical near field measurement systems. Also, the implementation of the CNF measurement technique should be investigated if it can be used to evaluate the On-body mode of wearable antennas and sensors communication performance.

6.3.3 Textile striplines interconnection

The Slotted Overlap (with via) (SO(c)) interconnection method should be realized with a more practical solution such as a Snap-On button or a screw instead of the copper via. Additionally, this should be fabricated as an all-textile flexible one so as to examine its potential, regarding the wearable criteria. Also, both all-textile flexible CO and SO-via interconnection scenarios should be tested in terms of longer striplines and in terms of bending, crumpling, twisting and general deformations which are possible in On-body applications.

6.3.4 Wearable textile patch antennas feeding

The probe fed patch antenna – slotted overlap via (PFPA-SO(c)) antenna structure should be realized with a more practical solution such as a Snap-On button or a screw and fabricated as an all-texile flexible one. The PFPA-SO(c) should be tested for possible real body wearable scenarios for e.g. a sensor mounted on a trunk connected via stripline with a patch antenna which is mounted on the back of the user. The PFPA-SOc and the MFPA-CO antenna structures should be designed for other useful, for wearable applications, frequencies, except than the examined 2.5GHz frequency band. Finally the capability of integrating the all-textile striplines into garments (e.g. jacket, smart robe), with the CO and the SO interconnection points adjusted which could provide flexibility to the user (depending on the wearable system application) where to connect or disconnect the other part of the stripline or the antenna. Finally the SO and CO should be investigated in terms of feeding other textile antennas than patch antennas (e.g. textile dipoles, monopoles, spiral)

APPENDIX A

DIPOLE AND MONOPOLE ANTENNAS

A.1 Cylindrical dipole antennas

The cylindrical dipole antennas [1] geometry, used in chapter 2 for the evaluation and characterization of HOCS torso phantom in terms of electric field penetration-distribution (subsection 2.3.1); on-body path loss (subsection 2.3.3) and reflection coefficient (subsection 2.3.2) (the 2GHz and 2.5GHz antennas were designed and fabricated by Alford Chauraya [2]), is shown in Fig. A-1 and the dimensions in Table A-1.
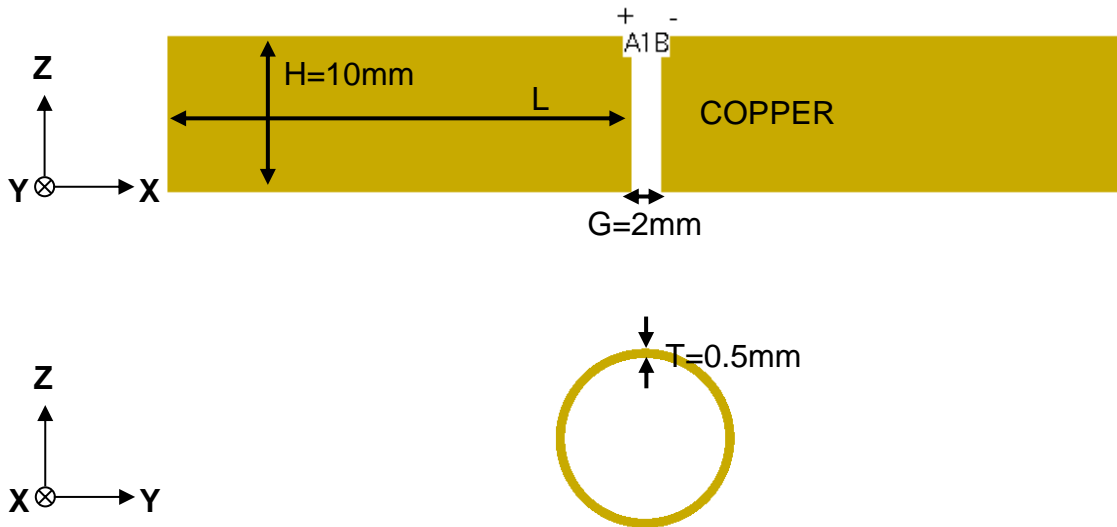

Fig. A- 1 Cylindrical dipole antennas geometry in XZ and YZ planes respectively

Table A- 1 Cylindrical dipole antennas length (L)

Dipole antenna	L (mm)
2GHz	30
2.5GHz	24
3.5GHz	16.5
5.5GHz	12

The simulated performance parameters for all dipole antennas are shown in Table A-2.

Table A- 2 Simulated cylindrical dipole antennas performance parameters

Dipole Antenna	S11 (dB)	BW (MHz)	Gain (dBi)	Directivity (dBi)	Radiation efficiency (%)
2GHz	-14.36	470	2.36	2.37	99.71
2.5GHz	-14.71	1000	2.61	2.65	99.12
3.5GHz	-17.41	2400	2.96	2.98	99.23
5.5GHz	-17.10	2200	4.58	4.66	98.14

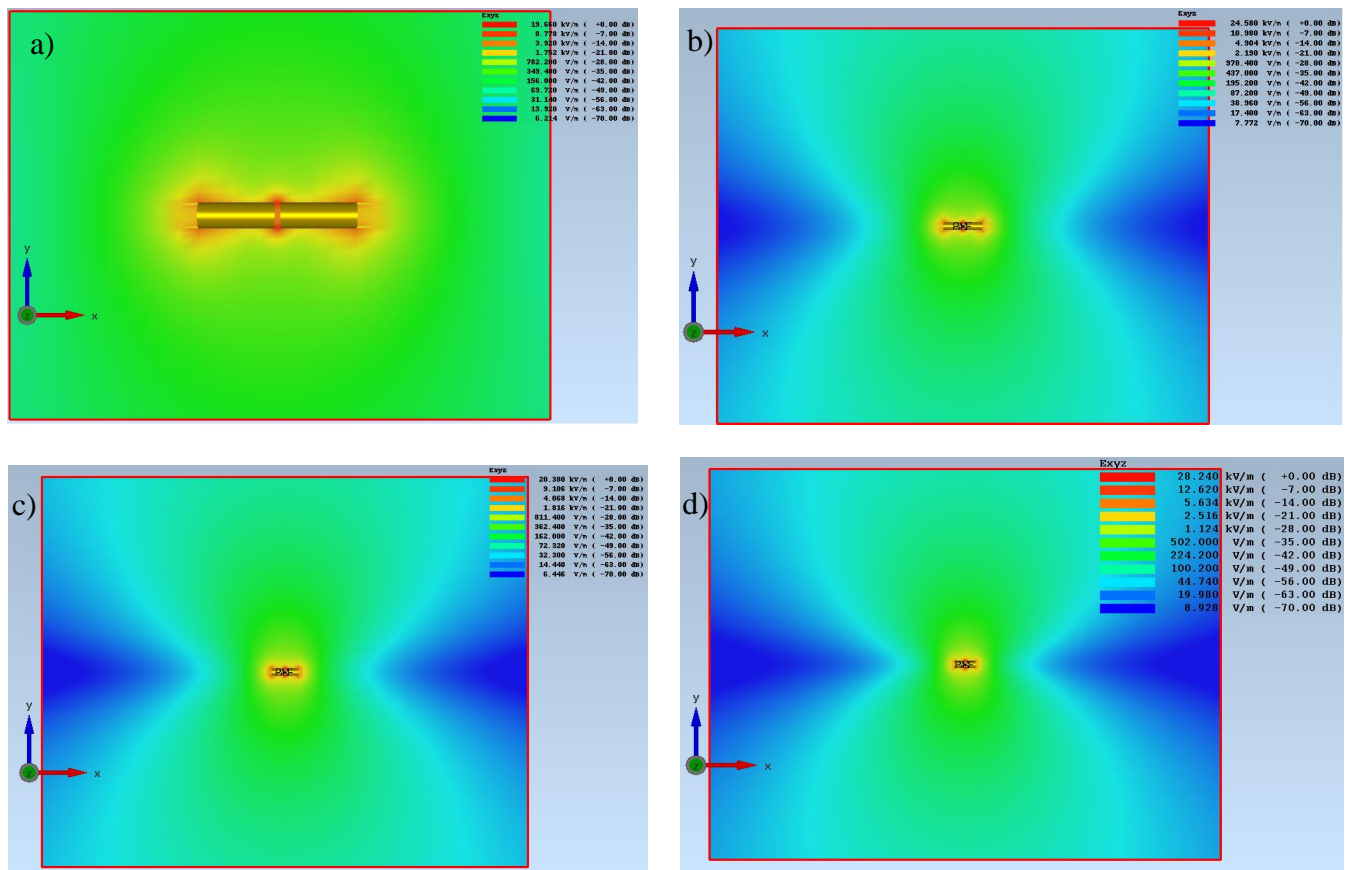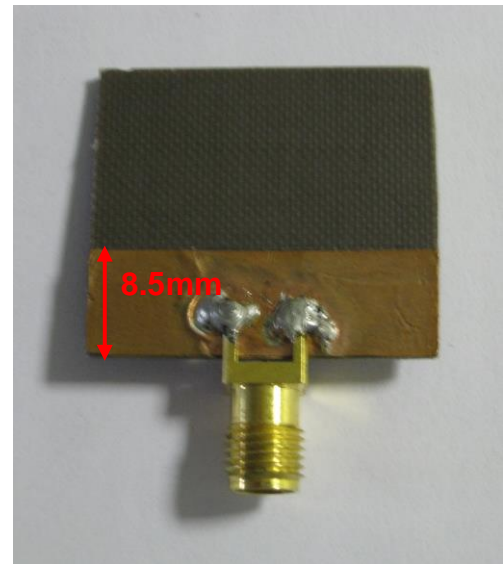The electric field distribution of the 2; 2.5; 3.5 and 5.5GHz dipole antennas is shown in Fig. A-2.

Fig. A- 2 Electric field distribution of: a) 2GHz, b) 2.5GHz, c) 3.5GHz and d) 5.5GHz cylindrical dipole antennas

A.2 5.8GHz printed monopole antenna

The 5.8GHz printed monopole antenna [1] geometry, used in Chapter 2, subsection 2.3.2, for the evaluation of HOCS torso phantom in terms of reflection coefficient is shown in Fig. A-3. The substrate used is Taconic – TLY (d = 1.6mm, εr = 2.2, tanδ = 0.0009).The monopole and the ground planes are made of copper with thickness t = 0.035mm.
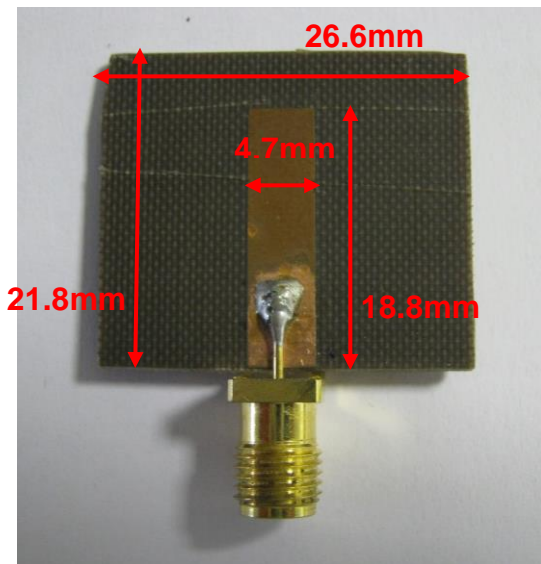
Front side (Monopole)   Back side (Ground plane)

Fig. A- 3 Geometry of 5.8GHz printed monopole antenna

The measured performance parameters of the 5.8GHz printed monopole antenna are shown in Table A-3.

Table A- 3 Measured performance parameters of the 5.8GHz printed monopole antenna

Fc (GHz)	S11 (dB)	BW (MHz)	Gain (dBi)	Directivity (dBi)	Radiation efficiency (%)
5.8	-29.21	1000	4.40	4.85	90.30

A.3 Printed monopole antennas

The geometry of the 2.5; 3.5 and 5.5GHz printed monopole antennas used in Chapter 2, sub subsection 2.3.4.1, for the simulation evaluation of HOCS phantom in terms of far field is shown in Fig. A-4 and the dimensions in Table A-4. The substrate is FR4-Epoxy (d=1.6mm, $\varepsilon r = 4.4$, tan$\delta = 0.002$). The monopole and the ground planes are copper with thickness t=0.035mm.
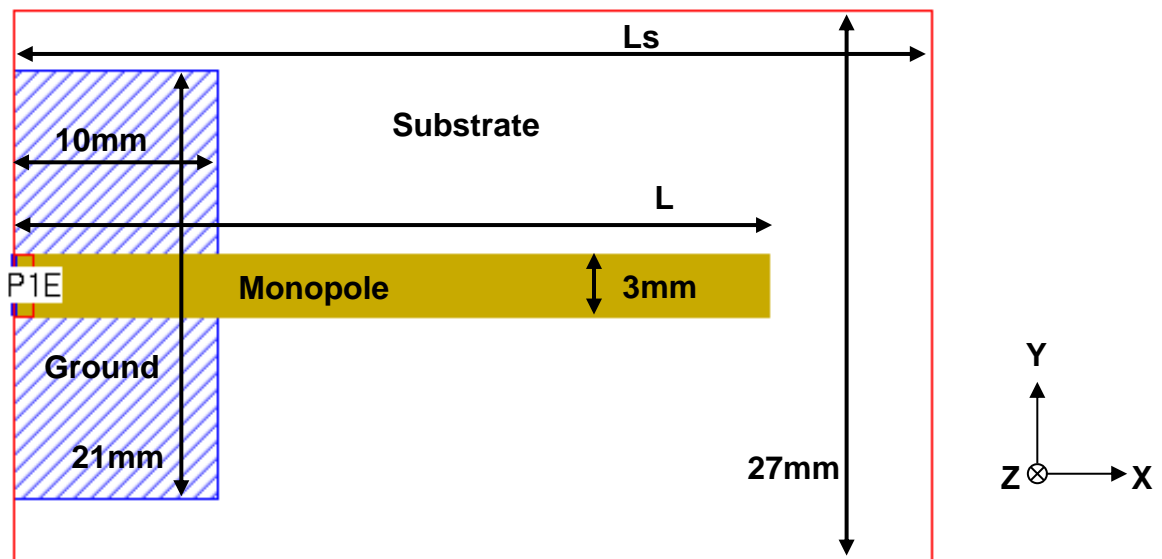

Fig. A- 4 5.8GHz printed monopole geometry

Table A- 4 Printed monopole antennas lengths (L, Ls)

Printed monopole antenna	L (mm)	Ls (mm)
2GHz	47	50
2.5GHz	37	45
3.5GHz	27	35
5.5GHz	19	30

References

[1]   C. A. Balanis, *Antenna Theory Analysis and Design*, 3rd ed. New Jersey: John Wiley & Sons, 2005.

[2]   A. Chauraya, "Photoconductive Switching using Silicon and its Applications in Antennas and Reconfigurable Metallodielectric Electromagnetic Band Gap (EBG)", PhD Thesis, Loughborough University, 2004.

APPENDIX B

PATCH ANTENNAS

The patch antennas used in Chapter 3 are three, operating at 2GHz, 2.5GHz and 5GHz [1]. The 2GHz patch was designed and fabricated by an older PhD work [2]. Though, it was re-measured so as to be characterized in the same measurement environment as the 2.5GHz and 5GHz were characterized. The 2.5GHz and the 5GHz patch antennas were designed and fabricated by the author of this thesis. These antennas were designed by using the Antenna Magus software and simulated via Empire-XPU software.

B.1 The 2GHz patch antenna

The 2GHz patch antenna geometry and dimensions are shown in Fig. B-1. The antennas ground plane and radiating parts are made of copper and copper tape respectively (**thickness =35μm**). The substrate is made of Rogers-RT/Duroid5880 (**εr=2.2 tanδ=0.0009, thickness=1.1mm**). The simulated and measured performance parameters of the 2GHz patch antenna are shown in Table B-1.

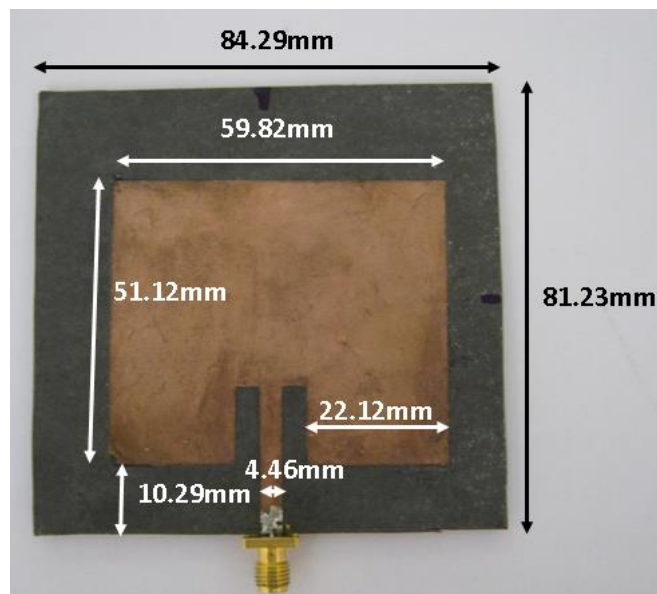**Fig. B- 1 The 2GHz patch antenna dimensions**

Table B- 1 2GHz patch antenna performance parameters

	Fc (GHz)	S11 (dB)	BW (MHz)	Gain (dBi)	Directivity (dBi)	Radiation efficiency (%)
Measurements	1.987	-21.76	20MHz	+7.05	+7.57	88.14
Simulations	1.950	-24.82	30MHz	+6.80	+7.10	93.32

B.2 The 2.5GHz patch antenna

The 2.5GHz patch antenna geometry and dimensions are shown in Fig. B-2. The antennas ground plane and radiating parts are made of copper (**thickness =35μm**). The substrate is Taconic-TLY-5 (**εr=2.2 tanδ=0.0009, thickness=1.6mm**). The simulated and measured performance parameters of the 2.5GHz patch antenna are shown in Table B-2.

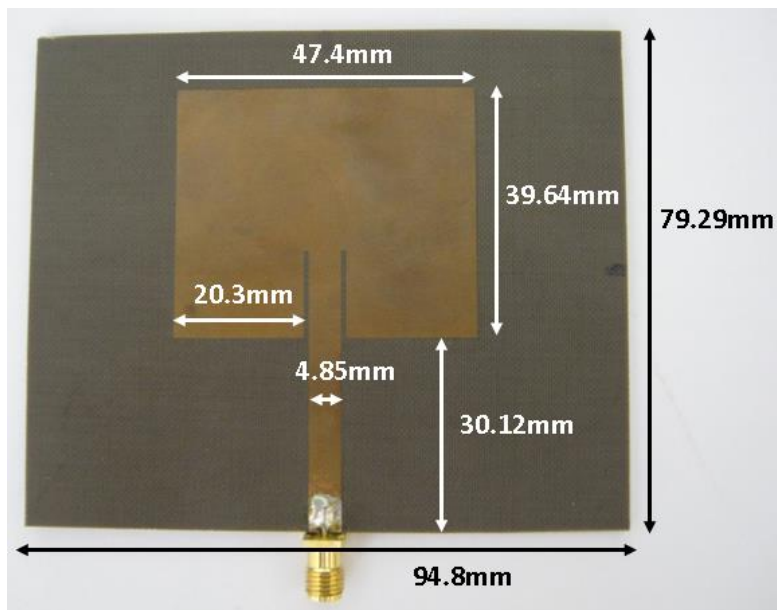**Fig. B- 2 The 2.5GHz patch antenna dimensions**

Table B- 2 2.5GHz patch antenna performance parameters

	Fc (GHz)	S11 (dB)	BW (MHz)	Gain (dBi)	Directivity (dBi)	Radiation efficiency (%)
Measurements	2.485	-24.47	30	+7.75	+8.07	92.62
Simulations	2.490	-30.76	35	+7.30	+7.61	93.11

B.3 The 5GHz patch antenna

The 5GHz patch antenna geometry and dimensions are shown in Fig. B-3. The antennas ground plane and radiating parts are made of copper (**thickness = 35µm**). The substrate is Taconic-TLY-5 (**εr=2.2 tanδ=0.0009, thickness=0.8mm**). The simulated and measured performance parameters of the 2GHz patch antenna are shown in Table B-3.
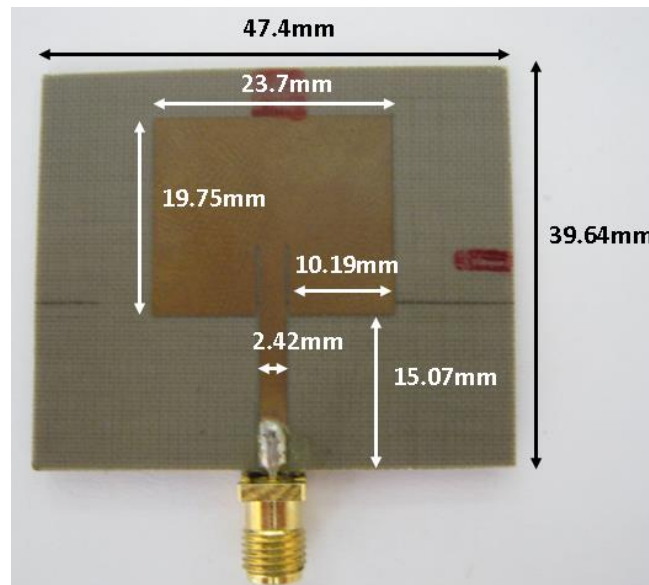

Fig. B- 3 The 5GHz patch antenna dimensions

Table B- 3 5GHz patch antenna performance parameters

	Fc (GHz)	S11 (dB)	BW (MHz)	Gain (dBi)	Directivity (dBi)	Radiation efficiency (%)
Measurements	4.965	-25.95	75MHz	+7.75	+8.09	92.39
Simulations	4.965	-30.60	75MHz	+7.30	+7.59	93.50

References

[1]   C. A. Balanis, *Antenna Theory Analysis and Design*, 3rd ed. New Jersey: John Wiley & Sons, 2005.

[2]   A. Chauraya, "Photoconductive Switching using Silicon and its Applications in Antennas and Reconfigurable Metallodielectric Electromagnetic Band Gap (EBG)", PhD Thesis, Loughborough University, 2004.